



Università degli Studi di Padova
Facoltà di Ingegneria

Corso di Laurea Specialistica
in Ingegneria Elettronica

TESI DI LAUREA

**Characterization and reliability
of NPD/ Alq_3 OLEDs,
submitted to thermal and
electrical ageing**

LAUREANDO: Junior Jader Framarin

RELATORE: Ch.mo Prof. Gaudenzio Meneghesso

CORRELATORE: Ing. Alessandro Pinato

Anno Accademico: 2009-2010

*“Considerate la vostra semenza:
fatti non foste a viver come bruti,
ma per seguir virtute e canoscenza”*

Dante Alighieri, Inferno, Canto XXVI

Indice

Abstract	9
Introduction	11
1 Organic Semiconductors	15
1.1 Historical background	15
1.2 π conjugated materials	16
1.2.1 Small molecules	19
1.2.2 Polymers	20
1.3 Materials	21
1.4 Electrical properties	22
1.4.1 Charge Carrier Transport	24
1.5 Optical Properties	28
1.5.1 Exciton	30
1.5.2 Luminescence	32
1.6 Device Structures and Properties	33
2 OLEDs	37
2.1 OLEDs Introduction	37
2.2 Basic Structure of OLEDs	41
2.3 Multilayer structure	42
2.4 Basic Operation of OLEDs	43
2.5 Carrier Transport in OLEDs	45
2.5.1 Polaron vs Disorder Models for Carrier Hopping	46
2.5.2 Long-Range Correlations	47
2.5.3 Carrier Injection	48
2.5.4 Space-Charge Limited Versus Injection-Limited Current Mechanisms	50
2.6 The Efficiency of OLEDs	52
2.7 Degradation Mechanisms	53
2.7.1 Dark spot formation	54
2.7.2 Photo-oxidation	54
2.7.3 Recrystallization	55
2.7.4 Metal atom migration	55
2.7.5 Molecule-specific degradation processes	55

2.7.6	Electrical breakdown	55
2.8	OLED Fabrication Procedures	56
2.8.1	Thermal Vacuum Evaporation	56
2.8.2	Wet-Coating Techniques	57
2.9	Materials for OLEDs	58
2.9.1	Anode Materials and HTLs or Buffers	58
2.9.2	Small Electron-Transporting and Emitting Molecules	60
2.9.3	Cathode and Organic/Cathode Buffer Materials	61
3	NPD/Alq₃	63
3.1	Alq ₃ Introduction	63
3.2	Crystalline Phases of Alq ₃	65
3.3	Thermal Properties of Alq ₃	68
3.4	The Molecular Structure of δ -Alq ₃	74
3.4.1	High resolution powder diffraction using synchrotron radiation	74
3.4.2	Vibrational Analysis	80
3.5	Population and properties of the electronic excited triplet state	81
3.5.1	Population of the triplet states	81
3.5.2	Phosphorescence of Alq ₃	86
4	Devices	95
4.1	Devices description	95
4.1.1	With HIL	96
4.1.2	Without HIL	97
4.1.3	Samples	97
4.2	Instruments	98
4.2.1	HP 4155 Semiconductor Parameter Analyzer	98
4.2.2	HP 4284A Precision LCR Meter	98
4.2.3	Newport 818-UV	99
4.2.4	Hamamatsu Phemos-200	100
4.2.5	Ocean Optics USB-4000	100
4.2.6	OLED fixture	102
5	Measurement setup and characterization techniques	103
5.1	Electrical measurement	103
5.1.1	Current-Voltage measurement (I-V)	103
5.1.2	Capacity-Frequency measurement (C-F)	105
5.1.3	Capacity-Voltage measurement (C-V)	105
5.2	Optical measurement	105
5.2.1	Optical power measurements (L-I)	106
5.2.2	Emission microscope measurements	108
5.2.3	Spectrum measurements	110

6	Results and discussions	113
6.1	Thermal/Electrical stress for OLED with HIL	113
6.1.1	Degradation of the electrical parameters	113
6.1.2	Degradation of the optical parameters	115
6.1.3	Positive charge and defect generation	117
6.1.4	Reference graphs	121
6.2	Thermal/Electrical stress for OLED without HIL	137
6.2.1	Degradation of electrical and optical parameters . . .	137
6.2.2	Intrinsic weakness of OLEDs without HIL	138
6.2.3	Reference graphs	139
6.3	Electrical stress for OLED with HIL at different current . . .	155
6.3.1	Reference graphs	156
6.4	Comparison and comments	165
6.4.1	Thermal stress	165
6.4.2	OLEDs with vs OLEDs without HIL	165
6.4.3	OLEDs with HIL submitted to different current . . .	165
	Conclusions	167
	Acknowledgement	169
	Bibliography	171

Abstract

In this thesis it is reported a study on the degradation and the reliability of organic semiconductor LEDs (OLEDs), submitted to different stress conditions. We have investigated two sets of devices: all the devices are built using as hole transport layer (HTL) an NPD layer, and as electron transport layer (ETL) an Alq₃ layer. The only difference is the presence of an hole injection layer (HIL) in 1 of the 2 sets. Its function, is to enhance the hole injection from ITO anode through the NPD improving the recombination of the carriers that takes place in the interface between the NPD and Alq₃ layers. We carried out thermal and electrical ageing at different temperature values and finally, an analysis of degradation kinetics has been performed.

Introduction

Organic light-emitting diodes (OLEDs) have attracted much attention for their large potential in flat-panel display application. However, the lifetime of OLEDs is still critical in order to fulfill market standards. OLEDs' luminance reduction over time has been deeply investigated [6-13], and driving strategies and new materials have been developed in order to solve this criticality in OLED spread [6], [14]. In this paper, we want to bring further investigation on the degradation mechanisms in Alq₃-based OLED devices. Since the report on the first efficient OLED by Tang and Van Slyke in 1987 [15], tris(8-hydroxyquinoline)aluminum (Alq₃) has been one of the most widely adopted emitter material in OLED technology. Alq₃ can be used for the realization of devices emitting in the green-red spectral region. The degradation of OLEDs during operation time can be strongly determined by the worsening of the properties of the Alq₃ layer. In fact, Alq₃-based OLEDs can be affected by several failure mechanisms, such as the formation of dark spots [16], [17], catastrophic failures [18], and long-term intrinsic degradation that is responsible for the OLED brightness decrease over time without any visible deterioration of the active area. Over the last decade, the first two issues have been overcome by both using improved sealing techniques and depositing organic materials with high purity degree. On the other hand, intrinsic degradation still remains an open issue, which is worth of investigation, even though several hypotheses on the origins of this kind of degradation have been already proposed.

For a long time, the morphological instability of the hole transport layer (HTL) has been depicted as one of the main mechanisms responsible for OLED degradation [19], [20]. This resulted into the research of hole transport materials with high glass transition temperatures (T_G) [21], [22]. These studies led to the synthesis of several important OLED materials. Although it has been demonstrated that the use of HTLs with high T_G increases the device robustness to high-temperature environments, it does not impact its operational stability, particularly at room temperature [23], [24]. Furthermore, OLED stability has been chased by different methods, such as the introduction of a Copper Phthalocyanine (CuPc) buffer layer between the ITO and the hole injection layer (HIL), and the doping of the HTL. Nevertheless, the argued reasons behind the success of these technological solutions were often incomplete and sometimes contradictory. In particu-

lar, the key issue concerned the localization of the degradation processes, in the HTL or in the electron transport layer (ETL). A turning point was set by Aziz et al. who observed that, in Alq₃, significant photoluminescence decrease is observed during hole injection, while the photoluminescence stays almost constant during electron injection [25]. These results therefore provided strong evidence that injection of holes into the Alq₃ layers can be responsible for the optical degradation of OLEDs. The enhanced stability of OLEDs developed by inserting a mixed layer at the HTL–Alq₃ interface confirmed this hypothesis, suggesting that OLED degradation mainly takes place at or close to that interface. Furthermore, the long-term luminance decrease has been related to the instability of the Alq₃ cationic species [26] and to the accumulation of positive charge at the emitting OLED interface [27], [28]. The instability of the cationic species induces the creation of by-products that have been related to a decrease in device electroluminescence. Moreover, it has been shown that these by-products play different roles as charge traps, electron–hole recombination centers, and fluorescence quenchers. However, hole injection into the Alq₃ layer still appears to be one of the main factors responsible for OLED optical degradation. This hypothesis is confirmed by the fact that cyclic voltammetry on Alq₃ in solutions showed the irreversibility of the Alq₃ oxidation process [29].

However, an accepted understanding on the chemical nature of the charge generation at the HTL/ETL interface is still lacking. Although significant progress in understanding OLED degradation phenomena has been accomplished in the last years, a deeper comprehension of the base mechanisms beneath the OLED intrinsic degradation is essential in order to improve the device lifetime, even in commercial multilayer OLEDs. With this thesis, we want to investigate the mechanisms responsible for OLED degradation by means of optical and electrical measurement techniques.

This thesis is organized as follows:

- Chapter 1 presents a general introduction to the organic semiconductor world.
- Chapter 2 discusses the basic theory of organic light-emitting-diodes (OLEDs), the main electro-optical characteristic and the equations governing their behavior.
- Chapter 3 presents the two organic layers of the devices under test studied in this work.
- Chapter 4 describes the devices under test and the instrument used.
- Chapter 5 deals in detail the measuring setup and the techniques used for characterization of devices.
- Chapter 6 summarizes the data obtained in characterizing the OLEDs during the electrical accelerated aging phase, in which is discussed the

degradation of the optical and electrical parameters and the generation of defects and positive charge.

Capitolo 1

Organic Semiconductors

1.1 Historical background

With the invention of the transistor around the middle of the last century, inorganic semiconductors like Si or Ge began to take over the role as dominant material in electronics from the before prevailing metals. At the same time, the replacement of vacuum tube based electronics by solid state devices initiated a development which by the end of the 20th century has lead to the omnipresence of semiconductor microelectronics in our everyday life. Now at the beginning of the 21st century we are facing a new electronics revolution that has become possible due to the development and understanding of a new class of materials, commonly known as Organic Semiconductors. The enormous progress in this field has been driven by the expectation to realize new applications, such as large area, flexible light sources and displays, low-cost printed integrated circuits or plastic solar cells from these materials.

Strictly speaking organic semiconductors are not new. The first studies of the dark and photoconductivity of anthracene crystals (a prototype organic semiconductor) date back to the early 20th century. Later on, triggered by the discovery of electroluminescence in the 1960s, molecular crystals were intensely investigated by many researchers. These investigations could establish the basic processes involved in optical excitation and charge carrier transport. Nevertheless, in spite of the principal demonstration of an organic electroluminescent diode incorporating even an encapsulation similar to the ones used in nowadays commercial display applications, there were several draw-backs preventing practical use of these early devices. For example, neither high enough current densities and light output nor sufficient stability could be achieved. The main obstacles were the high operating voltage as a consequence of the crystal thickness in the micrometer to millimeter range together with the difficulties in scaling up crystal growth as well as preparing stable and sufficiently well-injecting contacts to them.

Since the 1970s the successful synthesis and controlled doping of conjuga-

ted polymers established the second important class of organic semiconductors which was honored with the Nobel Prize in Chemistry in the year 2000. Together with organic photo-conductors (molecularly doped polymers) these conducting polymers have initiated the first applications of organic materials as conductive coatings or photo-receptors in electro-photography.

The interest in undoped organic semiconductors revived in the 1980s due to the demonstration of an efficient photovoltaic cell incorporating an organic hetero-junction of p- and n-conducting materials as well as the first successful fabrication of thin film transistors from conjugated polymers and oligomers. The main impetus, however, came from the demonstration of high-performance electroluminescent diodes from vacuum-evaporated molecular films and from conjugated polymers. Owing to the large efforts of both academic and industrial research laboratories during the last 15 years, organic light-emitting devices (OLEDs) have progressed rapidly and meanwhile lead to first commercial products incorporating OLED displays. Other applications of organic semiconductors e.g. as logic circuits with organic field-effect transistors (OFETs) or organic photovoltaic cells (OPVCs) are expected to follow in the near future.

1.2 π conjugated materials

The name organic semiconductor denotes a class of materials based on carbon, that display semiconducting properties. Most attractive opto-electronic properties of these materials arise from the carbon atom features. In its ground state, the carbon atom has the following particular electronic structure: $1s^2 2s^2 2p_x^1 2p_y^1$. This means that carbon has two electrons in orbital 1s, two in orbital 2s and 2 in orbitals 2p (Figure 1.1). Since the s orbitals are totally filled, an atom carbon should form only two bonds involving the two unpaired electrons in 2p orbitals. Instead, it is well known that carbon is tetravalent and forms four bonds. This can be explained using the valance bond theory. This theory asserts that a chemical bond is formed by the overlapping of the atomic orbitals which contain the electrons participating in the bond, in order to lower the total energy of the system. Since the atomic orbitals are the wave functions solving the Schrödinger equation for an atom, the overlapping between atomic orbitals corresponds to the combination of the wave functions describing the two electrons involved in the bond.

In the case of carbon atom the linear combination can be between 2s orbital and one, two or three 2p orbitals and is properly denominated “hybridization”. If the mix occurs between the 2s orbital and all the 2p orbitals, we obtain four degenerate sp^3 hybrid orbitals lying in a tetrahedral geometry around the central carbon atom ($109,47^\circ$ between bond axes). This hybridization is the one found in diamond, in which every carbon atom is bonded to another four carbons.

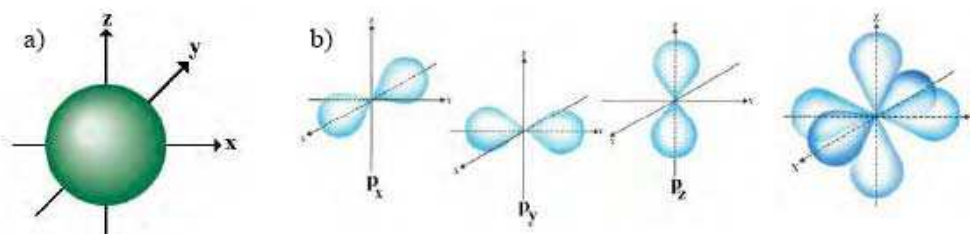


Figure 1.1: a) Spherical shape of s orbital. b) Representation of the three p orbitals (p_x , p_y and p_z) and of their spatial combination.

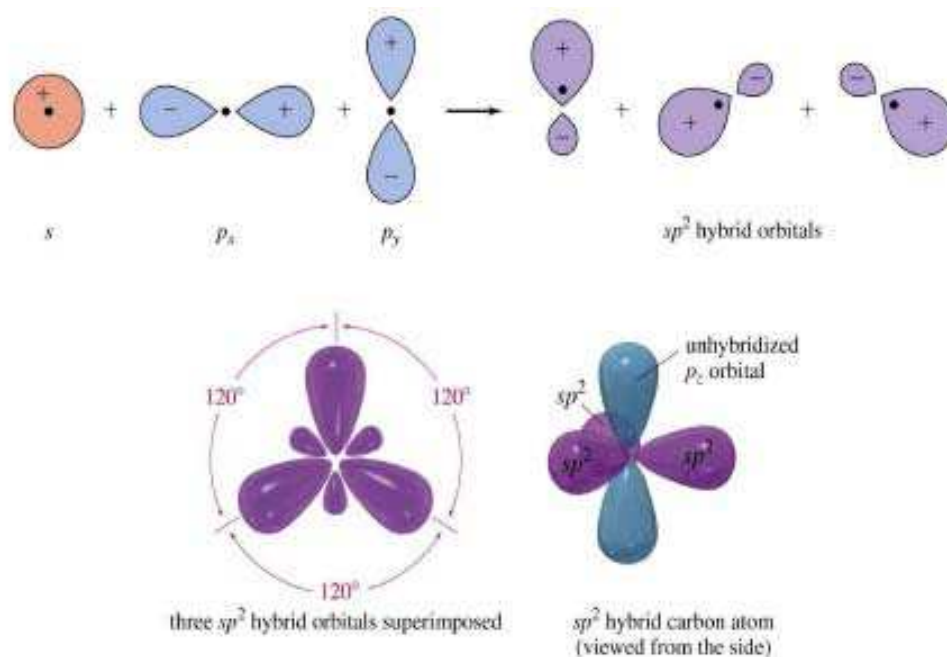


Figure 1.2: sp^2 hybridization of atomic orbitals s and p_x and p_y in a carbon atom.

Mixing can also occur between 2s orbital and one 2p orbital to form 2 equivalent sp orbitals. These are on the same plane passing through the nucleus, and lie at 180° from one each other. The 2 pure p remaining orbitals lie in a plane which is perpendicular to the former. In the case of the sp^2 hybridization, the 2s orbital is mixed with two 2p orbitals, for example the $2p_x$ and the $2p_y$ in Figure 1.1. Three new hybrid states are formed that lie in the XY plane, leaving the $2p_z$ orbital unchanged as it can be seen in Figure 1.2.

In the top view of the hybridized atom (Figure 1.2), it is possible to see that all the hybrid orbitals lie in the same plane at an angle of 120° to each other. This configuration is the one in which the electron pairs are further

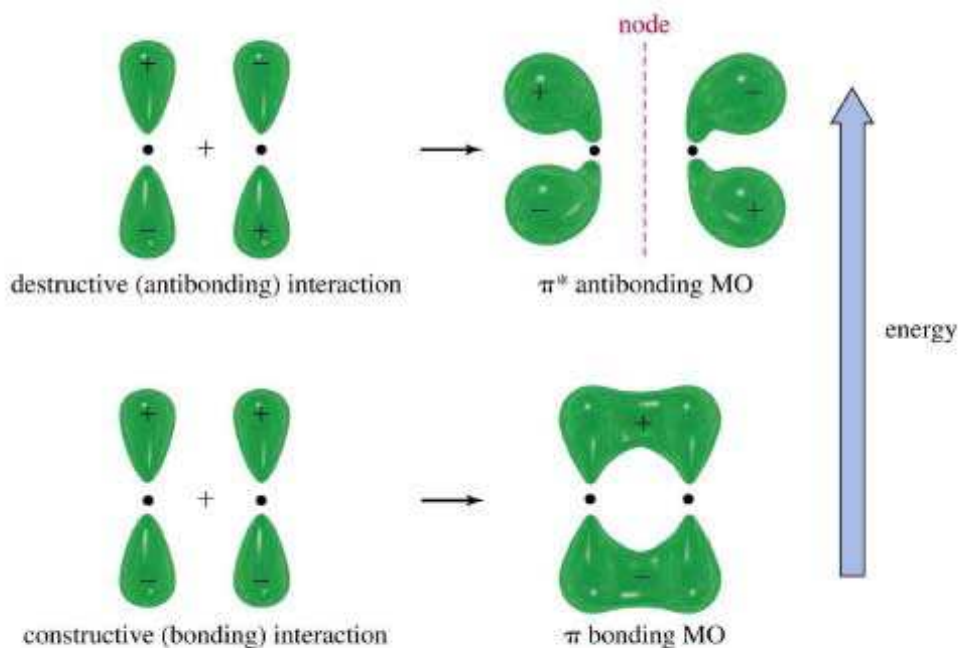


Figure 1.3: The two possible configurations of π bond due to p_z orbitals.

apart, thus being energetically the most favorable.

The first bond that occurs between two hybridized atoms is of the σ type. In this bond, the electron density lies between the nuclei, and one pair of electrons is shared. In order to form a second bond, the p_z orbitals from both atoms overlap laterally (i.e. sideways) and form a π bond. This lateral bonding is therefore weaker than the highly directional σ bond. One double bond consists of a σ bond and a π bond, both of them having one pair of electrons shared.

Since the electronic distribution in the π bond is less spatially localized than that of the σ bond, the energy difference between the ground state (bonding) and the excited state (antibonding) is smaller than for the σ case. The two possible configurations are shown in Figure 1.3.

One important point to highlight, is that single bonds, allow rotations along the σ bond axis, but double bonds, since they must have a π bond, do not allow any kind of rotation. In a way, double bonds induce more rigidity and hindrance in the molecular geometry that cannot be released unless the bond is broken.

Therefore π electrons are not confined between the nuclei, rather they form an electron density cloud above and below the plane of the σ bond. This cloud creates an electron system ideally delocalized over the entire molecule or polymer. In real cases, this delocalization can be confined in only a part of the molecule. As a matter of fact, conjugation exists, and it largely determines the electron energy structure of the organic materials.

Indeed in organic semiconductors, which are a class of materials based on carbon displaying semiconducting properties, the common characteristics is that the electronic structure is based on π -conjugated double bonds between carbon atoms. The delocalization of the electrons in the π -molecular orbitals is the key feature, that allows injection delocalization and charge transport.

Beside the strong intramolecular forces in the molecular skeleton, the solid (crystal or thin film) is held together by weaker van der Waals forces. Because of these weak interactions, it is to be expected that the properties of the individual molecules are mostly retained. Indeed, many studies show how it is possible to tune solid state properties adjusting the molecular structure by means of chemical tailoring. At the same time the “supra-molecular level” should not be disregarded. In this case the molecular order in the solid state packing and the polymorphism play a crucial role in determining properties such as optical emission and charge transport.

π -conjugated materials can be divided into two main classes according to their molecular weight (MW). Low MW organic semiconductors are usually named small molecules, whereas π -conjugated polymers have MW reaching many thousands of g/mol.

1.2.1 Small molecules

An organic small molecule is a molecule based on carbon which presents low MW, low spatial extent and generally short conjugation length. Typically, interactions between different small molecules are dominated by van der Waals forces.

A plethora of organic species belong to this class: polycondensate aromatic hydrocarbons as pentacene (Figure 1.4a) and perylene (Figure 1.4b), organo-metallic complexes such as metalphthalocyanines and oxy-quinoline (Figure 1.4c) fullerenes and dendrimers. However, the largest part of small molecules is represented by oligomers (from the Greek: oligos, “a few”, and meros, “part”). An oligomer consists of a finite number of monomer unit. Some examples of oligomers are: oligo-phenylenes or oligo-thiopenes (Figure 1.4d).

Generally, molecular materials are processed by vacuum sublimation and solution-based processing techniques can rarely be employed. Films grown on dielectric substrates are mainly poly-crystalline, and their growth (and consequently the morphology of the film) can be partially controlled acting on the vacuum sublimation parameters and selecting the nature of the substrate. Using small molecules, the analysis of the early growth stages of the active layer via atomic force microscopy (AFM) is also possible.

Concerning the transport properties, there is a large number of hole transport (p-type, e.g. α sexy-thiophene, named α -6T) and electron transport (n-type, e.g. perylene derivative, named PTCDI-C₁₃H₂₇) semiconductor small molecules. In the last years, ambipolar small molecules

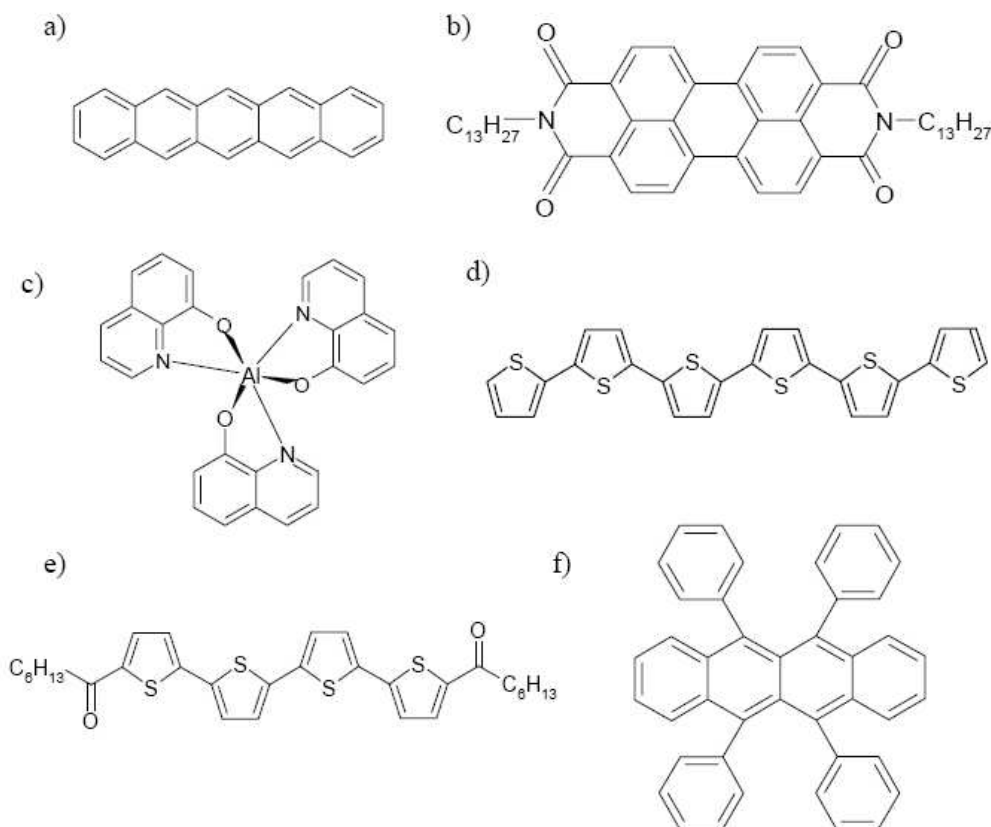


Figure 1.4: Chemical structure of some widely studied small molecule organic semiconductors. a) Pentacene; b) N,N-ditrydecylperylene-3,4,9,10-tetracarboxylic diimide (PTCDI- $C_{13}H_{27}$); c) Allumin oxyquinolina (Alq_3); d) α sexy-thiophene (α -6T); e) α, ω -dihexylcarbonylquaterthiophene ($DHCO_4T$); f) Rubrene.

(e.g. $DHCO_4T$, Figure 1.4e) have also been synthesized; these molecules are able to transport both electrons and holes.

1.2.2 Polymers

A polymer (from Greek: polu, “many”; and meros, “part”) consists of the repetition of structural units, typically large mass molecules called monomers (from Greek mono “one” and meros “part”) forming a long molecular chain along which π -electrons are delocalized. Chemical chains can take up a range of different conformations by rotating, twisting or distorting its backbone bonds. In addition, it may contain chain interruptions, chemical and structural defects which contribute to break the conjugation. So the π -electrons delocalization becomes shorter and with distributed lengths. Indeed, the fundamental studies of Bassler and co-workers have shown

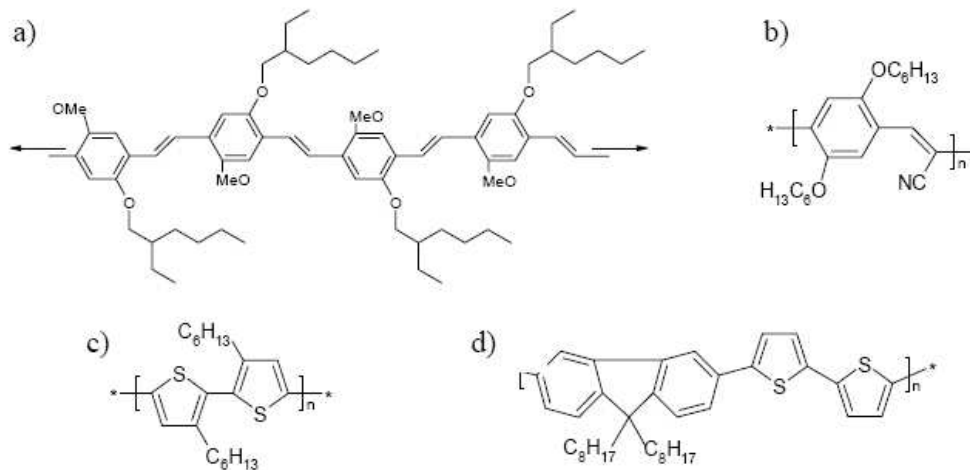


Figura 1.5: Chemical structure of some widely studied polymer organic semiconductors. a) Long chain of Poly[2-methoxy-5-(2-ethylhexyloxy)-1,4-phenylene-vinylene] (MEH-PPV); b) Poly[2,5,2',5'-tetrahexyloxy-7,8'-dicyano-di-p-phenylenevinylene] (CN-PPV); c) Poly[3-hexylthiophene] (P3HT); d) Poly[9,9'-dioctyl-fluorene-co-bithiophene] (F8T2).

that conjugated polymers must be considered rather as a linear arrays of conjugated segments [31].

In amorphous polymers (the great majority), the case is further complicated as each conjugation section of the chain is randomly oriented with respect to the others. In this situation there is a range of conjugation lengths, with the obvious consequence that energy levels are spread out over a wider interval.

The most studied organic semiconductor polymers belong principally to three families: poly (phenylenevinylene), e.g. MEH-PPV (Figure 1.5a); poly-thiophene, e.g. P3HT (Figure 1.5c); and poly-fluorenes, e.g. F8T2 (Figure 1.5d).

Processability of polymers is usually restricted to wet techniques; this can be an advantage, because of the inherently low cost and large area coverage of such techniques, but also a disadvantage, as the structural and morphological control of usually amorphous thin films is limited. As a consequence, charge mobility in polymeric thin films is typically lower with respect to that of small molecule films. Theoretically, there is no particular reason for the majority of polymers not to be ambipolar; however they are found to be mainly p-type, and only a few are n-type.

1.3 Materials

As already mentioned above, there are two major classes of organic semiconductors: low molecular weight materials and polymers. Both have in

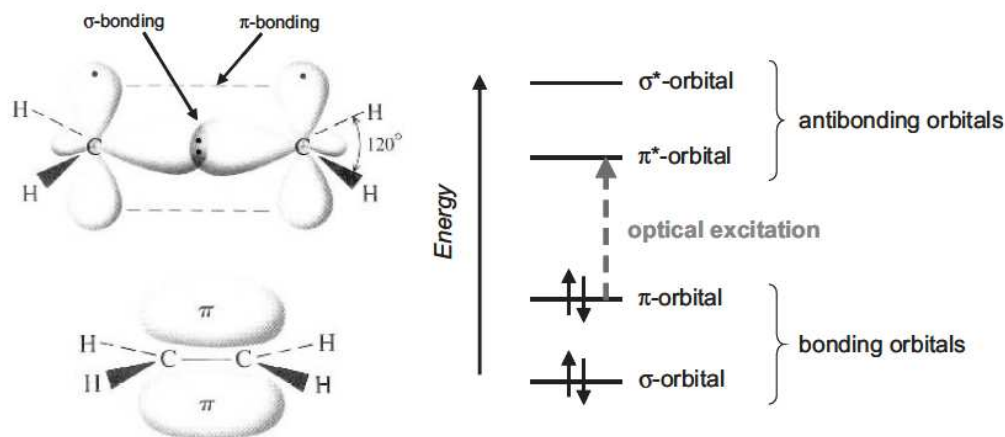


Figure 1.6: Left: σ - and π -bonds in ethene, as an example for the simplest conjugated π -electron system. The right viewgraph shows the energy levels of a π -conjugated molecule. The lowest electronic excitation is between the bonding π -orbital and the antibonding π^* -orbital (adopted from [22]).

common a conjugated p-electron system being formed by the p_z -orbitals of sp^2 -hybridized C-atoms in the molecules (see Figure 1.6). As compared to the σ -bonds forming the backbone of the molecules, the π -bonding is significantly weaker. Therefore, the lowest electronic excitations of conjugated molecules are the π - π^* -transitions with an energy gap typically between 1.5 and 3 eV leading to light absorption or emission in the visible spectral range. As shown in Table 1 for the family of the polyacenes the energy gap can be controlled by the degree of conjugation in a molecule. Thus chemistry offers a wide range of possibilities to tune the optoelectronic properties of organic semiconducting materials. Some prototype materials which are also discussed in this book are given in Figure 1.3.

An important difference between the two classes of materials lies in the way how they are processed to form thin films. Whereas small molecules are usually deposited from the gas phase by sublimation or evaporation, conjugated polymers can only be processed from solution e.g. by spin-coating or printing techniques. Additionally, a number of low-molecular materials can be grown as single crystals allowing intrinsic electronic properties to be studied on such model systems. The controlled growth of highly ordered thin films either by vacuum deposition or solution processing is still subject of ongoing research, but will be crucial for many applications.

1.4 Electrical properties

All the organic compounds designed as semiconductors are those made of sp^2 hybridized carbon atoms, also called conjugated. As we report in section 1.2, under such circumstances, each carbon is linked to its neighbors by

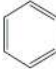
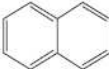
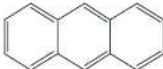
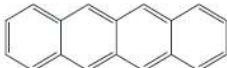
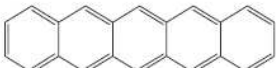
Molecule	Structure	Absorption Maximum
Benzene		255 nm
Naphthalene		315 nm
Anthracene		380 nm
Tetracene		480 nm
Pentacene		580 nm

Figura 1.7: Molecular structure of the first five polyacenes, together with the wavelength of the main absorption peak.

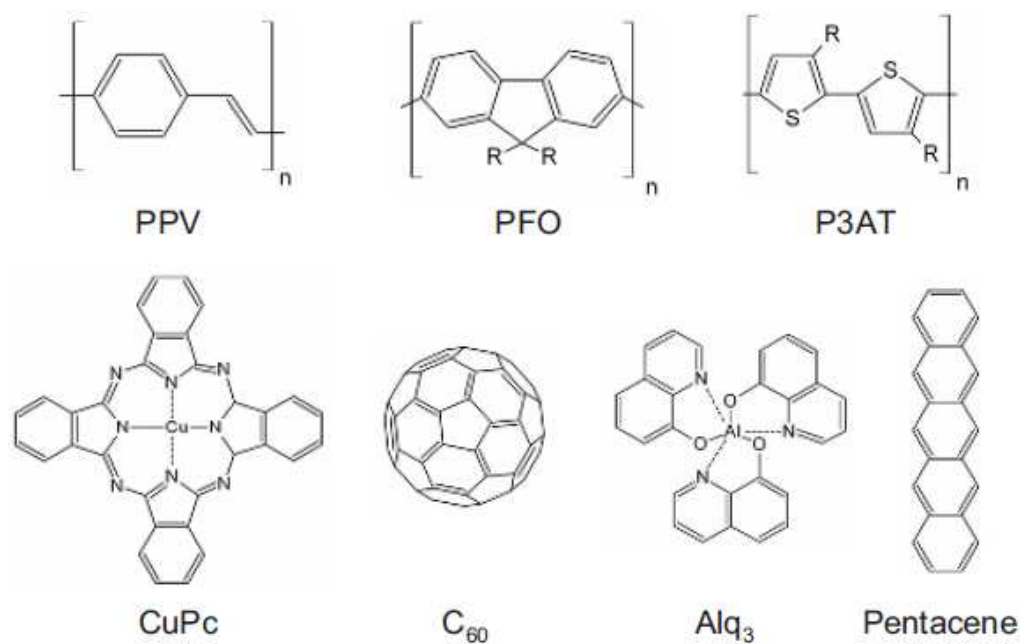


Figura 1.8: Molecular structure of some prototype organic semiconductors: PPV: poly(p-phenylenevinylene), PFO: polyfluorene, P3AT: poly(3-alkylthiophene), Alq_3 : tris(8-hydroxyquinoline)aluminium, fullerene C_{60} , CuPc: Cu-phthalocyanine, pentacene.

three σ bonds resulting from the hybridization of $2s$, $2p_x$, and $2p_y$ orbitals while the remaining $2p_z$ orbital forms a π bond which presents a signifi-

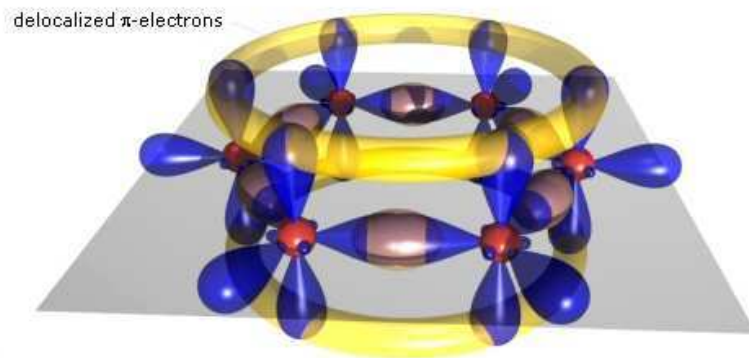


Figure 1.9: Electrons and orbitals delocalization in benzene complex

cantly less overlap with respect to σ bonds. For this reason, the energy distance between the bonding and the anti-bonding molecular orbitals is somewhat reduced thus allowing visible light absorption by the material and semiconductor behavior at nonzero temperature.

In the case of a ideal long chain of carbon atoms, the π bonds delocalize over the whole chain and form a one-dimensional electron system. The resulting one-dimensional band has substantial band width and the chain can be viewed as a one-dimensional semiconductor with a filled valence band originating from the HOMO (highest occupied molecular orbital) and an empty conduction band coming from LUMO (lowest unoccupied molecular orbital). In this scenario it is quite understandable why charges can be injected and reside in conjugated molecular system. However, the limiting step for charge transport in a solid is not within the molecular unity but it involves charge transfer between molecules (or molecular chain). Because orbital overlap between molecules is low the phenomenon of charge transport in conjugated solids is not unambiguously rationalized.

1.4.1 Charge Carrier Transport

When transport of electrons or holes in an organic molecular solid is considered, one has to bear in mind that this involves ionic molecular states. E.g. in order to create a hole, an electron has to be removed to form a radical cation M^+ out of a neutral molecule M . This defect electron can then move from one molecule to the next. In the same way, electron transport involves negatively charged radical ions M^- . (Qualitatively, the same arguments hold for polymers, however, in this case charged states are usually termed positive or negative polarons.) As compared to isolated molecules in the gas phase, these ionic states are stabilized in the solid by polarization energies leading to an energy level scheme as shown in Figure 1.4.1. From this picture one can clearly see that due to the already mentioned exciton binding energy the optical gap between the ground state and the first exci-

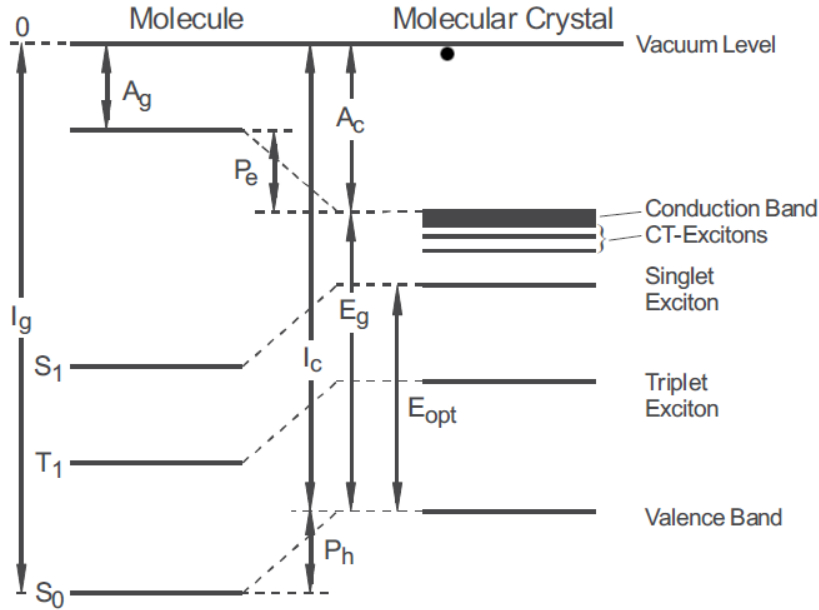


Figure 1.10: Energy levels of an isolated molecule (left) and a molecular crystal (right). I_g and A_g denote the ionization potential and electron affinity in the gas phase, I_c and A_c the respective quantities in the crystal. Due to the polarization energies P_h and P_e charged states are stabilized in the crystal. E_g is the single particle gap being relevant for charge carrier generation, whereas E_{opt} denotes the optical gap measured in absorption and luminescence. Their difference is the so-called exciton binding energy.

ted singlet state is considerably less than the single particle gap to create an uncorrelated electron-hole pair. In going from molecular crystals to disordered organic solids one also has to consider locally varying polarization energies due to different molecular environments which lead to a Gaussian density of states for the distribution of transport sites as shown in Figure 1.4.1.

Thus, depending on the degree of order the charge carrier transport mechanism in organic semiconductors can fall between two extreme cases: band or hopping transport. Band transport is typically observed in highly purified molecular crystals at not too high temperatures. However, since electronic delocalization is weak the bandwidth is only small as compared to inorganic semiconductors (typically a few kT at room temperature only). Therefore room temperature mobilities in molecular crystals reach only values in the range 1 to 10 cm^2/Vs . As a characteristic feature of band transport the temperature dependence follows a power law behavior

$$\mu \propto T^{-n} \quad \text{with } n = 1 \dots 3 \quad (1.1)$$

upon going to lower temperature. However, in the presence of traps significant deviations from such a behavior are observed [32].

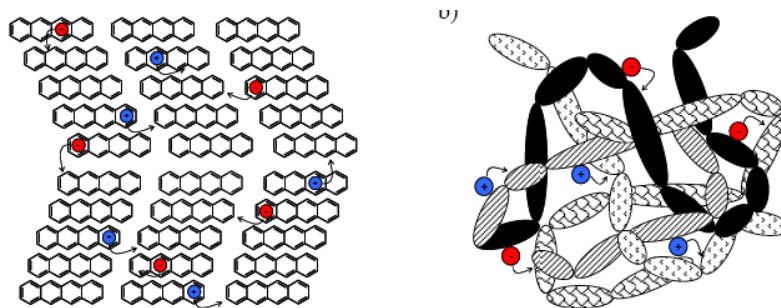


Figura 1.11: Scheme of electrons and holes hopping conduction. Holes are represented by blue circles and electrons by red circles. (a) Small molecules case (e.g. tetracene, that is an ambipolar materials): intramolecular and intermolecular hopping in a crystalline structure. (b) Polymers case: intra-chain and interchain hopping in an ideal ambipolar polymer.

The main reason why the model band is unable to describe completely for charge transport in organic semiconductors is that it fails to account for polarization in this materials. A charge carrier residing on a molecular site tends to polarize its neighboring region. As the barely-formed polarization cloud moves with then charge, the traveling entity is no longer a naked charge but a dressed charge. This quasi-particle is called *polaron*.

In conjugated solids the main polarization effect is that on the charge density formed by π -electrons. In order to estimate the stability of the polaron, two typical times are defined: (i) the residence time τ_{res} which corresponds to the average time a charge resides on a molecule and (ii) the electronic polarization time τ_{el} which is the time that the polarization cloud need to form around the charge.

By implementing the Heisenberg's uncertainty principle, an estimation of the order of magnitude for both time can be obtained. For the residence time, the pertinent energy is the width of the allowed band which is typically 0.1 eV in an organic semiconductor and 10 eV in an inorganic semiconductor, thus giving a residence time of 10-14 s and 10-16 s respectively. For the electronic polarization time, the corresponding energy is that of an electron transition, i.e. the energy gap (~ 1 eV), so that the time is of the order of 10-15 in both cases.

So in organic semiconductor, charges do not move so fast to prevent the polarization cloud to have time to form in the molecular site and charge transport is allowed by movements made by polarons along the conjugation, and by the jump of the charge carriers from one molecule to a neighbor, or from a polymer chain to a near chain (Figure 1.4).

So hopping transport prevails and leads to much lower mobility values (at best around $10^{-3} cm^2/Vs$, in many cases however much less). Instead of a power law the temperature dependence then shows an activated behavior

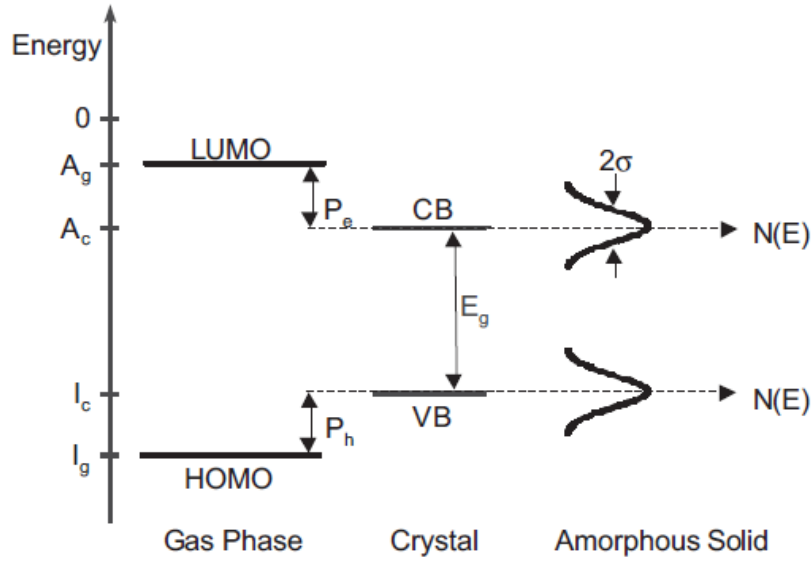


Figure 1.12: Energy levels of an isolated molecule (left), a molecular crystal (middle) and an amorphous solid (right). The width of the Gaussian density of states in an amorphous solid is typically in the range of $\sigma=80 \dots 120$ meV, whereas the band width in molecular crystals is less than 100 meV.

and the mobility also depends on the applied electric field:

$$\mu(F, T) \propto \exp(-\Delta E/kT) \cdot \exp(\beta\sqrt{F}/kT) \quad (1.2)$$

Depending on the model slightly different temperature dependencies for the mobility have been suggested. Furthermore, space-charge and trapping effects as well as details of the charge carrier injection mechanism have to be considered for describing electrical transport in organic solids [33]-[34].

On a macroscopic level, the current through a material is given by the charge carrier density n and the carrier drift velocity ν , where the latter can be expressed by the mobility μ and the electric field F :

$$j = en\nu = en\mu F \quad (1.3)$$

One has to bear in mind that in contrast to metals this is usually not a linear relation between j and F since both the carrier density and mobility can depend on the applied field. According to this equation, apart from the field, the two parameters n and μ determine the magnitude of the current. Thus it is instructive to compare their typical values with inorganic semiconductors and discuss different ways to control them.

As already discussed above, the mobility strongly depends on the degree of order and purity in organic semiconductors and therefore to a great deal on the preparation and growth conditions. It can reach values of 1-10 cm^2/Vs in molecular crystals, but values of only $10^{-5} \text{cm}^2/\text{Vs}$ in amorphous

materials are also not unusual. The highest mobility values achievable in thin films are nowadays comparable to amorphous silicon which is of course orders of magnitude less than crystalline Si.

The second parameter is the charge carrier density n . The intrinsic carrier density in a semiconductor with an energy gap E_g and an effective density of states N_0 (which is strictly speaking the product of valence and conduction band densities) is given by:

$$n_i = N_0 \cdot \exp(-E_g/2kT) \quad (1.4)$$

Taking typical values for an organic semiconductor with $E_g=2.5$ eV and $N_0 = 10^{21} \text{cm}^{-3}$ leads to a hypothetical carrier density of $n_i=1 \text{cm}^{-3}$ at room temperature, which is of course never reachable since impurities will lead to much higher densities in real materials. Nevertheless, the corresponding value for Si ($E_g=1.12$ eV and $N_0 = 10^{19} \text{cm}^{-3}$) is with $n_i = 10^{10} \text{cm}^{-3}$ many orders of magnitude higher, which demonstrates that organic semiconductors should have extremely low conductivity if they are pure enough.

In order to overcome the limitations posed by the low intrinsic carrier density, different means to increase the carrier density in organic semiconductors can be applied:

1. (electro-)chemical doping,
2. carrier injection from contacts,
3. photo-generation of carriers,
4. field-effect doping.

1.5 Optical Properties

The nature of bonding in organic semiconductors is fundamentally different from their inorganic counterparts. Organic molecular crystals are van der Waals bonded solids implying a considerably weaker intermolecular bonding as compared to covalently bonded semiconductors like Si or GaAs. The consequences are seen in mechanical and thermodynamic properties like reduced hardness or lower melting point, but even more importantly in a much weaker delocalization of electronic wave functions among neighboring molecules, which has direct implications for optical properties and charge carrier transport. The situation in polymers is somewhat different since the morphology of polymer chains can lead to improved mechanical properties. Nevertheless, the electronic interaction between adjacent chains is usually also quite weak in this class of materials.

Owing to the weak electronic delocalization, to first order the optical absorption and luminescence spectra of organic molecular solids are very similar to the spectra in the gas phase or in solution (apart from the trivial

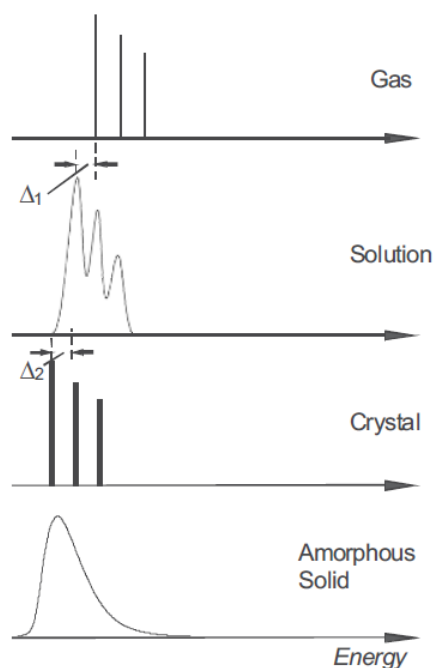


Figure 1.13: Schematical representation of optical spectra of organic molecules in different surroundings. Δ_1 and Δ_2 denote the respective solvent shift in solution and solid state.

solvent shift). In particular, intramolecular vibrations play an important role in solid state spectra and often these vibronic modes can be resolved even at room temperature. Thus the term “oriented gas” is sometimes used for molecular crystals. Nevertheless, solid state spectra can differ in detail with respect to selection rules, oscillator strength and energetic position; moreover, due to the crystal structure or the packing of polymer chains a pronounced anisotropy can be found. Additionally disordered organic solids usually show a considerable spectral broadening. This is schematically shown in Figure 1.5.

As a consequence of this weak electronic delocalization, organic semiconductors have two important peculiarities as compared to their inorganic counterparts. One is the existence of well-defined spin states (singlet and triplet) like in isolated molecules which has important consequences for the photo-physics of these materials (see Figure 1.5). However, since intersystem crossing is a weak process, this also sets an upper limit for the electroluminescence quantum efficiency in OLEDs. A second important difference originates from the fact that optical excitations (“excitons”) are usually localized on one molecule and therefore have a considerable binding energy of typically 0.5 to 1 eV. Thus in a photovoltaic cells this binding energy has to be overcome before a pair of independent positive and negative charge carriers is generated (see Figure 1.5).

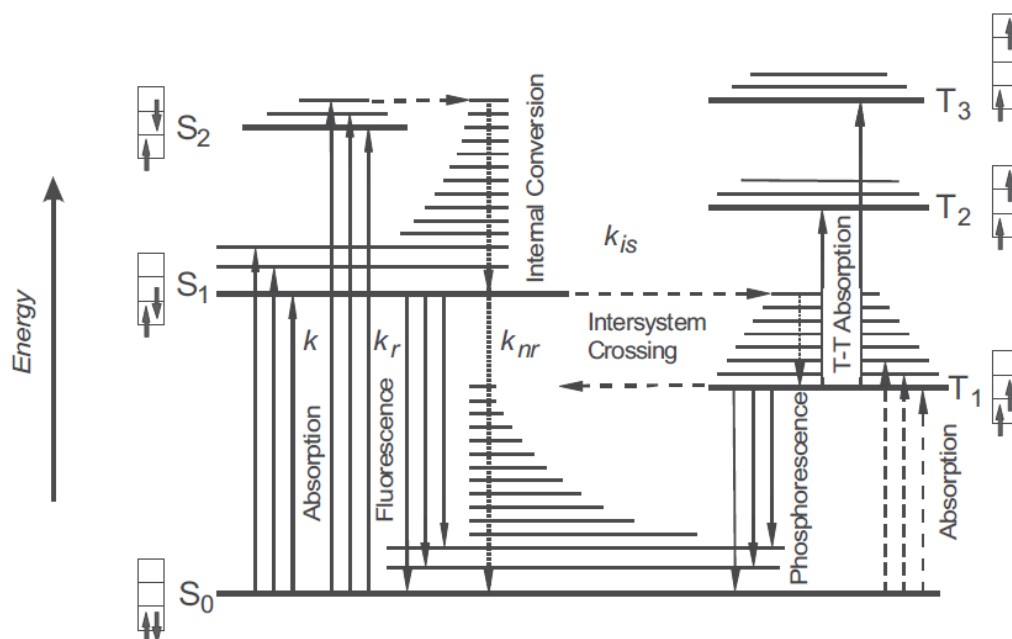


Figure 1.14: Energy level scheme of an organic molecule (left: singlet manifold, right: triplet manifold). Arrows with solid lines indicate radiative transitions, those with broken lines nonradiative transitions. Typical lifetimes of the S_1 state are in the range 1...10 ns. Triplet lifetimes are usually in the millisecond range for pure aromatic hydrocarbons, but can be considerably shorter in molecules incorporating heavy atoms, like e.g. Pt or Ir.

1.5.1 Exciton

A very simple but clear definition of the exciton can be this one: “It is a quantum of electronic excitation traveling in a periodic structure, whose motion is characterized by a wave vector” [35].

Many theoretical and experimental works have underlined that in van der Waals solids, due to the weak intermolecular interactions, the fundamental excitations are Frenkel excitons [36]. These are characterized by a very small radius of the electron hole pair (<5) due to a strong binding energy between them (~ 1 eV). Thus, the electron-hole pair is situated on only one molecular site, except in the case of charge transfer state (see below). The opposite case is represented by Wannier-Mott excitons, typical of covalent solids (inorganic semiconductors), where electron and holes are delocalized on many molecular or atomic sites of the solid. The Wannier-Mott exciton radius has values in the range 40- 100 .

Depending on how the electron-hole spin is willed, we can distinguish two types of exciton:

- Singlet exciton: state with an antisymmetric spin between electron and hole, so the total spin quantum number $S = 0$ (Figure 1.16a).

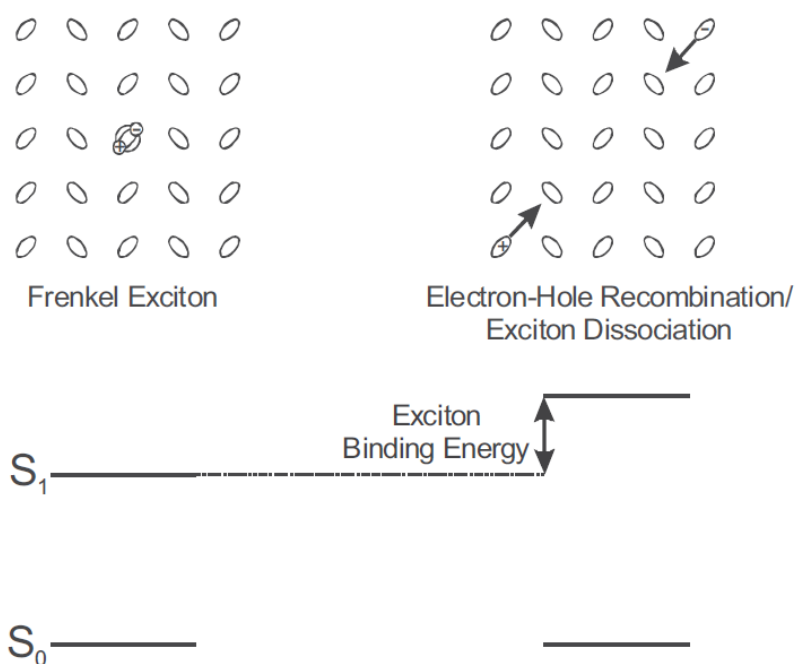


Figura 1.15: The energetic difference between an excited state sitting on one molecule (sometimes called a Frenkel exciton) and a pair of uncorrelated negative and positive carriers sitting on different molecules far apart defines the exciton binding energy. A simple estimation as the Coulomb energy of an electron-hole pair localized at a distance of about 10 Å in a medium with a dielectric constant of 3 yields a value of about 0.5 eV for the exciton binding energy.

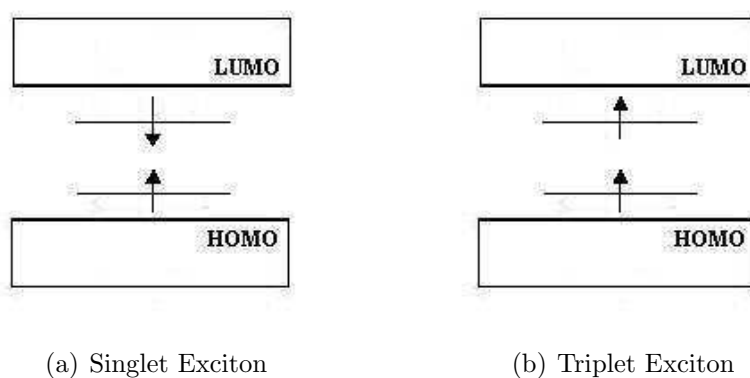


Figura 1.16: Exciton types

- Triplet exciton: state with a symmetric spin with $S=1$ (angular momentum states not null) (Figure 1.16b).

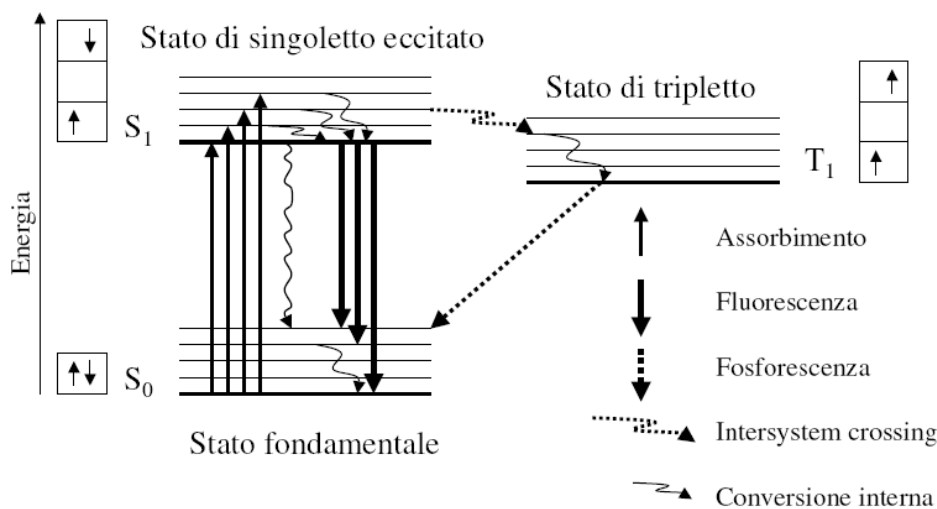


Figura 1.17: Jablonski Diagram

1.5.2 Luminescence

The process in which an excited state (exciton) is formed, due to the photon absorption, can be inverted. Indeed the exciton can de-excited returning in HOMO level resulting in a new photon emission. This phenomenon is called *photoluminescence* (PL) which denotes the complex of two fundamental radiative processes: *fluorescence* and *phosphorescence*.

Not all excitons can efficiently decay and emit light. The ground state of most molecules has a total spin, $S = 0$, and because the emission of a photon conserves spin, typically only $S = 0$ excited states can emit light in a fast (within nanoseconds) and efficient process known as *fluorescence*.

The radiationless transition from an excited singlet state to a triplet state can be induced by internal perturbations (*internal conversion*) as well as by external perturbations. These radiationless transitions are termed *intersystem crossing*. The transition from the first triplet state to the singlet ground state has a much longer lifetime (ranging from milliseconds to several seconds) with respect to fluorescence process since it is a forbidden transition and this process is known as *phosphorescence*.

Electroluminescence (EL) is a non-thermal generation of light resulting from the application of an electric field to a substrate. In the latter case, excitation is accomplished by recombination of charge carriers of contrary sign (electron and hole) injected in the presence of an external circuit.

As a consequence of the corresponding multiplicities of the angular momentum states (i.e. $m_S = 0$ for $S = 0$ and $m_S = -1, 0, 1$ for $S = 1$) and the random nature of spin production in electroluminescent devices, simple statistics predicts that only 25% of the injected charges result fluorescence (from singlet states) whereas 75% give phosphorescence (from triplet states)

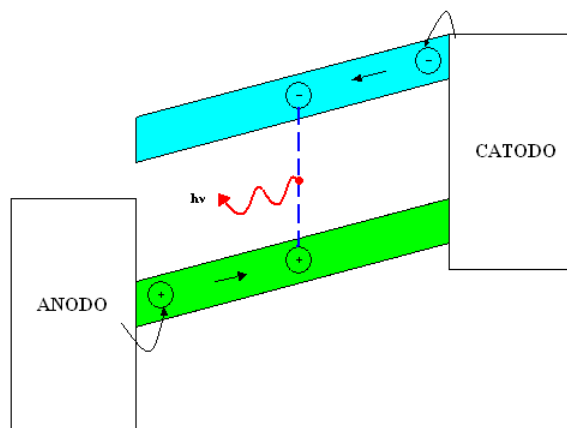


Figura 1.18: Electroluminescence (EL).

in suitable device architectures, while the excitons produced by radiation absorption are almost all singlet excitons. Thus, uncorrelated electrons and holes form triplet states with a threefold higher probability than singlet states [9]. Here it should be noted, that recent studies on spin statistics suggest variations in the singlet-to-triplet-ratios. These findings have also been confirmed by quantum mechanical calculations [37]. The ground states of most luminescent materials are singlet states and the vast majority of luminescent compounds exhibits only weak spin-orbit couplings rendering these small molecules and polymers fluorescent with negligible radiative rates from triplet states. Competing nonradiative processes (e.g. triplet-triplet annihilation or vibronic relaxation) effectively quench the phosphorescence of the associated excited states clearly limiting the maximum quantum efficiency achievable with fluorescent small molecules and polymeric materials [38].

1.6 Device Structures and Properties

Controlled doping has been one of the keys for the success of semiconductor microelectronics. There have been efforts to use tools like ion implantation doping also for organic semiconductors, however, due to the concomitant ion beam damages and the need for sophisticated equipment this method is probably not compatible with organic devices. Other techniques, like chemical doping by adding strong electron donors or acceptors as well as by electrochemical means have been successfully applied. At this point one should also mention that often unintentional doping of organic materials already occurs during the synthesis or handling of the materials since in many cases ambient oxygen causes p-type doping of organic materials. Thus

at present, controlled doping in organic semiconductors is still in its infancy and needs further investigations to employ it as a powerful tool for organic electronics.

Injection of charge carriers from contacts is essentially the process that governs device operation in organic light-emitting devices (OLEDs) (see Figure 1.6a). This requires low energetic barriers at the metal-organic interfaces for both contacts to inject equally high amounts of electrons and holes, which is required for a balanced charge carrier flow. Thus the interface energetic structure plays a very crucial role for achieving efficient OLEDs. Another process that comes into play is space-charge limitation of the current. Due to relatively high electric fields being applied to OLEDs (typically 5 to 10 V across a layer thickness of 100 nm yield $F = 0.5 \dots 1$ MV/cm) materials with low mobility such as Alq_3 (having an electron mobility of $10^5 \text{ cm}^2/\text{Vs}$) still yield high enough current densities for display applications. This is a consequence of the space-charge limited current scaling with the 3rd power of the reciprocal thickness:

$$j_{SCLC} = \frac{9}{8} \varepsilon \varepsilon_0 \mu \frac{V^2}{d^3} \quad (1.5)$$

Apart from charge carrier transport, the efficiency of OLEDs is also strongly influenced by photo-physical processes. First of all, materials with a high fluorescence quantum yield are required. However, since a large fraction of the excited states formed by charge carrier recombination are triplets, the most efficient OLEDs nowadays make use of energy transfer to so-called triplet emitters, where the presence of heavy metals renders the transition from the triplet state to the ground state via phosphorescence an allowed process.

The second important device application of organic semiconductors is in organic photovoltaic cells (OPVCs) (see Figure 1.6b). In spite of their high absorption coefficient, which exceeds 10^5 cm^{-1} in most materials, the application of organic semiconductors in OPVCs faces the problem of the large exciton binding energy which prohibits efficient exciton dissociation. This can be overcome by making use of a photoinduced charge transfer between an electron donor like PPV and the fullerene C_{60} as an acceptor. Due to the short exciton diffusion length of typically 10 nm only, efficient OPVCs use the so-called bulk-heterojunction concept of mixing donor and acceptor in one single layer. In spite of the huge progress recently achieved, there are still challenges to achieve sufficient lifetime of OPVCs under ambient conditions or the availability of low-band gap materials to make better use of the solar spectrum.

Organic field-effect transistors (OFETs) (see Figure 1.6c) are 3-terminal devices in which the charge carrier density in the channel between source and drain contacts can be controlled by the applied gate voltage across a

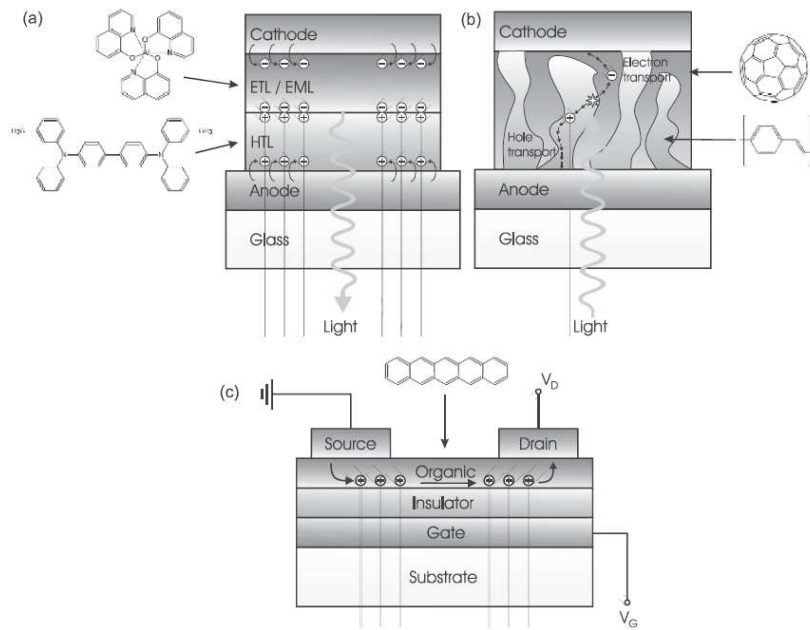


Figure 1.19: Different types of organic semiconductor devices are shown. (a) Organic lightemitting diode (OLED): Typically, a heterolayer structure is used, where HTL stands for hole transport layer and ETL for electron transport layer, EML denotes the emission layer. Instead of the displayed combination of a triphenylamine derivative and Alq_3 , polymeric OLEDs usually employ a conductive polymer (PEDOT:PSS) together with luminescent polymers like PPV or PFO derivatives. (b) Organic photovoltaic cell (OPVC): The so-called bulkheterojunction devices usually consist of a mixture of soluble PPV (or P3AT) and fullerene derivatives. Alternatively, mixed layers of evaporated small molecules like CuPc and C_{60} can be used. (c) Organic field-effect transistor (OFET): Prototypical materials in p-channel OFETs are pentacene as a low molecular weight material and P3AT as a conjugated polymer, respectively. Among others, e.g. C_{60} can be employed in n-channel transistors.

thin dielectric. The current is then given by

$$I_d = \frac{W}{L} C_i \mu (V_g - V_t) V_d \quad (1.6)$$

in the linear region, and by

$$I_d = \frac{W}{2L} C_i \mu (V_g - V_t)^2 \quad (1.7)$$

in the saturation regime. Thus the performance of OFETs can be tuned to some degree by using suitable geometries with short channel length L or thin insulating layers (leading to higher values for C_i), but it is clear that also the mobility needs to be high (in the range of amorphous Si) to realize

switching at frequencies higher than about 100 kHz which will be needed for more demanding applications in the future. This requires materials and methods to grow highly ordered organic semiconductor films. A further challenge will be to realize CMOS-like organic integrated circuits by using materials with ambipolar charge transport properties.

Capitolo 2

OLEDs

2.1 OLEDs Introduction

From their very beginning, OLEDs, which include both small-molecular- and polymer-based devices, were recognized as a promising display technology. As the dramatic improvements in the devices unfolded over the past two decades, the investment of research and development resources in this field grew exponentially. The fascination with these devices is due to several potential advantages: (1) Relative ease and low cost of fabrication, (2) their basic properties as active light-emitters (in contrast to liquid-crystal displays, which are basically polarizing filters requiring a backlight), (3) flexibility, (4) transparency, and (5) scalability. Once the performance of red-to-green OLEDs approached and then exceeded that of incandescent bulbs and fluorescent lights, it became clear that they are serious candidates for general solid-state lighting technology, competing directly with inorganic LEDs. Hence, while inorganic LEDs are the dominant solid-state lighting devices at present, OLEDs are expected to gradually replace the inorganic devices in more and more niche areas. Finally, OLEDs are attracting considerable attention as building blocks for some types of molecular electronic devices, and, most recently, for spintronic devices. In short, although their introduction into commercial products began only a few years ago, the breadth of their impact is widening rapidly.

The first reports of electroluminescence (EL) from an organic material can be traced back to 1907, and the first actual OLED, based on anthracene, was fabricated in 1963. However, it was not a thin-film device, and the operating voltage was extremely high. After years of efforts to improve its performance, interest in the subject waned. The breakthroughs that led to the exponential growth of this field and to its first commercialized products can be traced to two pioneering papers. The 1987 paper by Tang and Van Slyke demonstrated that the performance of green-emitting thin film OLEDs based on the small organic molecule tris(8-hydroxy quinoline) Al (Alq_3) is sufficiently promising to warrant extensive research on a wide variety of thin

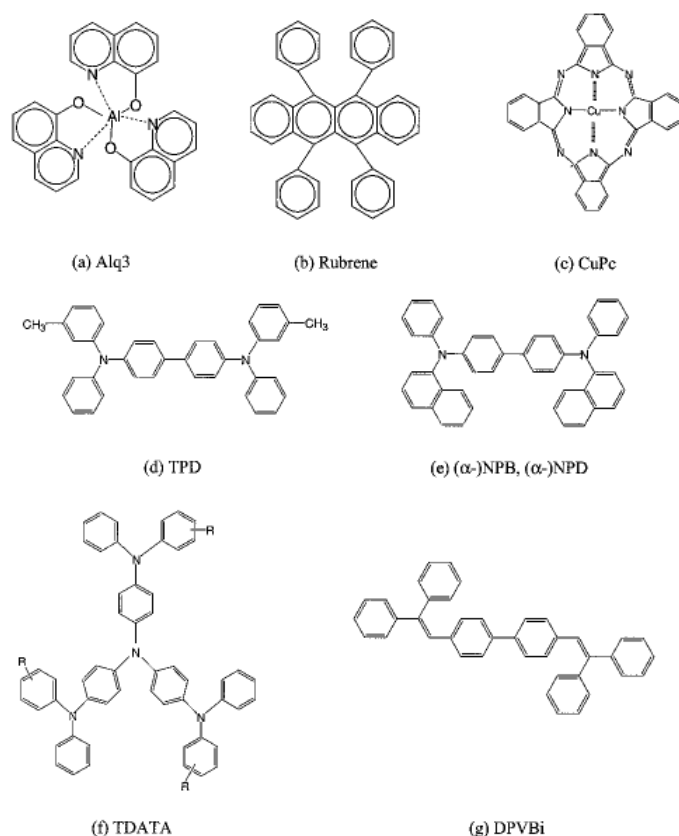


Figura 2.1: Molecular structure of widely used π -conjugated small molecules: (a) tris-(8-hydroxy quinoline Al) (Alq₃); (b) rubrene (5,6,11,12-tetraphenyl tetracene or 5,6,11,12-tetraphenyl naphthacene); (c) copper phthalocyanine, (CuPc); (d) N,N'-diphenyl-N,N'-bis(3-methylphenyl)-1,1'-biphenyl-4, 4'-diamine (TPD); (e) N,N'-diphenyl-N,N'-bis(1-naphthylphenyl)-1, 1'-biphenyl-4, 4'-diamine (NPB, α -NPB, NPD, or α -NPD); (f) 4, 4', 4''-tris(diphenyl amino)triphenylamines (TDATAs); (g) 4, 4'-bis(2, 2'-diphenylvinyl)-1, 1'-biphenyl (DPVBi).

film OLEDs. The 1990 paper by Bradley, Friend, and coworkers described the first polymer OLED (PLED), which was based on poly(p-phenylene vinylene) (PPV), and demonstrated that such devices warrant close scrutiny as well. Since then, the competition between small-molecular OLEDs and PLEDs continues in parallel with the overall dramatic developments of this field.

Using organic materials for light-emitting devices (LEDs) is fascinating due to their vast variety and the relative ease of controlling their composition to tune their properties by chemical means. The first organic electroluminescence (EL) cells were fabricated and studied in an ac mode in 1953 by Bernanose et al.,¹ and in a dc mode in 1963 by Pope and coworkers.² Soon after ac EL was also achieved using an emissive polymer.³ The observation

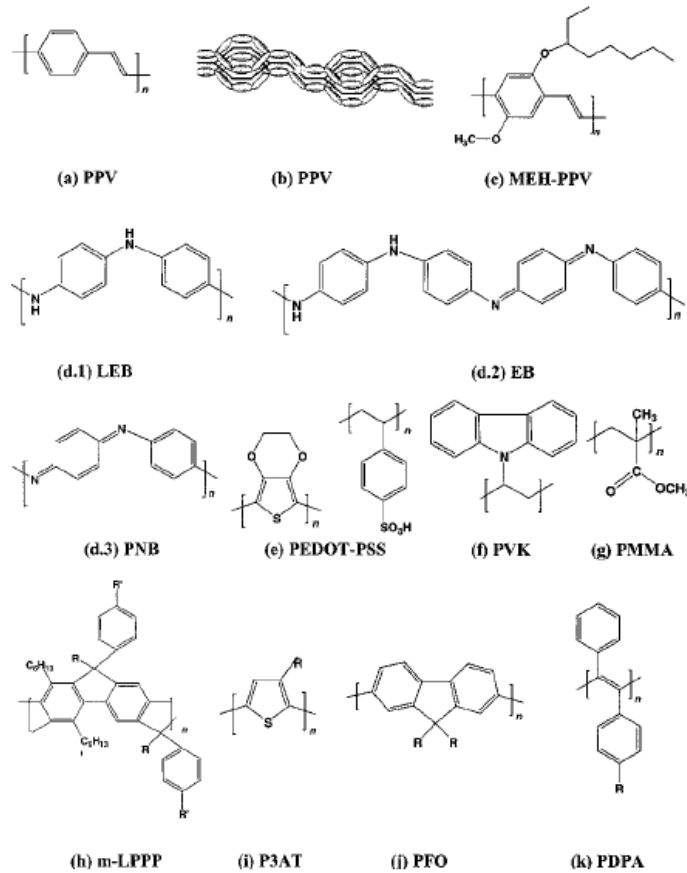


Figure 2.2: Molecular structure of widely used π -conjugated and other polymers: (a) poly(para-phenylene vinylene) (PPV); (b) σ (solid line along backbone) and π (“clouds” above and below the σ line) electron probability densities in PPV; (c) poly(2-methoxy-5-(2'-ethyl)-hexoxy-1,4-phenylene vinylene) (MEH-PPV); (d) polyaniline (PANI): (d.1) leucoemeraldine base (LEB), (d.2) emeraldine base (EB), (d.3) pernigraniline base (PNB); (e) poly(3,4-ethylene dioxy-2,4-thiophene)-polystyrene sulfonate (PEDOT-PSS); (f) poly(N-vinyl carbazole) (PVK); (g) poly(methyl methacrylate) (PMMA); (h) methylbridged ladder-type poly(p-phenylene) (m-LPPP); (i) poly(3-alkyl thiophenes) (P3ATs); (j) polyfluorenes (PFOs); (k) diphenyl-substituted trans-polyacetylenes ($t\text{-(CH)}_x$) or poly(diphenyl acetylene) (PDPA).

of bright EL with an external quantum efficiency η_{ext} , defined as the number of photons emitted from the face of the device per injected electron or hole, of 4-6% in anthracene crystals with powdered graphite electrodes marked another milestone.⁴ However, single-crystal anthracene-based organic LEDs (OLEDs) were thick and hence required very high operating voltages. The fabrication of bright green multilayer thin film devices based on tris-(8-hydroxy quinoline) Al (Alq_3), which yielded $\eta_{ext} \sim 1\%$,⁵ spawned a period

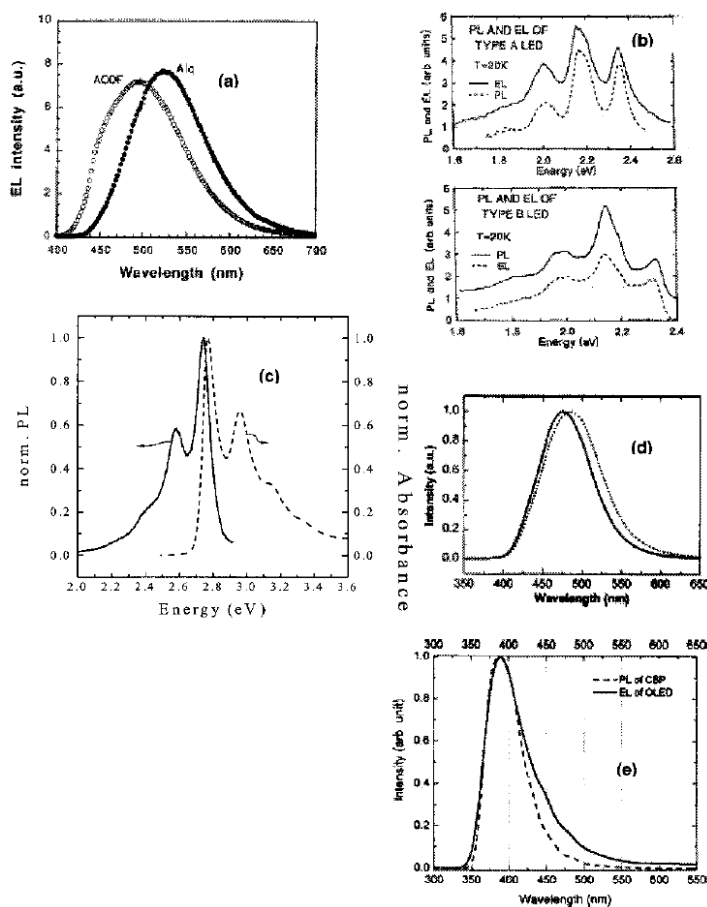


Figure 2.3: The photoluminescence (PL) and electroluminescence (EL) spectra of some representative π -conjugated films and OLEDs, respectively: (a) EL of blue aminooxadiazole fluorene (AODF) and green Alq₃ OLEDs,⁹ (b) PL and EL of PPV films and PLEDs, respectively,¹⁰ (c) PL of m-LPPP films, (d) EL of DPVBi (solid line) and DPVBi/Alq₃ (dashed line) OLEDs,¹¹ and (e) PL of CBP films and EL of CBP OLEDs.

of intense research and development, on both small molecular OLEDs and polymer LEDs (PLEDs), which continues to grow at a fast rate.^{6,7,8} Figure 2.1 shows the molecular structures of some small molecules widely used in OLEDs; Figure 2.1 shows the structures of some π -conjugated and other polymers. Figure 2.1 shows several photoluminescence (PL) spectra of films and EL spectra of OLEDs based on these molecules.

The work on Alq₃ and other small π -conjugated molecules that followed shortly thereafter^{13,14} demonstrated that multilayer OLEDs could be fabricated simply by thermal evaporation of these molecules. In 1990 Friend and coworkers described the first PLED,¹⁵ in which the luminescent poly(p-phenylene vinylene) (PPV) was fabricated by spin-coating a precursor polymer onto the transparent conducting indium-tin-oxide (ITO) anode sub-

strate, thermally converting the precursor to PPV, and finally evaporating the Al thin film cathode on the PPV. The developments in both small molecular OLEDs and PLEDs since the seminal reports of Tang and VanSlyke and of Friend and coworkers have been truly spectacular: from very dim devices with a lifetime of less than 1 minute in air, to green OLEDs that can operate continuously for over 20,000 hours (833 days) at a brightness of 50–100 Cd/m² (i.e., comparable to a typical TV or computer monitor),¹⁶ or in pulsed operation at >10⁶ Cd/m²,¹⁷ or blue, white, and red devices with continuous dc lifetimes of over 2000 hours. Indeed, the developments have been so remarkable, that serious effort is now underway towards the most ubiquitous application: replacing the incandescent and fluorescent light bulbs with OLEDs as the primary source for general lighting applications. However, even as they now enter the marketplace, outstanding challenges in the efficiency and long-term degradation processes of OLEDs remain. These are intimately tied to the dynamics of the basic excitations in these materials and devices, namely singlet excitons (SEs), triplet excitons (TEs), and p^- and p^+ polarons, to which the electrons and holes, respectively, relax as they are injected from the electrode into the organic layer of the OLED.

2.2 Basic Structure of OLEDs

The basic structure of a typical dc-biased bilayer OLED is shown in Figure 1.5. The first layer above the glass substrate is a transparent conducting anode, typically indium tin oxide (ITO). Flexible OLEDs, in which the anode is made of a transparent conducting organic compound, e.g., doped polyaniline, or poly(3,4-ethylene dioxy-2,4-thiophene)(PEDOT)-polystyrene sulfonate(PEDOTPSS) deposited on a suitable plastic, e.g., transparency plastic, have also been reported.

The single- or multi-layer small organic molecular or polymer films are deposited on the transparent anode. OLEDs based on single crystals (μ m) are not useful for practical applications. The high voltages, the small light-emitting areas, and the difficulty of single crystal processing are some of the shortfalls that would prevent their use as pixel elements in displays and solid state lighting. Appropriate multilayer structures typically enhance the performance of the devices by lowering the barrier for hole injection from the anode and by enabling control over the $e^- - h^+$ recombination region, e.g., moving it from the organic/cathode interface, where the defect density is high, into the bulk. Hence, the layer deposited on the anode would generally be a good hole transport material, providing the hole transport layer (HTL). Similarly, the organic layer in contact with the cathode would be the optimized electron transporting layer (ETL).

The cathode is typically a low-to-medium workfunction (ϕ) metal such as Ca ($\phi=2.87$ eV), Al ($\phi=4.3$ eV), or Mg_{0.9}Ag_{0.1} (for Mg, $\phi=3.66$ eV) deposited either by thermal or e-beam evaporation. However, in case of Al

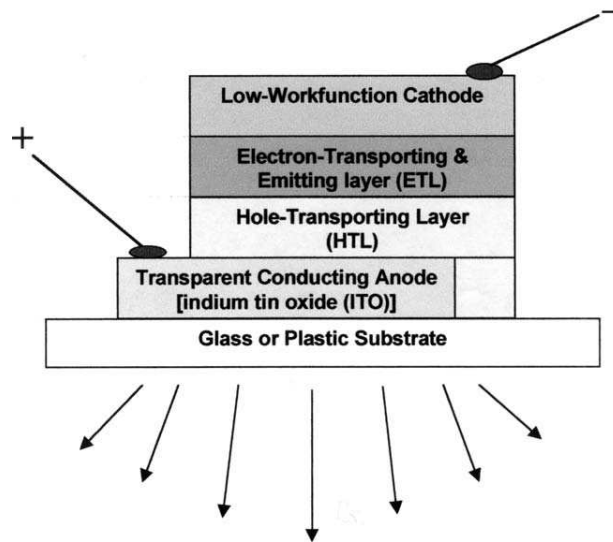


Figure 2.4: Basic structure of a bilayer OLED.

or Ca, addition of an appropriate buffer layer between the top organic layer and the metal cathode improves the device performance considerably.

2.3 Multilayer structure

The structure of OLEDs containing two organic layers consists of a transparent indium-tin-oxide (ITO) anode, an organic hole transport layer (HTL), an organic electron transport layer (ETL), and a metal cathode (Mg:Ag alloy film, for example). The HTL fulfills the roles of assisting the injection of holes from ITO and transporting them to the boundary of the two organic layers, while the ETL has the function of assisting the injection of electrons from a metal cathode and their transport throughout the bulk film. Recombination of holes and electrons occurs at the boundary regions between the two organic layers. When the recombination region is located within an ETL, the ETL behaves as an emissive layer (EML). When the recombination occurs within the HTL, on the other hand, the HTL can behave as an EML. Thus these devices are classified into two types; ITO/-HTL/ETL(EML)/ Metal and ITO/HTL(EML)/ETL/Metal. A three-layer structure may be also used where an independent thin EML is sandwiched between HTL and ETL (ITO/HTL/EML/ETL/ Metal), in case bipolar materials (which have the ability to transport both electrons and holes) are available. Figure 2.3 depicts these three typical device structures.

Even when HTL materials with low ionization potential are used to match the work function of the ITO anode, an energy barrier to hole injection from the ITO anode to HTL is usually present. In addition, chemical interactions between the ITO surface and the adjacent organic layer may cause

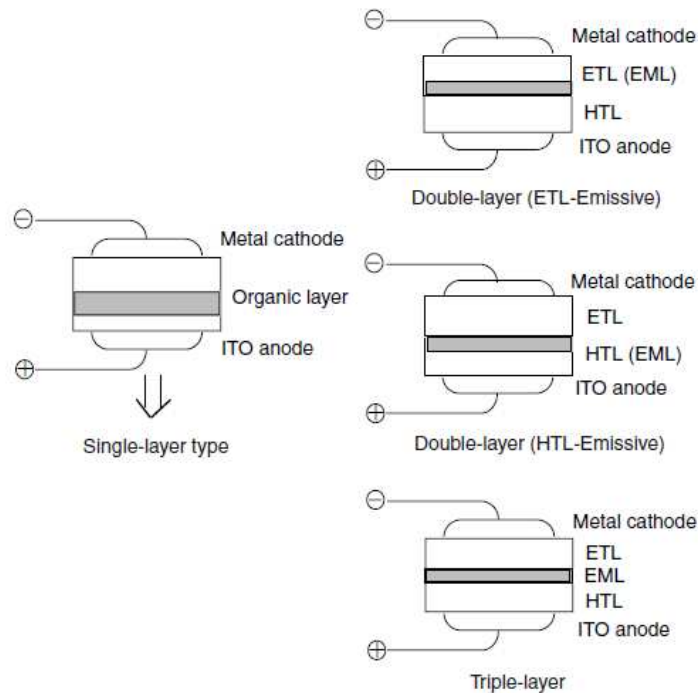


Figura 2.5: Illustrations of single-, double-, and triple-layer device structures. Charge recombination and emission are assumed to occur within the hatched regions.

degradation of the OLED device. Thus, the insertion of a thin buffer layer between the ITO and the HTL has been found very useful for both lowering the drive voltage and improving the device durability. The same is also true for the metal/organic interface between the metal cathode and the ETL. Many buffer layers have been proposed and used at this interface. The thickness of the buffer layer used varies depending on the material's resistivity. It is usually less than 10 nm for high-resistivity buffer layers. When doped semiconductor materials are used for the buffer layers, the thickness of the buffer layer may reach 1000 nm. Figure 2.3 depicts a variety of multi-layer OLED structures with different types of thin or thick buffer layers.

2.4 Basic Operation of OLEDs

In the basic operating mode of an OLED, holes are injected from the (transparent) anode and electrons from the metal cathode (see Figure 2.4). There is typically a roughly triangular barrier for both h^+ penetration into the HTL from the anode and e^- penetration of the ETL from the cathode. In the lower-current carrierinjection regime, the current is determined by the rate at which charge either hops over the barriers by thermionic emission, tunnels through it, or is transported through the barrier by hopping among

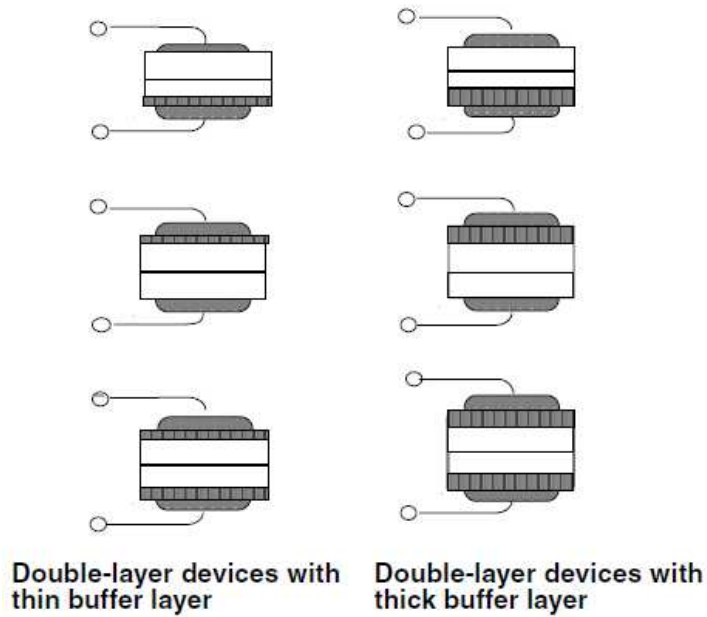


Figure 2.6: Illustrations of double-layer device structures with thin and thick buffer layers.

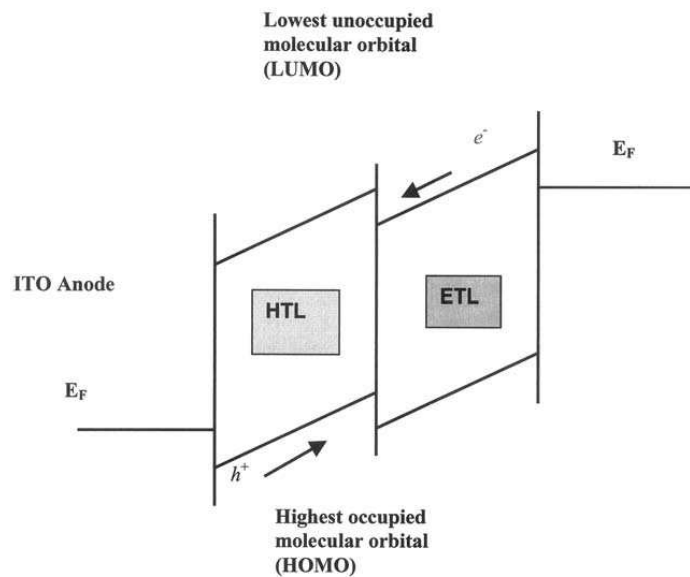


Figure 2.7: Basic operation of an OLED.

localized gap states in the barrier. In the higher-current space-charge limited current (SCLC) regime, the current is determined by the intrinsic properties of the layers through which it flows. We now proceed to consider carrier transport in OLEDs in greater detail.

2.5 Carrier Transport in OLEDs

Carrier injection and transport in OLEDs has been treated in detail by, among others, Kalinowski [82]. Most of the organic electroluminescent materials, small molecules and conjugated polymers are low-conductance materials. The h^+ mobility in these materials is typically $10^{-7} - 10^{-3} \text{ cm}^2/(\text{Vs})$, and the e^- mobility is typically lower by a factor of 10.100. However, it is now clear that the low mobility is due to the disorder in the amorphous or polycrystalline materials. Indeed, in high-quality single crystals of pentacene, the h^+ and e^- mobility are 2.7 and 1.7 cm^2/Vs at room temperature. Given the HOMO-LUMO gap of $\geq 2 \text{ eV}$, the thermal concentration of carriers at room temperature is insufficient for light generation. However, the application of an external field causes injection of h^+ 's from the ITO and of e^- 's from the cathode (see below). The injection from the metallic electrode is usually less efficient than from the ITO. The asymmetry in carrier injection leads to an imbalance in the concentrations of the injected carriers that reduces the device efficiency (see Section 2.6 below). Unlike inorganic semiconductors, the transport and the injection properties in OLEDs are determined by intersite hopping of charge carriers between localized states^{115,116} as well as hopping from delocalized states in the metal to localized states in the organic layer. The actual transition rate from one site to another depends on their energy difference and on the distance between them. The carriers may hop to a site with a higher energy only upon absorbing a phonon of appropriate energy. This decreases the probability of transition to a localized state with higher energy. The energetically allowed hops to a distant site are limited also by the localization length.¹¹⁷ The energy states involved in the hopping transport of h^+ 's and e^- form narrow bands around the HOMO and LUMO levels. The widths of these bands is determined by the intermolecular interactions and by the level of disorder.

The transport in OLEDs has been extensively studied by time-of-flight (TOF), and analysis of the dc current-voltage characteristics. In a number of cases the results produced by the two methods were compared and good agreement was generally found. In other cases the mobilities were measured using Hall-effect¹²¹ and delayed EL techniques.

The universal dependence of charge carrier mobility on the electric field

$$\mu(E, T) = \mu(0, T)e^{\gamma\sqrt{E}} \quad (2.1)$$

where $\mu(0, T)$ is the low-field mobility and γ is an empirically determined coefficient, is observed for the vast majority of materials. The method of delayed pulsed EL enabled measuring this dependence up to relatively high fields of $\sim 1 \text{ MV/cm}$, while TOF [79] or dc [80] transport measurements usually do not exceed 0.3 MV/cm . Several models have been invoked to explain the observed carrier mobility. Choosing between them is related to the basic issue of the nature of charge carriers in organic films formed by

conjugated molecules. The experimentally observed dependence is the same as observed earlier for the wide class of organic photo-conductors used in the photocopying process.

2.5.1 Polaron vs Disorder Models for Carrier Hopping

As suggested from Section 1.4.1 above, the models based on polaron formation assume that a localized carrier interacts strongly with molecular vibrations of the host and neighboring molecules, so significant relaxation of the local molecular structure occurs around the carrier. That carrier can move to an adjacent molecule only by carrying that relaxation (or strain field) along with it. Clearly, that relaxation or stabilization lowers the energy of the negative carrier below the LUMO level and the energy of the positive carrier above the HOMO level.

The experimental evidence for polarons in PPV and related polymers is extensive. For PPV it emerges from the comparison of resonant Raman spectra of bulk samples with those of anions in model compounds equivalent to segments of PPV with different lengths. In actual samples the polaronic stabilization may also be induced by defects such as chain breaks and various conjugation defects, e.g., sp^3 bonds, cross-links, and inclusions of catalysts and of precursor polymer that all act as chain breaks. The stabilization is found in calculations assuming the conjugation length is less than 50 sites. It is apparent, however, that on any length scale conjugation defects which are less severe than chain breaks, but raise the energy required to create the polaron on the segment, can help localize the polaron on other chain segments.

While experimental evidence for polaronic relaxation is extensive, other experiments render the polaron models problematic: (i) the use of the Arrhenius relation to describe the temperature dependence of the mobility (see above) leads to pre-factor mobilities well in excess of unity, and (ii) the polaron models cannot account for the dispersive transport observed at low temperatures. In high fields the electrons moving along the fully conjugated segments of PPV may reach drift velocities well above the sound velocity in PPV. In this case, the lattice relaxation cannot follow the carriers, and they move as “bare” particles, not carrying a lattice polarization cloud with them. In the other limit, creation of an orderly system free of structural defects, like that proposed by recently developed self-assembly techniques, may lead to polaron destabilization and inorganic semiconductor-type transport of the h^+ 's and e^- 's in the HOMO and LUMO bands, respectively.

The fundamental difference between disorder and polaron models is related to the difference in energy of hopping sites due to disorder and the change in molecular conformation upon addition or removal of a charge at a given site. In the disorder formalism it is assumed that the coupling of a

charge carrier to molecular modes is weak, and the activation energy reflects the static disorder of the hopping sites. In the polaron models, it is assumed that the energetic disorder energy is small compared to the deformation energy.

The polaron models predict that the mobility is a product of a Boltzmann probability of energy coincidence and the probability that a carrier will jump between adjacent sites by thermal activation once energy coincidence occurs. The most widely accepted model, proposed by Emin, yields

$$\mu \propto \frac{\sinh(E/E_0)}{E/E_0} \quad (2.2)$$

Yet this result agrees with the experimental results over a limited range only.

The calculations of the mobility of e^- 's hopping through the manifold of energetically and spatially disordered states yield Equation 2.1, and they show that γ is related to the diagonal disorder parameter σ and the off-diagonal disorder parameter χ . The former is usually interpreted as the width of the band of disordered states. Assuming a Gaussian distribution of site energies, σ is the full width of the distribution. Similarly, χ is interpreted as the full width of the distribution of the values of the overlap integrals. This distribution is also assumed to be Gaussian.

The field-dependent mobility expression is universal and applicable to a large class of materials including conjugated polymers, blends, and mixtures of polymers and dyes.

Generally, despite the better agreement between the disorder-based models and transport measurements, it is widely believed that the charge carriers exist as polarons rather than free e^- 's and h^+ 's. It should be noted that the basic disorder-based calculations yield the experimentally observed field dependence of the carrier mobility for a relatively narrow range of fields only.

2.5.2 Long-Range Correlations

The range of agreement between the disorder-based models and the experimental results improves when the correlation of the energies of adjacent sites is taken into account. Recently, analytical solutions which relate the field dependent mobility to intermolecular interactions in the polymer were obtained for this case. This correlation model results in the following dependence of γ on the electric field:

$$\sigma = C_0(\sigma_d^{(3/2)} - \Gamma) \sqrt{\frac{ea}{\sigma_d}} \quad (2.3)$$

with $C_0=0.78$, $\Gamma=2$ and μ_0 containing the temperature dependence. The model treats carrier hopping among sites arranged on a cubic lattice of spa-

cing a, but differs from the regular disorder models in the way site energies are determined. An independent and randomly oriented dipole of moment p is placed at each lattice site, and the energy of a carrier at a given site is then given by the Ewald method, i.e., the sum calculated through its interaction with dipoles at all sites except its own [74]:

$$U_m = - \sum_{n,m} \frac{e\vec{p}_n |\vec{r}_n - \vec{r}_m|^3}{\varepsilon |\vec{r}_n - \vec{r}_m|}. \quad (2.4)$$

The site energy distribution in this model has been extensively studied and shown to be approximately Gaussian with a width

$$\sigma_d = 2.35 \frac{ea}{\varepsilon a^2} \quad (2.5)$$

where p is a randomly oriented dipole moment, ε is the dielectric constant, and a is the spacing on a cubic lattice for which the calculation was carried out. The crux of the improved disorder models is that the many long-range contributions comprising U_m introduce correlations in the distribution of site energies, yielding a version of the disorder model with specific kinds of correlations. In addition, these equations are derived assuming a simple cubic lattice, and thus cannot be expected to be valid for the disordered material. However, they do show how the long range interactions may be rationalized in terms of the experimentally observed dependence of the mobility on the electric field.

2.5.3 Carrier Injection

We now proceed to briefly describe e^- injection from the metallic electrode into the adjacent band of LUMO states and the hopping transport in this band.

In the absence of e^- injection and an external electric field, the Fermi level of the metallic electrode is at negative energy Δ , with respect to the center of the LUMO band (see Figure 2.5.3). When a contact between the electrode and the organic is established, there is some initial injection of e^- 's into (probably trap) states in the organic/metal interface. This results in an "image force" potential ϕ_i (shown by a solid thick line in Figure 2.5.3) due to Coulomb attraction between these electrons and the holes which are left behind in the metal after the electron injection. This image potential lowers the energy of the interface states and renders them energetically available for the e^- 's hopping from the metal Fermi surface. However, the image force potential decreases with increasing distance from the interface and thus the bulk states deep in the organic layer remain energetically unavailable for charge hopping. Application of an external field lowers the energy of the available states in the bulk of the polymer. As a result, hopping into bulk states away from the interface becomes more probable. Figure 1.7

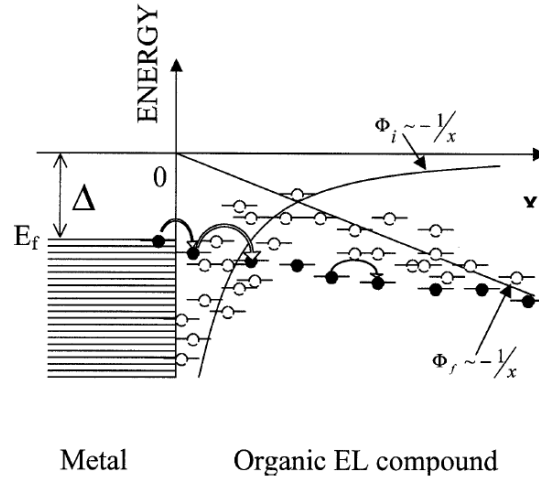


Figure 2.8: The energy of the available sites versus the distance x from the metallic electrode under the influence of the “image force” potential and the applied electric field.

describes the energy of the available sites versus the distance x from the metallic electrode under the influence of the “image force” potential and the applied electric field. It should be emphasized that the carrier motion in the organic layer occurs everywhere through hopping, including injection from the metallic electrode through the interface and the hops in the opposite direction (or “back flow” [75]). At least one of the states involved in each hopping event is localized. Based on the above description of injection and transport, the current vs voltage (I-V) in OLEDs was calculated using a model for electron diffusion in an Onsager-type potential with random site energies. It is noteworthy that this treatment not only predicts the correct dependence of I on V but the magnitude of I as well.

The voltage dependence of the injection-limited current resulting from this treatment, as well as experimentally observed I-V characteristics are Fowler- Nordheim (FN)-like, i.e., similar to that obtained by tunneling through a triangular barrier. This similarity suggested a number of treatments that analyzed injection into OLEDs in terms of this model, which predicts that

$$J \propto V^2 e^{-\text{frac}bV} \quad (2.6)$$

where J is the current density, V is the voltage and b is a constant that may be analytically derived as a combination of the energy band parameters for the semiconductor material and the contact metal.

Notwithstanding the similarities between the observed $I(V)$ in the current injection regime and the FN relation (Equation 2.6), the physics that underlies e^- injection from the metal into the insulator described above differs radically from a FN mechanism and should not be mistaken for one.

The localized states of the insulator become energetically available for the e^- at the metal Fermi energy due to the application of the external field that drives them down in energy, not unlike the energy bands of the semiconductor or the vacuum level in the original FN treatment. However, the k -vector is inappropriate for describing the e^- motion through the system of localized states. Hence, e^- injection into such a material cannot be treated as a plane wave scattered by a triangular barrier, which is the basis for the FN model. The hopping mechanism is incoherent and the phase of the electron in the metal is completely lost during the first hopping step into the organic. The mirror image attraction significantly affects the process of the charge motion after hopping into the first organic site. Due to the low bulk mobility, this carrier is effectively trapped in the potential well near the interface, and may leave it only upon absorption of a phonon. Thus, the whole process resembles the Shottky-Richardson mechanism of thermally-stimulated emission, rather than the FN picture of coherent wave tunneling. As several in-depth numerical treatments show, the injection yield, i.e., the probability for a carrier at the first near-interface site to reach across the film, depends critically on the energy of the near-interface sites [76]. Several fundamental considerations defeat the mechanistic treatment of injection into the unperturbed LUMO state: (i) injection occurs into a polaron level [77]; (ii) in the close vicinity of the metallic electrode, the high-mobility image charges in it screen out the dipole terms in the Coulomb interactions at 5–7 nm at least [78]; (iii) even when contamination with, e.g., water vapor or oxygen are excluded, the interface is modified by the direct chemical interaction between the low-work function metal and the organic molecules. As result, no general treatment can be expected, with each process to be analysed on a case-by-case base.

2.5.4 Space-Charge Limited Versus Injection-Limited Current Mechanisms

Injection EL with characteristic efficiencies of 0.5-3 Cd/A that are standard in modern OLEDs demand current densities ≤ 3 mA/cm² for this purpose. Mobilities in organic luminescent materials are low, typically $10-5-10^{-3}$ cm²/(Vs). Such strong injection into low-mobility materials inevitably leads to charge accumulation in the organic film. This charge build-up partially screens out the applied electric field, leading to its redistribution. The resulting behavior of I-V is that of space-charge limited current (SCLC). The I-V curves predicted by this model are supralinear, typically quadratic in the absence of traps or with a single shallow trap level. The local increase in the quasi-Fermi level due to strong injection may lead to charge immobilization in the deep states of the disorder-induced distribution of the HOMO and LUMO levels. In that case, however, the resulting trapped-charge limited current (TCLC) model predicts a generally high-exponent power law $I \propto V_\alpha$

with $7 \leq \alpha \leq 9$. The study of trap levels in various electrically active organic films yielded the data required to explain the DC I-V curves in the most common types of OLEDs.

Single-carrier-dominated transport, including a detailed treatment which includes space-charge effects that are prominent in single layer devices, have been developed to provide a satisfactory explanation of the I-V characteristics in OLEDs. Models accounting for the motion of both holes and electrons in singlelayer PLEDs elucidated the issue of emission efficiency in these devices. These approaches were later extended for the case of multi-layer devices as well. A deeper insight into the sub-band electronic structure and the dynamics of their charging under different injection conditions was achieved with application of impedance spectroscopy to studies of the space-charge in PLEDs. While these experiments revealed a rich structure of charged gap states acting as traps, a number of recent studies show that the field-dependent mobility alone may account for the steep current-voltage characteristics, without invoking the complicated trap structure. This approach is particularly attractive due to its generality; however, no description for the dependence of the efficiency on injection level or applied bias has been provided yet. The SCLC-type mechanisms are invariably found to dominate the conduction in devices where strong injection is achieved from both electrodes. The structure of bilayer devices (and multilayer devices derived from them) gives rise to charge trapping and formation of charge dipole layers at the internal interfaces. When the external electric field is applied, the holes are injected from the anode into the HTL and drift or hop across it. However, they decelerate at the internal interface due to the lower hole mobility in the ETL. This leads to substantial charge accumulation which is not unlike the most common type of injection-induced space charge build-up in low-mobility insulators. The same mechanism should also be true for electrons as they cross the organic/organic interface. We stress that for this “interface” trapping of charge carriers an energy offset at the internal interface is not necessary, as the carriers are immobilized by the mobility offset. In steady-state this carrier localization leads to increased charge concentration away from the electrodes where the majority of the radiative SEs would be quenched. On the other hand, at high injection levels strong carrier concentration gradients may build up at the interface, leading to increased local electric fields. Yet these field are formed exactly where most of the light is emitted. When the local field at the HTL/ETL interface exceeds the critical value for SE dissociation, it leads to a dramatic decrease in emission efficiency. This decreased efficiency has been observed at high injection levels in virtually all multi-layer OLEDs. Obviously, balancing injection and mobility in the HTL and ETL respectively may significantly improve the steady-state efficiency at high brightness levels.

2.6 The Efficiency of OLEDs

Efficiency is a key issue not only for energy-consumption, but also for its effect on the longevity of the devices, since the ability to operate the device at a lower input power at a given luminance decreases ohmic heating and increases the device lifetime. A high power efficiency implies a low I-V product for a given luminance. However, much of the analysis of the efficiency in the literature has been devoted to the external quantum efficiency η_{EL} , i.e., the number of photons emitted through the front face of the device per injected electron. One of the forms in which the basic equation for the external quantum efficiency η_{EL} of the OLED can be written is

$$\eta_{EL} = \xi\gamma r_{ST}\eta_{PL} \quad (2.7)$$

where (i) ξ is the out-coupling efficiency (i.e., the fraction of the photons which are emitted from the front surface of the device), (ii) γ is the ratio of the number of exciton-forming events to the electrons flowing in the external circuit (basically a measure of the fraction of electrons and holes which recombine with each other), (iii) r_{ST} is the ratio of SEs to TEs formed from the recombining charge carriers, and (iv) η_{PL} is the PL quantum yield (i.e., the radiative yield of SEs). We now dwell briefly on each of these terms.

1. It can be shown that for a large refractive index of the emitter layer n and for isotropic dipoles not subjected to optical interference with the cathode reflector,

$$\xi \approx \frac{0.5}{n^2}. \quad (2.8)$$

Hence for $n \approx 1.7$, $\xi \approx 0.17$. However, the recent detailed analysis by Kim et al. [68] shows that if the optical interference with the cathode reflector is taken into account, for isotropic and in-plane dipoles $\xi \approx A/n^2$ where $A \approx 0.75 \pm 0.1$ and 1.2 ± 0.1 , respectively.

2. The factor $\gamma \leq 1$, which is a measure of the balance between h^+ and e^- injection, and of the probability that each of them will recombine with the other, is very difficult to measure, but it has been argued that in the relatively efficient OLEDs studied to date, it is close to 1. This factor is optimized by varying the composition and thickness of the HTLs and ETLs, and monitoring the response of the I-V and I_{EL} -V curves to these variations. For practical display devices however, there exists a certain tradeoff between a low turn-on voltage on the one hand, and high efficiency on the other. Hence considerable effort is being invested into promoting the injection of both types of carriers in order to restrict not only the active matrix but in particular passive matrix driving circuitry to lower operating voltages. However,

strong injection of majority carriers (usually holes) leads to decreased efficiency, excess Joule heating, and should actually be avoided. Hence highly efficient devices generally operate in the injection-limited current regime. The validity of this approach for multi-layer OLEDs was recently confirmed by Forsythe et al., who introduced trap-free CuPc as a hole-limiting layer immediately on top of the ITO anode to control excessive hole injection.

3. From spin-statistics the ratio r_{ST} of SEs to TEs formed from the recombining polaron pairs should be $r_{ST} = 0.25$, since parallel spin pairs would recombine to TEs and antiparallel pairs would recombine equally to SEs and TEs. However, several recent independent studies suggest that the cross-section for SE formation σ_S is greater than that for TE formation σ_T , so $r_{ST} > 0.25$ [70], [69]. However, the actual value for different polymers is still not well-established, and for small π -conjugated molecules it is essentially unknown.
4. The PL quantum yield η_{PL} . While η_{PL} of many dyes is close to 100% in solution, in almost all cases that yields drops precipitously as the concentration of the dye increases. This well-known “concentration quenching” effect is due to the creation of nonradiative decay paths in concentrated solutions and in solidstate. These include nonradiative torsional quenching of the SE, fission of SEs to TEs in the case of rubrene, or dissociation of SEs to charge transfer excitons (CTEs), i.e., intermolecular polaron pairs, in most of the luminescent polymers and many small molecular films or other nonradiative quenching of SEs by polarons or trapped charges. In view of these numerous nonradiative decay paths, the synthesis of films in which η_{PL} exceeds 20%, such as in some PPVs, exceeds $\sim 30\%$, as in some films of *m*-LPPP, and may be as high as 60%, as in diphenyl substituted polyacetylenes, is impressive.

In summary, in evaluating the upper limit of η_{PL} from Equation 2.6, the upper limits of the different terms, appear to be $\xi \approx 0.35$, $\gamma \approx 1$, and $r_{ST} \approx 0.5$. Hence fluorescence (as opposed to phosphorescence)-based OLEDs with these values of ξ , γ and r_{ST} should yield $\eta_{PL} \approx 0.15\eta_{PL}$.

2.7 Degradation Mechanisms

The stability of OLEDs is obviously a key element in determining their technological impact. The common degradation mechanisms were recently summarized by Sato et al. [83]. We now briefly review these mechanisms.

2.7.1 Dark spot formation

One of the most prominent mechanism of degradation in OLEDs is through the formation of non-emissive “dark” spots along with a long-term decrease in the device efficiency. As found for both OLEDs and PLEDs, these defects result from delamination of the metal at the organic/metal interface initiated by pinholes on the cathode in the presence of significant Joule heating. In-situ imaging of the electrode surface using time-resolved confocal laser-scanning microscope revealed the appearance of dome-shaped defects corresponding to the locations of the “dark spots”. Some parts of a strongly degraded sample are short-circuited by the carbonized polymer; in other parts an open circuit condition is found. Cumpston and Jensen [84] proposed that electromigration of the electrode material may occur in the areas where the local conductance is high. It leads to inhomogeneities and, in the final account, to the loss of electrode continuity.

2.7.2 Photo-oxidation

Many conjugated polymers undergo photo-oxidation during device operation. The extended conjugation length of the polymer may increase the electron density at the double bond, thereby making it more reactive to the excited singlet 1O_2 electrophile than in the respective oligomers. There is also evidence that the presence of electron-rich groups on the phenyl rings, such as alkoxy groups, may increase the likelihood of 1,2-cycloaddition of 1O_2 at the vinyl double bond, which convert to two C=O carbonyl groups spontaneously. These two carbonyl groups are not bonded to each other, so their formation physically cuts the polymer chain into two segments. In addition, the C=O group is a very efficient non-radiative SE quenching center, and hence its formation rapidly decreases the PL and EL yield of the PPV films and PLEDs.

The source for the formation of the highly reactive 1O_2 is the energy transfer from the polymer. The SE of the polymer is responsible for light emission but it is too short lived to transfer energy to oxygen efficiently. However, the copious non-emissive triplet state has a far greater lifetime and is sufficiently energetic to excite the ground state 3O_2 to the singlet 1O_2 state.

It should be emphasized that neither exposure to *only* light or *only* O_2 lead to the degradation in PPV derivatives. The combination of these factors, however, leads to the oxygen addition at the double bond in the vinyl group. It is important to mention, however, that while many common derivatives of PPV, such as MEHPPV, are highly vulnerable to photooxidation, others, such as unsubstituted PPV or other polymers such as poly(3-octylthiophene) (P3OT), photooxidation does not appear to be the leading limitation on the longevity.

2.7.3 Recrystallization

This process is one of the primary degradation mechanism of OLEDs based on amorphous organic layers, since SEs are efficiently quenched by defects and charge-dipole-induced fields at the surface of a grain boundary. Since any given amorphous layer will recrystallize slowly as its temperature reaches the glass transition temperature T_g , major efforts to synthesize materials with high T_g have been reported [71], [72]. Indeed, the considerably higher $T_g \approx 95^\circ\text{C}$ of NPB as compared to TPD, where $T_g \approx 63^\circ\text{C}$ [71], is a major reason for the improved stability of NPB/Alq₃ devices relative to those of TPD/Alq₃ OLEDs.

The major efforts to increase T_g include two noteworthy innovative approaches: (i) Synthesis of “starburst molecules”, suitable for HTLs, whose patently nonplanar structure inhibits recrystallization [72], and (ii) synthesis of novel molecules in which familiar luminescent molecules are synthesized around a spiro-bifluorene core [71]. As shown by Spreitzer et al. [71], T_g of these spiro derivatives, such as spiro-DPVBi, is considerably higher than that of the parent molecules, yet their PL and EL spectra are essentially identical. As expected, the lifetime of the OLEDs fabricated from the spiro derivatives is considerably higher than that of the parent-compound-based devices, both at room and at elevated temperatures.

2.7.4 Metal atom migration

Several studies have shown that while migration of cathode metal atoms such as Mg is not significant, indium migration from the ITO is a very considerable problem. Indeed, Lee et al. have shown that In migration occurs mainly during operation of the devices, i.e., it is an electro-migration process, and that its presence is correlated with performance degradation.

2.7.5 Molecule-specific degradation processes

Some degradation processes are molecule-specific. The widely used Alq₃ was found to be unstable in the +1 oxidative state. Therefore, hole migration from the HTL to the Alq₃ layer causes degradation unless the injected electrons first charge the Alq₃ negatively. In PPV-based devices, the hole injection process was also found to degrade the ITO/PPV interface.

2.7.6 Electrical breakdown

Finally, damage patterns observed at the Al (Mg) interface with PPV in PLEDs under strong pulsed bias are reminiscent of those observed in AC thin-film inorganic devices. The mechanism of their formation is the electrical breakdown in the form of pinhole electrical arcs. These breakdowns occur at some typical voltage, which in capacitor device technology is called

the “clearing voltage”. In this case the circuit opens around the pinhole that stops the arcing. The resulting burnout typically does not exceed 50 μm . It leaves an injury through which moisture can penetrate and lead to hydrolysis and subsequent delamination. Also, when the burn-outs become too numerous, they limit the light output and open up an entire circuit eventually. The interesting feature is the propagation of “tributaries”. In inorganic devices they were found to be formed by arc-induced dielectric melting, which becomes conductive. The tributaries run all the way through to the opposite electrode, thus completing the electric circuit and leading to a short-circuit condition. This picture is completely compatible with experimental observations in PPV and appears to be adoptable without significant changes.

2.8 OLED Fabrication Procedures

The existing OLED fabrication procedures fall into two major categories: (1) thermal vacuum evaporation of the organic layers in small molecular OLEDs, and (2) wet coating techniques of the polymer layers in PLEDs.

2.8.1 Thermal Vacuum Evaporation

Thermal evaporation of small molecules is usually performed in a vacuum of ~ 10.6 torr or better. However, it has been observed that the residual gases in the chamber may affect the performance of the devices significantly. For example, Br̄somas et al.⁴⁷ found that the performance of OLEDs in which a Ca film was deposited as the cathode in a high vacuum (HV; ~ 10.6 torr) system was far better than that of OLEDs deposited under ultra-high vacuum (UHV; ~ 10.10 torr). This was apparently due to the formation of an oxide buffer layer between the top organic layer and the metal cathode and, indeed, led to the deliberate introduction of an AlO_x buffer layer by Li et al.⁴⁸ In another case, it was found that Au/[organic]/Au device structures were rectifying when deposited under HV but symmetric when fabricated under UHV.⁴⁹

One of the most salient advantages of thermal vacuum evaporation is that it enables fabrication of multilayer devices in which the thickness of each layer can be controlled easily, in contrast to spin coating (see below). In addition, 2- dimensional combinatorial arrays of OLEDs, in which two parameters (e.g., the thickness or composition of two of the layers) may be varied systematically across the array, can be relatively easily fabricated in a single deposition procedure.^{50,12} This combinatorial fabrication greatly enhances the efficiency of systematic device fabrication aimed at optimizing the various parameters.

The major appeal of vacuum deposition techniques is that they employ the generally available vacuum equipment existing in the semiconductor in-

dustry. Using properly matched shadow masks for depositing RGB emitting materials allows a relatively simple way to achieve multi-color displays in segmented-color, active-matrix (AM) full color, and passive-matrix (PM) configurations. The commercial Pioneer vehicular stereo OLED display (1999) and Motorola cell phone OLED display (2000) were prepared with Kodak-licensed small molecule vacuum sublimation technology.

2.8.2 Wet-Coating Techniques

General remarks and spin-coating

Since polymers generally crosslink or decompose upon heating, they cannot be thermally evaporated in a vacuum chamber (in case of PPVs, rapid photo-oxidation is an additional problem as even residual quantities of oxygen lead to significant emission quenching). Hence, they are generally deposited by wet-coating a thin film from a solution containing them. That, however, imposes restrictions on the nature of the polymers and the sidegroups attached to the polymer backbone, since the polymer must be soluble. For example, unsubstituted PPV is insoluble. Hence, it is generally fabricated by spin-coating a soluble precursor polymer onto the desired substrate (typically ITO). The precursor polymer film is then converted to PPV by annealing at a temperature $150 \leq T \leq 250^\circ\text{C}$ for up to ~ 24 hours. As this conversion process yields an insoluble layer of PPV, additional layers may be deposited on it by spin-coating.^{51,52} However, when soluble PPV derivatives such as 2,5-dialkoxy PPVs are spun-coated onto the substrate, only solvents which would not redissolve the deposited film can be used to deposit additional layers. Thus, Gustaffson et al. [56] fabricated flexible PLEDs by sequentially spin-coating an aqueous solution of water-soluble, conducting transparent polyaniline onto a transparency, and a xylene solution of poly(2-methoxy-5-(2'-ethyl)-hexoxy-1,4-phenylene vinylene) (MEH-PPV).

Although the thickness of spun-coated films may be controlled by the concentration of the polymer in the solution, the spinning rate, and the spin-coating temperature, it is difficult to fabricate thick films and the thickness obviously cannot be monitored during deposition. In addition, no combinatorial fabrication methods have been developed for spun-coated PLEDs (see above).

Spin-coating is an established procedure in the semiconductor and display industries, widely used in photolithography of silicon and ITO and polycrystalline backplanes for liquid-crystal displays. However it may not be used for large size single plane displays for rapid web coating in reel-to-reel processes desired in flexible display manufacturing. An even more important limitation of spin-coating is that it does not provide a way to pattern full-color display. The whole surface of the substrate is covered with the light-emitting polymer, and the devices are created through cathode patterning.

Doctor blade technique

In this technique, a film of the solution containing the soluble polymer is spread with uniform thickness over the substrate using a precision “doctor blade” [57]. In contrast to spin-coating, the doctor-blade technique is very useful for fabricating relatively thick films, but does not enable the fabrication of films <100 nm thick, which are commonly used in OLEDs.

Wet-Casting

An important development of wet-casting is inkjet printing, achieved by Yang and coworkers [58]. It is currently being utilized for the development of organic high-information content (HIC) displays by, e.g., Cambridge Display Technology, Seiko-Epson, and Philips. This technique is currently leading the pursuit for commercially viable HIC displays, as the organic layers are deposited directly as an array of pixels. While several companies have announced the development of ink-jet printed displays, the numerous intricacies of this technique are delaying the commercialization of PLEDs. As in the case of spin-coating, when used for patterning bilayer PLEDs, wet casting techniques impose an additional demand of mutual insolubility of organic layers. Other important techniques currently studied in the area of wet casting are screen printing, micro-stamping, and hot microprint contact.

2.9 Materials for OLEDs

2.9.1 Anode Materials and HTLs or Buffers

Indium–Tin–Oxide (ITO)

In the most common “cathode on top” device configuration the OLED is prepared on a glass substrate pre-coated with ITO. The ITO-coated backplane is an established component in the LC-display industry with very large well-developed facilities dedicated to its preparation and handling. The availability of these elaborate facilities, each of which reflects a minimal investment of as much as \$400m, is an important prerequisite for OLED penetration of the existing flat-panel display (FPD) market. The fact that these facilities were not in place when the early attempts were made to introduce the inorganic EL displays contributed to their failure to enter the display market. The initial cost models for OLEDs manufacturing are all built on the assumption of low cost of retooling the LCD manufacturing facilities based on patterning and handling of ITO backplanes. The commercial batches of ITO-coated glass are normally characterized by square or sheer resistance, material roughness, and layer transparency. All of these parameters have important implications for device functionality and dura-

bility. However, it should be emphasized that ITO is a non-stoichiometric mixture of In, In₂O, InO, In₂O₃, Sn, SnO, and SnO₂ (it is sometimes even referred to as “In-doped tin oxide” or vice versa). It also appears that the workfunction ϕ_{ITO} of ITO films, typically ~ 4.5 eV, increases with the O content up to ~ 5.1 eV. It was found that device brightness and efficiency tend to increase with increased ϕ_{ITO} . Hence several procedures for saturating the O content of ITO have been developed. The most common is UV-ozone treatment, in which the ITO film is exposed to ozone produced by a UV lamp. Other procedures involve partial etching of the ITO in aquaregia⁶¹ or plasma etching. However, since the excess oxygen typically evolves out of the treated ITO within a few hours, the organic layers must be deposited promptly on the ITO after the treatment. Using ITO-coated glass in the common configuration is problematic in several respects. One of them is strong coupling of the emitted light to the evanescent mode inside the glass that leads to extremely high light losses. Therefore, an alternative “anode on top” configuration has also been developed. We return to this issue below, when discussing device optimization.

Pt

Since Pt has a very high $\phi=5.6$ eV, it could strongly enhance hole injection. However, since it must be very thin to be transparent, it would be deposited on, e.g., the conventional ITO. Indeed, Malliaras et al. [65] have very recently shown that a thin layer (≤ 10 Å) of Pt on ITO enhances hole injection by up to a factor of 100 relative to the uncoated ITO.

ZnO

Although ZnO also forms transparent conducting films, it has drawn surprisingly little attention for use as the anode in OLEDs. On top of the ITO layer one usually deposits an HTL or more-recently “buffer” layer. It serves to planarize the irregularities present at the ITO surface, produces an interface with an emitting layer that confines charge carriers away from the electrodes, and provides the h⁺ delivery for exciton formation.

N,N'-diphenyl-N,N'-bis(3-methylphenyl)-1,1'-biphenyl-4,4'-diamine (TPD)

This material has been used extensively as the HTL. However, its glass transition temperature T_g is a relatively low 65°C. Hence, it causes a failure of OLEDs as it recrystallizes. The recrystallization may be suppressed and the device lifetime greatly enhanced by adding a guest molecule such as rubrene. However, in that case carriers may recombine on the rubrene, resulting in red EL from that guest molecule.

Good HTL materials should satisfy one or more of the general requirements given below.

1. Materials are morphologically stable and form uniform vacuum-sublimed thin films.
2. Materials have small solid state ionization potential.
3. Materials have small solid state ionization potential. 3. Materials have high hole mobility.
4. Materials have small solid state electron affinity.

These requirements can be used as the general guiding principles for screening new hole transport materials.

N,N'-diphenyl-N,N'-bis(1-naphthylphenyl)-1,1'-biphenyl-4,4'-diamine, (NPB, α -NPB, NPD, or α -NPD)

NPB is very similar to TPD, but the methylphenyl groups are replaced by naphthylphenyls. This modification has been shown to enhance the stability of the OLEDs very significantly, apparently due to the higher glass transition temperature $T_g \sim 95^\circ\text{C}$ of NPB

Doped or Guest-Host Materials

As mentioned above and treated in detail below, crystallization of compounds such as TPD is one of the main degradation processes in OLEDs. Doping of these compounds enhances stability by inhibiting the crystallization process and by localizing the excitation energy on the dopant or guest molecule.

2.9.2 Small Electron-Transporting and Emitting Molecules

Alq₃

This green emitter has probably received more attention than any other small molecular emitter. It is not only commonly used as a green emitter, but also as a host for lower-gap emitter guest molecules, to which the SE energy is transferred very efficiently via the radiationless Förster mechanism. Such dopant or guest molecules have typically included dyes such as yellow-emitting coumarin 540 or red-emitting DCM1. For further details see Section 3.

Oxadiazoles

These compounds provided the source material for the first blue OLEDs. However, these devices were short-lived. Yet devices fabricated with improved blue-emitting amino oxadiazole fluorene did exhibit greater efficiency and stability, although their performance was still inferior to that of polyfluorene-based PLEDs.

Distyrylarylenes

These generally blue-emitting materials were studied extensively by Hosokawa and coworkers [66]. Among them, 4,4'-bis(2,2'-diphenylvinyl)-1,1'-biphenyl (DPVBi) has proven to be a particularly promising material for blue OLEDs. The degradation of OLEDs based on this material is apparently due to its crystallization, which results from its relatively low $T_g \sim 64^\circ\text{C}$. Indeed, the related spiro-DPVBi, with $T_g \sim 100^\circ\text{C}$, yields considerably more stable devices. Other widely-used electron-transporting materials include 2-(4-biphenyl)-5-(4-tert-butylphenyl)-1,3,4-oxadiazole (butyl-PBD), which is essentially nonemissive and often introduced between the cathode and the emitting layer precisely for that reason, and 3-(4-Biphenyl)-5-(4-tert-butylphenyl)-4-phenyl-1,2,4-triazole (TAZ-1).

Finally, although CuPc is used mostly as an HTL, it is also effective as an intermediate layer between the emitting layer and sputter deposited cathode. In these structures it serves a dual function, promoting electron injection during device operation and protecting the OLED from sputter damage during inorganic cathode deposition. As shown in Ref. [67], the electron injection is promoted by damage-induced states at the inorganic/-CuPc interface. This finding demonstrates again that the electronic function of organic materials in OLEDs are not derived only from their energy band characteristics. In case of the Li/Al inorganic cathode a significant amount of Li is incorporated into CuPC that leads to increased device efficiency. When ITO is sputter-deposited on top of the CuPc layer [67], the fully transparent cathode is formed and successfully utilized in stacked multi-color devices.

2.9.3 Cathode and Organic/Cathode Buffer Materials

The cathode is typically a low-to-medium workfunction (ϕ) metal such as Ca ($\phi=2.87$ eV),⁹⁸ Al ($\phi=4.3$ eV),¹⁵ or Mg_{0.9}Ag_{0.1} (for Mg, $\phi=3.66$ eV),⁵ deposited either by thermal or e-beam evaporation. In the latter case of Mg_{0.9}Ag_{0.1}, the Ag is codeposited with the Mg since the low sticking coefficient of Mg on most organic surfaces requires the presence of Ag to enable the deposition of the Mg.

X-ray and ultraviolet photoelectron spectroscopy (XPS and UPS, respectively) studies and thermally stimulated current (TSC) measurements¹⁰²

revealed that the energy offsets at the organic/metal cathode interface generally cannot be predicted using the “affinity rule”, which is based on the difference between the work functions. This is due to the chemical interactions between the metals and the organic films. In the case of PPV/Al, the Al may bind to the vinylene-carbon atom, with slightly more elaborate configurations in PPV derivatives. The interface layer of Al atoms covalently bonded to the polymer or small molecule is typically 2–3 nm thick. Ca atoms diffuse into the organic layer and then donate their electrons to the π -electron system and form Ca^{2+} ions. This Ca-doped interface layer is also 2–3 nm thick. The deposition of these and some other metals onto clean surfaces of phenylenevinylene oligomers and Alq_3 were studied under high vacuum conditions. It was found that deposition of even submonolayer quantities of metal leads to a dramatic quenching of photoluminescence from the field. On the other hand, independent studies showed that deposition on the oxygen-contaminated interfaces leads to better OLEDs. The obvious scenario was that oxidation bonds the metallic atoms thus preventing bonding to organics. This scenario is supported by the recovery of the deposition-induced quenching by subsequent oxidation. A special case is presented by Mg electrodes, which perform best when prepared under high vacuum conditions in the absence of oxygen.

The quenching recovery provided the motivation for fabrication of OLEDs with $\text{Al}_2\text{O}_3/\text{Al}$ cathodes. The Al_2O_3 was obtained by the natural oxidation of a pre-deposited ultrathin layer of Al on the organic surface. It led to improved EL efficiency as long as the thickness of the initially deposited Al layer did not exceed the depth of the native oxide layer. Further improvement was achieved when the Al cathode was separated from the organic layer with a ~ 1 nm layer of LiF. It was found that significant improvement can be achieved by introduction of LiF or CsF composites with Al, suggesting that the role of fluorides is to prevent chemical bonding of Al to organics and/or enable the alkali atoms to dope the organic as donors, rather than band matching.

Besides preventing the interaction between the organic layer and the Al or Ca cathode or n-type doping of the organic by alkali atoms, the insulating buffer layer introduced between them also results in the formation of a dipole charge layer. This dipole charge layer increases the vacuum level of the metal cathode, which reduces the barrier for electron injection from the metal to the organic layer. A detailed treatment of the changes in the vacuum level and band-bending effects at the organic-metal interface is given by Ishii et al [81].

Capitolo 3

NPD/Alq₃

3.1 Alq₃ Introduction

8-hydroxyquinoline metal chelate complexes were used for many years in analytical chemistry for a gravimetric determination of various metal cations in solution. The development of more convenient spectroscopic techniques has meanwhile replaced this method and concomitantly decreased the interest of researching chemists in this reagent. Increasing interest in tris(8-hydroxyquinoline)aluminum(III) (Alq₃) shown in Figure 1 for technical applications started with a report on efficient electroluminescent devices using Alq₃ as the active medium. These so-called organic light emitting diodes (OLEDs) opened the way for a new generation of flat panel displays. After nearly two decades of intensive research and development of OLEDs, Alq₃ still continues to be the workhorse in low-molecular weight materials for these devices. It is used as electron-transporting layer, as emission layer where green light emission is generated by electron-hole recombination in Alq₃, and it also serves as host material for various dyes to tune the emission color from green to red. Many studies in this field have focused on the optimization of device performance with respect to efficiency and long-term stability or on the understanding of charge transport properties of amorphous thin films. These investigations revealed that electrical transport in Alq₃ is characterized by a hopping-type charge carrier mobility displaying a Poole-Frenkel-like dependence on the electric field and on temperature. It was further found that trapping in distributed trap states is involved in charge transport, in particular at low fields. Different suggestions as to the origin of these traps were made, including a polaronic self-trapping effect, extrinsic traps due to impurities and the presence of a mixture of isomers of the Alq₃ molecule having different energy levels. However, no clear proof for one or the other possibility explaining the microscopic nature of these traps was given.

Another surprising circumstance was that in spite of the widespread usage of Alq₃ as amorphous films in OLEDs, comparatively few investigations

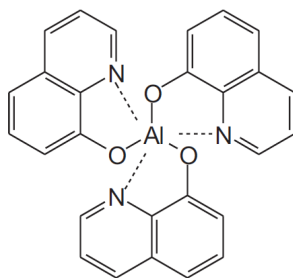


Figura 3.1: Chemical structure of Tris(8-hydroxyquinoline) aluminum(III) (Alq₃).

were devoted to the material's structural, electronic and optical properties in the crystalline state, as well as to the dependence of these properties on the preparation conditions until recently. On the other hand, it was mentioned in one of the very first publications on OLEDs based on thin films that the so-called "amorphous" film of Alq₃ might have nanocrystalline domains, which raises questions concerning the morphology and properties of Alq₃. For example, what kind of crystalline phases can be formed by Alq₃ and what are their electronic and optical properties? What is the packing of the molecules? Packing and intermolecular interactions are important for optical properties as well as for their electrical characteristics and the transport mechanism of charge carriers.

Another unresolved issue concerns the isomerism of the Alq₃ molecule. It is well known that octahedral complexes of the type MN₃O₃, where M is a trivalent metal and N and O stand for the nitrogen and oxygen atoms in the quinoline ligands, can occur in two different geometric isomers: meridional and facial, as shown in Figure 3.1. Nevertheless, until recently only the meridional isomer had been clearly identified and no direct experimental evidence for the facial isomer had been found. Therefore it was generally believed that the meridional isomer is predominant, both in amorphous films and crystals of Alq₃. The existence and the properties of the facial isomer are discussed in detail in the literature and a key issue is its possible presence in sublimed Alq₃ films. Many suggestions have been made about its influence on trap density, charge carrier transport and thus on the characteristics and performance of OLEDs. For example, the higher dipole moment of the facial isomer is expected to influence the morphology of the film as well as the injection of charge carriers at the interface. In addition the different HOMO and LUMO levels predicted for the two isomers are expected to influence the injection barrier and could act as traps for charge carriers. Therefore the question is whether the facial isomer is present in one or the other modification of Alq₃, and if so, if it is possible to isolate it. The isolation of the facial isomer is of great interest, as it will allow its properties to be examined separately and thus its role in OLEDs to be

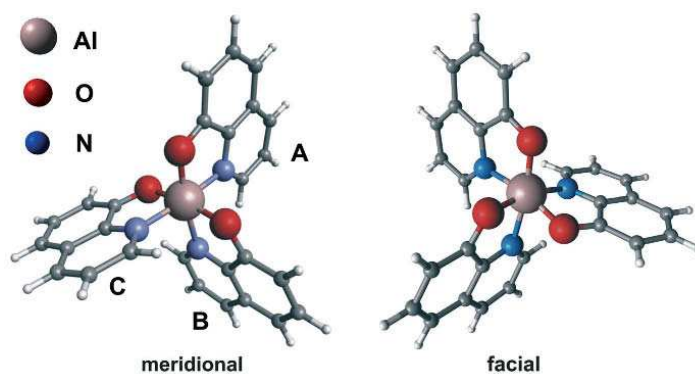


Figura 3.2: Chemical structure of Tris(8-hydroxyquinoline) aluminum(III) (Alq₃).

clarified.

3.2 Crystalline Phases of Alq₃

This section describes the preparation and identification of different crystalline phases of Alq₃ obtained by sublimation. In order to induce growth of different phases, the temperature gradient in a sublimation tube was used. Phases that grow at different temperatures were obtained and their crystal structures were investigated.

Temperature gradient sublimation is a common method for purification of organic materials. After this purification procedure polycrystalline powders of different appearance were found in the sublimation tube and thus we distinguished between three different zones in the glass tube. The materials in these zones, hereafter called fractions, differ in their shape of crystals, their color, their solubility and their fluorescence.

A typical example of these glass tubes after sublimation is shown in Figure 3 with indicated areas for the three different fractions. In the hottest zone of the growth area there is an approximately 1.5 cm wide region with very small needle-like crystals with white or slightly yellow appearance (fraction1). This zone is followed by the main fraction (about 8.5 cm) with yellow cubic crystals and dimensions up to $500 \times 500 \times 500 \mu\text{m}^3$, showing yellowish-green fluorescence (fraction2). In the subsequent colder zone of the sublimation tube another fraction is obtained with dark yellow-green needle-like crystals with a size of $50 \times 50 \times 500 \mu\text{m}^3$ (fraction 3).

These fractions have different solubility in organic solvents. While fraction 3 and (apart from a small residue) also fraction 2 are readily dissolved in chloroform at a relatively high concentration of more than 1% by weight, the solubility of fraction 1 is extremely poor. It takes several hours to dis-

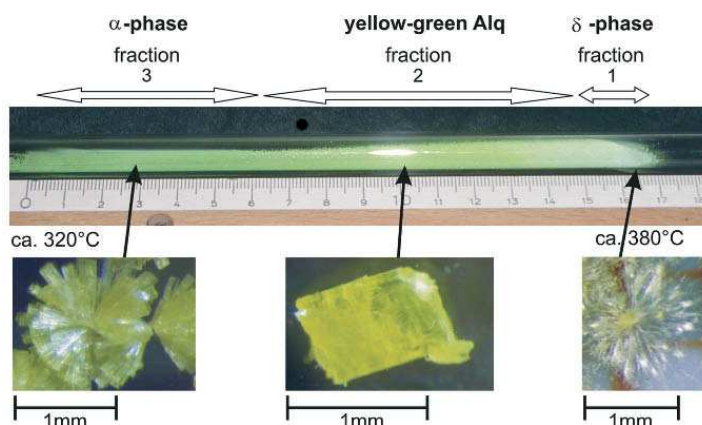


Figure 3.3: Picture of a sublimation tube. Due to the temperature gradient in the sublimation tube, the material obtained is separated into three zones, which are labeled by fraction 1, fraction 2 and fraction 3. Crystals of these fractions in the tube are also shown.

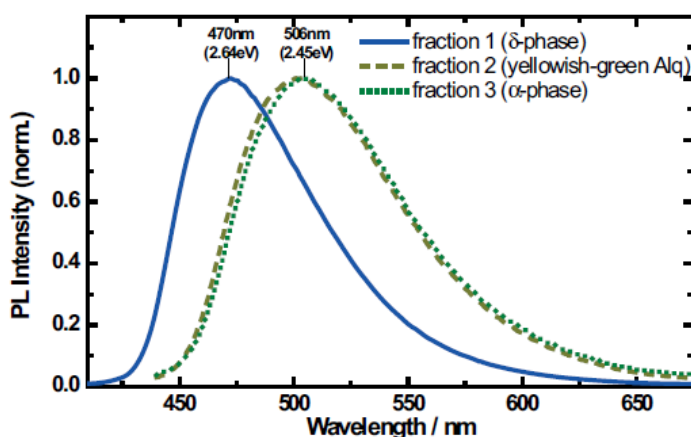


Figure 3.4: PL spectra of the three fractions obtained from the sublimation tube, excited at 350nm and measured at room temperature.

solve a sizeable amount in chloroform, but then the color of the solution becomes similar to that of the other fractions.

Further differences between the three fractions are found in their photoluminescence (PL) spectra. Figure 3.2 shows the spectra measured with an excitation wavelength of 350nm at room temperature. All fractions show one broad PL band with no additional structures and a tail at the side of longer wavelengths. Their main difference is the large blue shift of the PL maximum of about 0.19eV (36nm) from fraction 3 to fraction 1 with a PL maximum at about 506nm (2.45eV) and 470nm (2.64eV), respectively.

In order to investigate the origin of these differences, the crystallographic data of the three fractions were determined by using X-ray powder diffraction as shown in Figure 5. As a result two different phases were found.

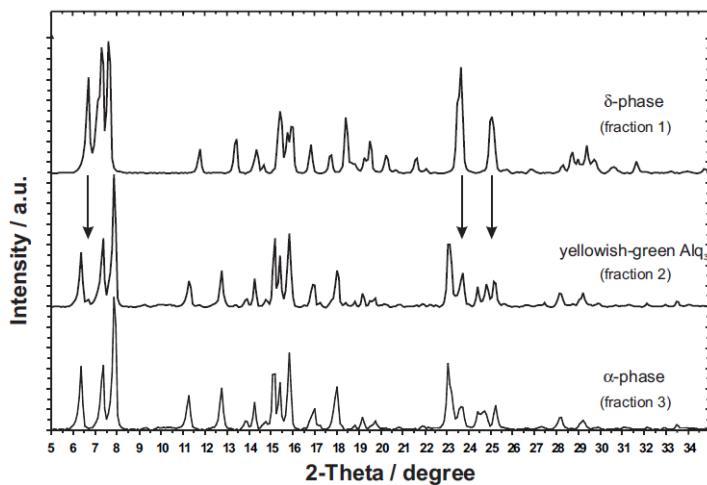


Figure 3.5: PL spectra of the three fractions obtained from the sublimation tube, excited at 350nm and measured at room temperature.

Fraction 1 and fraction 3 show the main differences. These differences are best seen for small angles below 9 degrees and in the region between 22 and 26 degrees. From these two spectra the unit cells for fraction 1 and fraction 3 were determined. Indexing of the peaks observed is given in Reference [39] and [40] and the cell parameters determined for the different phases of Alq₃ are summarized in Table 1 together with two other phases (β - and γ -) found by Brinkmann et al. The spectrum of fraction 2 seems to be a mixture of two phases. Basically the spectrum is similar to that of fraction 3 apart from some small peaks or shoulders at positions where fraction 1 and fraction 3 are different, for example at 23.5 degrees and especially at 6.69 degrees. This suggests that fraction 2 mainly consists of the same phase as fraction 3, but has some small admixtures of material from fraction 1. The result that fraction 2 is a mixture of two different phases is relevant for applications, as it is mainly this fraction that is used for fabrication of OLEDs. From these X-ray data it becomes clear that the main difference is between fraction 1 and fraction 3, which have different unit cells given in Figure 3.2.

It is possible to compare these crystal data obtained above with results of other researchers. Brinkmann et al. reported on three different crystalline structures called α -, β - and γ -phase. The published data for the α -phase are identical to those of fraction 3. β -Alq₃ is grown from solution and its properties are in principle similar to the α -phase, only with a small red shift in the PL due to slightly different intermolecular interaction in the crystal. The published data of γ -Alq₃ are listed in Table 1 for completeness. All phases and evaporated films were identified as consisting of the meridional isomer, and therefore only the meridional molecule was found at that time.

The denotation of the phases in our work is in accordance with these

	α -phase (fraction 3) [14, 15]	β -phase [14]	γ -phase [14]	δ -phase (fraction 1) [16, 17]
crystal system	triclinic	triclinic	trigonal	triclinic
space group	P-1	P-1	P-31c	P-1
Z	2	2	2	2
a [Å]	12.91	10.25	14.41	13.24
b [Å]	14.74	13.17	14.41	14.43
c [Å]	6.26	8.44	6.22	6.18
α [°]	89.7	97.1	90	88.55
β [°]	97.7	89.7	90	95.9
γ [°]	109.7	108.6	120	113.9
V [Å ³]	1111	1072	1118	1072.5

Figure 3.6: Crystallographic data of the polycrystalline phases of Alq₃.

published data. Fraction 3 and the main part of fraction 2 consist of the α -phase. The structure of fraction 1 is new and no corresponding phase has been published so far. Accordingly fraction 1 is hereafter called the δ -phase of Alq₃.

δ -Alq₃ exhibits major differences to all other phases obtained from the sublimation tube. It is a whitish powder, has a different crystal structure and, importantly, a strongly blue-shifted PL. On the other hand the α - and β -phase are very similar, as reported by Brinkmann et al. Consequently it seems to be most interesting to investigate the differences and similarities of the α - and δ -phase of Alq₃, as will be done in the following sections of this article.

3.3 Thermal Properties of Alq₃

The phases discussed above were grown in different areas of the sublimation tube in regions of different temperature. Thus temperature obviously has a strong influence on the formation of these phases and it is important to learn more about the thermal properties of Alq₃. Therefore the formation conditions of the different phases of Alq₃ were investigated using differential scanning calorimetry (DSC) measurements in combination with structural and optical characterization.

Figure 3.3 shows the DSC measurement of polycrystalline Alq₃ powder (α -phase) taken at a heating rate of 20°C/min. Coupled endothermic and exothermic peaks are observed at about 395°C prior to the large melting transition at 419°C. This additional phase transition has also been reported in the literature and has been attributed to polymorphism of the crystalline material. It is very pronounced at fast heating rates (above 15°C/min). For slow heating rates the endothermic and exothermic transitions become broader and the peak height decreases as compared to the strong melting peak. The peaks start to intermingle and are shifted to a slightly lower temperature, as shown in the inset of Figure 6 for heating rates of 20°, 10°, 5° and 2°C per minute. This behavior is similar to known irreversible

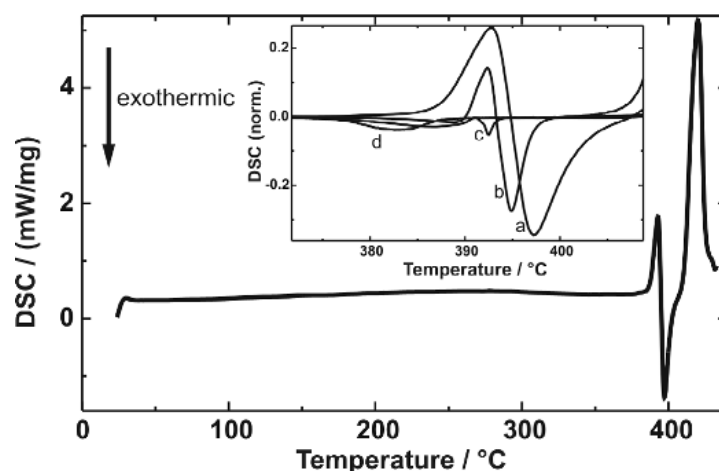


Figura 3.7: DSC trace of Alq₃ with pronounced thermal transitions at 393°, 396° and 419°C measured at a heating rate of 20°C/min. Inset: Broadening and intermingling of the endothermic and exothermic peaks around 395°C in the DSC signal related to the sweep speed (a: 20°C/min, b: 10°C/min, c: 5°C/min, d: 2°C/min; normalized on the melting peak intensity). At low measuring speed only the more pronounced exothermic transition is visible.

monotropic solid-solid transitions. Typically, the monotropic transition is slow and is mostly observed a few degrees below the melting point. Thus it is advisable to measure the monotropic transition isothermally at very slow heating rates.

It should be noted that increasing the temperature above 430°C results in decomposition of the material and that a small broad transition at 320°C reported by Sapochak et al. [41] was not observed in our samples. For the following measurements a slow heating rate of 2°C/min was used, where the shift of the peak temperatures is fairly small (see Figure 3.3) and where it is possible to stop the process at a defined temperature. Using this procedure the conditions for the preparation of different Alq₃ phases by a controlled thermal annealing process were investigated.

For these slow DSC measurements three different regions are distinguished in Figure 3.3: In the first region (A) below the exothermic phase transition Alq₃ is the usual yellowish-green powder, in the second region (B) between this phase transition and the melting peak Alq₃ is a whitish powder, and finally in region C Alq₃ is a liquid melt. The glassy state of Alq₃ was obtained by quenching this melt in liquid nitrogen. Its highly amorphous character was verified by using X-ray powder diffraction measurements with an image plate detection system. Cooling down the liquid melt slowly resulted in yellowish-green powder (A) again, as was previously reported [42]. All of these materials are stable at room temperature.

Figure 3.3 shows the PL spectra measured at room temperature of annealed polycrystalline Alq₃ powder from regions A and B as well as of the

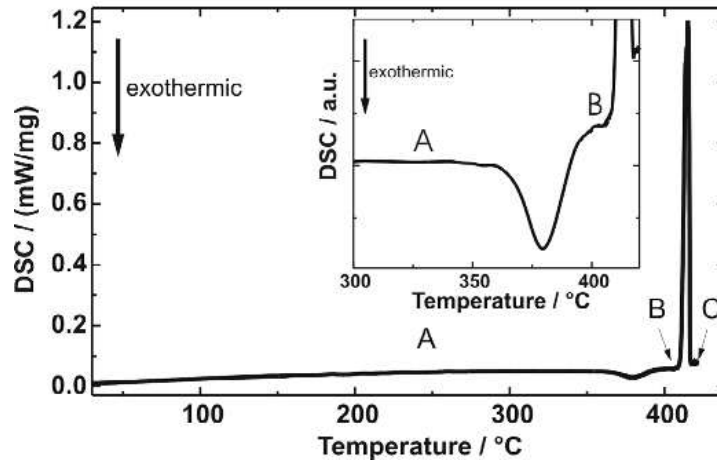


Figure 3.8: DSC trace of Alq₃ measured at a heating rate of 2°C/min. The clearly pronounced exothermic phase transition at 380°C prior to the melting point is enlarged in the inset, as it becomes broad and less intense compared to the melting peak for this slow heating rate. A, B and C mark the regions of yellowish-green Alq₃, blue Alq₃ and melt, respectively.

quenched amorphous melt (C). For annealing temperatures up to 365°C Alq₃ is a yellowish-green powder with a PL maximum at 506nm (curve A). After the exothermic transition at about 380°C, there is a big blue shift of 0.18eV (37nm), associated with a slight change in the shape of the PL spectrum (curve B), which is less symmetric for blue Alq₃. The quenched melt (curve C) is clearly red-shifted (0.14eV) compared to the yellowish-green Alq₃-powder (curve A). The strong difference in the emission color can be seen in Figure 3.3, where samples of the quenched melt, yellowish-green and blue Alq₃ are shown in daylight (a) and under UV-irradiation (b), respectively. The emission color is shifted from green (CIE coordinates: x=0.27, y=0.5) to blue (x=0.16, y=0.26). From Figure 3.3 one can also see the relatively low PL intensity of the quenched melt compared to the very intense PL emission of blue Alq₃. For PL quantum efficiency the values obtained for blue Alq₃, yellowish-green powder, evaporated film and quenched amorphous melt were 51%, 40%, 19% and 3%, respectively.

For comparison the dashed line in Figure 8 is the PL spectrum of an evaporated Alq₃-film as used in OLEDs. Although these films are commonly called “amorphous”, one can clearly see that the PL maximum is located between the quenched melt and crystalline Alq₃. This is an indication of the nanocrystalline character of these films, as noted already by Tang et al. [43].

Yellowish-green Alq₃, blue Alq₃ and amorphous melt can be converted into each other. As described above, yellowish-green Alq₃ annealed above the phase transition at 380°C results in blue Alq₃. Annealing blue Alq₃ above the melting point and cooling it down slowly, as shown in Figure

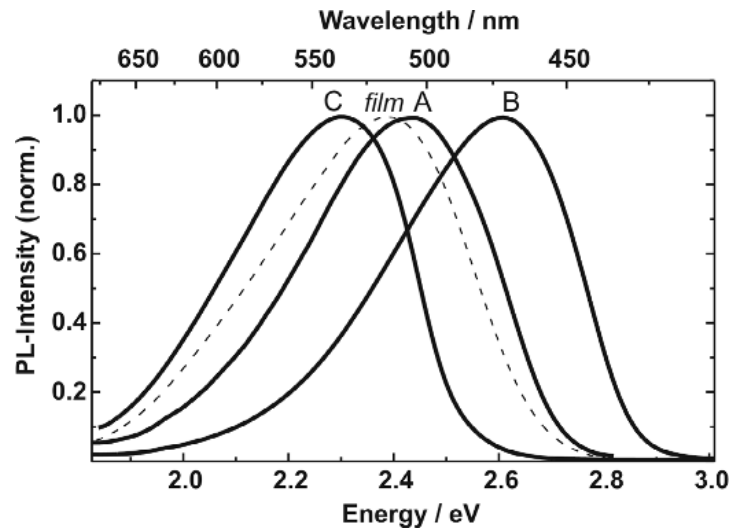


Figure 3.9: PL spectra of Alq₃ samples taken from regions A, B and C of Figure 3.3, respectively, excited at 350nm. The PL of an evaporated Alq₃ film (dashed line) is shown for purposes of comparison. All spectra were measured at room temperature.

3.3, yields yellowish-green powder again and a pronounced recrystallization peak is observed. With the same procedure of annealing the quenched melt above the melting point and cooling it down slowly, yellowish-green powder is obtained again, and the quenched melt is converted into blue Alq₃ by annealing it between 380°C and 410°C. The successful conversion from one phase into the other was confirmed by measurements of the PL spectra, FT-IR spectra, Raman spectra, and X-ray diffraction.

Obviously, blue Alq₃ is formed during the phase transition at about 380°C. This phase transition appeared when starting the measurement with yellowish-green Alq₃, as shown in Figure 3.3. On the other hand, when starting the annealing procedure with blue Alq₃ material no such phase transition was observed, as shown in Figure 3.3 i) and ii) trace b. However, measurements taken after the sample in Figure 3.3 b had cooled down showed the exothermic peak again, as can be seen in trace c of Figure 3.3 i).

As blue Alq₃ is formed in the region between the crystallographic phase transition and the melting point, the influence of temperature and preparation conditions in the region between 385°C and 410°C was investigated. Figure 3.3 shows X-ray powder diffraction spectra of blue Alq₃ prepared under three different conditions. For spectrum (I) yellowish-green Alq₃ powder (α -Alq₃) was annealed at 400°C for 2h. This spectrum is similar to the one obtained for fraction 1 in the sublimation tube shown in Figure 3.2. The shoulder at $2\theta=7.05^\circ$ for different samples of blue Alq₃ was variably pronounced. From this one may assume another high-temperature phase to be present in these samples. To test this, Alq₃ was annealed for several

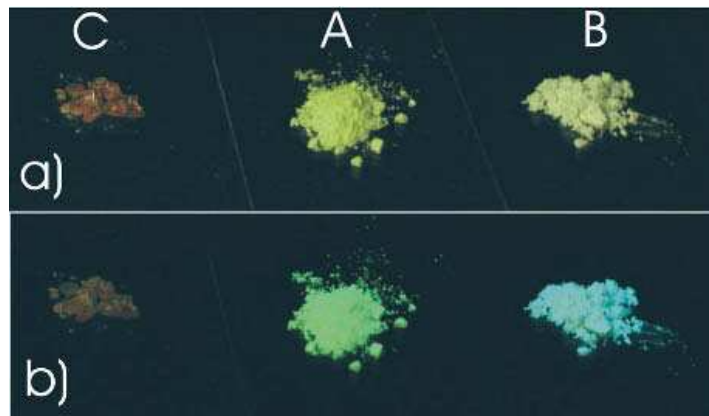


Figure 3.10: Photographs of AlQ_3 samples taken from regions A, B and C in Figure 8: a) in usual daylight and b) under UV-irradiation (excitation wavelength: 366nm), clearly showing the strong blue shift of the luminescence of the annealed material (CIE color coordinates for A: $x=0.27$, $y=0.50$; for B: $x=0.16$, $y=0.26$).

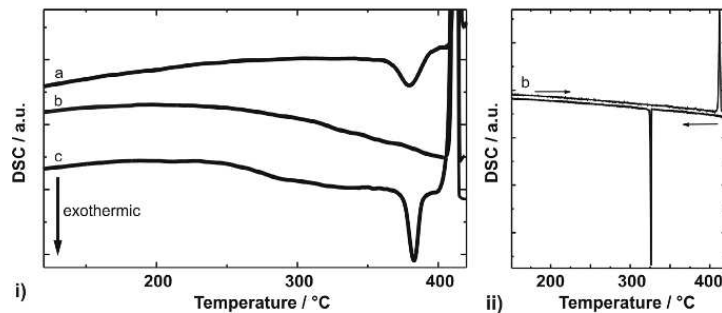


Figure 3.11: DSC traces of a: yellowish-green AlQ_3 and b: blue AlQ_3 . Trace c shows a second heating cycle after cooling down the melt (b) again. By annealing blue AlQ_3 no phase transition at 380°C is observed (trace b in i) and ii)). Cooling down the melt gives a strong recrystallization peak.

minutes at a higher temperature of 410°C (very close to the melting point) and a dark yellow substance was obtained, which exhibited only poor photoluminescence together with blue luminescent material. Its X-ray spectrum (Figure 3.3 (II)) has a number of new peaks, which become very obvious for example at $2\Theta=7.05^\circ$ (the position of the shoulder in spectrum (I)) and 25.85° . On the other hand, spectrum (III) shows AlQ_3 - powder annealed at 390°C for 6 hours. The additional lines observed in spectrum (II) are no longer present in this spectrum.

Based on these investigations, blue luminescent AlQ_3 obtained by annealing yellowish-green AlQ_3 (α -phase) above the phase transition at about 380°C was identified as the δ -phase of AlQ_3 with the unit cell given in Table 1. As seen in curves (I) and (II) of Figure 11, annealing AlQ_3 at temperatu-

res higher than 380°, close to the melting point, results in the appearance of new peaks in the X-ray spectra, which can be attributed to an additional high temperature phase. Brinkmann et al. have reported on such a high temperature phase, namely γ -Alq₃. Using the given unit cell parameters from their work, the positions of all possible X-ray peaks for this phase were calculated, as indicated by the vertical bars in curve (II) of Figure 3.3. These calculated peaks are located at the positions where spectrum (II) and (III) are different. Therefore it suggests that in sample (II) there is a high concentration of γ -Alq₃, whereas sample (III) is practically pure δ -Alq₃, as will be confirmed in the next section. From this it can be concluded that there are two high temperature phases of Alq₃: δ -Alq₃ and the γ -phase.

Blue luminescent Alq₃ obtained by train sublimation as described in the previous section and by annealing showed the same behavior with respect to its solubility as well as its properties in PL, DSC, and IR measurements, confirming that in both cases the δ -phase of Alq₃ was obtained. In the sublimation tube the different phases were separated due to the temperature gradient. Since *delta*-Alq₃ and the other high temperature phase (most likely γ -Alq₃) are formed in a relatively narrow temperature region, the separation of the two phases by train sublimation is difficult and a certain ratio of γ -Alq₃ is still present in the samples of δ -Alq₃, as indicated by the small shoulder at $2\Theta=7.05^\circ$ in the X-ray spectrum. On the other hand, under appropriate annealing conditions it is possible to obtain pure δ -phase without any visible admixtures of other phases, as demonstrated in curve (III) of Figure 3.3. A further advantage of this simple annealing process compared to temperature gradient sublimation is the possibility of obtaining large amounts (several grams) of pure δ -Alq₃ in a well-controlled process.

The relative content of δ - and γ - Alq₃ very critically depends on the preparation conditions (e.g. vacuum/atmosphere and temperature) as can also be seen in Figure 3.3 and can thus be tuned at will choosing suitable parameters. The samples measured in Figure 3.3 (III) and Figure 3.4.1 consist of more than 98% of δ - Alq₃.

Chemical reactions during the annealing process can be excluded because the usual yellowish-green Alq₃ (α -phase) and the blue luminescent δ -Alq₃ can be easily converted into each other. Annealing yellowish-green Alq₃ at temperatures higher than 380°C results in δ -Alq₃, while heating δ -Alq₃ above the melting point and cooling the melt down slowly results in yellowish-green powder again. Another method of reconverting blue Alq₃ into yellowish-green Alq₃ is to evaporate the material or to dissolve it in any appropriate solvent (e.g. chloroform). The same holds for the glassy state of Alq₃ obtained by quenching the melt. It is readily dissolved in chloroform and films of good quality can be cast from such solutions. The PL spectrum of such films is the same as for evaporated films of Alq₃. By annealing material in the glassy state, it is possible to obtain both the yellowish-green α -Alq₃ and the blue δ -Alq₃, depending on the temperature. In all cases

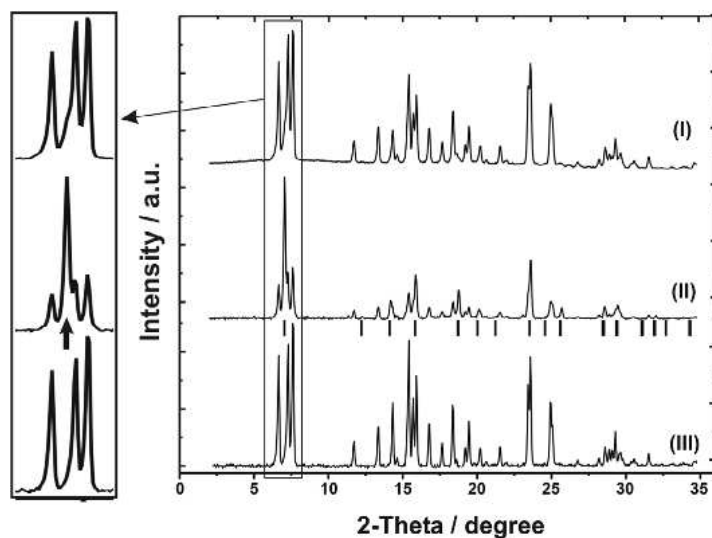


Figure 3.12: X-ray powder diffractograms of polycrystalline blue Alq_3 prepared under different conditions. For spectrum (I) yellowish-green Alq_3 -powder ($\alpha\text{-Alq}_3$) was annealed at 400°C for 2 hours. In spectrum (II) the powder was annealed at 410°C (close to melting point). For spectrum (III) Alq_3 was annealed at 390°C for 6 hours. The additional lines and shoulders observed in spectrum (II) are not present in spectrum (III). Bars in spectrum (II) mark calculated positions for all possible X-ray peaks of $\gamma\text{-Alq}_3$.

pure Alq_3 with no visible contaminating material is obtained. The possibility of transforming Alq_3 from one phase into the other implies that even at these high temperatures there is no decomposition or chemical reaction of the material. So it is important to emphasize that for all temperatures up to 425°C we are dealing with Alq_3 , in agreement with ^1H NMR and FT-IR analysis of Alq_3 annealed at 422°C , where no decomposition products have been found. By excluding chemical reactions the difference in the phases must be of physical and structural origin.

3.4 The Molecular Structure of $\delta\text{-Alq}_3$

3.4.1 High resolution powder diffraction using synchrotron radiation

In the previous sections a new phase of Alq_3 , the d-phase, which exhibits major differences to all other phases, was introduced and characterized. Based on the observed blue-shift of the PL by almost 0.2eV and the quantum chemical calculations of Curioni et al., which predicted a difference in the energy gap of the two isomers in that range, it could be supposed that the δ -phase contains the facial isomer of Alq_3 . However, to prove this hypothesis it was necessary to resolve the crystal structure of the new phase,

including the structure of the constituting molecules. The problem in determining the structure of organic molecular crystals is mainly due to the large number of atoms (104 for Alq₃) in the unit cell. Standard laboratory equipment requires single crystals to solve the structure of a new phase of a material; however, so far single crystals large enough for a full analysis of the structure have only been available for the β -phase of Alq₃. On the other hand, due to the use of high brilliance synchrotron radiation sources powder diffraction methods have progressed substantially in recent years, allowing very reliable determination of the structure from powder material without the need for larger single crystals. For this, high quality experimental data and specialized software for the analysis of the structure are required. These methods are very sensitive and unambiguous results are only to be expected if samples of one uniform crystal phase are measured. As the δ -phase can be isolated and *delta*-Alq₃ is easily obtained as a fine polycrystalline powder, these are good preconditions for this method.

In the case of a molecular crystal like Alq₃ it is necessary to start the simulation of the spectrum with an assumed configuration of the molecules within the unit cell in order to achieve convergence within a reasonable calculation time. Therefore we assumed a molecular configuration on the basis of the known connectivity of the molecule. The ligands were assumed to be planar and were randomly moved within a range of $\pm 20^\circ$ by a simulated annealing procedure until a minimal difference to the measured spectrum was obtained. After this, the position of the atoms was optimized by Rietveld refinements. The accuracy of the structure obtained is given by the R-values and the goodness of fit χ . More information on the experimental procedure and analysis is found in Ref. [44] as well as in the literature [55].

The following analysis of the data of the δ -phase of Alq₃ was made on the assumption that one of the two isomers is the constituent of this phase. First the results for the facial isomer are given, followed by the results for the meridional isomer for comparison.

Figure 3.4.1 shows the spectrum observed together with the best Rietveld-fit profiles for the assumption of the facial isomer. The enlarged difference curve between observed and calculated profiles is given in an additional window below. Indexing of this very well resolved powder spectrum with the ITO routine led to a primitive triclinic unit cell for Alq₃ with lattice parameters given in Table 2. The number of formula units per unit cell could be determined as $Z=2$ from packing considerations and density measurements. P-1 was selected as the most probable space group, which was confirmed by Rietveld refinements. The high quality of the refinement becomes obvious from the excellent differential pattern in particular at high diffraction angles (corresponding to small distances in real space), the R_{wp} value of 6.5%, and the Bragg R value $R-F^2$ of 10.5%. Crystallographic data for δ -Alq₃ are listed in Figure 3.4.1.

The molecular structure of *delta*-Alq₃ obtained from these measuremen-

Formula	$\text{Al}(\text{C}_9\text{H}_6\text{NO})_3$	$\rho\text{-calc} [\text{g}/\text{cm}^3]$	1.423
Temperature [K]	295	2Θ range [°]	4-35.7
Formula weight [g/mol]	918.88	Step size [° 2Θ]	0.005
Space group	P-1	Wavelength [Å]	1.14982(2)
Z	2	μ [1/cm]	2.48
a [Å]	13.2415(1)	Capillary diameter	0.7
b [Å]	14.4253(1)	R_p [%]	5.0
c [Å]	6.17727(5)	R_{wp} [%]	6.5
α [°]	88.5542(8)	R-F ² [%]	10.5
β [°]	95.9258(7)	Reduced χ^2	1.6
γ [°]	113.9360(6)	No. of reflections	337
V [Å ³]	1072.52(2)	No. of variables	115

Figure 3.13: Crystallographic data for *delta*- Alq_3 . R_p , R_{wp} , and R-F² refer to the Rietveld criteria of the fit for profile and weighted profile respectively, defined by Langford and Louer.

ts is shown in Figure 3.4.1. Compared to the idealized isolated facial Alq_3 isomer, the molecule is only slightly distorted, which reduces its symmetry only negligibly, and the planes defined by the O- and N-atoms, respectively, are parallel. The molecules form linear stacks in the c-direction of the crystal. The projection along the c-axis as well as the projection perpendicular to the planes of the hydroxyquinoline ligands, which shows the overlap between ligands of neighboring Alq_3 molecules, are shown in Figure 3.4.1.

The data was also evaluated on the assumption of the meridional isomer. The best fit obtained for this case is plotted in Figure 15 together with the differential curve. A comparison with Figure 3.4.1 clearly shows that the

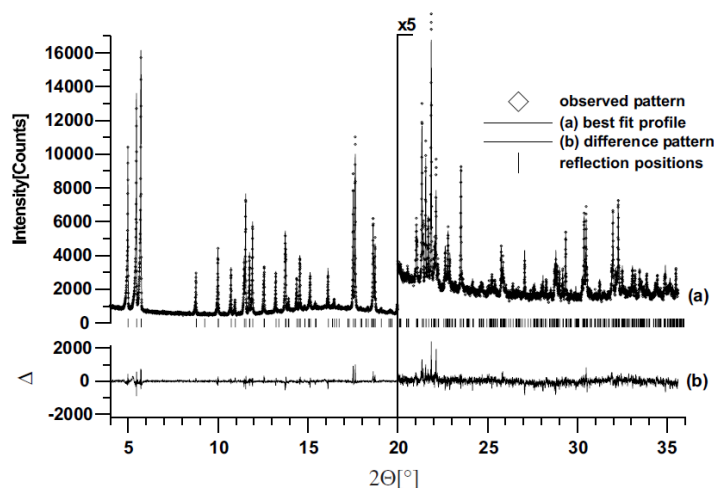


Figure 3.14: Scattered X-ray intensity for *delta*- Alq_3 under ambient conditions as a function of diffraction angle 2Θ . Shown are the observed patterns (diamonds), the best Rietveld-fit profiles on the assumption of a facial isomer (line) and the enlarged difference curves between observed and calculated profiles in an additional window below. The high angle part is enlarged by a factor of 5, starting at 20° . The wavelength was $\lambda = 1.15$.

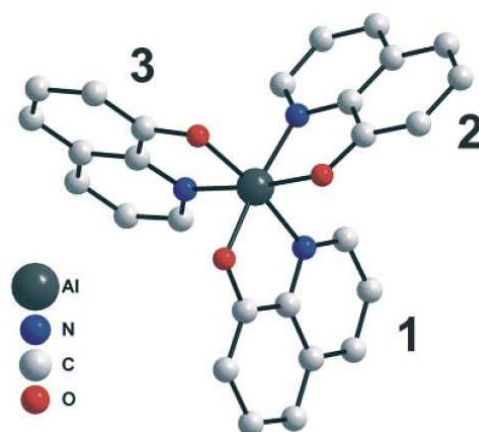


Figura 3.15: Facial Alq₃ molecule of the δ -phase with the three hydroxyquinoline ligands labeled by 1, 2 and 3. H-atoms are omitted for simplicity.

fit assuming the meridional isomer is far worse than the result for the facial isomer. Refinement resulted in a distorted meridional molecule, whereby the distance for one coordination bond (Al-N) was elongated more than 10% compared to the others (ligand A and B: ca. 2.1 Å, ligand C: 2.39 Å) and a Bragg R value $R-F^2$ of 19.4% was obtained. R-Values, tables and a picture of the distorted meridional molecule are given in Ref. [44] and [61].

The most important outcome of these refinements is that the δ -phase of Alq₃ consists of the facial isomer. For a long time it was believed that the facial isomer is unstable and would not exist. Thus the results shown here give clear evidence for the existence of this facial isomer. The simulations assuming the facial isomer closely match the measured spectrum, as can be seen in the differential spectrum in Figure 3.4.1, which is much better than the differential spectrum in Figure 3.4.1 of the best possible fit for the meridional isomer. For the meridional isomer the molecule is distorted and a substantially higher Bragg R value (by 9%) was obtained compared to the facial isomer ($R-F^2 = 10.5\%$ facial, 19.4% meridional). The R values for the facial isomer indicate a high quality of the refinement, resulting in a very high probability that the δ -phase consists of this isomer. Furthermore, the high quality of the fit and the very well resolved spectrum suggests that the samples of δ -Alq₃ are an almost pure phase, confirming the results in the previous section. Therefore it can be concluded that the δ -Alq₃ samples prepared under defined annealing conditions as described above are a pure phase without significant admixtures of other phases and that δ -Alq₃ consists of the facial isomer. Thus, as a result of the preparation of δ -Alq₃, we have for the first time successfully isolated the long sought-after facial isomer of Alq₃.

This assignment of the facial isomer as being the only constituent of the δ -phase of Alq₃ was also very recently confirmed by NMR measurements

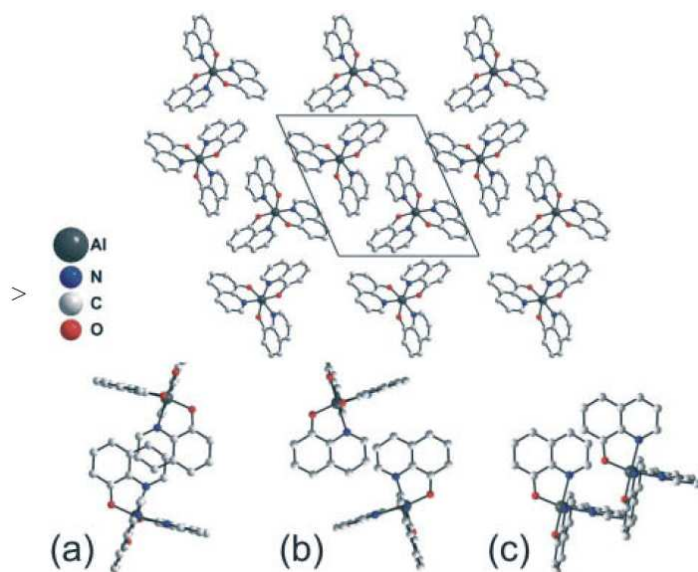


Figure 3.16: Crystal structure of δ -Alq₃ in a projection along the c -axis. (a), (b), and (c) are projections perpendicular to the planes of the hydroxyquinoline ligands 1, 2, and 3, respectively, showing the overlap between ligands of neighboring Alq₃ molecules

[59] where the different electric field gradient tensors for the two isomers give characteristic fingerprints for their identification in solid state Al-NMR spectra. Moreover, the group at Eastman Kodak has recently grown single crystals of δ -Alq₃ large enough for a single crystal structure analysis. An excellent confirmation of the structure and the packing presented here was obtained [60].

The data also gives information about distance and orientation of the molecules and thus about molecular packing in the crystal. It is noteworthy that the molecules are arranged in a manner minimizing the possible overlap of the π -orbitals between pairs of hydroxyquinoline ligands belonging to neighboring Alq₃ molecules, as shown in Figure 3.4.1. As demonstrated by Brinkmann et al., the orbital overlap influences the optical properties and can explain shifts in the photoluminescence spectra of different phases of Alq₃. In δ -Alq₃ the pyridine rings of antiparallel ligands 1 face each other with an interligand distance of 3.4 Å (Figure 3.4.1a). The partial overlap of the rings is smaller than in the other known phases, and the atoms are slightly displaced, further reducing the overlap of the p-orbitals. Figure 3.4.1b and (c) show the projection perpendicular to the planes of ligand 2 and ligand 3, respectively. The inter-ligand distance is about 3.45 Å and these ligands do not overlap at all. Thus a strongly reduced π -orbital overlap of neighboring ligands is found in δ -Alq₃ as compared to the α - and β -phase. As only one ligand of each molecule overlaps with a neighboring molecule, there are no $\pi - \pi$ links generating an extended one-dimensional chain, as

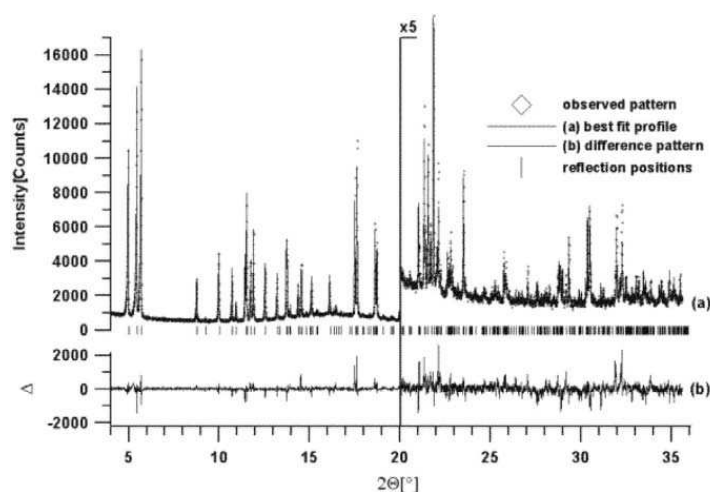


Figure 3.17: Scattered X-ray intensity for δ -Alq₃ at ambient conditions. Shown are the observed patterns (diamonds), the best Rietveld-fit profiles on the assumption of a meridional isomer (line) and the enlarged difference curves between observed and calculated profiles in an additional window below. Best values obtained for R_p , R_{wp} and $R-F^2$ are 7.3%, 9.4% and 19.4%, respectively.

reported for the β -phase. In view of this, both the packing effect with reduced intermolecular interaction and the changed symmetry of the molecule are likely to be responsible for the large blue-shift of the photoluminescence by 0.2 eV, which is in the same range as predicted theoretically by Curioni et al. for the two isomers [46].

For transformation from the meridional isomer to the facial isomer one ligand, namely ligand C in Figure 3.1, has to flip by 180°. From our results the facial isomer is formed at temperatures above 380°C; thus the question is of interest whether this transition is energetically allowed for this molecule. Amati et al. made theoretical calculations for several possible transition processes between the geometric isomers of Alq₃ and its stereoisomers, and they found that thermal conversion from the meridional isomer to the facial isomer is energetically possible [52]. Very recently Utz et al. reported on NMR measurements of solutions demonstrating an internally mobile nature of the Alq₃ complex [53]. They found a high probability of ligands flipping by 180° and suggested that this process takes place on a time scale of about 5s⁻¹ at room temperature in solution. In these measurements they were only able to determine the meridional isomer for two reasons: First, the facial isomer is predicted to be less stable by about 17kJ/mol for the isolated molecule, thereby reducing its lifetime in solution; second, only the flip of ligand C may result in the facial isomer, giving a lower probability for this process, and thus the expected concentration of this isomer in solution is likely to be too small to be measured [53]. These measurements and

the theoretical work of Amati et al. demonstrate that the transformation from the meridional isomer to the facial isomer at elevated temperature is possible, as was carried out for the δ -phase.

Brinkman et al. used the preparation method that is described in this review to obtain different phases of Tris(8-hydroxyquinoline) Gallium(III). It is highly remarkable, that they observed the same behavior as we describe here for Alq₃. Thus it is not simply related to the Alq₃ molecule but seems to be a general property of this class of chelate complexes.

3.4.2 Vibrational Analysis

Due to the different molecular symmetry of the meridional and facial isomers (C_1 versus C_3), vibrational analysis using infrared (IR) spectroscopy should be another possible method to differentiate between them. In particular, the first coordination sphere or central part of the molecule AlO_3N_3 should show characteristic vibrational properties for each isomer (Al-O and Al-N modes located below 600 cm^{-1} , as calculated by Kushto et al. [45]). Furthermore, there is a weak coupling of the three ligands via the central part, and movements around the central aluminum atom are involved in most of the molecular vibrations below 1700 cm^{-1} . This coupling depends on the relative positions of the oxygen atoms of the ligands (compare Figure 3.1). For the facial isomer each oxygen atom faces a nitrogen atom, and thus the coupling via the Al atom is identical for all ligands, whereas for the meridional isomer one can clearly distinguish between the ligands labeled by A, B and C in Figure 3.1. For the meridional isomer, the coupling mainly affects the ligands B and C, where the oxygen atoms face each other, and to a lesser extent the A and B ligands, which have the oxygen and nitrogen atoms opposite. The coupling mechanism of ligand A and C is mainly characterized by the modes of the two opposite nitrogen atoms. This means that due to the lower symmetry of the meridional molecule each vibrational mode has a slightly different energy for the three ligands.

For the δ -phase of Alq₃ it was shown above by structural investigations to consist of the facial isomer. We can therefore use the IR spectra to identify characteristic differences in the vibrational properties of the two isomers. Figure 16 shows a comparison of the FT-IR-spectra of δ -Alq₃, α -Alq₃, and the ligand hydroxyquinoline (8-Hq) alone. In principle one has to distinguish between two regions, above and below 600 cm^{-1} . The lines above 600 cm^{-1} are mainly related to vibrations within the ligands, as one can see from comparison with the 8-Hq spectrum. Due to the different symmetry of the isomers there is a different interaction of the ligands via the Al-atom leading to small differences in this region. The region below 600 cm^{-1} is dominated by the modes of the first coordination sphere or central fragment around the Al-atom. A detailed discussion of these spectra and individual lines as well as a discussion of the influence of crystallinity of the

sample can be found in Refs. [54] and [61]. In this review we only give the main results and exemplify the discussion by the Al-N and Al-O stretching modes that are marked with arrows in Figure 3.4.2.

If we consider the central fragment AlO_3N_3 , the local symmetry for each isomer is C_{2v} and C_{3v} , respectively, as shown in Figure 3.4.2. The separation of the central part from the ligands is justified by the different and well-separated vibrational energies belonging to these groups, as observed in the comparison of Alq_3 with the hydroxyquinoline parent of the ligands in Figure 3.4.2. Particular focus is on the stretching vibrations of this central part. For $\alpha\text{-Alq}_3$, which consists of the meridional isomer (C_{2v}), six stretching vibrations are expected, three involving Al-N and three involving Al-O modes (see Figure 3.4.2). As they are all dipole-allowed, they are observable by IR-spectroscopy. According to Kushto et al. the following assignments for $\alpha\text{-Alq}_3$ are made: Al-N stretching: 396 cm^{-1} , 405 cm^{-1} , 418 cm^{-1} , Al-O stretching: 522 cm^{-1} , 542 cm^{-1} , 549 cm^{-1} . By contrast $\delta\text{-Alq}_3$ shows a total of only four bands in this region (397 cm^{-1} , 423 cm^{-1} , 531 cm^{-1} , 548 cm^{-1}). As the AlO_3N_3 fragment of the facial isomer belongs to symmetry C_{3v} , six stretching vibrations are expected here too, but four of them belong to two degenerate vibrational states and therefore only four bands should be observed in IR-spectroscopy, as is the case for $\delta\text{-Alq}_3$. The Al-N stretching is found at 397 cm^{-1} and 423 cm^{-1} , the Al-O stretching at 531 cm^{-1} and 548 cm^{-1} . The degeneracy of the first and last band is not present in the a-phase of Alq_3 (see Figure 3.4.2 and Figure 3.4.2), which consists of the meridional isomer. Two lines are observed at 400 cm^{-1} and at 550 cm^{-1} in $\alpha\text{-Alq}_3$, in agreement with theoretical calculations of Kushto et al. [45]. From this and the discussion in Ref. [54] it can be seen, that the analysis of the IR-spectra for the region above as well as below 600 cm^{-1} confirms the presence of the meridional and facial isomer in $\alpha\text{-Alq}_3$ and $\delta\text{-Alq}_3$, respectively. Furthermore, the specific fingerprints of the two isomers obtained by IR-spectroscopy may help to identify the isomers in other Alq_3 -samples [54].

3.5 Population and properties of the electronic excited triplet state

3.5.1 Population of the triplet states

In the previous part of this review structural investigations and properties of the molecule in the electronic ground state were discussed, giving evidence for the existence of the two different geometric isomers. However, not only the electronic ground state should be different for the two isomers, but also the excited states are expected to have different properties due to the different geometry of the molecule. Two types of photo-excited states are

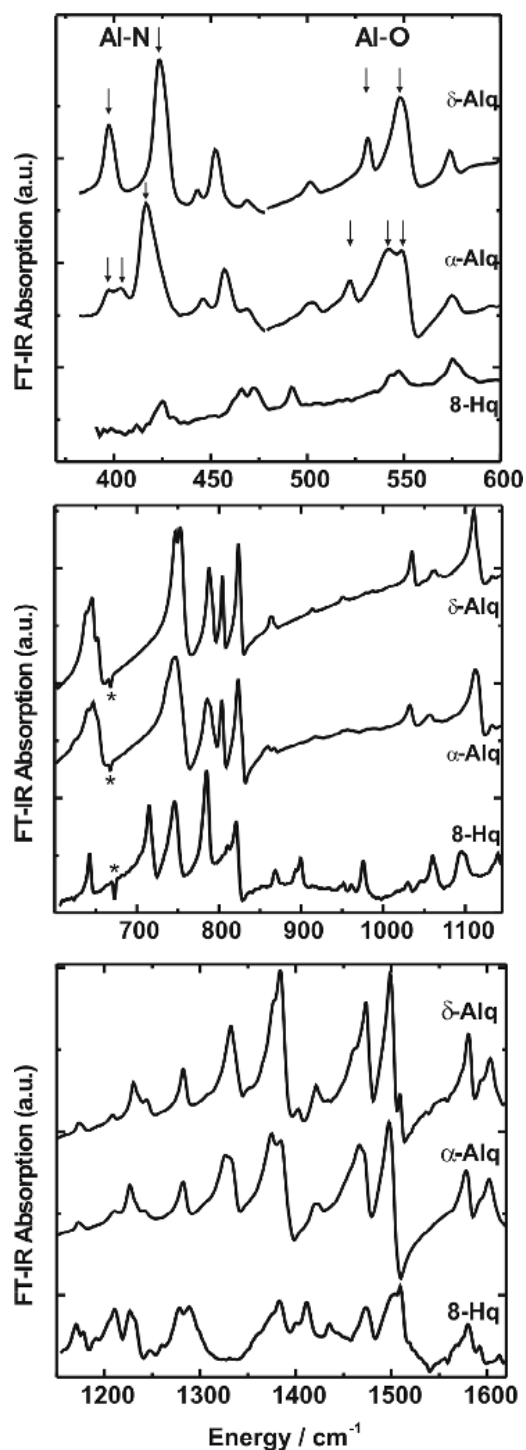


Figure 3.18: Comparison of the FTIR-spectra of δ (upper trace), α -Alq₃ (middle trace) and hydroxyquinoline (8-Hq, lower trace) in the range from 350 cm⁻¹ to 1650 cm⁻¹.

distinguished: the singlet state and the triplet state. In the singlet state the total spin quantum number of the unpaired electrons $S=0$, whereas in

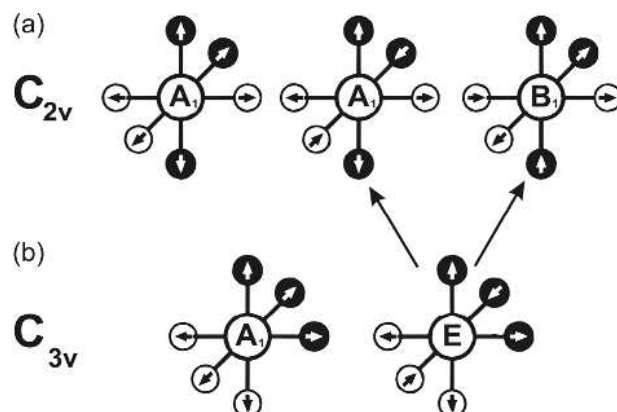


Figure 3.19: Schematic picture of the central part of the meridional (a) and the facial (b) isomer of Alq₃. Hollow and filled circles around the central Al-atom represent oxygen and nitrogen atoms, respectively. The three stretching modes of the meridional molecule (C_{2v}-symmetry) and the two for the facial molecule (C_{3v}-symmetry, one is degenerated) are marked by arrows in the O and N atoms.

the triplet state the total spin quantum number is $S=1$.

As in most cases the S_0 - S_1 transition is an allowed transition, the lifetime of the S_1 -state is very short. For Alq₃ it was measured to be about 12ns. On the other hand, the S_0 - T_1 transition is a so-called forbidden transition and thus the lifetime of the T_1 state is expected to be several orders of magnitude larger. However, so far very few experimental data on the triplet state of Alq₃ have been available, and thus this section includes the first direct measurements of the triplet state. First, a method to investigate the population of the triplet states due to intersystem crossing (ISC) is introduced and applied to discuss the properties of the different phases. Then we briefly discuss very recent results related to the characterization of the electronic excited triplet state in Alq₃.

The triplet state T_1 is populated due to inter-system crossing, as schematically shown in Figure 18. In reality the triplet state splits into three levels $|x\rangle$, $|y\rangle$ and $|z\rangle$. Their energetic distance is characterized by the zero field splitting parameters E and D . To simplify the following discussion this splitting of the triplet state is neglected and only T_1 is given in the schematic Figure 3.5.1. Due to photo-excitation by the absorption of incident laser light, mainly the singlet states S_n are excited ($S_0 \rightarrow S_n$) and relax to the lowest excited singlet state S_1 (process a). The excited singlet state S_1 can relax to the ground state ($S_1 \rightarrow S_0$) by emission of a photon (process b) or simply relax thermally (process c). The triplet state is populated by intersystem crossing with the rate constant d and f is the rate constant for the $T_1 \rightarrow S_0$ transition. In the literature f is often denoted as k_T .

Under constant photo-excitation and for long periods of time ($t \rightarrow \infty$)

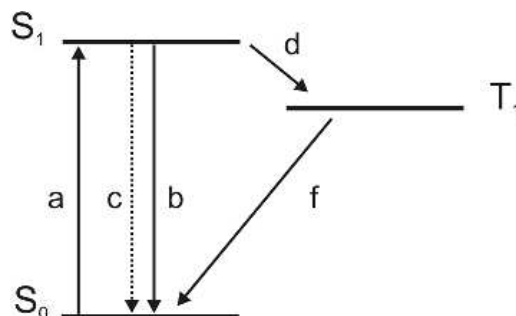


Figura 3.20: Schematic diagram of the electron levels and the transitions between the levels in an organic molecule. S_0 , and S_1 are the non excited ground state and the first excited singlet level; T_1 is the lowest triplet level. The coefficient a is proportional to the intensity of the exciting light and the probability of excitation of the molecule. b , c , d and f are the corresponding rate constants. The transition d is the population of the triplet state due to intersystem crossing.

there is a dynamic equilibrium of the $S_1 \rightarrow T_1$ and $T_1 \rightarrow S_0$ transitions, resulting in a constant concentration of the triplet states $[T_1]^\infty$. The molecules which are in the long-lived triplet state are not able to emit fluorescent light and, at high excitation density, this leads to a decrease in fluorescence intensity. Therefore the process of inter-system crossing can be investigated by transient PL measurements and as a result the ratio of molecules in the triplet state can be estimated. The time dependence of the population process and the concentration of the triplet states $[T_1]^\infty$ is obtained from the rate equations (see Figure 3.5.1):

$$\frac{d[S_0]}{dt} = -a[S_0] + b[S_1] + c[S_1] + f[T_1] \quad (3.1)$$

$$\frac{d[S_1]}{dt} = a[S_0] - b[S_1] - c[S_1] + d[S_1] \quad (3.2)$$

$$\frac{d[T_1]}{dt} = d[S_1] - f[T_1] \quad (3.3)$$

These equations were solved by Sveshnikov, and Smirnov et al. As the rate constants b and c cannot be distinguished experimentally here, they can be replaced by $b' = b + c$. Further, if we bear in mind both that the lifetime of the triplet state is much longer than the lifetime of the singlet state and that the rate of intersystem crossing is much higher than the rate of triplet decay ($b \gg f, d \gg f$), the solutions are

$$[S_1] = \frac{af[S_0]^0}{(b' + d)f + da} + \frac{Aa^2[S_0]^0}{(b' + d)f + da} e^{-\frac{1}{\tau_1}t} - \frac{a[S_0]^0}{b' + d + Ba} e^{-\frac{1}{\tau_2}t} \quad (3.4)$$

$$[T_1] = \frac{ad[S_0]^0}{(b' + d)f + da} \left(1 - e^{-\frac{1}{\tau_1}t}\right) \quad (3.5)$$

con

$$f + \frac{d}{b' + d}a = f + Aa = \frac{1}{\tau_1} \quad (3.6)$$

e

$$b' + d + \frac{b'}{b' + d}a = b' + d + Ba = \frac{1}{\tau_2} \quad (3.7)$$

From these equations it is evident that τ_1 is the characteristic time for the accumulation of molecules in the triplet state. For $t \rightarrow \infty$ (stationary regime) the concentration of molecules in the triplet state is given by

$$[T_1]^\infty = \frac{ad[S_0]^0}{(b' + d)f + da} = Aa[S_0]^0\tau_1 \quad (3.8)$$

and finally with equation (6) one can express $[T_1]^\infty$ by the characteristic accumulation time s_1 and the lifetime of the molecules in the triplet state $\tau_0 = 1/f$.

$$[T_1]^\infty = [S_0]^0 \left(1 - \frac{\tau_1}{\tau_0}\right) \quad (3.9)$$

As a result it is possible to estimate the ratio of the molecules excited in the triplet state $[T_1]^\infty$ from the lifetime τ_0 , determined from delayed fluorescence measurements that will be discussed below, and the characteristic accumulation time τ_1 , which can be measured using transient PL studies.

These measurements for the Alq₃ phases as well as for an evaporated amorphous film are shown in Figure 3.5.1. Instantaneously with the turning-on of the excitation light the fluorescence is observed, which subsequently decreases with a decay time τ_1 to an equilibrium value. α -Alq₃, yellowish-green Alq₃ and the evaporated amorphous film behave in a similar fashion. Their decay time s_1 is 11ms, 11ms, and 7 ms, and the triplet lifetime τ_0 at that temperature (1.3K) was measured as 15 ms, 14 ms, and 9ms respectively. Therefore in these samples about 20% to 30% of the molecules are in the triplet state. This similarity between these samples of Alq₃ containing the meridional isomer is remarkable, because it clearly demonstrates that the morphology and thus intermolecular interactions seem to have no significant influence on the intersystem crossing process in Alq₃. However, for δ -Alq₃ there is only a very small decrease in the PL intensity and the equilibrium value remains at 98%. Due to the small decay and the noise of the measurement, the error for determination of τ_1 is too large, but from the decrease in intensity one may roughly estimate that only about 2% of the molecules in δ -Alq₃ are in the triplet state. From the independence of the morphology of the samples it can be concluded that the low population of the triplet state due to strongly reduced intersystem crossing is a molecular property of the facial isomer in δ -Alq₃. This has also been confirmed recently by Amati et al. using quantum chemical calculations [62].

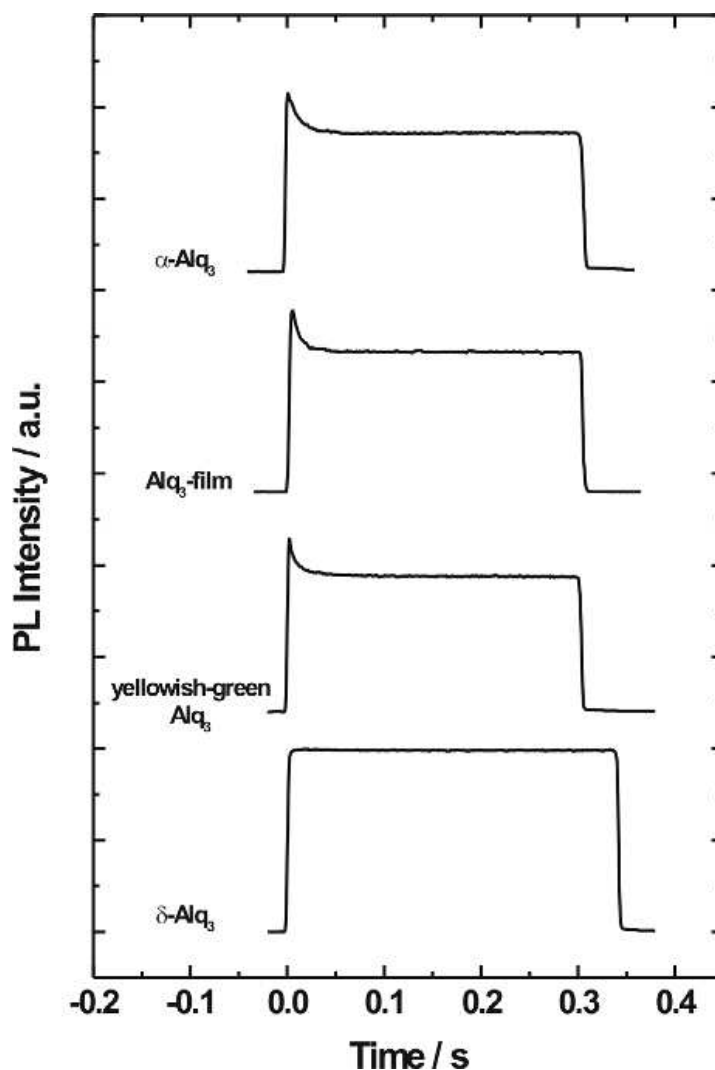


Figure 3.21: Time dependence of the PL-intensity during an optical excitation pulse for polycrystalline Alq₃ phases and an evaporated film. The measurements were performed at 1.3K by using excitation at 363.8nm. The signal was detected at 2.64eV (470nm) for δ -Alq₃ and at 2.48eV (500nm) for all other samples.

3.5.2 Phosphorescence of Alq₃

The measurement of the transient PL discussed above gives information about intersystem crossing to the triplet state but not about its energetic position and lifetime. Until recently, the determination of the triplet properties has been based on theoretical calculations [51] and only very few experimental data were available so far: for example, the lifetime of the triplet state was derived from measurements of the diffusion length at room temperature using a phosphorescent sensing layer on the assumption of non dispersive transport, and the triplet energy was inferred from other

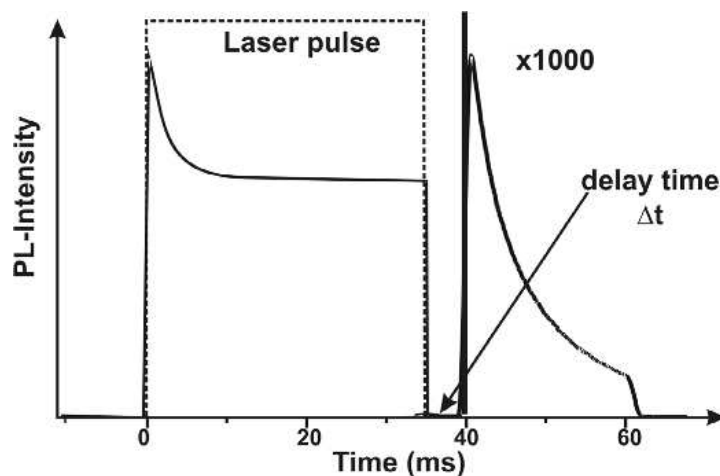


Figure 3.22: Principle of the transient PL measurements shown for α -Alq₃ measured at 20 K. By applying an intense rectangular laser pulse, PL from the sample is observed instantaneously. During the first 10-15 ms the PL-signal decreases due to intersystem crossing to a constant equilibrium value. After the laser is turned off, the spontaneous PL decreases within less than 1 μ s. The fluorescence observed after the laser has been turned off is called delayed fluorescence, with an intensity of about three orders of magnitude less than the spontaneous PL. In our experiments this delayed fluorescence was measured after a delay time Δt of several milliseconds. The cutoff of the delayed fluorescence, here at about 60 ms, is due to the chopper system of the setup.

metal-chelate complexes. These experimental methods were necessary because no radiative triplet emission of Alq₃ (no phosphorescence) has been found. Only very recently direct observations of the electronic excited triplets have been reported: H.D. Burrows et al. published a phosphorescence spectrum of Alq₃ in an ethyl iodide glass matrix. It is measured the electrophosphorescence of Alq₃- based OLEDs by using delayed electroluminescence, further, phosphorescence was also shown for all crystalline phases and for the evaporated amorphous film. Here we summarize the results that were mainly obtained by delayed fluorescence as well as by phosphorescence of Alq₃.

The zero-field splitting parameters E and D are characteristic values for the triplet state. They were determined by ODMR measurements at zero field [63]. The measured values of the zero-field splitting parameters of $|E|=0.0114 \text{ cm}^{-1}$ and $|D|=0.0630 \text{ cm}^{-1}$ are in the same range for the crystalline phases (α - and yellowishgreen Alq₃) and for evaporated amorphous films, indicating a weak influence of the morphology. Calculations of the zero-field splitting parameters of the meridional Alq₃ molecule, starting from the D and E values of the isolated ligands, seem to support a mini-exciton-like behavior of the triplet state on the three ligands of the Alq₃

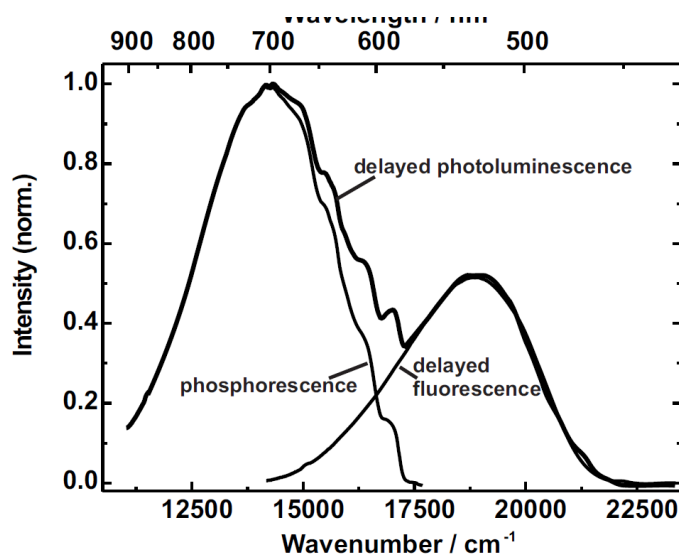


Figure 3.23: Delayed PL spectrum of α -Alq₃ at 10 K measured with a delay time Δt of 4 ms. Excitation wavelength was 442 nm. The spectrum shows two distinct bands: the typical PL spectrum and a new additional band at about 700 nm (1.77 eV). The band at about 525 nm is the delayed fluorescence (DF), the band at about 700 nm the phosphorescence of Alq₃.

molecule [63].

In order to learn more about the properties of the triplet state, measurements of the transient PL in the millisecond time range were taken. From these it is possible to obtain information about the lifetime and the population of the long-lived triplet state due to inter-system crossing. The principle of these measurements is shown in Figure 3.5.2. The sample is excited by a rectangular laser pulse (dotted line), and as soon as the excitation light is turned on the spontaneous Alq₃ fluorescence is observed, which subsequently decreases to an equilibrium value with a decay time of about 10 ms. This decay is related to the population of the triplet states by ISC as discussed in detail above.

After the laser is turned off, the intensity of spontaneous PL from the singlet states decreases very fast due to their short lifetime of about 10 ns and only the triplet state whose lifetime is often in the range of several milliseconds, is still populated; thus after just 1 μ s no spontaneous fluorescence is present any more. However, even after a delay time Δt of 4 ms, a weak PL is still observed. It is about three orders of magnitude less intense than the spontaneous PL and shows a slow decay rate. This process is known as delayed fluorescence (DF) in the literature. It occurs due to collision of two triplet excitations and is therefore a bimolecular process, which has a probability proportional to the square of the density of the triplet states $[T_1]$. The collision process is also often referred to as triplet exciton fusion or sometimes as T-T annihilation. If the energy of the lowest excited singlet

state is less than the sum of the energies of the colliding triplet excitons, the fusion reaction may yield triplet and singlet states. The generated singlet exciton S_1 then decays, as would be the case for a directly excited singlet exciton state. As the DF originates from the $S_1 \rightarrow S_0$ transition, its spectrum is the same as observed in usual PL measurements, only significantly less intense than the instantaneous PL spectrum (in our case the difference is about three orders of magnitude). The distinguishing feature of the fluorescence from the S_1 -state generated by the fusion process is that its apparent lifetime is determined by the triplet excitons and hence is much longer than the lifetime of the spontaneous fluorescence.

Figure 3.5.2 shows the delayed PL spectrum of α -Alq₃ at 10 K measured with a delay time Δt of 4 ms and the spectrum was integrated over about 20 ms. It shows two distinct bands, one at about 500 nm, similar to spontaneous PL, and an additional band at about 700 nm. For α -Alq₃, yellowish-green Alq₃ and the evaporated film the position of the bands is approximately the same, whereas for δ -Alq₃ the bands are slightly blue-shifted. The relative intensity of the two bands is different for the different phases and temperature-dependent. As the excitation wavelength of 442 nm is located below the absorption edge of δ -Alq₃, the obtained density of excited states is significantly lower for δ -Alq₃. Under these experimental conditions only a very weak band at 500 nm was observed for *delta*-Alq₃ due to the low density of triplet states, but the band at 700 nm was still clearly resolved [63].

The vibronic progressions on the high energy side of the band at 700 nm are clearly resolved. By subtraction of the usual PL spectrum from the delayed PL spectrum bands at 700 nm with vibronic progressions are obtained as shown for α -Alq₃ in Figure 3.5.2. These are at approximately the same positions for α -Alq₃ and yellowish-green Alq₃. The vibronic progressions for α -Alq₃ and yellowish-green Alq₃ are located at about 586 nm, 606 nm, 627 nm, 645 nm and 668 nm (17065 cm⁻¹, 16502 cm⁻¹, 15950 cm⁻¹, 15504 cm⁻¹ and 14970 cm⁻¹), and for *delta*-Alq₃ at about 574 nm, 594 nm, 613 nm and 635 nm (17422 cm⁻¹, 16835 cm⁻¹, 16313 cm⁻¹ and 15748 cm⁻¹), and thus have an average distance of about 550 cm⁻¹, similar to the vibronic progression observed for the PL [15]. For the amorphous film the distance between the vibrational modes are similar but their position seems to be slightly red-shifted as reported in Refs [59,63]. The vibrational modes of the new band at about 700 nm are due to the vibrational modes of the Alq₃ molecule in its electronic ground state.

Later on it is shown, that the new band at about 700 nm is the $T_1 \rightarrow S_0$ transition. As this phosphorescence spectrum shows well-resolved vibronic progressions, one can directly determine the triplet energy by assignment of the lowest resolved vibronic band to the 0-0 transition. Hence the triplet energy for the meridional isomer (in α -Alq₃) can be determined as 2.11 ± 0.1 eV and for the facial isomer (in δ -Alq₃) as 2.16 ± 0.1 eV. For the evaporated

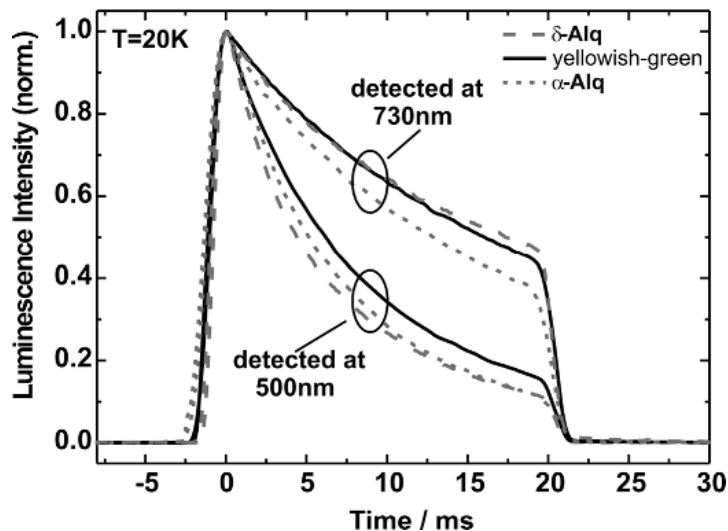


Figure 3.24: Transient intensity of the delayed luminescence shown in Figure 5 detected at 500 nm and at 730 nm, respectively. The delay time Δt was 4 ms in all cases. The steep edge at 20 ms is due to the experimental setup. The temperature was 20 K

film the lowest resolved vibronic progression seems to be slightly red-shifted [63]. These experimental values are similar to the values roughly estimated by Baldo et al. (2 eV) [64], are very close to the theoretical value calculated by Martin et al. for an isolated molecule (2.13 eV) [51] and also close to the triplet energy of 2.17 ± 0.1 eV that has been estimated from the phosphorescence spectrum of Alq₃ in an ethyl iodine glass matrix.

The transient PL intensity of both bands was also investigated. By measuring the decay of the intensity of the DF (I_{DF}), the lifetime of the triplet states can be determined [61], [63]. For this one has to distinguish between two regimes, namely high and low triplet concentration. At very

	τ_{DF}	$\tau_0 (=2\tau_{DF})$	τ_{700}	τ_{700}/τ_{DF}
α -Alq ₃	6.6 ± 0.5	13.2 ± 1	13.6 ± 0.5	2.05
Yellowish-green	7.8 ± 0.5	15.6 ± 1	16.2 ± 0.5	2.08
δ -Alq ₃	6.2 ± 0.5	12.4 ± 1	13.2 ± 0.5	2.13
Film	4.33 ± 0.5	8.66 ± 1	9.3 ± 0.5	2.15

Figure 3.25: Lifetimes obtained from the transient measurements of I_{DF} of the different polycrystalline Alq₃ phases and amorphous films at a temperature of about 20 K. τ_{DF} is the time constant for the exponential decay of I_{DF} and from this the triplet lifetime τ_0 was obtained. τ_{700} is the time constant of the exponential decay of the luminescence intensity measured at 730 nm.

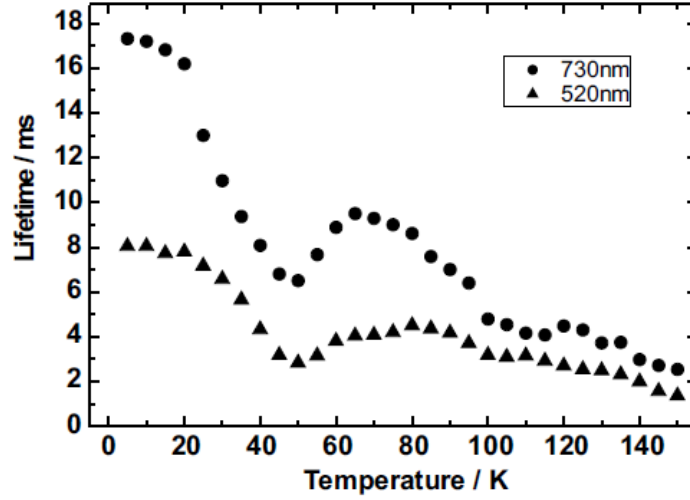


Figure 3.26: Lifetimes of both bands of the delayed PL of yellowish-green Alq_3 -powder shown in Figure 2 in a temperature range between 6 K and 150 K. The lifetimes of both bands increase with decreasing temperature but show a local minimum at about 50K that is assigned to a phase transition [63].

high triplet densities the T-T-annihilation directly influences the lifetime of the triplets in the sample and therefore the regime of low concentration has to be chosen to measure the correct triplet lifetime s_0 . This is equivalent to $(k_T[T_1] \gg \gamma_{tot}[T_1]^2)$, where k_T is correlated with the triplet lifetime τ_0 by $(\tau_0 = 1/k_T)$ and γ_{tot} is the total bimolecular annihilation (fusion) rate constant. In this case IDF decays according to a monoexponential law $I_{DF}(t) \sim e^{-2k_T t}$. The decay time of I_{DF} is half of the correlated triplet lifetime s_1 , and thus it is possible to determine the lifetime of the triplet state by transient measurements of I_{DF} . By choosing the delay time Δt to be at least 4 ms we obtained very good monoexponential decays of the DF detected at 500 nm, confirming that the measurements were in the correct regime.

Figure 3.5.2 shows the intensity decay of the delayed luminescence of polycrystalline samples detected at 500 nm and of the additional band detected at 730 nm and measured at a temperature of 20 K. The measured apparent lifetimes of the delayed fluorescence detected at 500 nm are 6.6 ± 0.5 ms, 7.8 ± 0.5 ms and 6.2 ± 0.5 ms, resulting in triplet lifetimes of 13.2 ± 1 ms, 15.6 ± 1 ms and 12.4 ± 1 ms for α - Alq_3 , yellowishgreen Alq_3 and δ - Alq_3 , respectively. The values are summarized in Table 3.5.2. Although in the film the triplet lifetime is about 60% - 70% of that in the polycrystalline samples, all values are in the same range and thus the morphology of the samples seems to have only little influence on the lifetime of the triplet states.

The decay of the band at about 700 nm is also shown in Figure 3.5.2. All polycrystalline phases show a similar monoexponential decay, which is

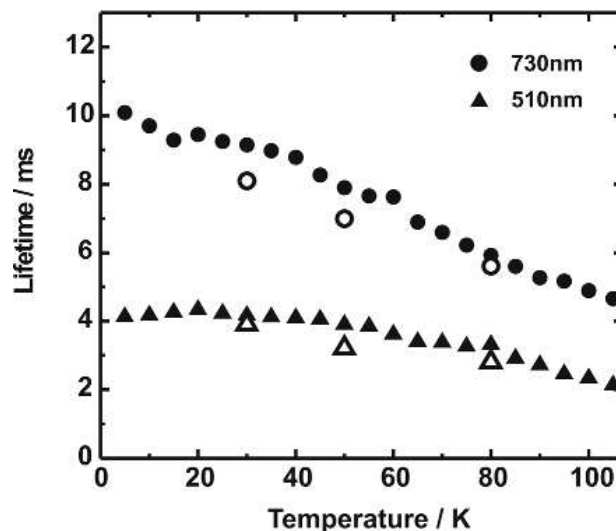


Figure 3.27: Lifetimes of both bands of the delayed PL of an evaporated amorphous film (thickness $5 \mu\text{m}$) over a temperature range of 100 K. Delay time Δt was 4 ms, the detection wavelengths were 510 nm and 730 nm, respectively. Hollow symbols indicate values measured by delayed electroluminescence of an Alq₃-LED which lead approximately to the same results as measurements using photo-excitation.

significantly slower than that detected at 500 nm. Measured monoexponential decay times are also given in Table 3.5.2. Within the accuracy of the measurement these values are about a factor of 2 higher than the values for the band at 500 nm and thus almost identical to the triplet lifetimes obtained.

The temperature dependence of the decay of both bands was investigated for all phases of Alq₃ including amorphous thin films, and as a result it became clear that both bands are directly correlated [61], [63]. In principle the lifetime of the delayed fluorescence and the band at 700 nm increases with decreasing temperature, as shown in Figure 3.5.2 for yellowish-green Alq₃ powder. A local minimum is observed at about 50 K. This is due to a reversible phase transition that we also observed in temperature-dependent PL quantum efficiency measurements and ESR measurements [66]. Similar behavior was observed for δ -Alq₃ and amorphous films. For the evaporated amorphous film the local minimum is located at about 100 K (Figure 3.5.2). Measurements of the delayed fluorescence and phosphorescence of Alq₃-based OLEDs gave similar values and are also included for comparison. As shown in Figure 3.5.2 for yellowish-green Alq₃-powder and in Figure 3.5.2 for the evaporated film, the lifetime of the band located at about 700 nm and the apparent lifetime of the delayed fluorescence always differ by a factor of 2 within the accuracy of the measurements, and thus the lifetime of this band is identified to be the lifetime of the triplet state. Therefore it

is obvious that the band at 700 nm is directly linked with the triplet state of Alq_3 . This justifies the assignment of this band to the $T_1 \rightarrow S_0$ transition and thus this spectrum is the phosphorescence spectrum of Alq_3 .

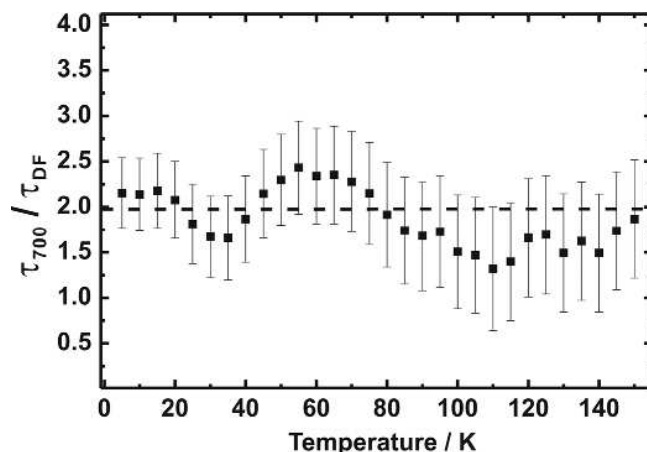


Figure 3.28: Temperature dependence of the factor (τ_{700}/τ_{DF}) between the decay times measured for the DF at 500 nm (τ_{DF}) and for the band at 700 nm (τ_{700}) of yellowish-green Alq_3 -powder.

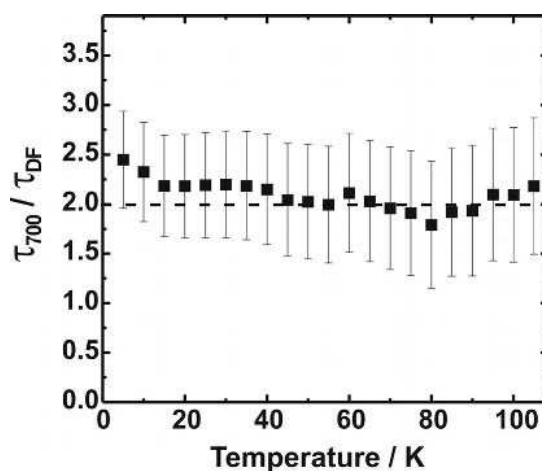


Figure 3.29: Factor (τ_{700}/τ_{DF}) between the decay times measured for the delayed fluorescence at 500 nm (τ_{DF}) and for the band at 700 nm (τ_{700}) of the Alq_3 film. The dashed line at the factor (τ_{700}/τ_{DF})=2 serves as a guide to the eye. The lifetimes of both bands are correlated by a factor of 2. The dashed line at the factor (τ_{700}/τ_{DF})=2 serves as a guide to the eye. From theory the lifetime of the DF should be half of the lifetime of the phosphorescence. Within the accuracy of the measurement τ_{700} and τ_{DF} are very well correlated by a factor of 2 over a wide range of temperatures, which confirms the assignment of the band at 700 nm to the phosphorescence of Alq_3 .

Capitolo 4

Devices

4.1 Devices description

In this work, we tested OLEDs with N,N'-Di-[(1-naphthyl)-N,N'-diphenyl]-1,1'-biphenyl-4,4'-diamine (NPD) as HTL and tris(8-hydroxyquinolato) aluminum (Alq₃) as ETL and as emitting layer. The device structure is shown in Figure 4.2. The analysis was performed on devices with and without "hole injection layer" (HIL) (as summarized in Table I), in order to understand whether the presence of a HIL layer could influence the OLED reliability.

Samples were prepared on commercial glass/ITO substrates, which consisted of a 20-nm SiO₂ barrier layer between the soda lime glass and 120-nm-thick ITO. All organic layers were deposited under high-vacuum conditions (1×10^{-7} torr), and the devices were transferred directly from vacuum into an inert environment glove box, where they were encapsulated using a UV-curable epoxy and a glass lid with a moisture getter. A 10-nm-thick HIL is deposited between the HTL and the ITO, in order to improve the hole injection rate from the anode during the forward bias condition. The cathode consisted of aluminum (Al) deposited on lithium fluoride (LiF), and the active areas were defined by an insulating grid. SEM and AFM analyses on ITO substrate have been performed in order to check the uniformity of the transparent conductive oxide. The samples thus built, have an active area of 2 mm².

Figure 4.1 shows the OLEDs schematic structure. The stripes marked as anodes and cathode are an extension of the real anodes and cathode located in the multilayer structure inside the package. Every anode stripe is connected to a different active area, in order to choose which one will be stressed. The entire structure is realized using glass. Figure 4.3 shows one of the samples used.

As mentioned earlier, we have studied two kind of OLED structures: both are built using as hole transport layer (HTL) an NPD layer, and as electron transport layer (ETL) an Alq₃ layer. The only difference is the

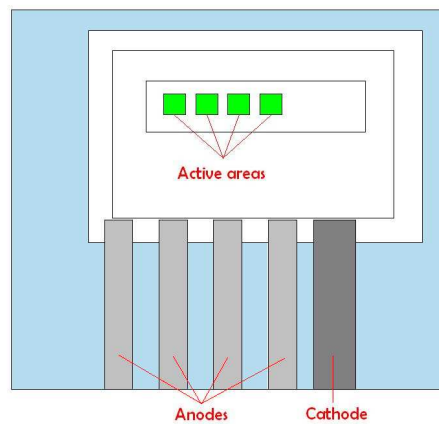


Figura 4.1: Schematic OLED structure.

presence of a hole injection layer (HIL) in 1 of the 2 sets (Figure 4.2). Its function, as the name suggests, is to facilitate the hole injection from ITO anode through the NPD improving the recombination of the carriers that takes place in the interface between the NPD and Alq_3 layers. Cathode is made by LiF/Al .

4.1.1 With HIL

Typically, the hole injection layer (HIL) can reduce the operating voltage and increase the device lifetime either by lowering energy barrier for hole injection from the anode such as an indium–tin oxide (ITO) to the hole transport layer (HTL) and by providing more favorable work function compared with ITO [9–12]. Therefore, it improves the hole-injection at the anode/HIL interface, and consequently increases the light output and efficiency of the OLED.

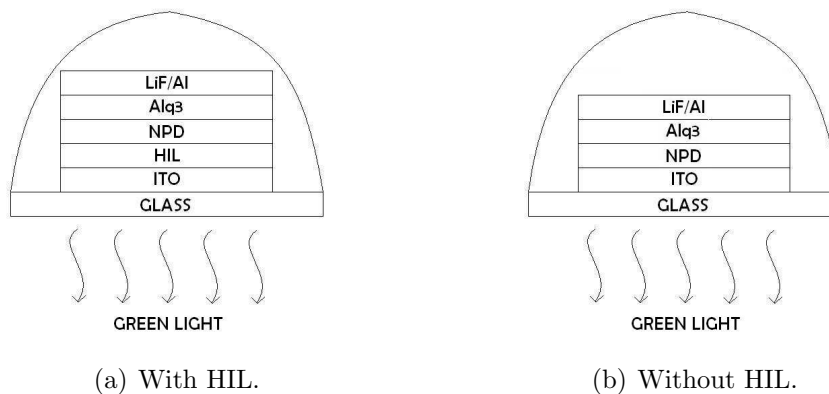


Figura 4.2: OLED structure.

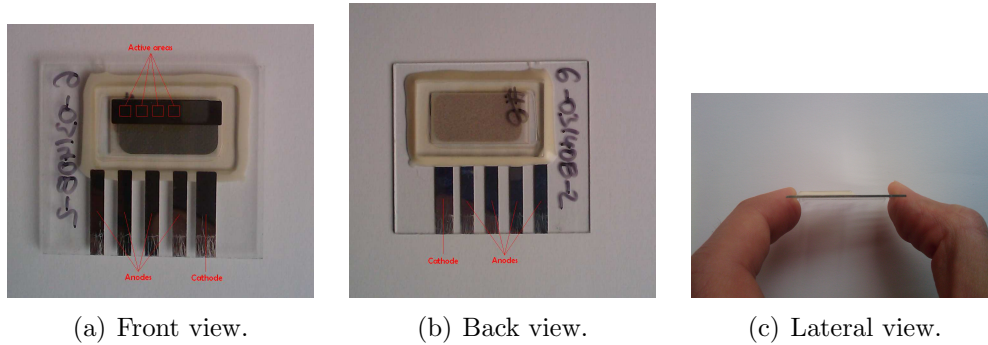


Figura 4.3: OLED device.

Tabella 4.1: Samples.

Device #	ITO	HIL	HTL (NPD)	HIL (Alq ₃)	Cathode (LiF/Al)
6-031408-2-4	120nm 15 ohm/sq.	LG101 [10nm]	60nm	60nm	1nm/100nm
6-031408-2-5	120nm 15 ohm/sq.	LG101 [10nm]	60nm	60nm	1nm/100nm
6-031408-2-6	120nm 15 ohm/sq.	LG101 [10nm]	60nm	60nm	1nm/100nm
6-031408-1-4	120nm 15 ohm/sq.	No	60nm	60nm	1nm/100nm
6-031408-1-5	120nm 15 ohm/sq.	No	60nm	60nm	1nm/100nm
6-031408-1-6	120nm 15 ohm/sq.	No	60nm	60nm	1nm/100nm
6-031408-1-7	120nm 15 ohm/sq.	No	40nm	60nm	1nm/100nm
6-031308-7-3	120nm 15 ohm/sq.	No	60nm	100nm	1nm/100nm
6-031308-1-2	120nm 15 ohm/sq.	No	100nm	60nm	1nm/100nm

A multilayer OLEDs structure that includes is shown in Figure 4.2a. Hereafter with-HIL devices will be called “wHIL” OLEDs.

4.1.2 Without HIL

On the other hand, devices which don't used the hole injection layer are submitted to a higher operating voltage due to the higher energy barrier from the anode to the hole transport layer. This can lead to an accelerate degradation, a decrease in their lifetime and thus a lower efficiency.

Multilayer without-HIL OLED structure is shown in Figure 4.2a. Hereafter without-HIL devices will be called “woHIL” OLEDs.

4.1.3 Samples

Samples used in this work are shown in Table 4.1.

As mentioned earlier, for every conductive glass are present 4 active areas, and thus, 4 different OLEDs which could be stressed. For this reason, every device can be labeled as *6-031408-(type number)-(device number)d(OLED number 1-2-3-4)* depending on which OLED we are going to stress. For convenience, hereafter, we will call the used OLED using only (type number)-(device number)d(OLED number 1-2-3-4) i.e. 2-4d3.

4.2 Instruments

4.2.1 HP 4155 Semiconductor Parameter Analyzer



Figura 4.4: HP 4155 Semiconductor Parameter Analyzer.

For this kind of measurement a HP 4155 Semiconductor Parameter Analyzer was used (Figure 4.2.1). It has 4 SMU and can measure current within the 1 nA-100 mA range. This instrument has been used to measure the current flowing through the device in reverse and forward bias conditions. The high precision of HP 4155 allows to analyze some characteristics of the devices visible only at very low current levels, such as the parasitic shunt resistance and the increase in the reverse current during the degradation of the device. At these low current levels the noise generated by a high power SMU prevent us to get reliable measurements and the effects of self heating and cables resistance for low bias current are negligible.

4.2.2 HP 4284A Precision LCR Meter



(a)



(b)

Figura 4.5: HP 4284A Precision LCR Meter (a) and LCR fixture (b).

The 4284A Precision LCR Meter can be used to improve component quality by providing an accurate, high-throughput test solution. The wide 20Hz to 1MHz test frequency range and superior test signal performance

allow the 4284A to test components to the most commonly used test standards, such as IEC/MIL standards, and under conditions that simulate the intended application.

In this work LCR meter is used to get the capacity at different frequencies and voltages. For this purpose was used a fixture device support.

LCR Fixture

Figure 4.5b shows the LCR fixture. It is connected to the LCR meter through 2 couple cable sets whose impedance is eliminated by a specific calibration in order detect only the OLED impedance (capacity).

4.2.3 Newport 818-UV

The detector used with this instrumentation is a Newport 818-UV, which has a spectral range that covers the spectral region within 200 nm and 1100 nm. This range is more than enough to cover the emission spectrum of green OLEDs used. In Figure 4.6a it is possible to see the spectral responsivity and linearity of the detector used.

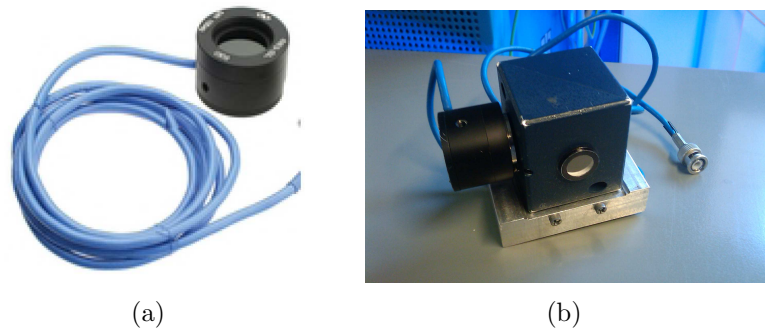


Figura 4.6: Newport 818-UV detector (a) and integrating sphere with its support for luminance measurements(b).

In Figure 4.7 it is possible to see the spectral responsivity and linearity of the detector used.

Integrating sphere

In order to amplify the OLED emission, light emitted from the device is collected by an integrating sphere. Exposure of the detector at direct illumination is avoided using a simple coverage, to mitigate the noise effect that could result from it. Integration sphere used with the detector is shown in Figure 4.6b.

Sphere support

Figure 4.6b also shows that the integration sphere has a metallic support which is used to fix the setup during measurements using the appropriate anchors. Hereafter, the configuration shown in Figure 4.6b consisting in Newport 818-UV, integrating sphere and sphere support connected together will be called “photo-diode”.

4.2.4 Hamamatsu Phemos-200

Phemos-200 (shown in Figure 4.2.4) is an emission microscope which has a narrower scope of basic measurement performance. It comes equipped with a 1024×1024 pixel high-resolution cooled CCD camera as a detector and it is designed for analyzing relatively small elements. It can cope with a specific range of applications, including localizing ESD damage from static electricity during mounting or incorrect usage. As an optional feature, it can also analyze backside emission on IC chips. Optional CAD navigation and LSI tester connection are also possible.

4.2.5 Ocean Optics USB-4000

The USB4000 is a compact fiber optic spectrometer (Figure 4.9a), it has a 3648-element detector with shutter and high-speed electronics and is responsive from 200 nm to 1100 nm but the specific range and resolution depends on grating and entrance slit used.

These are the main components of the USB 4000 (see Figure 4.9b):

- collimating mirror (4): light enters the spectrometer, passes through the SMA connector(1), slit(2), and filter(3), and then reflects of the collimating mirror onto the grating(5),

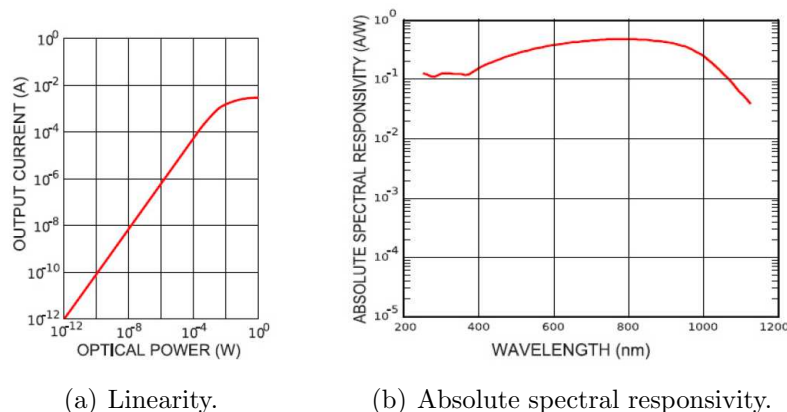


Figure 4.7: Detector features.



Figura 4.8: Hamamatsu Phemos-200.

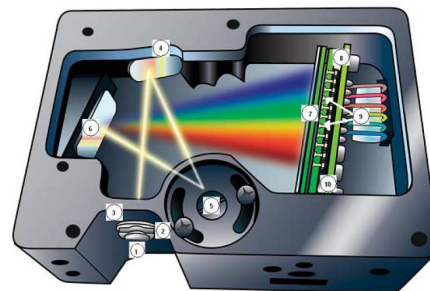
- grating (5): diffracts light from the collimating mirror and directs the diffracted light onto the focusing mirror(6),
- focusing mirror (6): receives light reflected from the grating and focuses first-order spectra onto the detector plane,
- detector (8): collects the light received from the focusing mirror and converts the optical signal to a digital signal; each pixel on the detector responds to the wavelength of light that strikes it, creating a digital response.

Integrating sphere

Similarly to photo diode integrating sphere, in order to amplify the OLED emission, light emitted from the device is collected by another integrating sphere. Again, exposure of the detector at direct illumination is avoided using a simple coverage, to mitigate the noise effect that could result from it. Integration sphere used with the detector is shown in Figure 4.2.5.



(a) External view.

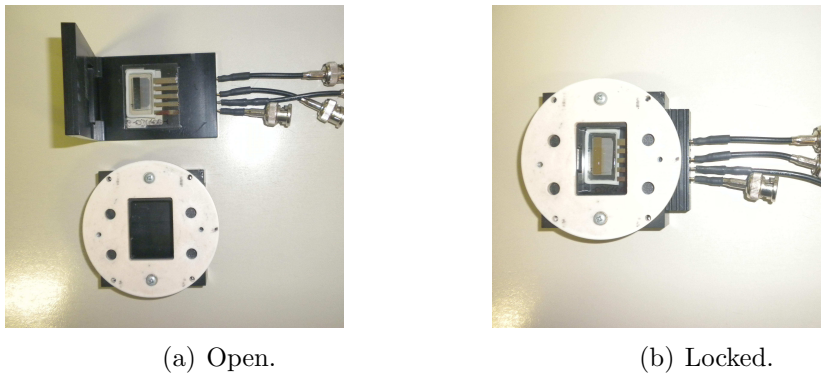


(b) Internal section.

Figura 4.9: Ocean Optics Spectrometer USB-4000



Figura 4.10: Integrating sphere for spectrum measurements.



(a) Open.

(b) Locked.

Figura 4.11: OLED fixture.

4.2.6 OLED fixture

For all measures whose instruments do not provide a suitable fixture for the OLED connection, a new one was created (Figura 4.11).

Each anode and cathode, go to lean on a special sheath which, once closed the fixture, allows the polarization of the device connecting the BNC-connectors to an external voltage-current generator. Thus, the OLED is placed into the OLED fixture which is then closed and locked by a special support. Holes on support surface allow to fit the fixture with subsequent measurement setup. Hereafter the configuration shown in Figure 4.11b will be called “OLED locked configuration (OL configuration)”.

Capitolo 5

Measurement setup and characterization techniques

In this work the reliability of two types of fluorescent undoped green organic light emitting diode is studied through thermal and electrical ageing. In order to have a full overview of the kinetics degradation, we carried out several optical and electrical measurement that now we are going to show. Each measurement was carried out under controlled conditions (in air at a room temperature of $\sim 24-25^{\circ}\text{C}$) and using always the same measurement setup. These working methods will be presented shortly too in the following pages.

5.1 Electrical measurement

In order to have a complete reliability study, we carried out a complete set of electrical measurements:

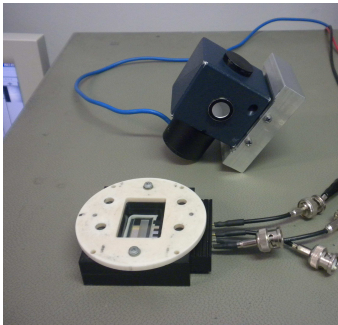
- Current-Voltage measurements (I-V),
- Capacity-Frequency measurements (C-F),
- Capacity-Voltage measurements (C-V).

The former was performed for fresh devices and after every degradation step, whereas, the latter two were performed for fresh devices and solely when and optical power degradation (see Section 5.2.1) higher than 5% was detected. Every measurements were carried out in dark condition to prevent direct light exposure, which could lead to an unwanted carrier photo-generation resulting in a measurement error.

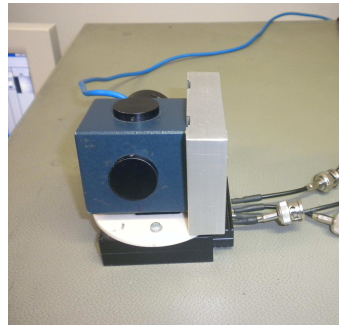
5.1.1 Current-Voltage measurement (I-V)

I-V characteristic shows the voltage trend as function of the applied current. It has been carried out by using the 4155 parameter analyzer. This

setup is shown in Figure 5.1.1 (even though the photo-diode appears in the figure, it was not used in this measurement). First of all, OLED is setted in OL configuration. Then, OLED fixture is connected to the 4155 using 2 crocodile cables (red color to connect the anode and black color to connect the cathode) through the BNC fixture supports. Finally, OLED fixture is covered with a box to reach dark condition. Figure 5.2 shows a typical I-V OLED characteristic for fresh wHIL (a) and fresh woHIL OLEDs (b).



(a) First step.

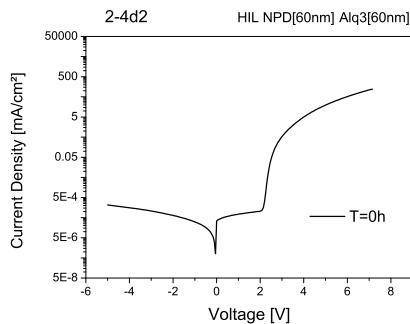


(b) Second step.

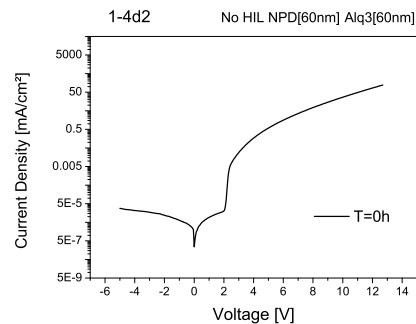
Figure 5.1: I-V and L-I measurement setup.

Data Processing

With a simple data processing we have obtained the voltage-time characteristic in which is shows the voltage trend increasing the ageing hours. For this aim, we chose 4 different current density value respectively of 4-40-80-120 mA/cm^2 , at which the voltage-time trend was assessed. Figure 5.3 shows a typical voltage-time characteristic example for stressed wHIL (a) and fresh woHIL OLEDs (b) at different current values.



(a) With hole injection layer.



(b) Without hole injection layer.

Figure 5.2: I-V characteristics.

5.1.2 Capacity-Frequency measurement (C-F)

C-F characteristic shows the capacity trend as function of the work frequency. It has been carried out by using the LCR as shown in Figure 5.1.2. The OLED is connected to the LCR fixture using 2 special cocodriles and LCR fixture is connected to the LCR meter through 2 cable pairs. Finally, LCR fixture is closed to reach dark conditions. Figure 5.5 shows a typical C-F OLED characteristic for fresh wHIL (a) and fresh woHIL OLEDs (b).

5.1.3 Capacity-Voltage measurement (C-V)

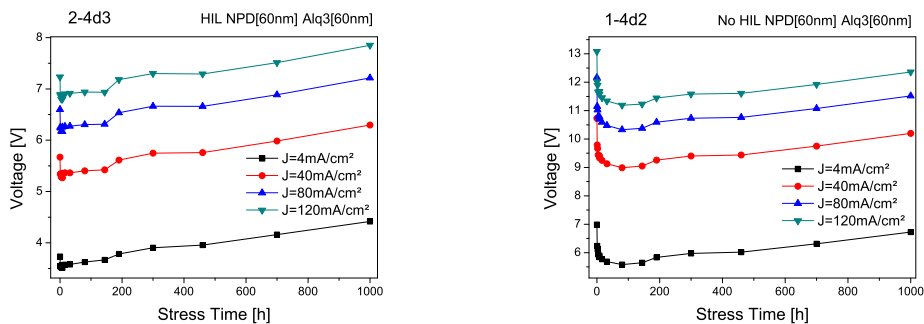
C-F characterization shows the capacity trend as function of the work voltage at 4 fixed frequency respectively of 300-1000-10000-100000 Hz. The measurement setup is the same used for C-F measurement in the previous section. Figure 5.5 shows a typical C-F OLED characteristic for fresh wHIL (a-c-e-g) and fresh woHIL OLEDs (b-d-f-h).

5.2 Optical measurement

In order to complete the degradation profile, we have also carried out a complete set of optical measurements:

- Optical power measurements (L-I),
- Emission microscope measurements,
- Spectrum measurements.

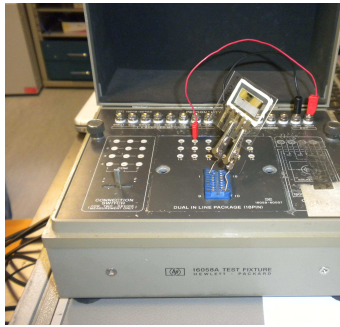
The former was performed for fresh devices and after every degradation step, whereas, the latter two was performed for fresh devices and only when and optical power degradation upper to 5% was detected. Every measurement was carried out in dark condition to prevent direct light exposure



(a) With hole injection layer.

(b) Without hole injection layer.

Figure 5.3: C-F characteristics.



(a) With hole injection layer.



(b) Without hole injection layer.

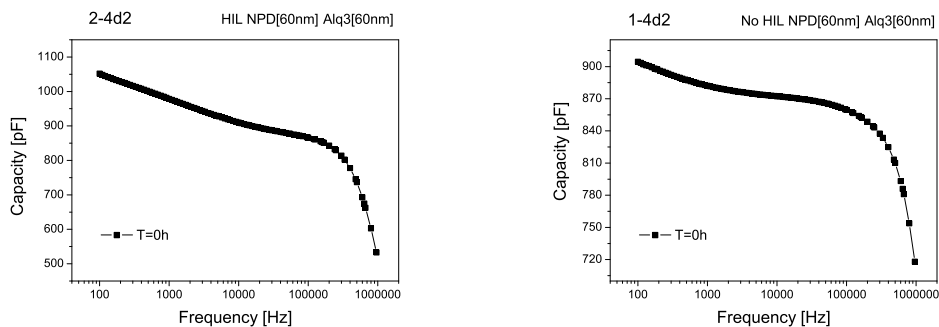
Figura 5.4: C-F and C-V measurement setup.

which could lead to an unwanted carrier photo-generation resulting either in a different optical power.

5.2.1 Optical power measurements (L-I)

L-I characteristic shows the optical power trend as function of the applied current, an increase of the current lead to a linear increase of the optical power. Similarly for I-V measurement, it was performed combining the 4155 with the OLED fixture in the same setup outlined above (see Section 5.1.1). Furthermore, in addition it is used the photo-diode (see Section 4.2.3) also connected to the 4155. The screws, located under the sphere support, allow a perfect joint with the support holes in the OL configuration. Figure 5.1.1 shows this measurement setup. Finally, OLED fixture is covered with a box to reach dark condition.

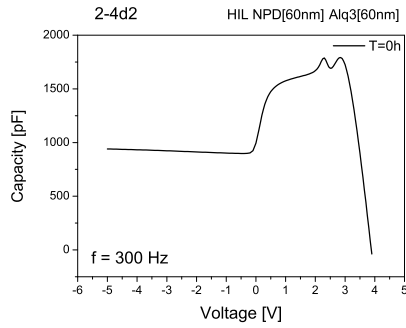
Measurements was carried out sweeping the current value from 0 to 120 mA/cm² recording the optical power. In order to reduce the measurement error related to the instruments sensitivity and the setup, the measurement was repeated 3 times every time disassembling and reassembling the setup as



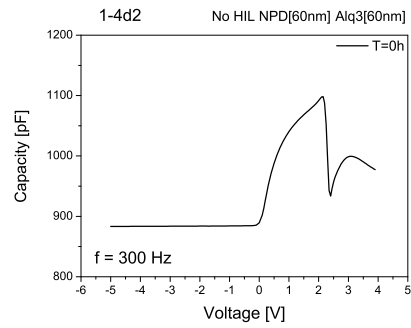
(a) First step.

(b) Second step.

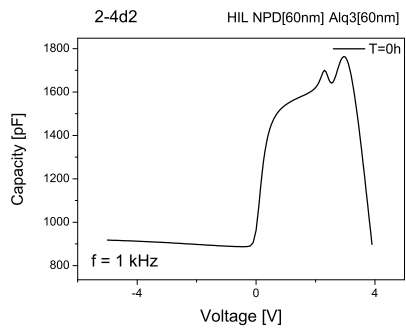
Figura 5.5: C-F characteristics.



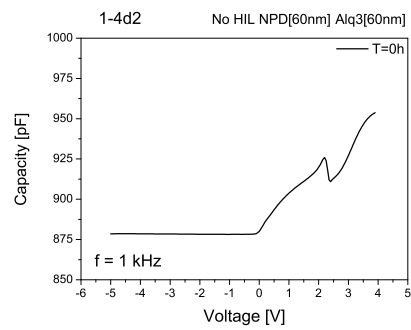
(a) With hole injection layer.



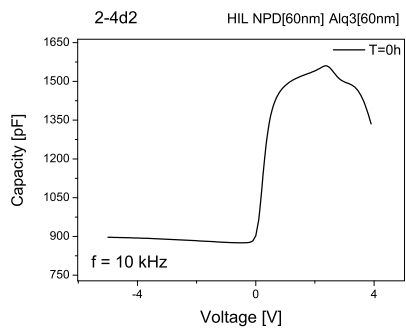
(b) Without hole injection layer.



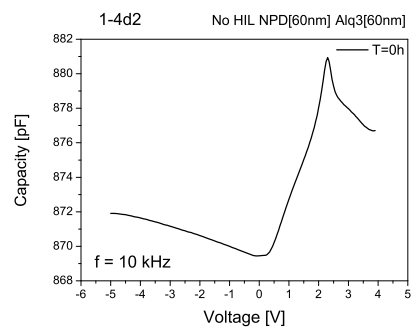
(c) Without hole injection layer.



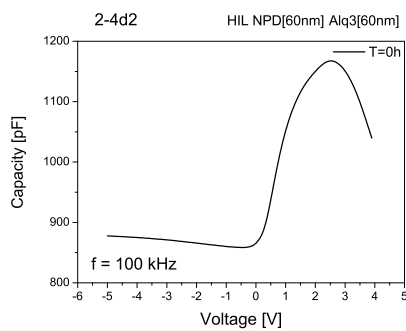
(d) Without hole injection layer.



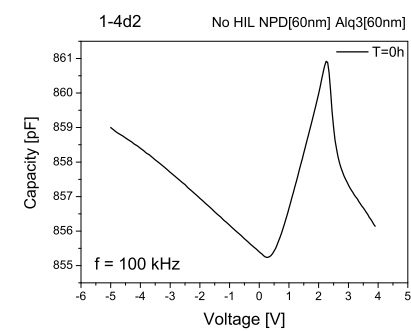
(e) Without hole injection layer.



(f) Without hole injection layer.



(g) Without hole injection layer.



(h) Without hole injection layer.

Figura 5.6: C-V characteristics.

just described above. Then it was made the average of the 3 measurements taking this optical power value for further processing from which, however, has not yet been removed from the dark condition. Figure 5.7 shows a typical L-I OLED characteristic for fresh wHIL (a) and fresh woHIL OLEDs (b).

Data Processing

From the L-I characterization data we can also obtain some interesting data and graphs by a simply data processing.

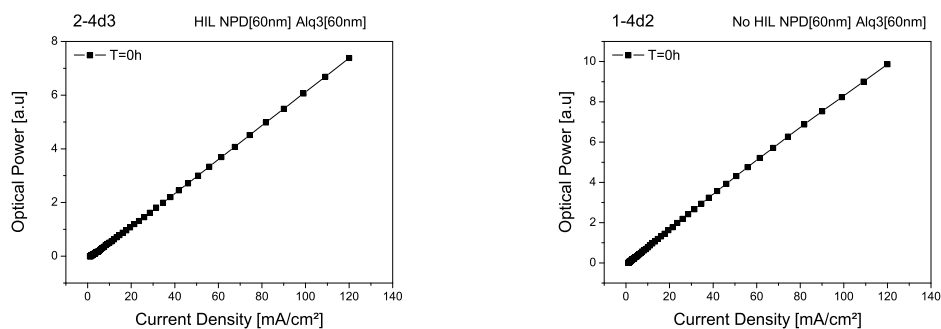
Normalized Optical Power represents the optical power normalized to its initial value. Figures 5.8a-b show the normalized optical power for fresh wHIL (a) and fresh woHIL OLEDs (b).

Optical Power Degradation Rate represents the normalized optical power when the stress current is reached (120 mA/cm^2) and gives the optical power degradation trend during the device ageing. Figures 5.8c-d show a degradation kinetic example applying this definition for stressed wHIL (c) and woHIL (d) OLEDs.

Efficiency represents how efficiently the injected carriers recombine leading to light emission and it is obtained by dividing the optical power for the current. Figures 5.8e-f show the efficiency for fresh wHIL (a-c-e) and fresh woHIL OLEDs (b-d-f).

5.2.2 Emission microscope measurements

Emission microscope measurements show the OLED surface emission, highlighting in which points the emission is higher or the presence of any anomalies. Measurements was performed using Hamamatsu Phemos-200 and 4155 which was used simply as current generator, connected to the



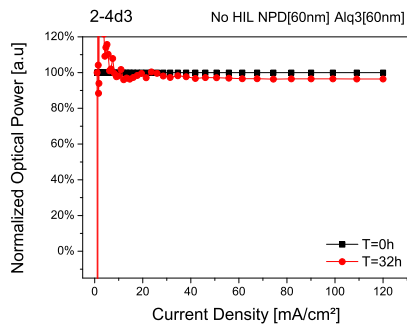
(a) With hole injection layer.

(b) Without hole injection layer.

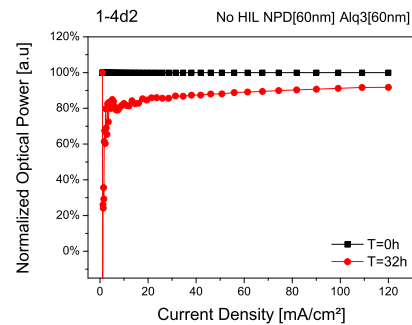
Figure 5.7: C-F characteristics.

BNC OLED fixture through external and internal cables. Using the joystick console, an appropriate microscope lens was positioned on the device under test, focalizing it in order to have its best active area view. Finally, the phemos door was close to guarantee dark conditions. Figure 5.2.2 shows as just described.

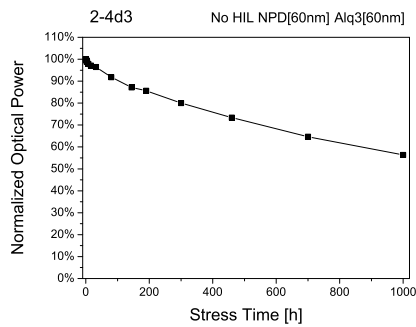
Measurements was carried out polarizing the device with two different reference currents (1 and 30 mA/cm²) to assess the emission profile changing at low and higher current values. Figure 5.10 shows a typical emission measurements for fresh wHIL (a-c) and fresh woHIL OLEDs (b-d).



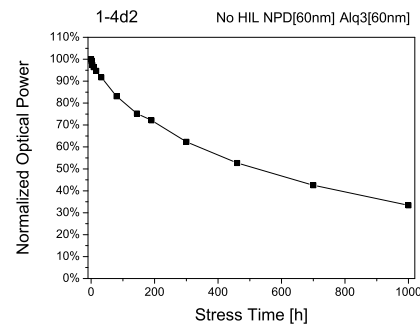
(a) With hole injection layer.



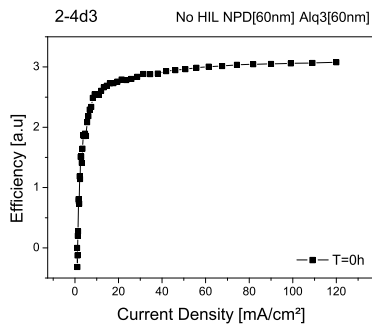
(b) With hole injection layer.



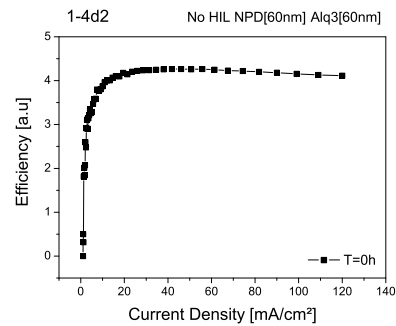
(c) With hole injection layer.



(d) With hole injection layer.



(e) With hole injection layer.



(f) Without hole injection layer.

Figure 5.8: Emission profile.

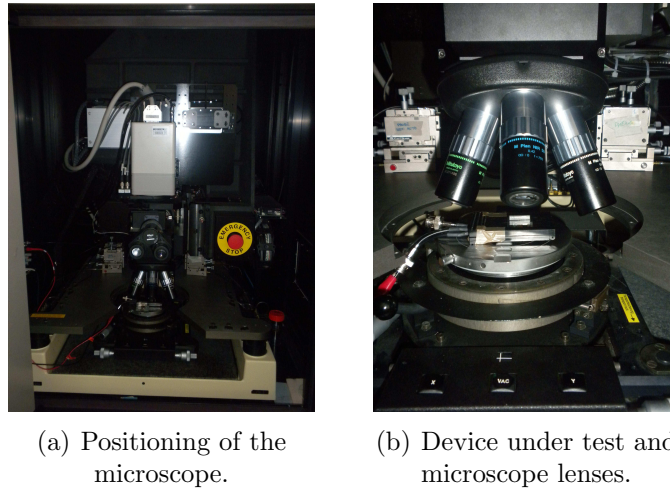


Figure 5.9: Phemos measurement setup.

5.2.3 Spectrum measurements

Spectrum measurements reveal the OLED spectrum during its emission, highlighting in which wavelength there is the higher OLED emission. In our case, since green fluorescent OLED are used, the emission will be concen-

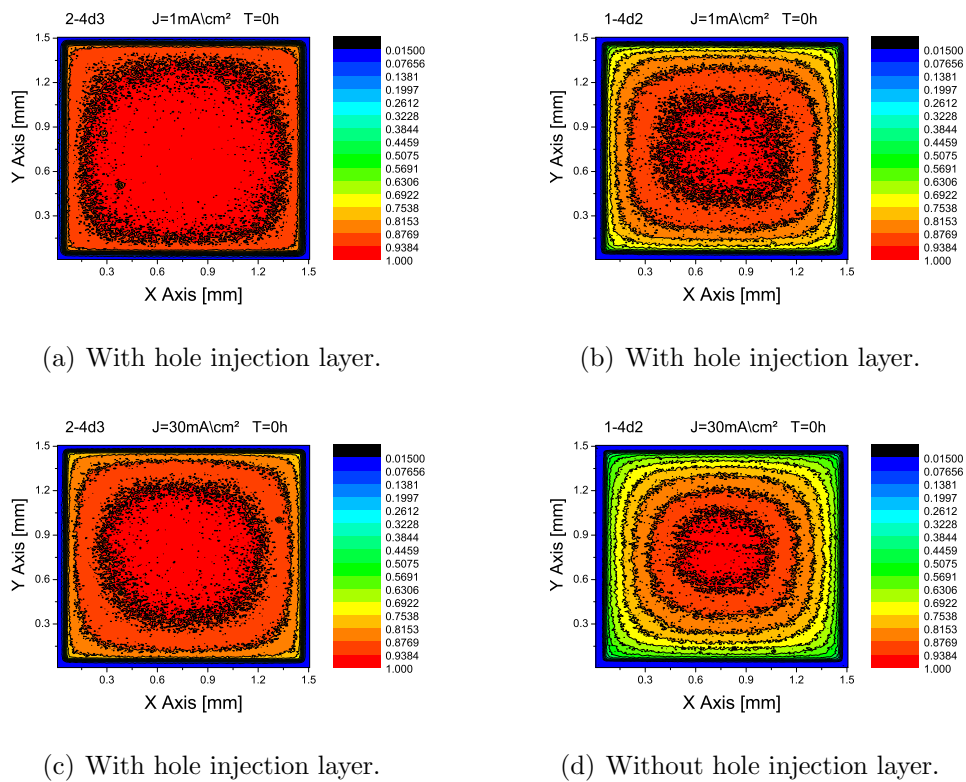
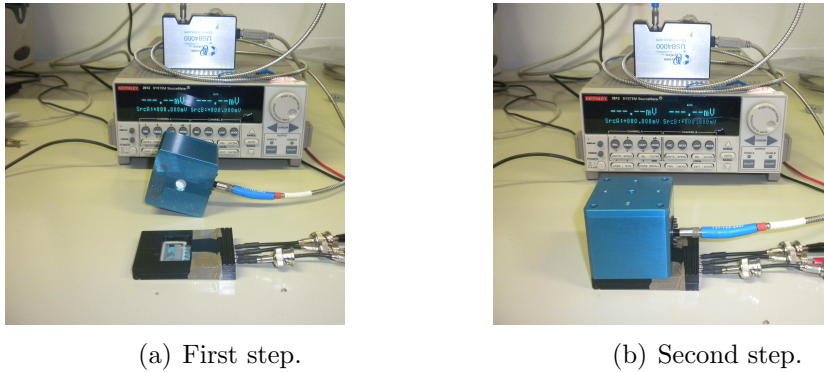


Figure 5.10: Emission profile.

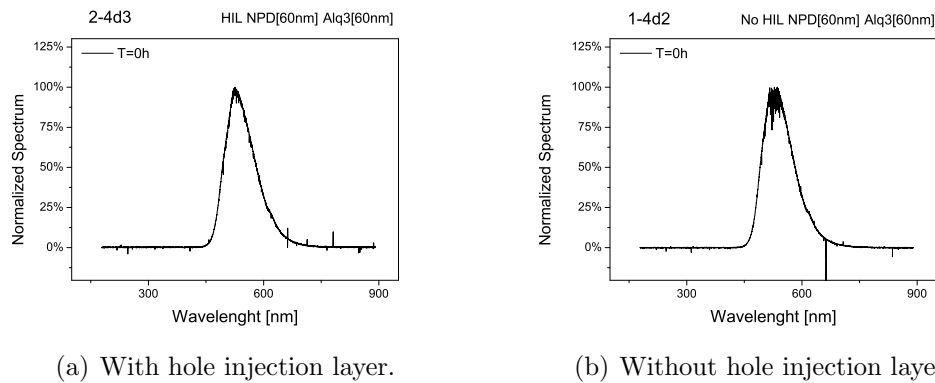


(a) First step.

(b) Second step.

Figure 5.11: Spectrum measurement setup.

trated around 530 nm. Measurements was performed using Ocean Optics USB-4000 with its integrating sphere and polarizing the device through a current generator. Ocean Optics was connected to the integrating sphere using a special optical fiber cable. After which, integrating sphere was placed above the OLED fixture, putting attention in trying to obtain a position as repeatable as possible. Then, the OLED was polarized connecting its BCN to a current generator using two crocodile cables as just described previously. Figure 5.2.3 shows this measurement setup. Finally, OLED fixture is covered with a box to reach dark condition.



(a) With hole injection layer.

(b) Without hole injection layer.

Figure 5.12: Spectrum emission.

Measurements was carried out polarizing the device at a reference current of 2 mA for an integrating time of 15 s for 3 times and then mediating them together. This long integrating time is due to the low OLED power emissions compared to devices for which this setup was created, thus use a lower integrating time would be result in a noisy and low emission spectrum. Furthermore, that used is not a really suitable measurement setup. Indeed from it, we can only have the spectrum shape and thus we can only check that it does not undergoes changes during the ageing. On the other hand, a more realistic degradation kinetic is already shown by optical po-

wer measurements. For obtain the spectrum shape, each spectrum was in turn normalized to its maximum peak. Figure 5.12 shows a typical emission spectrum for fresh wHIL (a-c) and fresh woHIL OLEDs (b-d).

Capitolo 6

Results and discussions

6.1 Thermal/Electrical stress for OLED with HIL

In order to assess the role of temperature on OLED degradation, we performed constant current stress (CCS) on OLED kept at a constant temperature $T = 20^{\circ}\text{C}$, 40°C , and 60°C . All the devices were stressed at a constant current density of $120 \text{ mA}/\text{cm}_2$, i.e., three times larger than the nominal current density of $40 \text{ mA}/\text{cm}_2$ (we will arbitrarily refer to V_{ON} as the anode voltage needed to achieve such current density level). We chose such a current in order to achieve a reasonable acceleration of the life tests, avoiding the formation of parasitic leakage paths across the organic films and the consequent device breakdown.

For comparison, we also carried out thermal stress (without current injection) at the same temperature values (20°C , 40°C , and 60°C).

6.1.1 Degradation of the electrical parameters

Figure 6.2 (a-c-e) shows the I-V typical characteristics taken on wHIL devices submitted to CCS at different temperatures, plotted in semilogarithmic scale. We can arbitrarily distinguish four regions on the basis of current dependence on applied voltage (V^*):

1. the reverse bias region $V^* < 0 \text{ V}$;
2. the low-forward bias regions $V^* > 0 \text{ V}$ and $V < 2 \text{ V}$;
3. the exponential forward region (namely, $2 < V^* < 5 \text{ V}$), where the current exponentially increases with voltage;
4. the linear forward region (namely, $V^* > 5 \text{ V}$), where the current linearly increases with the anode voltage.

In the reverse-bias region (Region 1), we did not observe appreciable variations of the leakage current. Down to -5 V there is an almost linear dependence between current and voltage, suggesting that this current is due to different contributions, such as the drift of the intrinsic carriers, the surface conduction at device borders and the parasitic current contribution of our equipment.

Instead, the leakage current increases during stress if a weak forward bias is applied (Region 2), however, this behavior seems to be independent from the temperature stress values applied. Generally, in this region, applying a positive voltage, we observe that the rapid increase in the current starts at a voltage of about 2 V, which corresponds to the estimated work function difference between the ITO and the Al-LiF. This value is in agreement with those reported in literature [47].

We observe that, in Region 3, the slope of the semilogarithmic I-V decreases, indicating a slower turn-on as the time stress increases. This drop clearly increases with increasing temperature where the right-shift of the curve is increasingly evident, this translates into increased power consumption. This change suggests the buildup of a negative trapped charge at the interface, which, on the one hand, tends to reduce the electric field across the ETL and, on the other hand, tends to increase the electric field across the HTL. In order to explain the I-V slope decrease during stress, we must assume that the quantity of negative charge rises as the gate voltage increases. This occurs if defects are pushed below the quasi-Fermi level, capturing one electron, as the anode voltage is increased. Remains to be said however, that for the first hours stress, I-V characteristic show an initial left-shift, denoting an improvement in power consumption. This behavior is found in all electronic organic devices.

On the other hand, stress induced a significant rigid right-shift of the linear I-V curves toward higher voltage levels (Region 4), corresponding to an increase in the operating voltage (V_{ON}) of the devices. In the linear forward region, the behavior of the OLED is mainly influenced by the series resistance of the device, resulting in a linear relation between voltage and current for high bias conditions. Interestingly, the slope of the I-V characteristics in this region does not strongly change during stress, suggesting that the series resistances of the ETL and HTL remain nearly constant during the aging. This result supports the idea that the degradation of the electrical characteristics is dominated by an intrinsic degradation at the interface between NPD and Alq₃. The interfacial degradation mechanism is also supported by the fact that different thicknesses of NPD and Alq₃ do not affect the OLED lifetime [1]. Obviously, as discussed a few lines above, also in this case there is an initial left-shift of the I-V curve.

Figure 6.2 (b-d-f) shows the voltage-time characteristic at different current values (4-40-80-120 mA/cm²). The voltage trend as function of the time confirms what said earlier, showing the increase in OLED operating volta-

ge V_{ON} . Increasing temperature stress value results in a higher operating voltage at the same reference time.

Figure 6.11 (a-c-e) shows the I-V characteristic for wHIL devices where CCS is not applied. In this case, for every temperature values, curves at different stress time appear to be perfectly overlapped, denoting that an appreciable degradation is not occurred. This is confirmed by voltage-time characteristic at different current reference values, where CCS is not applied too. Indeed, as shown Figure 6.11 (b-d-f), the voltage trend as function of the time at different temperatures, result to be perfectly horizontal for each current reference value, denoting no variations of the OLED operating voltage V_{ON} and thus that electrical degradation is not occurred.

In order to achieve a more comprehensive picture of the degradation process, during stress, we have carried out C-V measurements at four different frequencies, namely, 300-1000-10000-100000 Hz. The evolution of the C-V curves during stress taken at these different frequencies for devices submitted to CCS at different temperature values are shown in Figure 6.44. Remarkably, during the electrical stress, the C-V curves shift rightward, and the transition region of the C-V curves is progressively more stretched as the stress time increases. This phenomena become more evident driving the devices through higher temperature values. Quantifying the shift of the C-V measuring the position of the inflex point as conventionally done in literature [27], [30] a linear relation between the C-V shift and the stress time is highlighted. We believe that most of the charge trapping derives from irreversible phenomena.

Comparing these C-V characteristics with devices thermally stressed (unbiased) ones (Figure 6.18), no degradation is observed and the curves are mostly quite overlapped.

Hence, comparing the OLEDs submitted to CCS or not at different ambient temperature, we just can observe a general trend:

- Temperature enhances the degradation rate. This enhancement is moderately small from 20°C to 40°C, and much stronger, if the temperature is increased up to 60°C.
- Thermal stress alone cannot produce appreciable degradation of the electrical characteristics.

6.1.2 Degradation of the optical parameters

The behavior above described is substantially confirmed also by optical measurement. In Figure 6.3 (a-c-e), L-I curves at different temperature values are plotted. A good linear relation exists between the luminance and the current density both before and after stress, but the slope monotonically decreases as the stress time increases, indicating a reduction of the OLED

efficiency. This slope decrease, undergoes to and higher drop when the devices is submitted to CCS at greater temperature values.

A quantitative description of the reduction in device efficiency is shown in Figure 6.3 (b-d-f), where the optical power degradation at the current stress density (120 mA/cm^2) as a function of the stress time at different temperature values is plotted. As we expect, the curve slop increase as the temperature increase, resulting in a higher degradation. However, for both the temperatures, the degradation have a strong reduction approaching the 1000 h stress.

It is worth noticing that the percentage of optical power degradation is independent of the measuring current level as is shown in Figure 6.38 (a-c-e). This behavior can also be seen considering the efficiency trend as function of the current density in Figure 6.38 (b-d-f). From both we observe a constant degradation during the stress time.

After 1000-h stress, the luminance of the devices reduce down to different values depending on the temperature. Table 6.1 summarized it.

As already described for the I-V and voltage-time characteristics, also for these optical parameters, no degradation at different temperatures is observed if CCS is not applied. Indeed, Figures 6.12 (a-c-e)-6.13 show how the curves at different stress time are perfectly overlapped, whereas optical degradation curve in Figure 6.12 (b-d-f) has approximately an horizontal trend denoting that degradation is not occurred.

The optical degradation of all the devices was characterized also by monitoring the light emission profile (LEP) using a light emission microscope (LEM) over the device active area. Figures 6.39-6.40-6.41 represent the LEPs through false-color maps at different current density values, respectively of 1 and 30 mA/cm^2 . The emission scale has been normalized to the maximum detected on the scanned area. Before stress, the emission intensity is slightly concentrated at the center of the device area. In fact, the edges have a 10% lower luminance compared with the center of the active area. This result suggests that the devices show some current and emission crowding that should be correlated with a stronger self-heating near the center of the emitting area. Figures 6.39-6.40-6.41 show how the spatial distribution of the emitted light is modified after the accelerated electrical and thermal stress of the device, providing a direct indication of the intensity decrease at each point on device area. The emission decrease along the entire active area is in agreement with the luminance decrease shown in Figure 6.3 (a-c-e) and reported in Table 6.1 for each temperature value.

In order to achieve more quantitative information on the degradation

Tabella 6.1: Optical power reduction after 1000-h stress for wHIL OLEDs.

T=20°C	T=40°C	T=60°C
56.37 %	41.10 %	26.60 %

of the emission profiles, we have analyzed the intensity profiles on the median lines of the devices (linear intensity profiles). Figures 6.42 show the variation of the longitudinal LEP at 1 and 30 mA/cm². At 30 mA/cm² the emission is more uniform on the active area, whereas, at 1 mA/cm² it is more pronounced in the center area with respect to the border region. However, in both cases, during stress time, the emission intensity becomes lower, but more uniformly distributed on device active area. Noticeably, the intensity decrease is more pronounced in the center of the OLED area, with respect to the border region. This idea is consistent with the fact that the current density is higher at the center of the devices and therefore can explain the stronger degradation.

Again, as expected, no degradation on the profile is observed at different temperature values if CCS is not applied. Indeed, Figures 6.14-6.15 show that the emission intensity did not change during the stress time (initial false-color map of every devices is almost the same also after the ageing) and the longitudinal light emission profile curves are perfectly overlapped (Figure 6.16), denoting that no degradation is occurred.

Concluding, we believe that this behavior may be mostly ascribed to an inhomogeneous temperature increase, which is larger in the center of the device rather than in the corner or border regions. This temperature increase play an important role in the degradation kinetics by two ways:

1. The increase of temperature in the center allow a larger degradation kinetics, as confirmed by the results previously discussed (see Figures 6.2a-c-e-6.3a-c-e and 6.11a-c-e-6.12a-c-e).
2. The increase of temperature may produce, in turn, a small increase of the carrier mobility and then, a local increase of the OLED current (which is more pronounced in the center). This fact may further enhance the OLED degradation rate in the central region.

Finally, we verified that, even though the light emission profile changes, the normalized optical power spectral distribution is unchanged regardless the thermal and electrical stress conditions (see Figures 6.43 (a-c-e) and 6.17 (a-c-e)).

6.1.3 Positive charge and defect generation

The electrical aging of OLEDs generates defects near the HTL/ETL interface, which are likely responsible for the luminance decrease during electrical stress. In order to ascertain the nature of the NPD/Alq₃ interface defects, we performed and analyzed the evolution of the C-V curves during the accelerated thermal and electrical stress. At this purpose, we have adopted the model described by Kondakov et al. [48]. First of all, we have to consider the band model of the OLED that is qualitatively shown in Figure 6.1.3a. The cathode work function (in our case, LiF-Al) is close to the

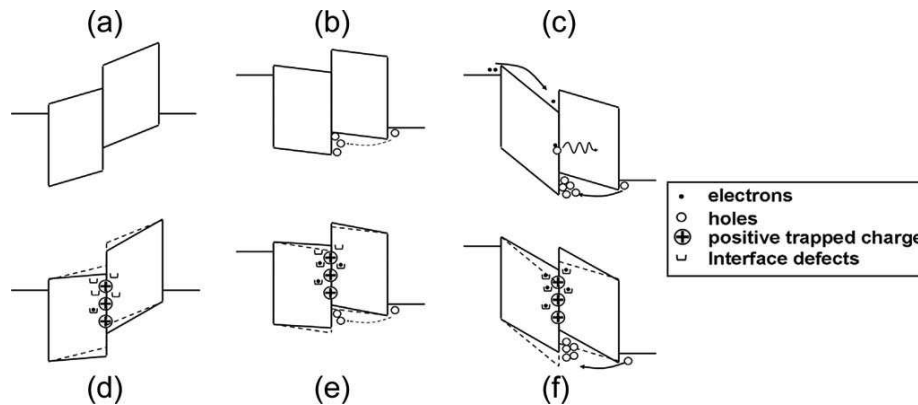


Figure 6.1: Qualitative and simplified band diagram model of the OLED structure considered in this paper (not to scale). Figs. (a), (b), and (c) refer to the qualitative band positions of a fresh OLED. For the sake of simplicity, we neglected any charge trapped in the fresh device before stress, and we omitted the HIL between ITO and NPD. Figures (d), (e), and (f) represent the modification of the band structure induced by the stress. The dashed lines represent the band structure before stress, and the solid line represents the band structure after stress. The position of the trapped charges and the neutral defects is only qualitative, and it must be concentrated very close to the organic film interfaces.

LUMO level of the Alq_3 , allowing for a good electron injection in the ETL. Still, the employment of a HIL grants a good hole injection in the HTL. In first approximation, ITO (Al) does not allow the injection of minority electrons (holes) during reverse bias. Kondakov's model also assumes that the interface between HTL and ETL blocks holes in the HTL and electrons in the ETL. In the reverse-voltage condition, there are no carriers inside the device, and two equal amounts of charges with opposite polarities are stored in the cathode and in the anode. The total capacitance measured in this region is given by the series of the three dielectrics (HIL, HTL, and ETL). If we move from 0 V to positively biased voltage values (Figure 6.1.3b and c), the capacitance increases due to the onset of the hole injection from the anode. Since the hole injection is more efficient than electron injection, a higher electric field is generated across the ETL than across the HTL. This difference in electric field is maintained by a net positive charge at the HTL/ETL interface. Under high hole injection conditions, the capacitance of the HIL and HTL is screened, and the resulting capacitance is equal to that of the Alq_3 layer.

In our devices, the capacitance transition occurs almost at 0 V (see Figure 6.44), which is not the same voltage at which the conduction starts (approximately 2 V in Figure 6.2a-c-e). This is because the C-V transition is correlated to the formation of a mobile hole charge sheet at the Alq_3/NPD interface, due to the different carrier injection efficiency from the cathode

and the anode. Instead, the OLED current is determined at a larger degree by the electron injection rather than hole injection.

We can tentatively explain what occurs during the constant current stress with the aid of Figure 6.1.3d and f. It has been reported in literature that accelerated electrical stress produces positive charge at the Alq₃/NPD interface [49]. This charge is likely responsible for the rightward shift of the C–V curves in Figure 6.44. In fact, the positive charge trapping decreases the electric field across the NPD layer, and it opposes to the hole injection from the anode. This is schematically shown in Figure 6.1.3d, where the dashed lines represent the band structure before stress and the solid lines are the bands after stress. Hence, a higher voltage is needed to produce the same electric field across the NPD layer and the consequent capacitance transition. The evolution of the I–V curves in Figure 6.2 (a-c-e) is apparently in contrast to this interpretation. In fact, because the OLED current is determined at a larger degree by the electron injection, we should expect a leftward shift of the I–V curves, due to the increase of the electric field across the ETL. This is not observed either at low positive voltage (around 2 V), where the current is only marginally modified by the stress, or at high electric field, where V_{ON} even behaves oppositely [see 6.2b-d-f].

We have already discussed that the increase in V_{ON} cannot be ascribed (only) to an increase in the series resistance, because OLEDs with different thicknesses feature quantitatively the same behavior during stress as demonstrated by Pinato et al. In fact, if some appreciable change in the series resistance occurred, we would expect to observe a much larger increase of V_{ON} in those devices with greater layer thicknesses, which is not observed.

The I–V behavior can be tentatively explained by assuming that the constant current stress produces both a fixed interface trapped charge and a number of neutral interface states, as schematically shown in 6.1.3d. These states may come from the oxidation of the Alq₃, as previously reported [26], and they should act as electron interface traps, which captured an electron as soon as its energy level moves below the Fermi level.

As soon as the voltage increases, more and more defects are pushed below the quasi-Fermi level at the NPD/Alq₃ interface; if we assume that, each time a defect goes below the Fermi level, it captures an electron or, equivalently, releases a hole, the increase in the anode voltage translates into a progressive increase in the net negative charge, which compensates the initial positive fixed charge. This is confirmed by Kondakov who showed the formation of weakly emissive deep electron traps in the vicinity of the interface between the HTL and ETL. Following this interpretation, at moderately low voltage, i.e., when only the hole injection should be appreciable, the contribution of the positive charge is dominating because the majority of the defects are empty, being located above the Fermi level. Therefore, the C–V curves are expected to shift rightward, due to the reduction of the hole injection rate at the anode interface. On the other hand, electron injection

should be easier, owing to the positive charge (see 6.1.3e). In principle, this should increase the OLED current in that voltage range. Unfortunately, in that voltage range, the OLED current is dominated by parasitic leakages and transient trapping/detrapping contributions. If we consider the current above 2 V, the contribution of the neutral defects becomes comparable to that of positive charge. In fact, for voltage around 2 V, there is a moderate shift of the I–V curve. When the bias voltage exceeds 2 V, the contribution of the neutral defects becomes dominant (6.1.3f), and the rightward shift of the I–V curves becomes larger and larger as the anode voltage increases. As soon as the electric field across the ETL is high enough, an appreciable electron conduction begins, the device enters the linear region, the band bending of the NPD becomes negligible (see, for instance, [50]), and the quasi-Fermi level at the Alq₃/NPD interface is pinned to that of the NPD layer. In this way, the interface trapped charge reaches its maximum value, and the I–V curves remain parallel to each other. The fact that VON increases during stress suggests that the contribution of the electron interface traps is dominant at high electric field (6.1.3f), with respect to the positive fixed trapped charge.

6.1.4 Reference graphs

OLEDs submitted to CCS at different temperature values

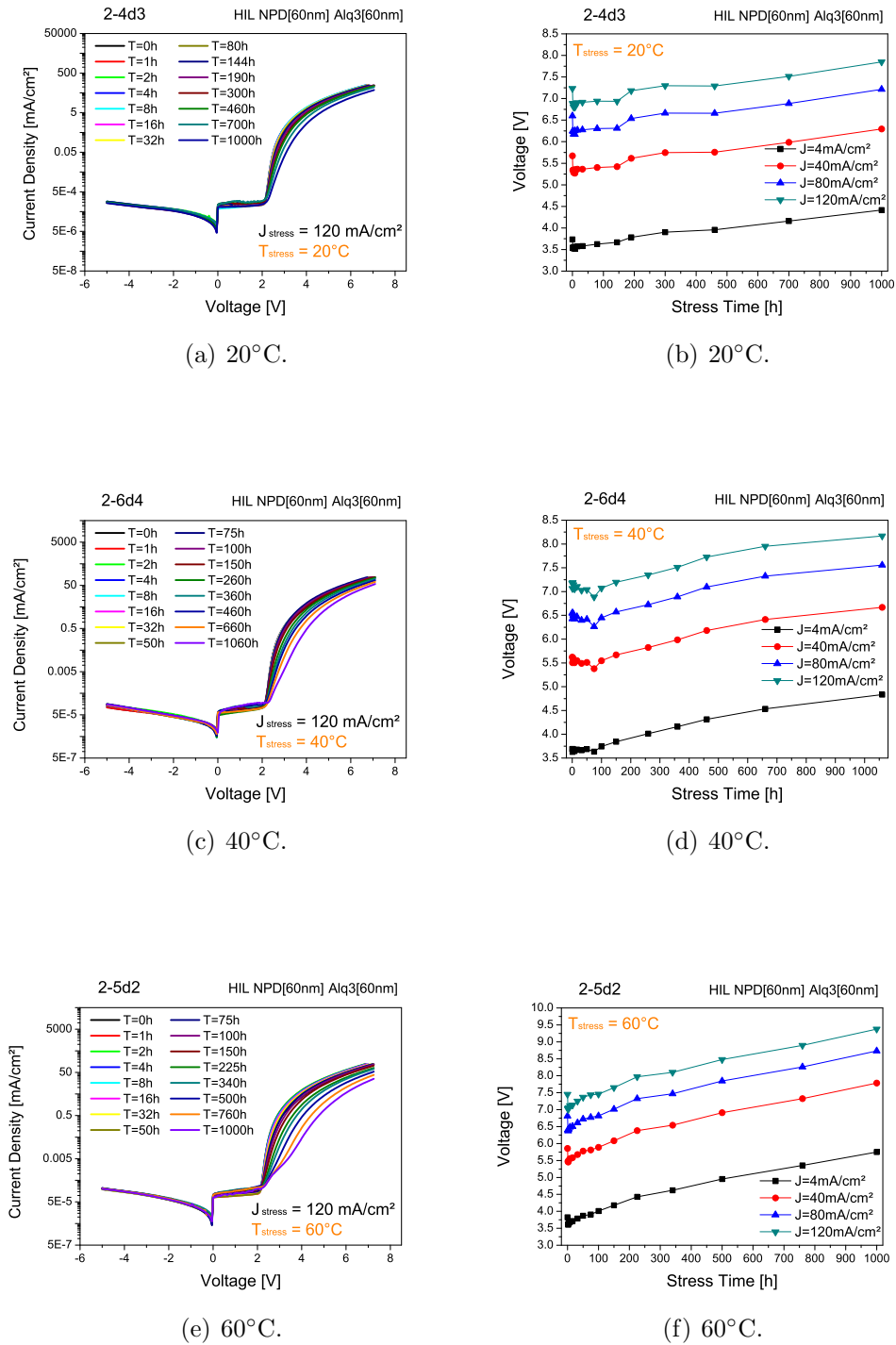
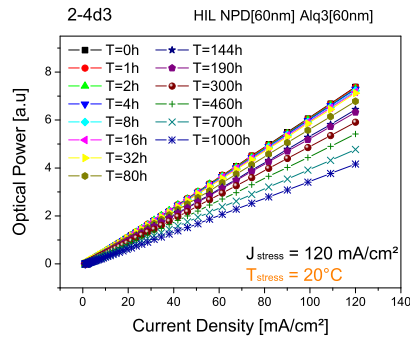
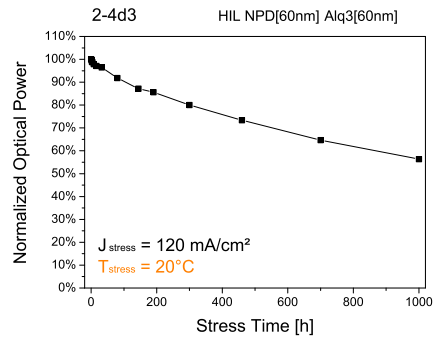


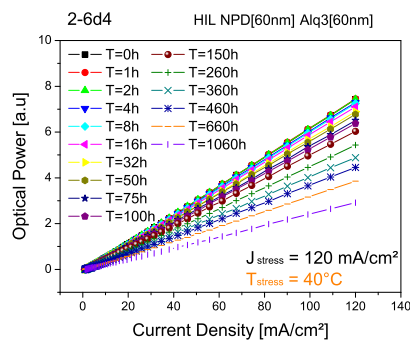
Figure 6.2: I-V characteristics (a-c-e) and voltage-time characteristics (b-d-f) for wHIL OLEDs submitted to CCS at different temperature values.



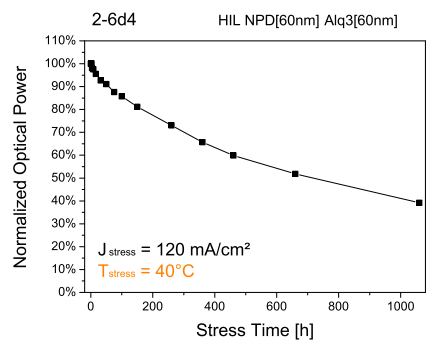
(a) 20°C.



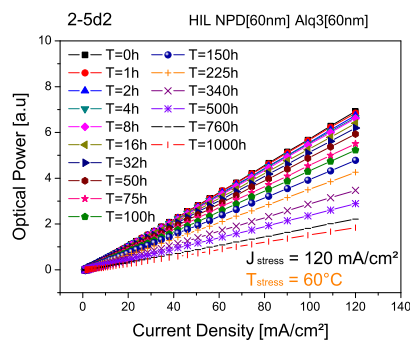
(b) 20°C.



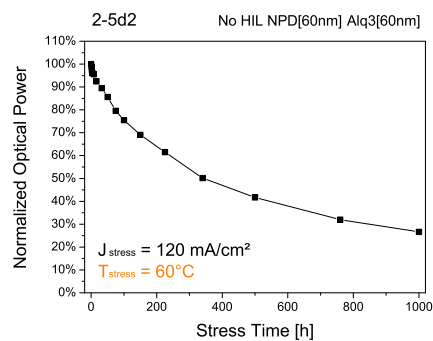
(c) 40°C.



(d) 40°C.



(e) 60°C.



(f) 60°C.

Figure 6.3: L-I characteristics (a-c-e) and optical power degradation read at 120 mA/cm^2 (b-d-f) for wHIL OLEDs submitted to CCS at different temperature values read at 120 mA/cm^2 .

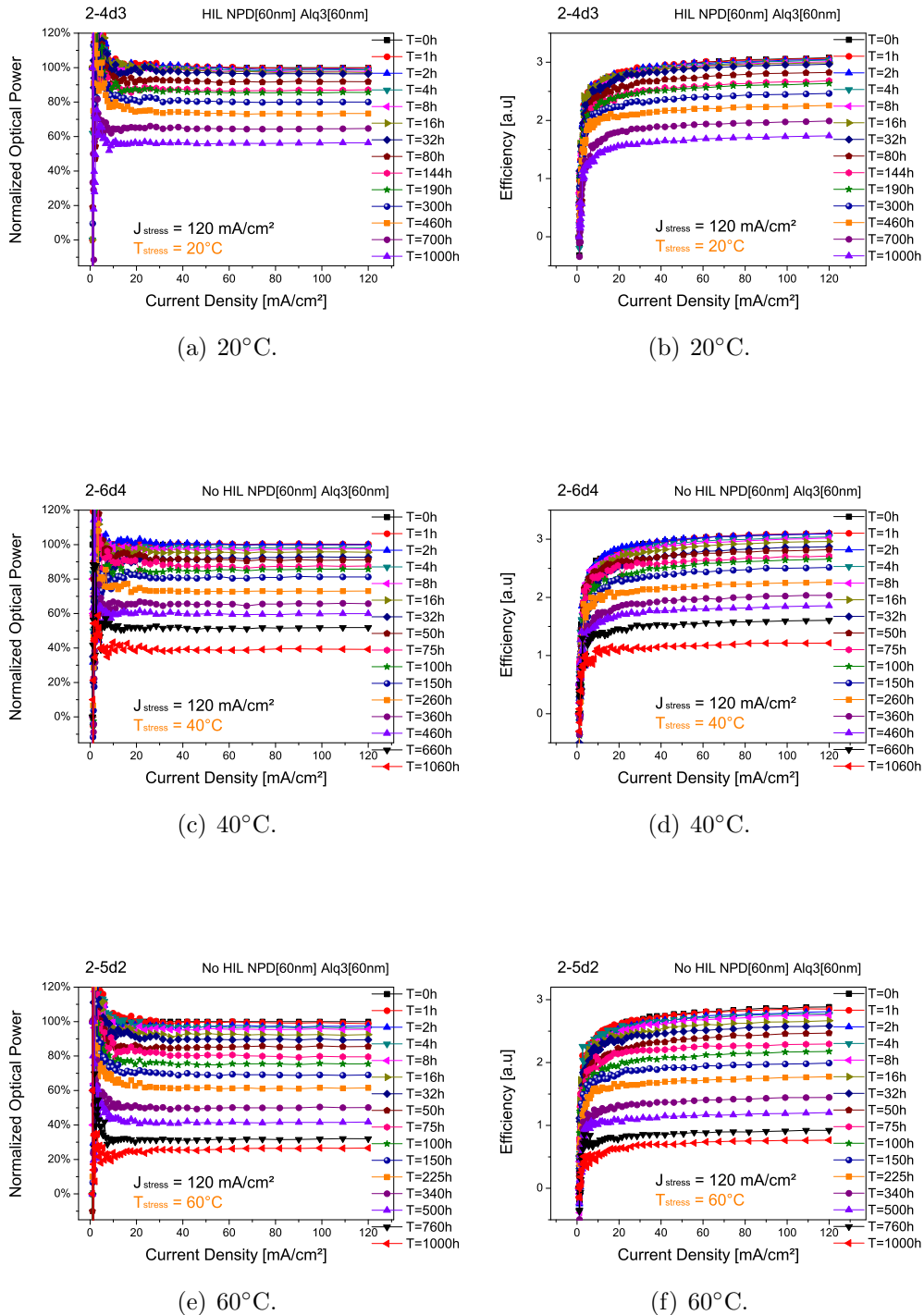


Figure 6.4: Normalized optical power degradation (a-c-e) and efficiency (b-d-f) of wHIL OLEDs submitted to CCS at different temperature values.

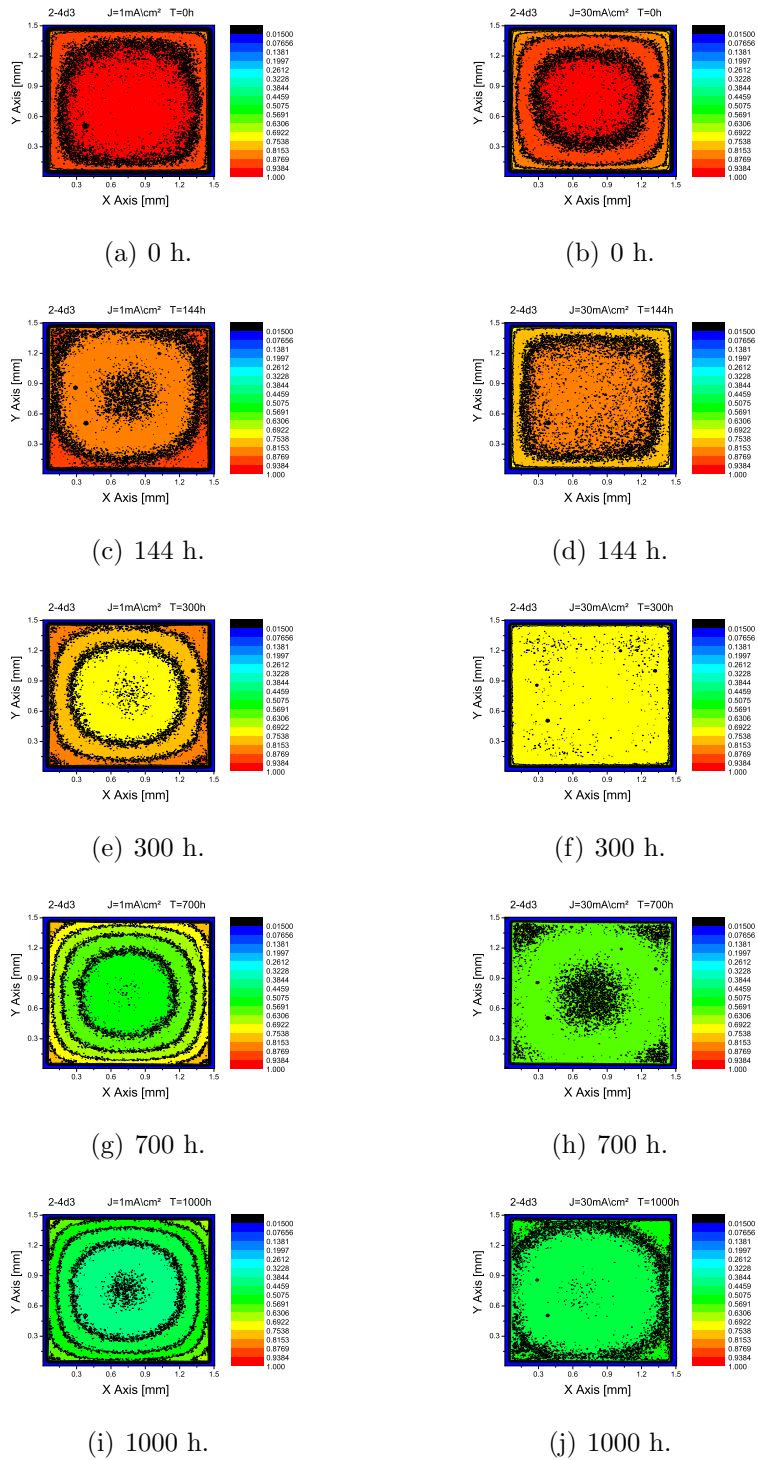


Figure 6.5: Light emission profile for wHIL OLEDs submitted to CCS at 20°C read at 1mA/cm^2 (a-c-e-g-i) and 30mA/cm^2 (b-d-f-h-l).

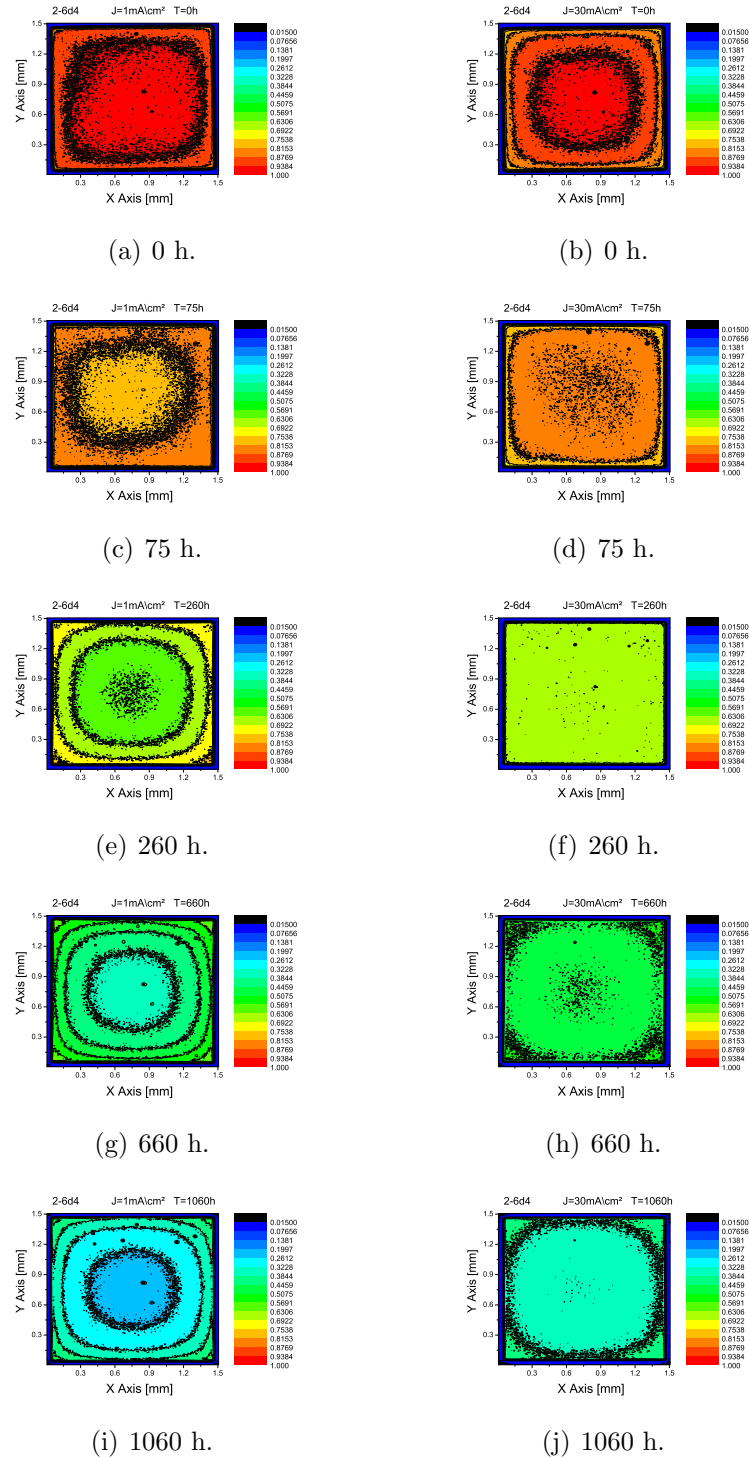


Figure 6.6: Light emission profile for wHIL OLEDs submitted to CCS at 40°C read at 1mA/cm^2 (a-c-e-g-i) and 30mA/cm^2 (b-d-f-h-l).

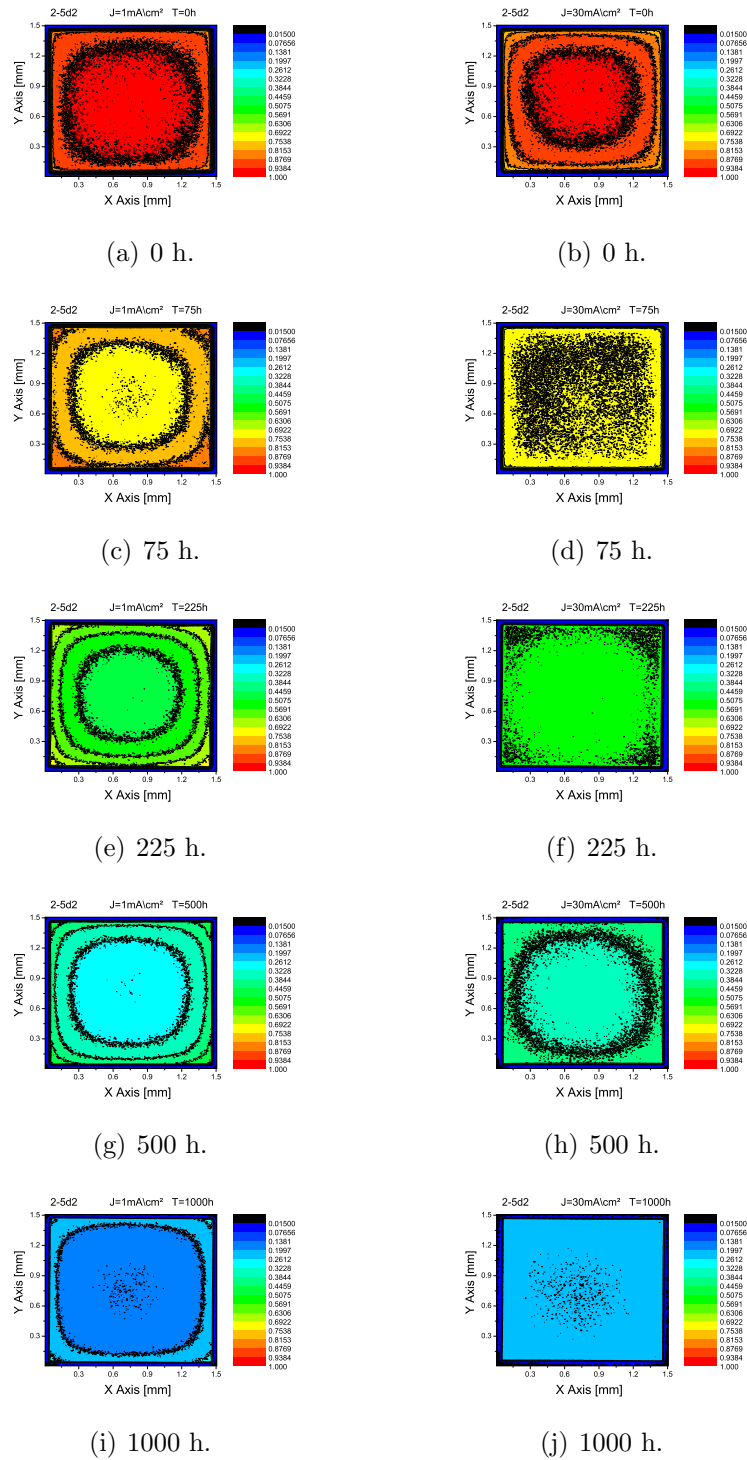


Figure 6.7: Light emission profile for wHIL OLEDs submitted to CCS at 60°C read at 1mA/cm^2 (a-c-e-g-i) and 30mA/cm^2 (b-d-f-h-l).

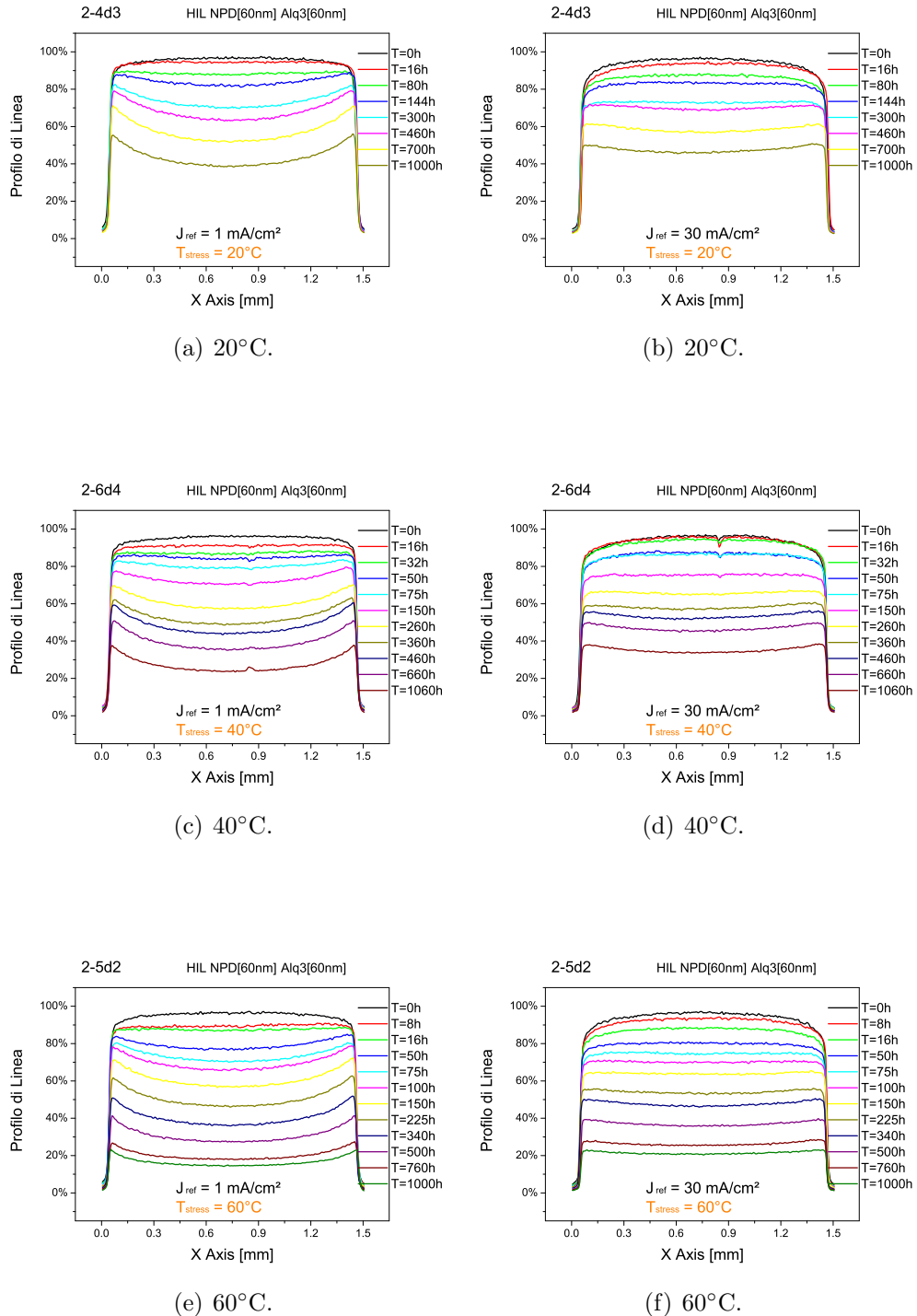


Figura 6.8: Longitudinal light emission profile for wHIL OLEDs submitted to CCS at different temperature values read at 1 (a-c-e) and 30mA/cm² (b-d-f).

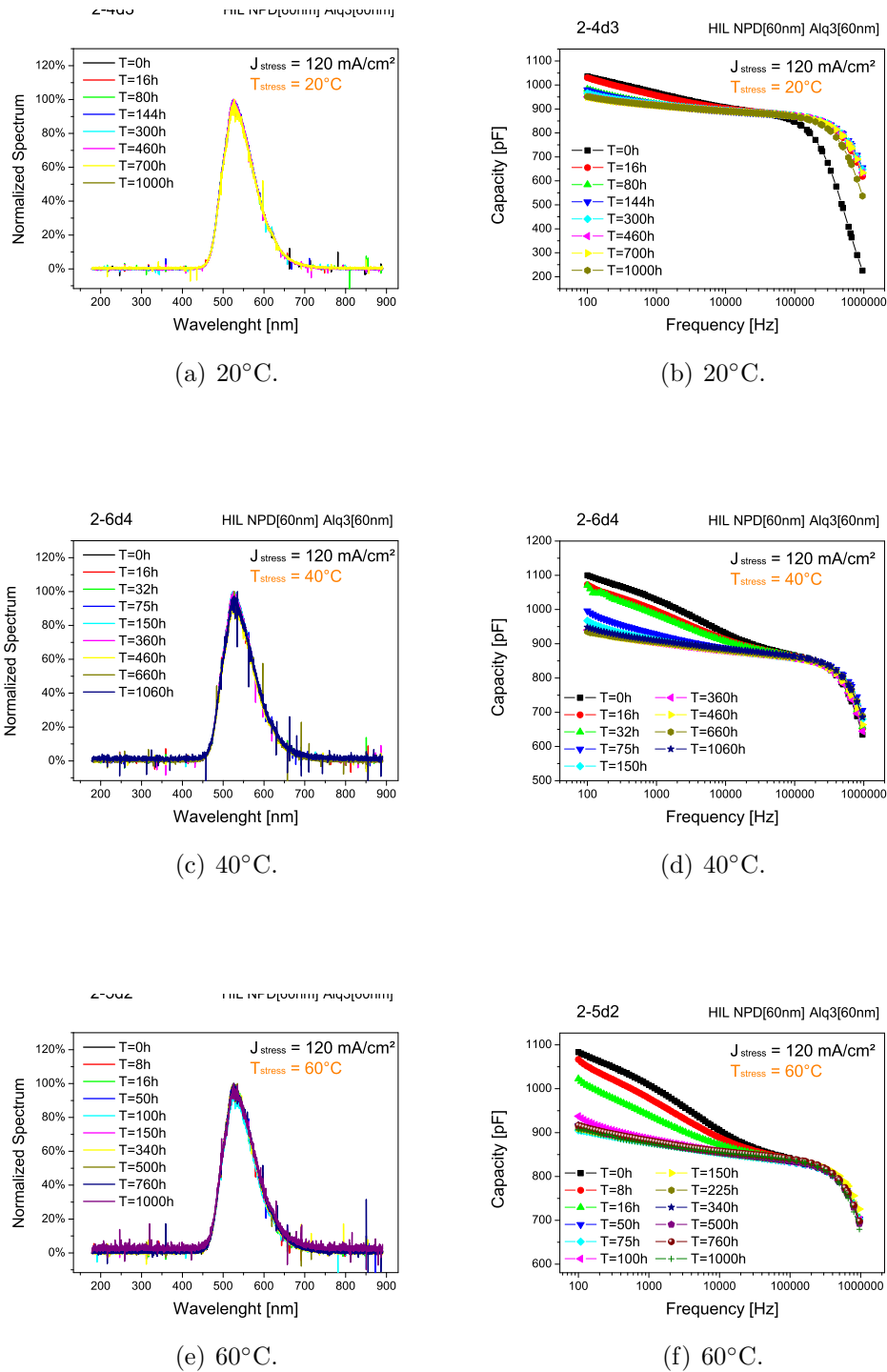


Figure 6.9: Optical power spectral distribution (a-c-e) and C-F characteristics (b-d-f) of wHIL OLEDs submitted to CCS at different temperature values.

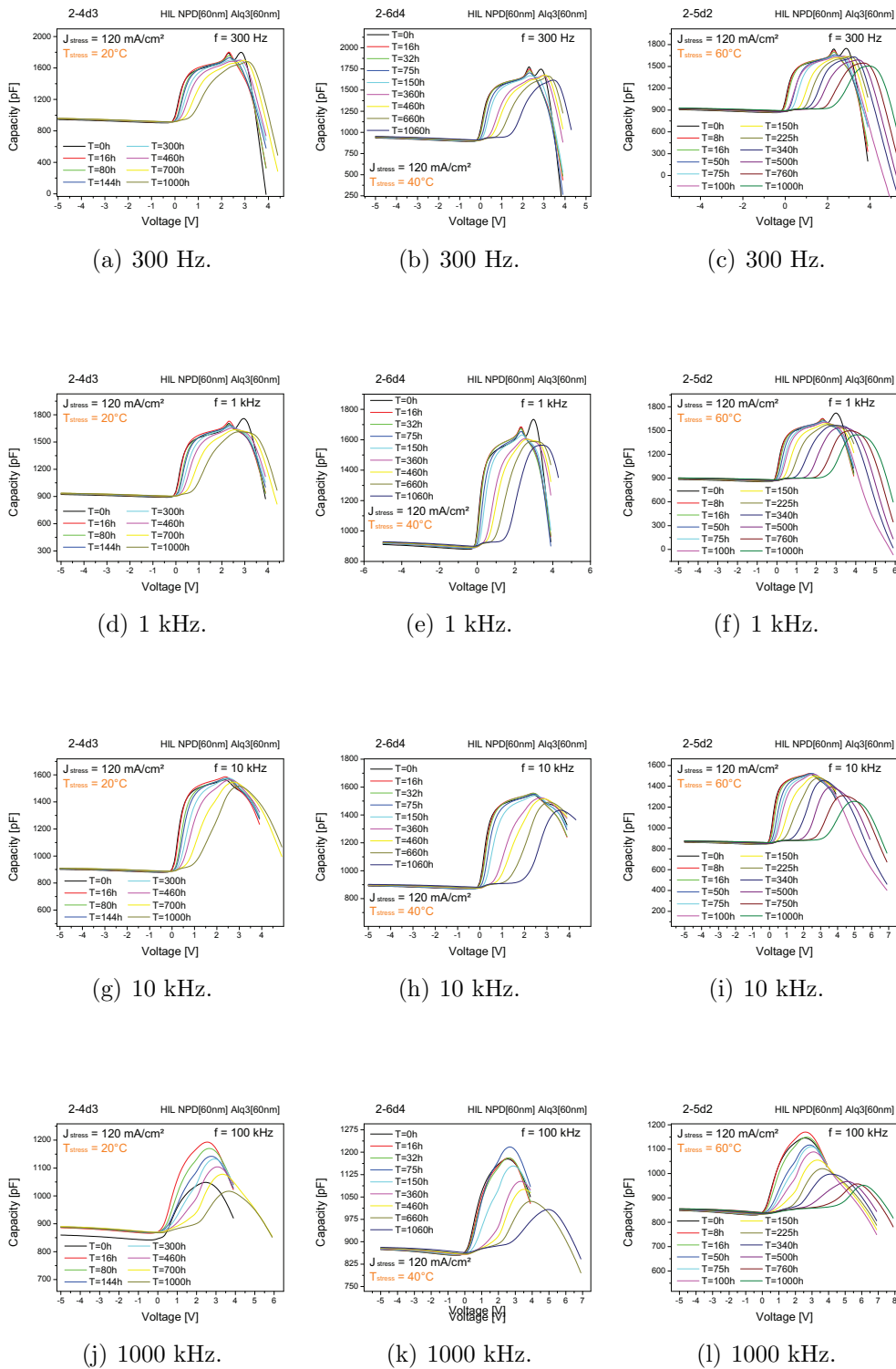


Figure 6.10: C-V characteristics for wHIL OLEDs submitted to CCS at 20 (a-d-g-l), 40 (b-e-h-m) and 60°C (c-f-i-n) at different frequencies.

OLEDs not submitted to CCS at different temperature values

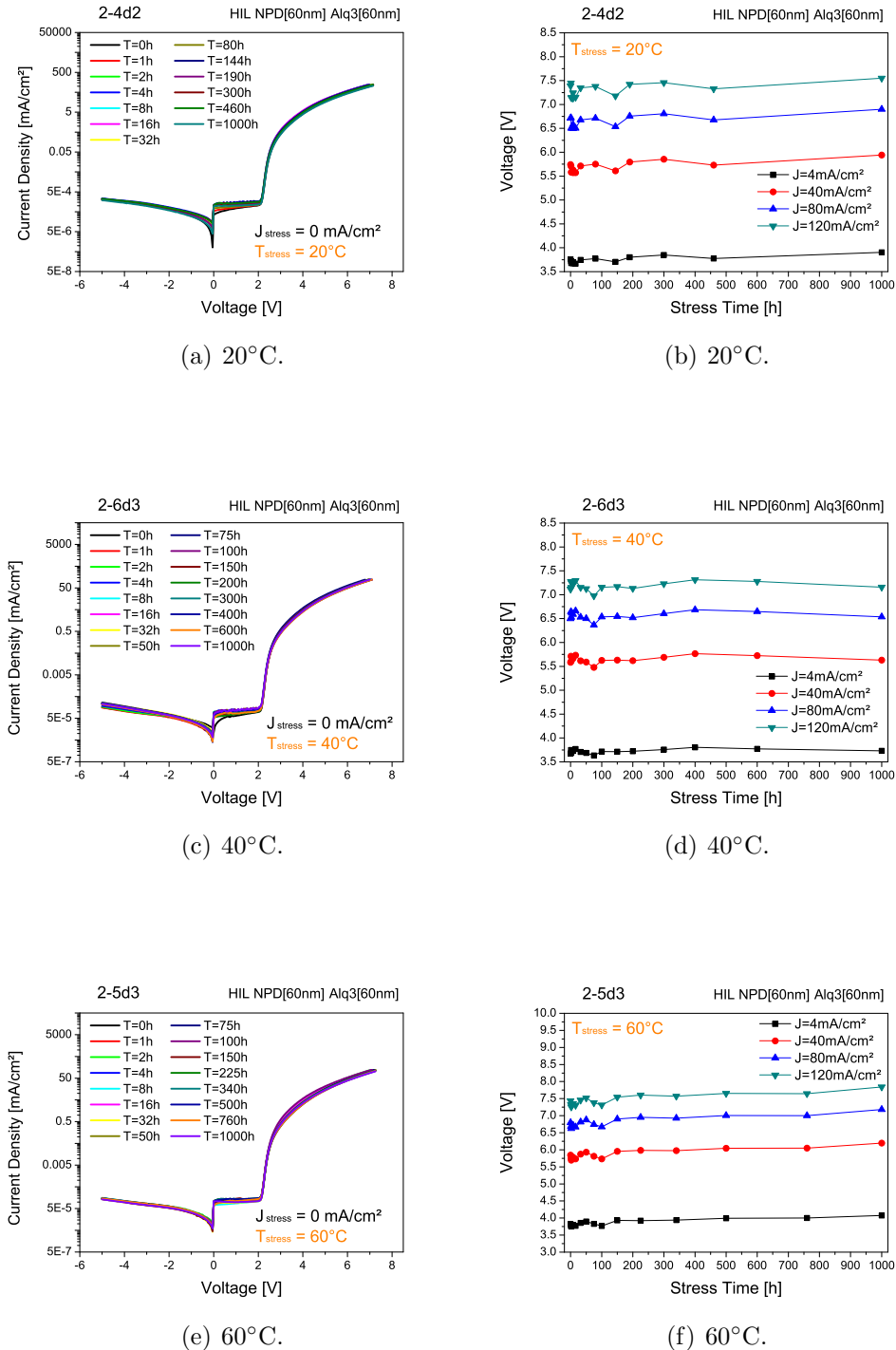
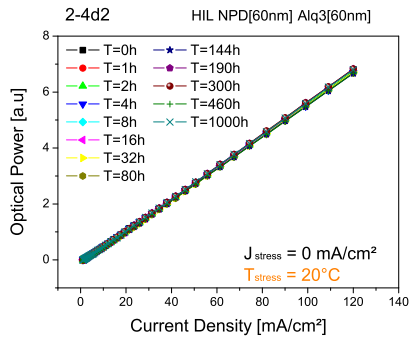
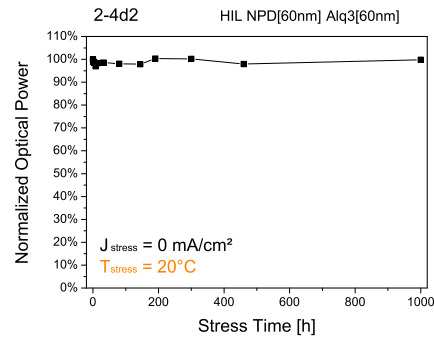


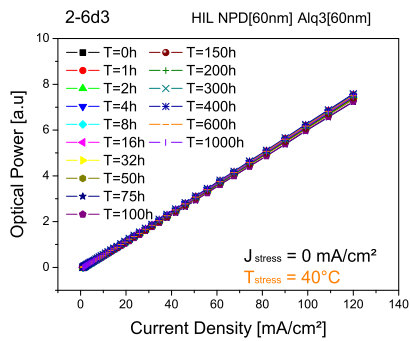
Figure 6.11: I-V characteristics (a-c-e) and voltage-time characteristics (b-d-f) for WHIL OLEDs not submitted to CCS at different temperature values.



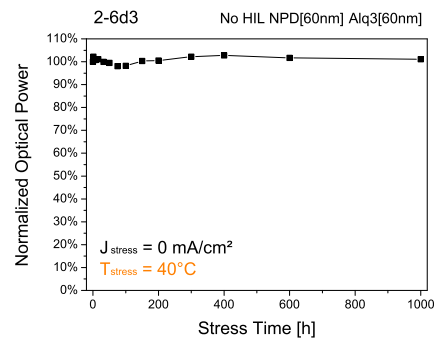
(a) 20°C.



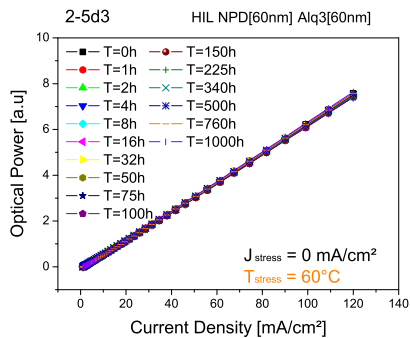
(b) 20°C.



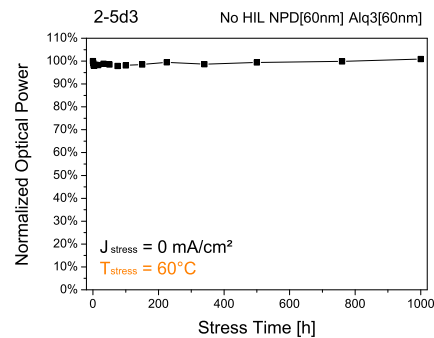
(c) 40°C.



(d) 40°C.



(e) 60°C.



(f) 60°C.

Figure 6.12: L-I characteristics (a-c-e) and optical power degradation read at 120 mA/cm^2 (b-d-f) of wHIL OLEDs not submitted to CCS at different temperature values.

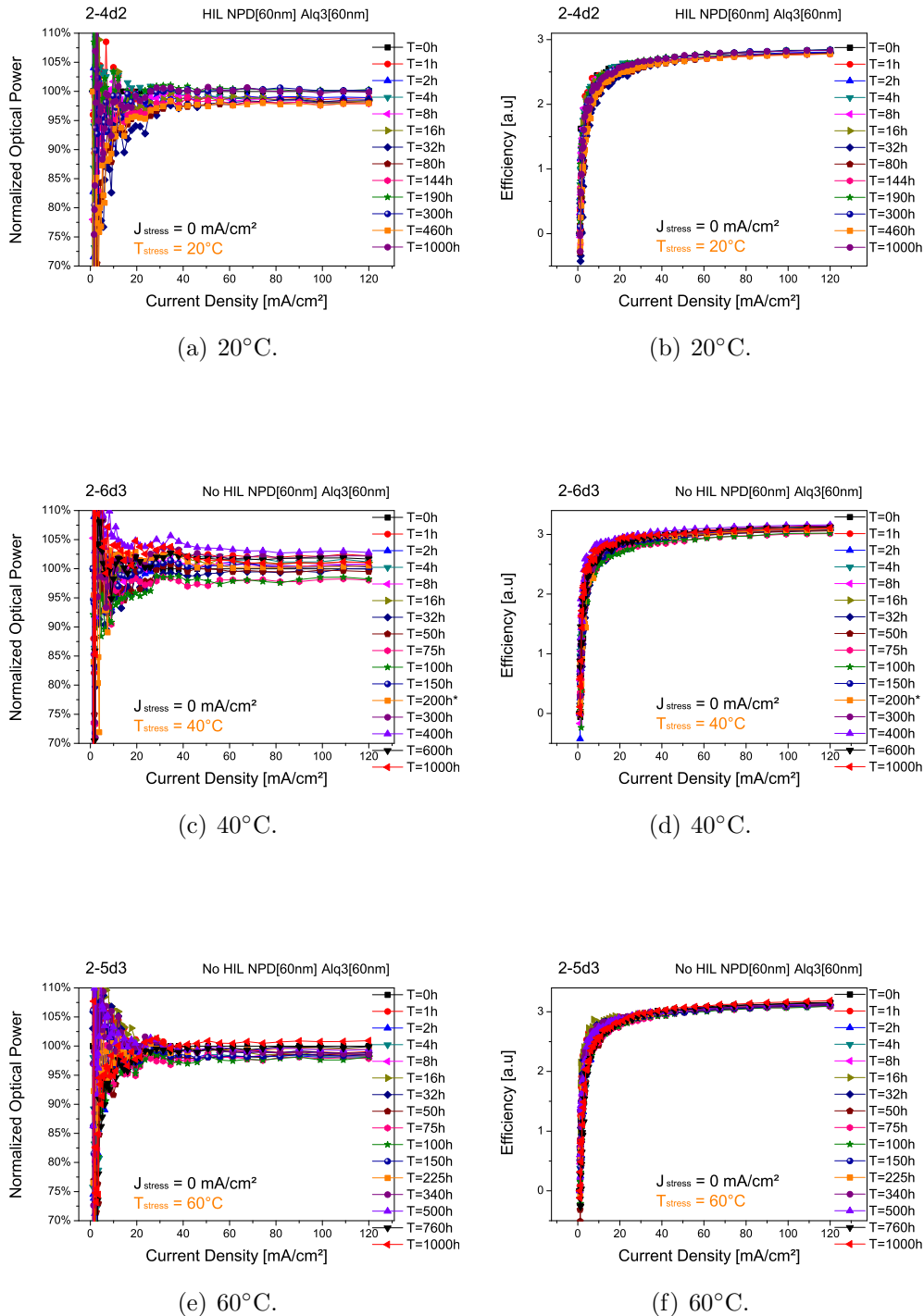


Figure 6.13: Normalized optical power degradation (a-c-e) and efficiency (b-d-f) of wHIL OLEDs not submitted to CCS at different temperature values.

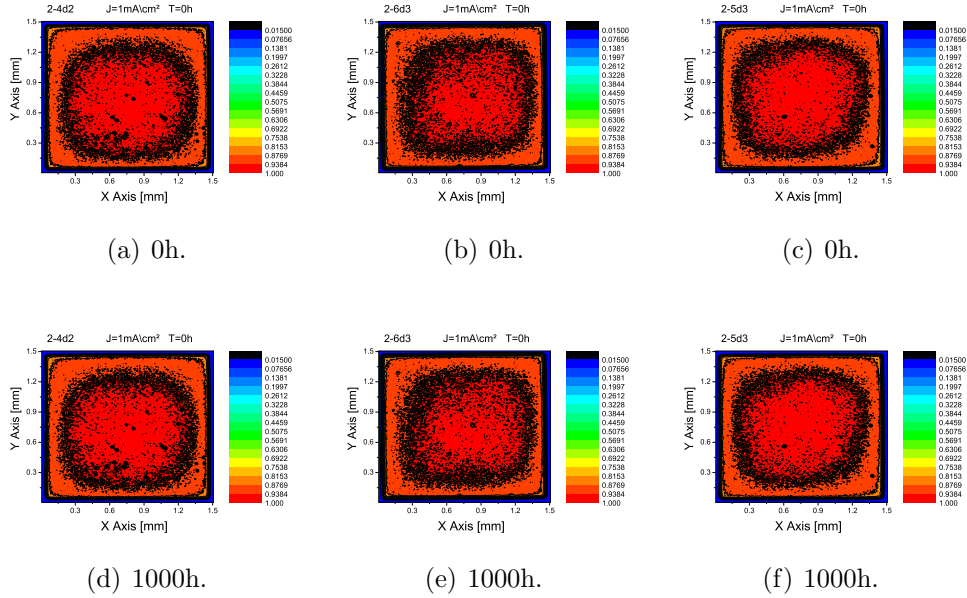


Figure 6.14: Light emission profile for wHIL OLEDs not submitted to CCS at 20 (a-d), 40 (b-e) and 60°C (c-f) read at 1 mA/cm².

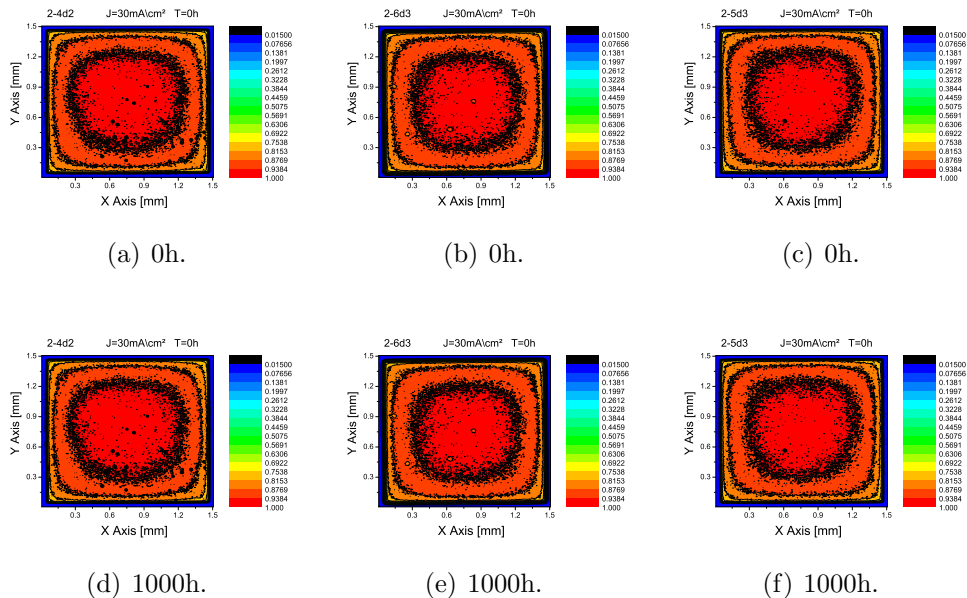


Figure 6.15: Light emission profile for wHIL OLEDs not submitted to CCS at 20 (a-d), 40 (b-e) and 60°C (c-f) read at 30 mA/cm².

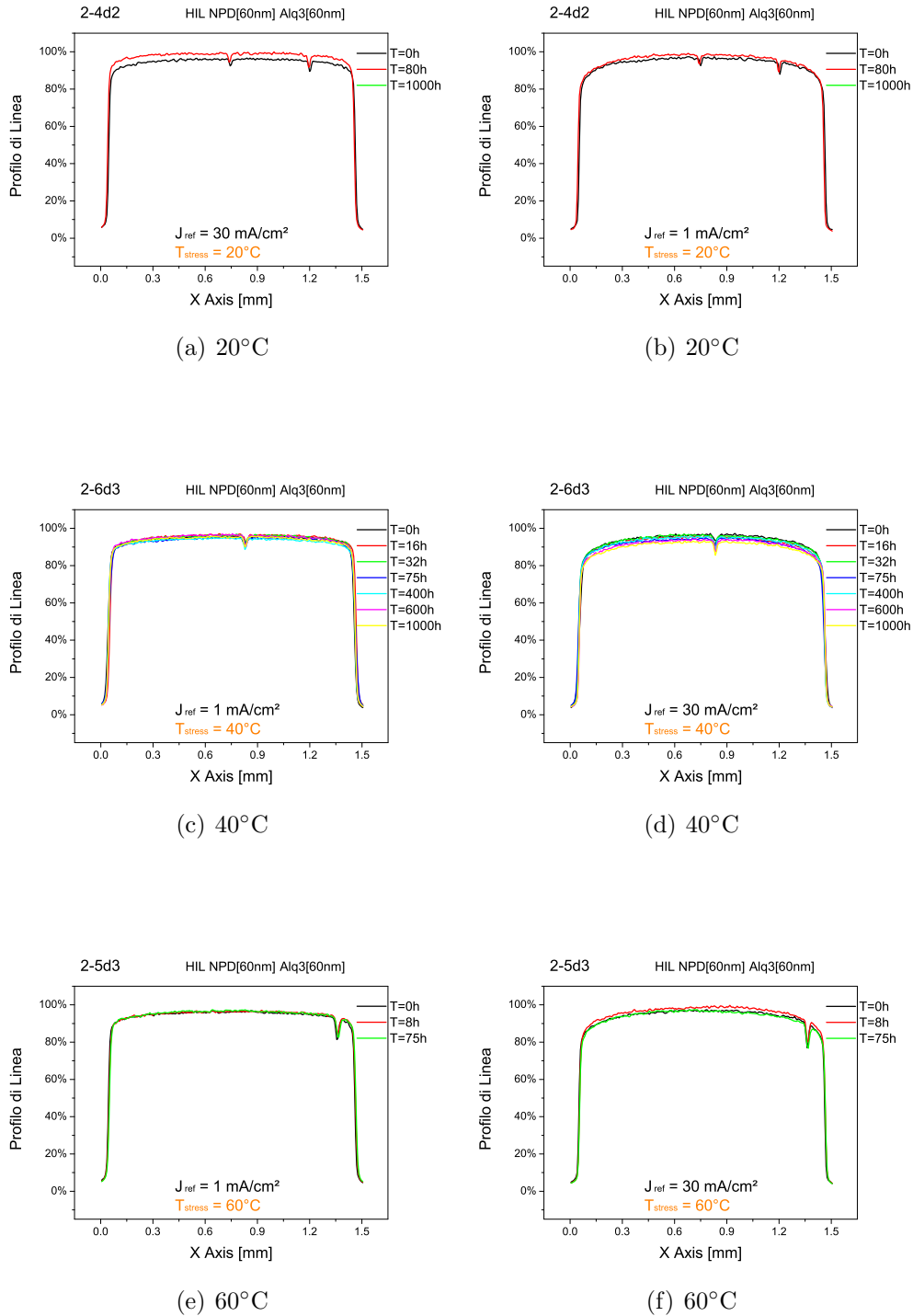


Figura 6.16: Longitudinal light emission profile for whIL OLEDs not submitted to CCS read at 1 (a-c-e) and 30 mA/cm² (b-d-f).

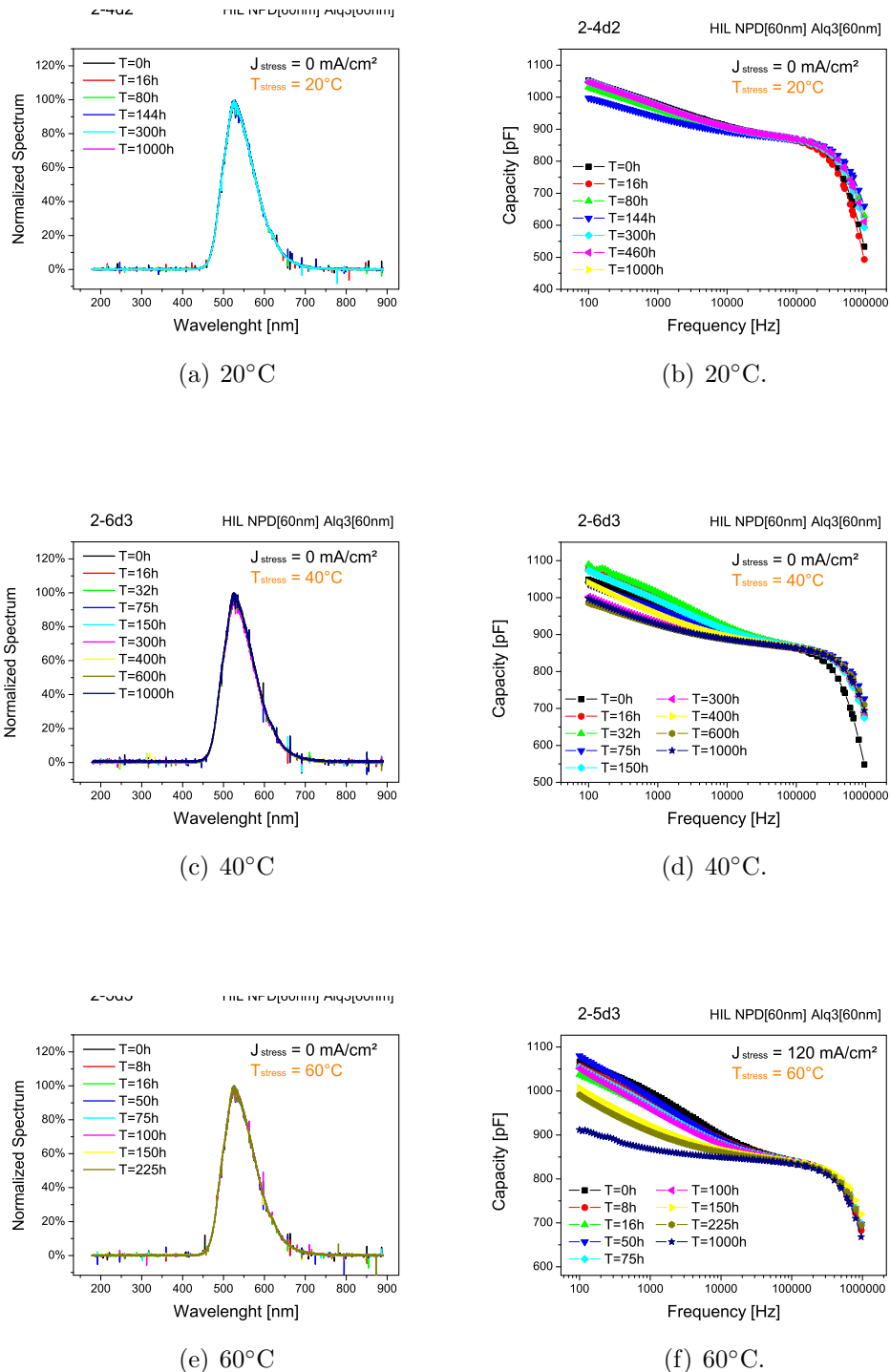


Figure 6.17: Optical power spectral distribution (a-c-e) and C-F characteristics (b-d-f) of wHIL OLEDs not submitted to CCS at different temperature values.

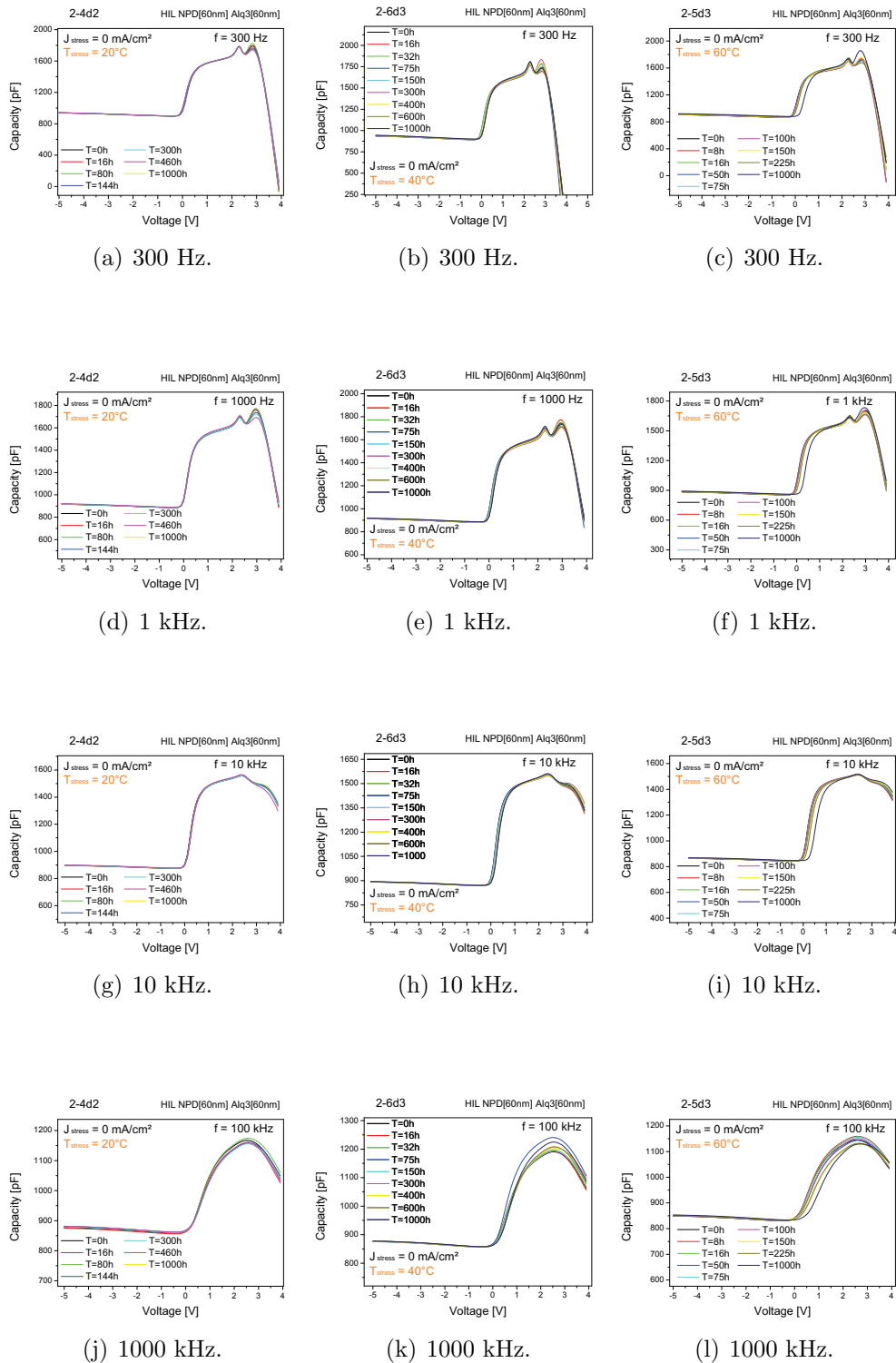


Figure 6.18: C-V characteristics for wHIL OLEDs submitted to CCS at 20 (a-d-g-l), 40 (b-e-h-m) and 60°C (c-f-i-n) at different frequencies.

6.2 Thermal/Electrical stress for OLED without HIL

6.2.1 Degradation of electrical and optical parameters

We carried out the same experiments also on OLED without the HIL. Figures 6.19 (a-c-e) and 6.19 (b-d-f) show the degradation of the J-V curves and the voltage-time characteristics, respectively, during CCS at 20-40-60°C, whereas, Figures 6.20 (a-c-e) and 6.20 (b-d-f) show the corresponding optical power degradation and normalized optical power degradation read at 120 mA/cm². These degradation kinetics for woHIL OLEDs follow the same trend of wHIL ones, but, with a higher degradation rate. This is confirmed also seeing Figure 6.21 (a-c-e) and 6.21 (b-d-f) which represent the optical power degradation as function of the current until 120 mA/cm² and the device efficiency. Similar to that seen for wHIL OLEDs, no degradation is shown when CCS is not applied. Indeed, curves in Figures 6.28 (a-c-e)-6.29 (a-c-e)-6.30 are perfectly overlapped, whereas, curves in Figure 6.28 (a-c-e) and 6.29 (a-c-e) follow a horizontal evolution.

After 1000 h stress, the luminance of the devices reduce down to different values depending on the temperature, similarly to wHIL OLEDs and approximately twice than them. Table 6.2 summarized it.

The reason whereby we reported will be explained shortly in Section 6.2.2.

Also the light emission profile at 1 and 30 mA/cm² (Figures 6.22-6.23-6.24) and the longitudinal light emission profile at the same reference current value (Figures 6.25) highlight a greater degradation rate respect wHIL OLEDs. Then, considering, thermal stressed devices without bias, we can do the same considerations described for wHIL OLEDs: curves in Figure 6.33 appear perfectly overlapped, whereas, curves in Figures 6.31-6.32 show a horizontal trend, denoting that no degradation is occurred.

C-F characteristics show the same trend for both devices submitted to CCS (Figure 6.34b-d-f) and devices only thermal stressed (Figure 6.34). For C-V characteristics (Figure 6.26 (b-d-f), instead, also in this case during the electrical stress (CCS), the C-V curves shift rightward and the transition region of the C-V curves is progressively more stretched as the stress time increases, but their trend is quite strange comparing with wHIL OLEDs one. This is likely due to a additional series resistance at moderately high frequency and we are still working to give them a reasonable explanation.

Tabella 6.2: Optical power reduction after 1000-h stress for wHIL OLEDs.

T=20°C	T=40°C	T=60°C
33.43 %	36.92 % (after 580h)	36.92 % (after 580h)
	29.65 % (fitting 1000h)	14.63 % (fitting 1000h)

Instead, regard to devices only thermally stressed (unbiased), no significant degradation is observed (Figure 6.35).

Finally, in Figures 6.26 (a-c-e) and 6.34 (b-d-f) are shown, respectively, the normalized optical power spectral distribution for devices thermal and electrical stressed and for devices only thermal stressed. For both no shape change are observed before and after the ageing.

The behavior of this set of devices is qualitatively the same of those samples featuring the HIL, and the same consideration drawn in the previous section are worth. The major differences between device with and without HIL are:

1. The degradation rate of devices without HIL is almost twice than the devices with HIL;
2. The light emission profile distribution in the virgin devices is much more uniform in device with HIL.

6.2.2 Intrinsic weakness of OLEDs without HIL

In this section we are going to give an explanation regarding the missing point in the degradation kinetics of some devices. First of all, we should be noted, that woHIL OLEDs are submitted to an higher operating voltage at 120 mA/cm^2 due to the absence of the HIL between the ITO anode and the NPD layer. Indeed, the hole injection layer, as the name suggests, is used as intermediate layer to reduce the barrier gap of the NPD hole conduction band (LUMO), facilitating the hole injection from the anode. Thus, holes, seeing a lower barrier, need less energy to be injected and hence less voltage.

Therefore, the absence of the HIL results in higher operating voltage and higher power stress condition which most likely lead to an accelerated ageing of the devices under test. We find from our data, that woHIL OLEDs suffer a degradation almost twice than wHIL OLEDs, this achievement is likely due to the twice operating voltage of woHIL OLEDs ($\sim 13\text{-}14 \text{ V}$) than wHIL ones ($\sim 6\text{-}7 \text{ V}$) at the stress current value (120 mA/cm^2).

For this reason, woHIL OLEDs revealed to be weaker than wHIL OLEDs during both ageing and measurements. Apart woHIL OLEDs submitted to CCS at 20°C , which shown good degradation kinetics, for the OLEDs stressed at 40 and 60°C , we met several reliability problems that led to the death of the device. Indeed, more longevous devices arrived at 580-h, for OLEDs stressed at 40°C , and at 330-h stress for OLEDs stressed at 60°C . But, before this achievement, we employed other 2 samples for each critical temperature values resulting in the premature death of the devices. For this reason, the kinetics stop respectively at this two times and we have not data after these two points. Hence, in order to have a full view of the degradation kinetic until 1000-h stress, we had to use an exponential fitting as reported in Table 6.2.

6.2.3 Reference graphs

OLEDs submitted to CCS at different temperature values

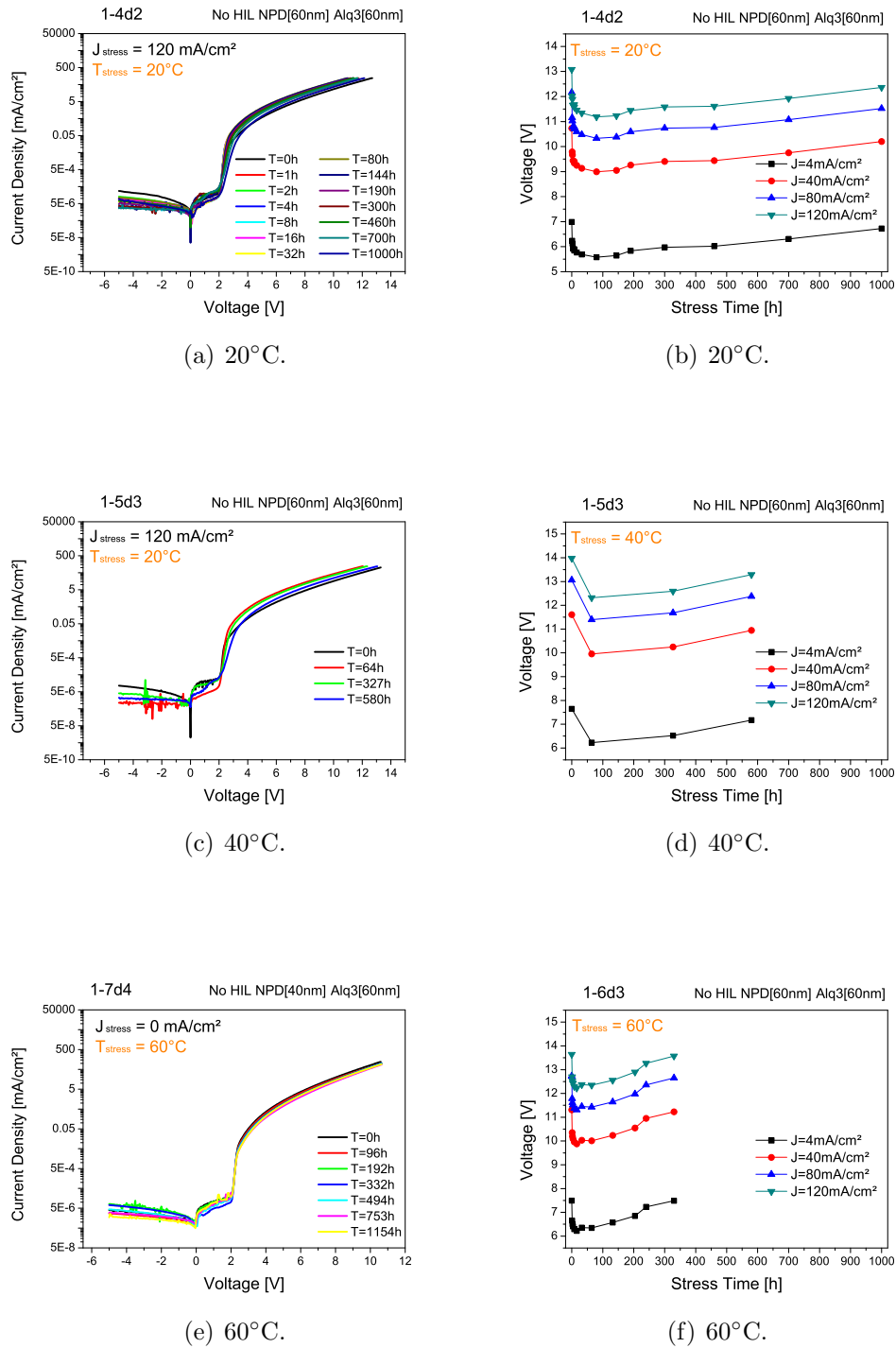
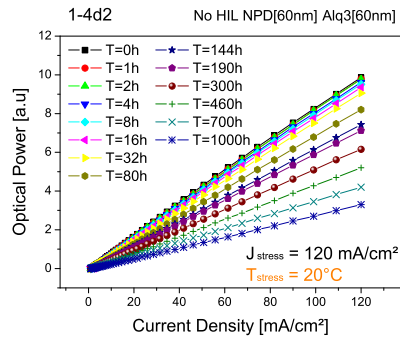
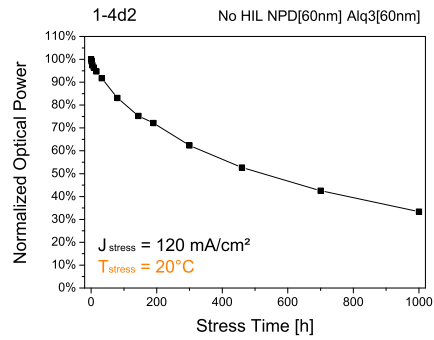


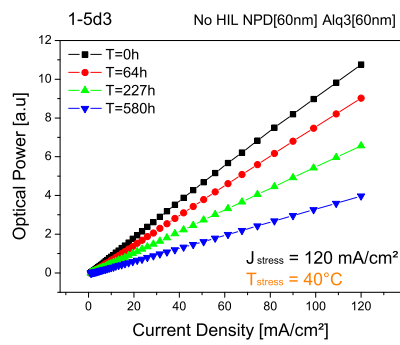
Figure 6.19: I-V characteristics (a-c-e) and voltage-time characteristics (b-d-f) for woHIL OLEDs submitted to CCS at different temperature values.



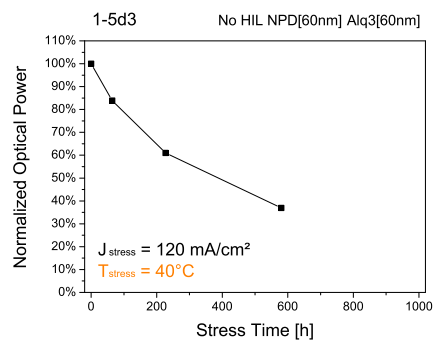
(a) 20°C.



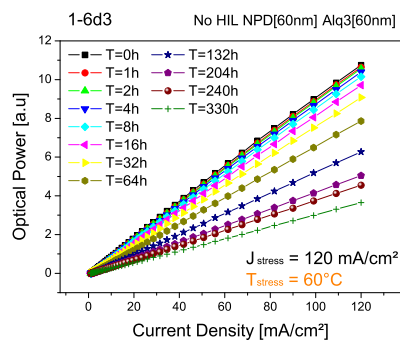
(b) 20°C.



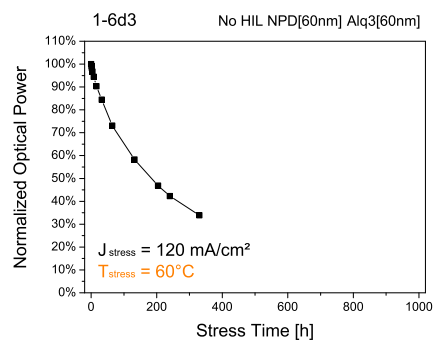
(c) 40°C.



(d) 40°C.



(e) 60°C.



(f) 60°C.

Figure 6.20: L-I characteristics (a-c-e) and optical power degradation read at 120 mA/cm^2 (b-d-f) for woHIL OLEDs submitted to CCS at different temperature values.

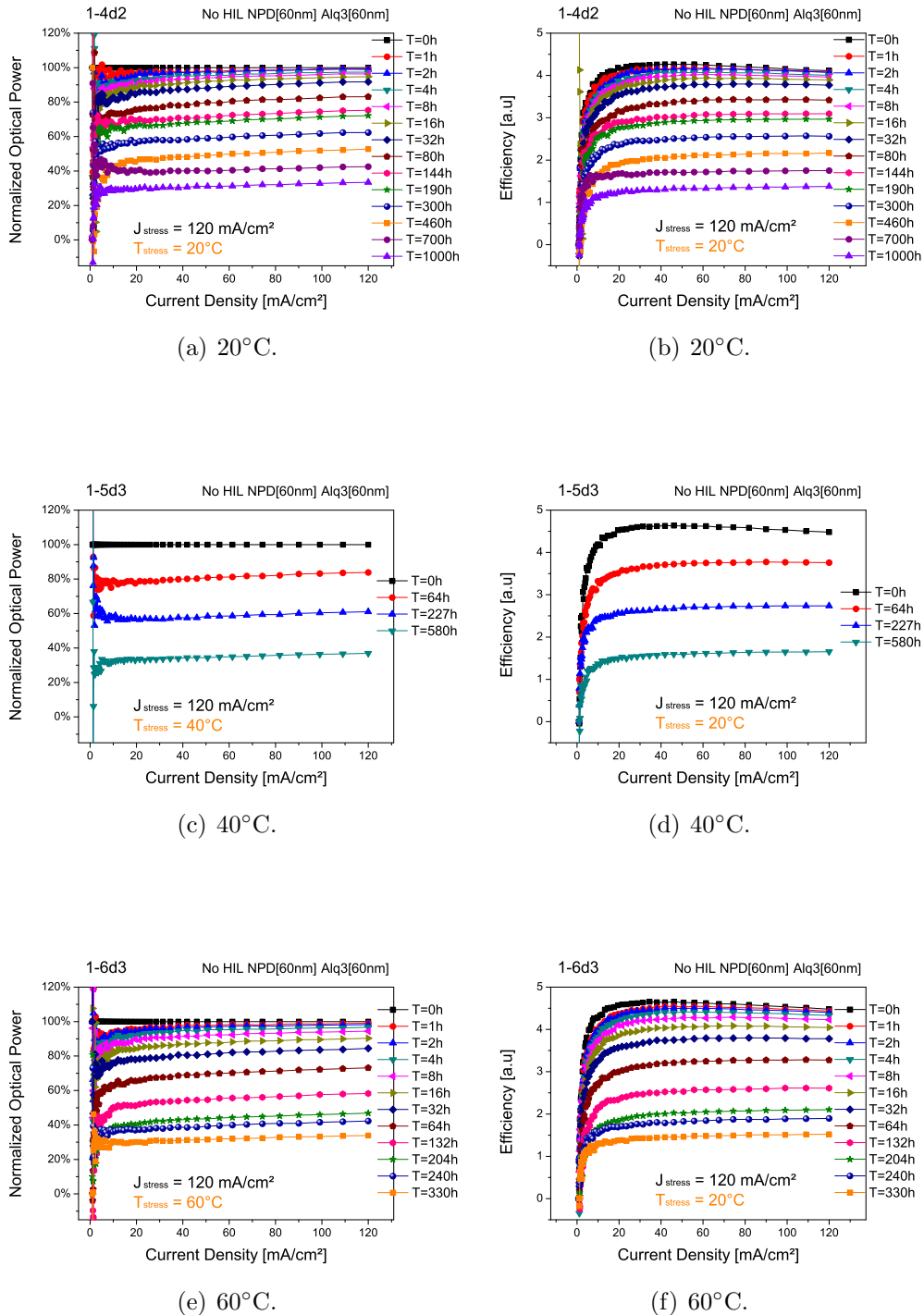


Figure 6.21: Normalized optical power degradation (a-c-e) and efficiency (b-d-f) of woHIL OLEDs submitted to CCS at different temperature values.

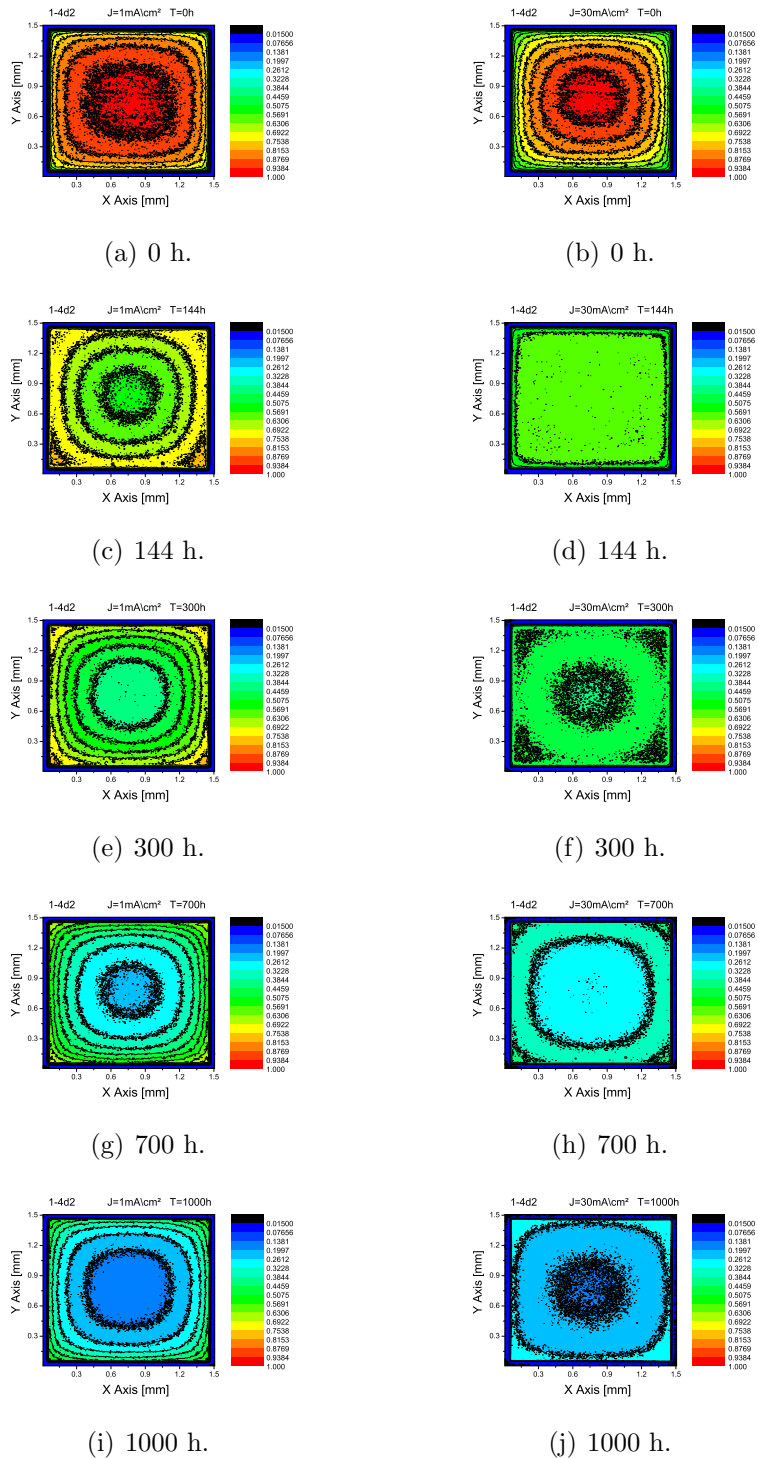


Figure 6.22: Light emission profile for woHIL OLEDs submitted to CCS at 20°C read at 1 (a-c-e-g-i) and 30mA/cm^2 (b-d-f-h-l).

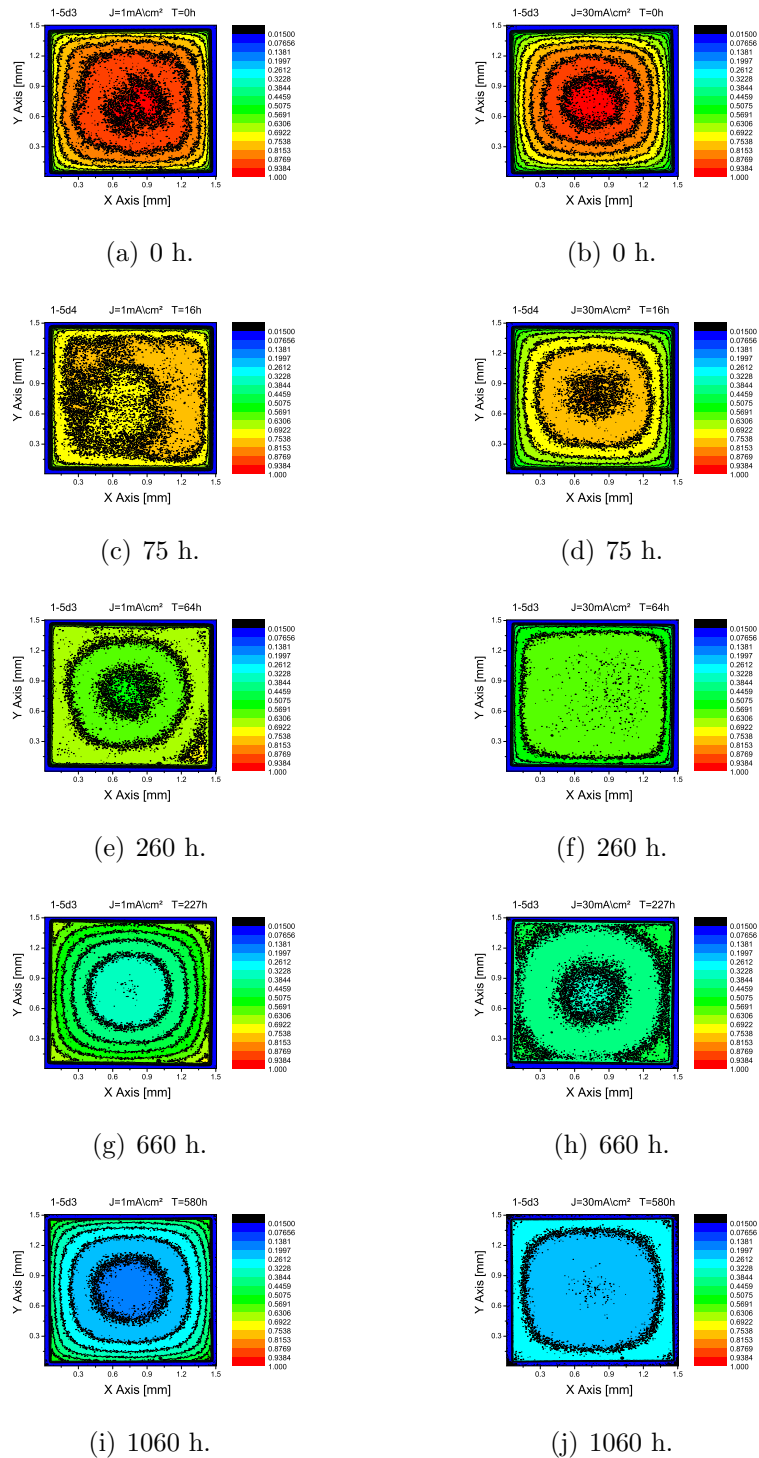


Figure 6.23: Light emission profile for woHIL OLEDs submitted to CCS at 40°C read at 1 (a-c-e-g-i) and 30mA/cm² (b-d-f-h-l).

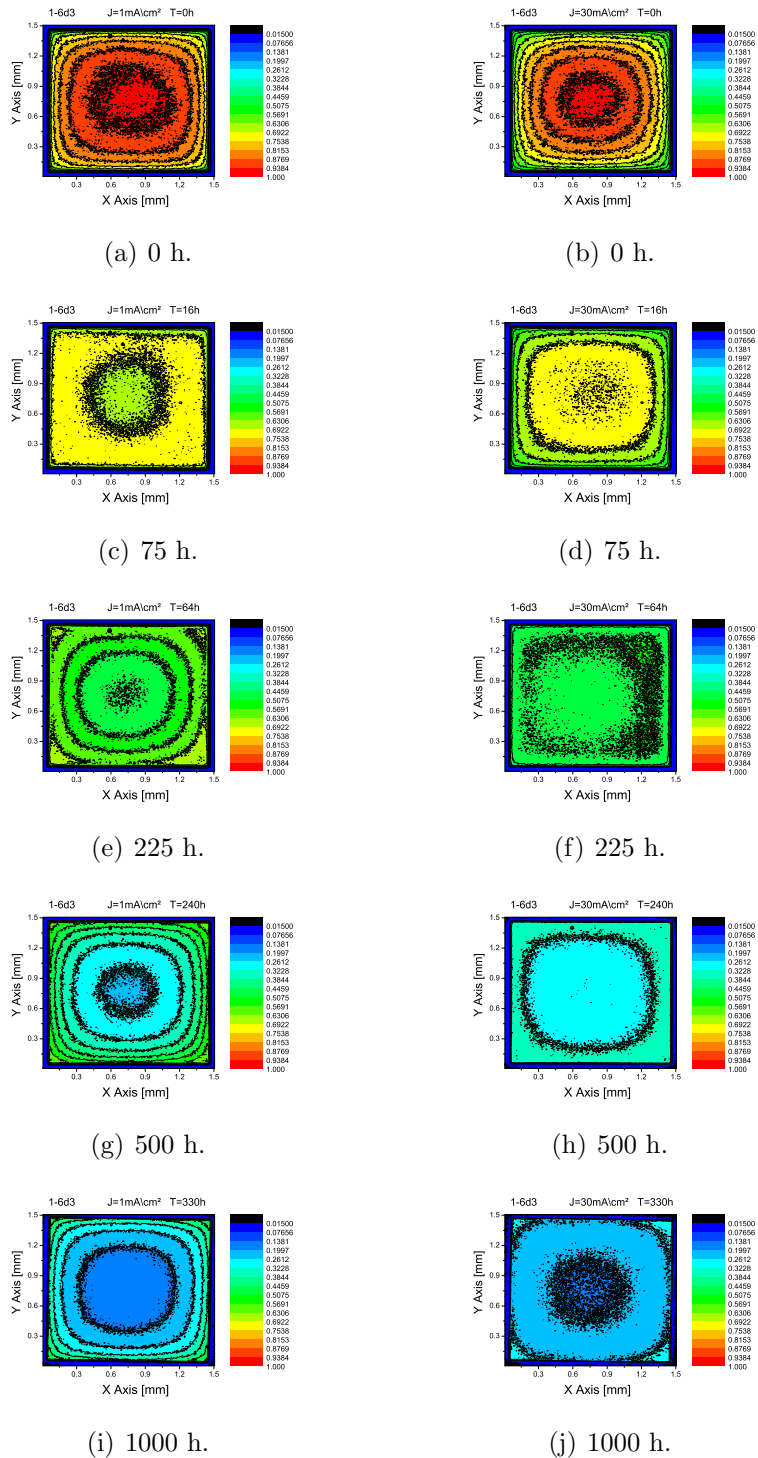


Figure 6.24: Light emission profile for woHIL OLEDs submitted to CCS at 60°C read at 1 (a-c-e-g-i) and 30mA/cm^2 (b-d-f-h-l).

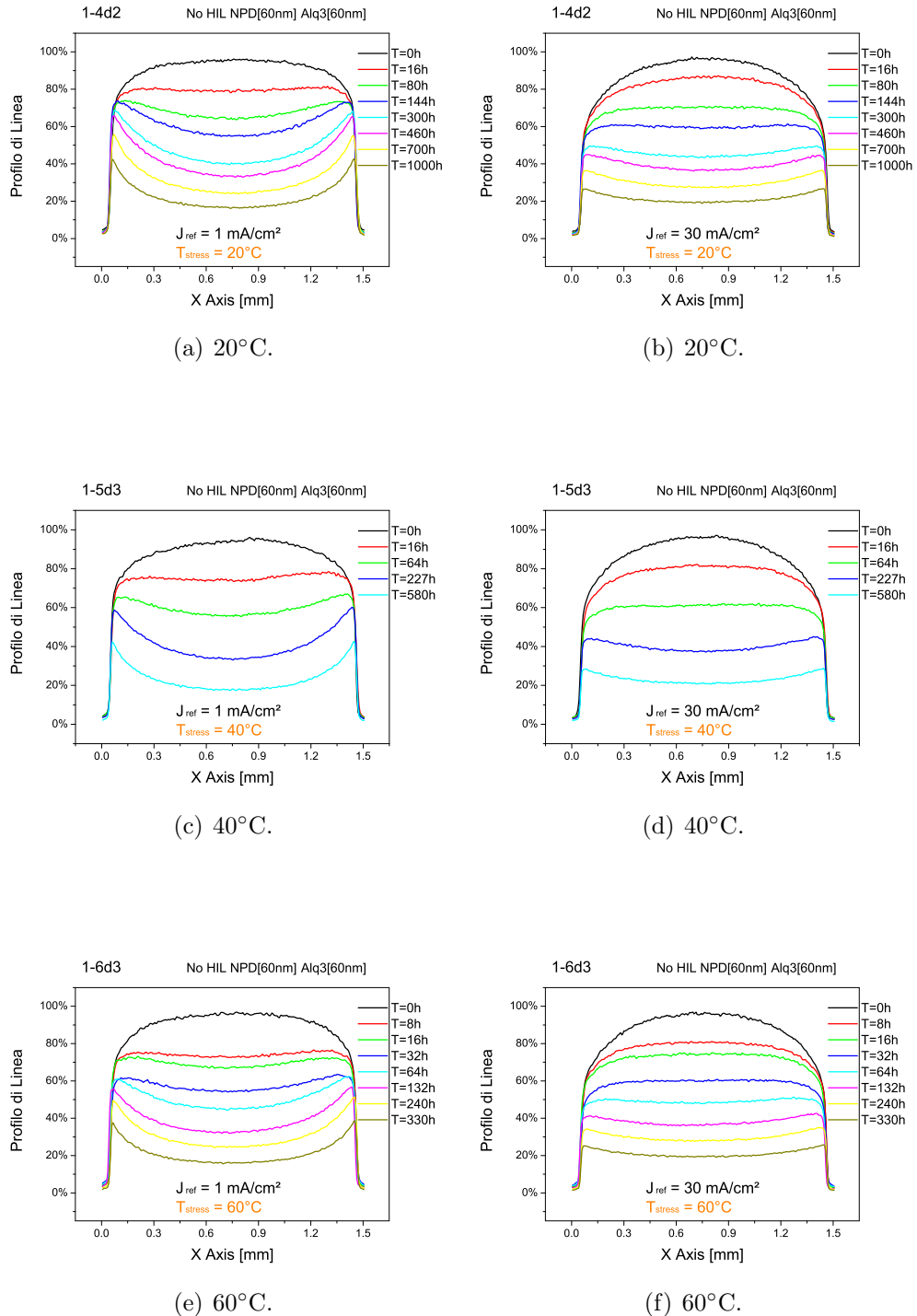


Figura 6.25: Longitudinal light emission profile for wHIL OLEDs submitted to CCS at different temperature values read at 1 (a-c-e) and 30 mA/cm^2 (b-d-f).

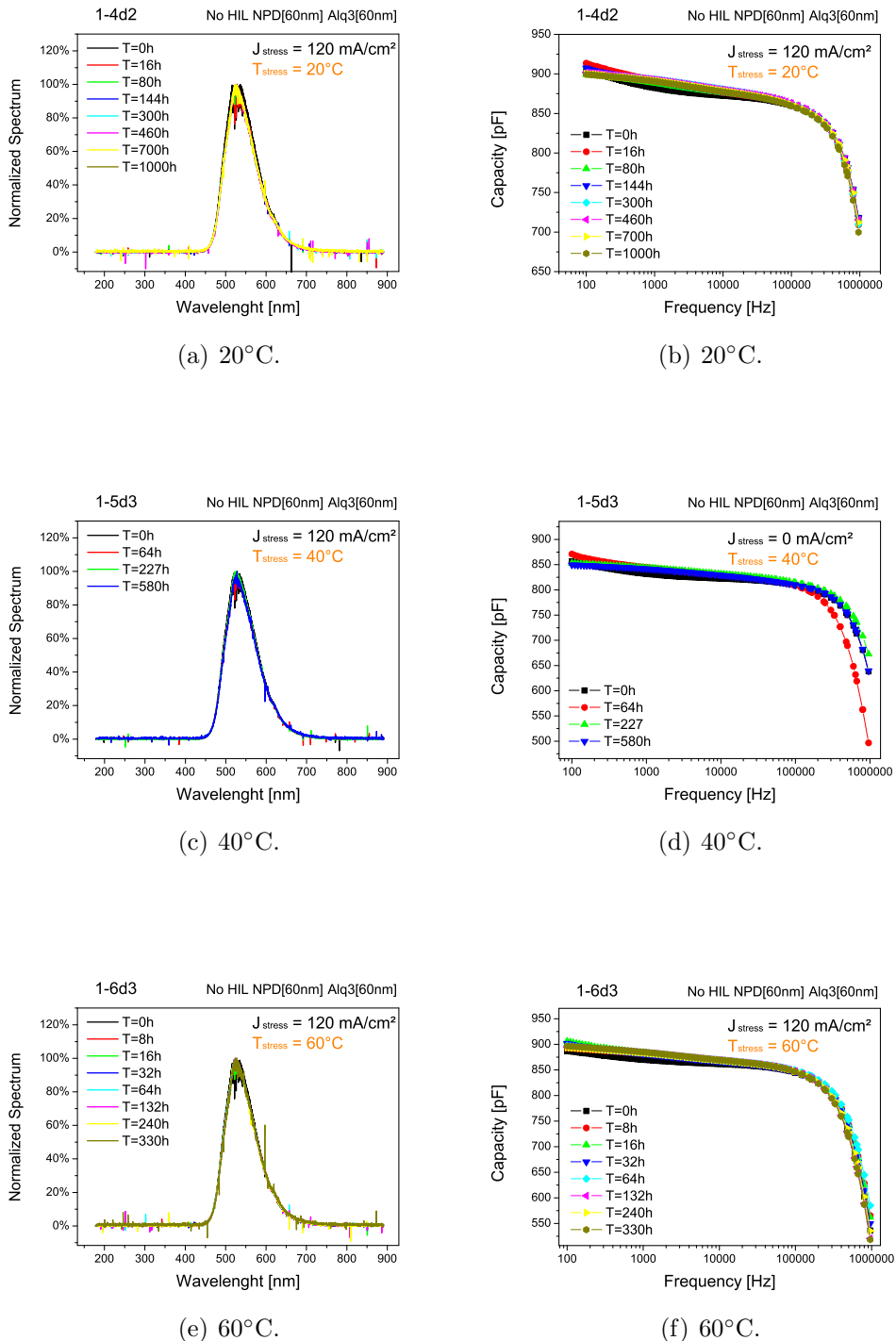


Figure 6.26: Optical power spectral distribution and C-F characteristics for woHIL OLEDs submitted to CCS at different temperature values.

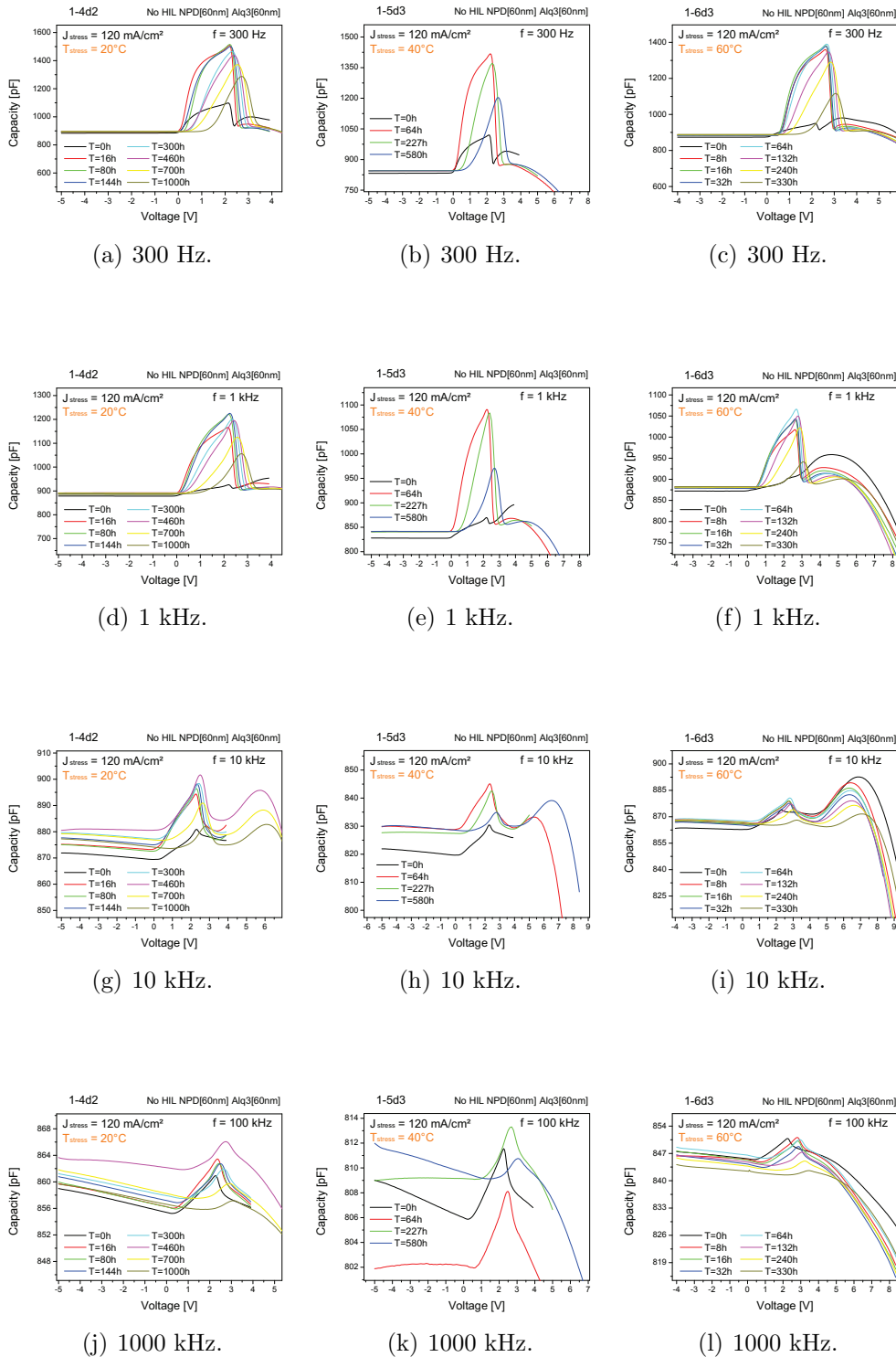


Figure 6.27: C-V characteristics for woHIL OLEDs submitted to CCS at 20 (a-d-g-l), 40 (b-e-h-m) and 60°C (c-f-i-n) at different frequencies.

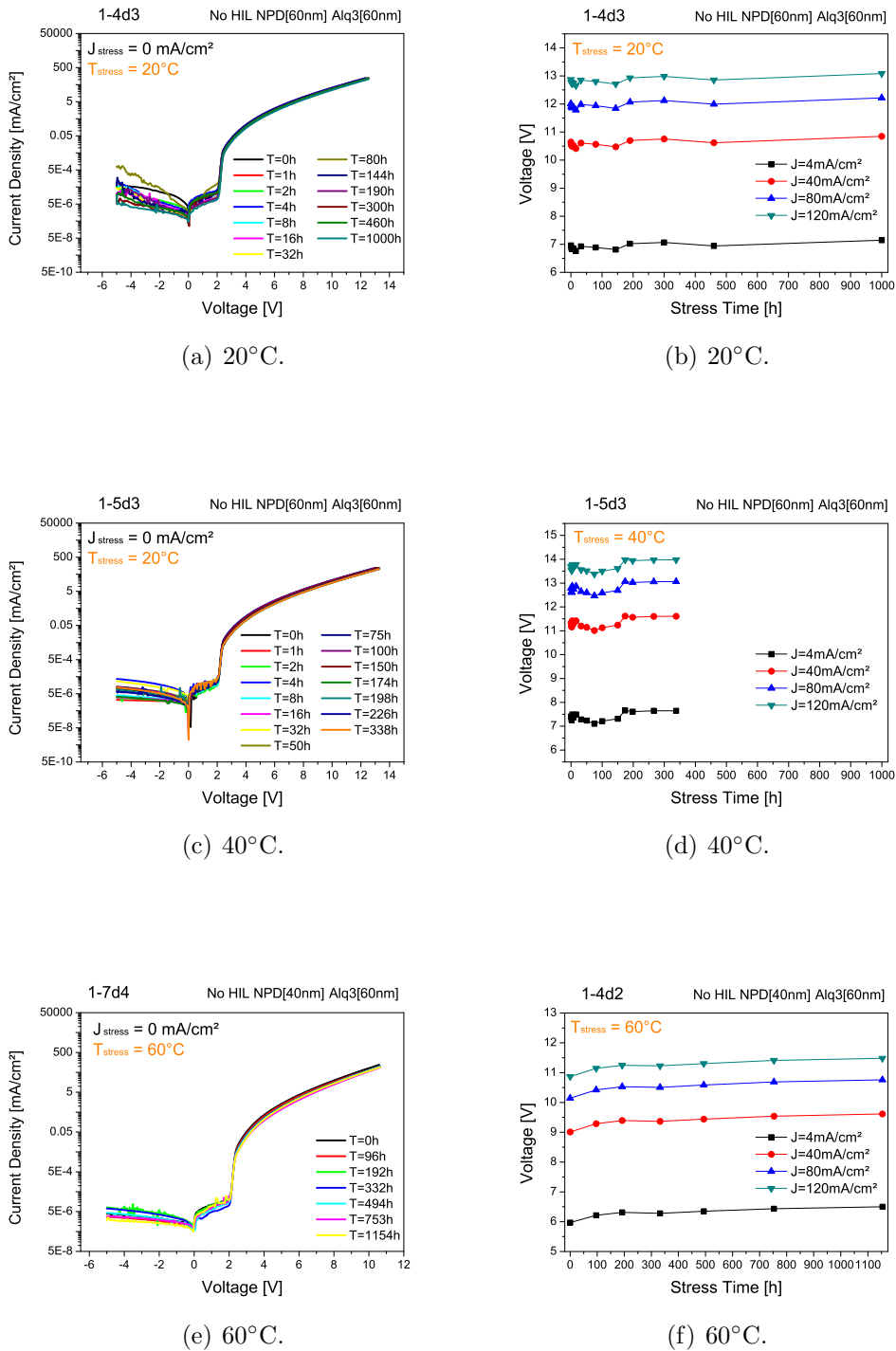
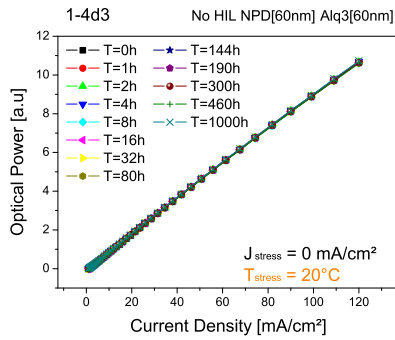
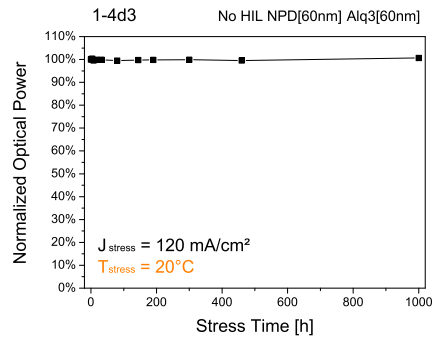


Figure 6.28: I-V characteristics (a-c-e) and voltage-time characteristics (b-d-f) for woHIL OLEDs not submitted to CCS at different temperature values.

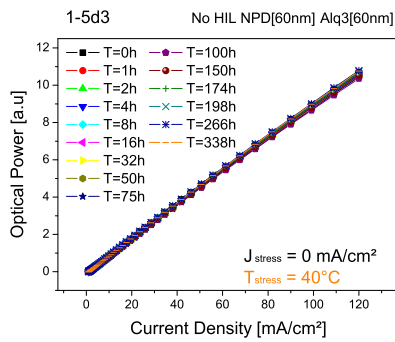
OLEDs not submitted to CCS at different temperature values



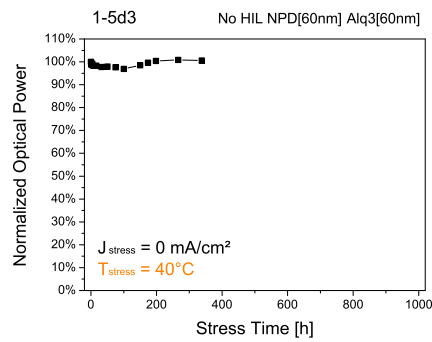
(a) 20°C.



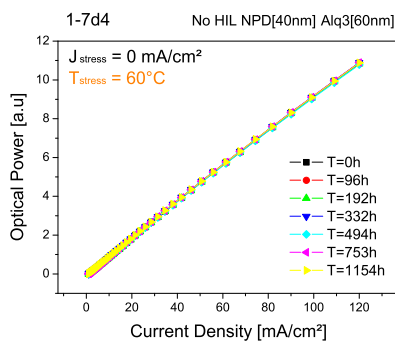
(b) 20°C.



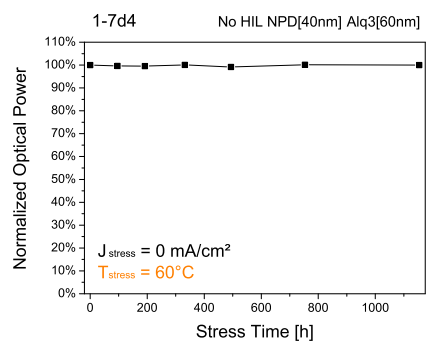
(c) 40°C.



(d) 40°C.



(e) 60°C.



(f) 60°C.

Figura 6.29: L-I characteristics (a-c-e) and optical power degradation read at 120 mA/cm^2 (b-d-f) of woHIL OLEDs not submitted to CCS at different temperature values.

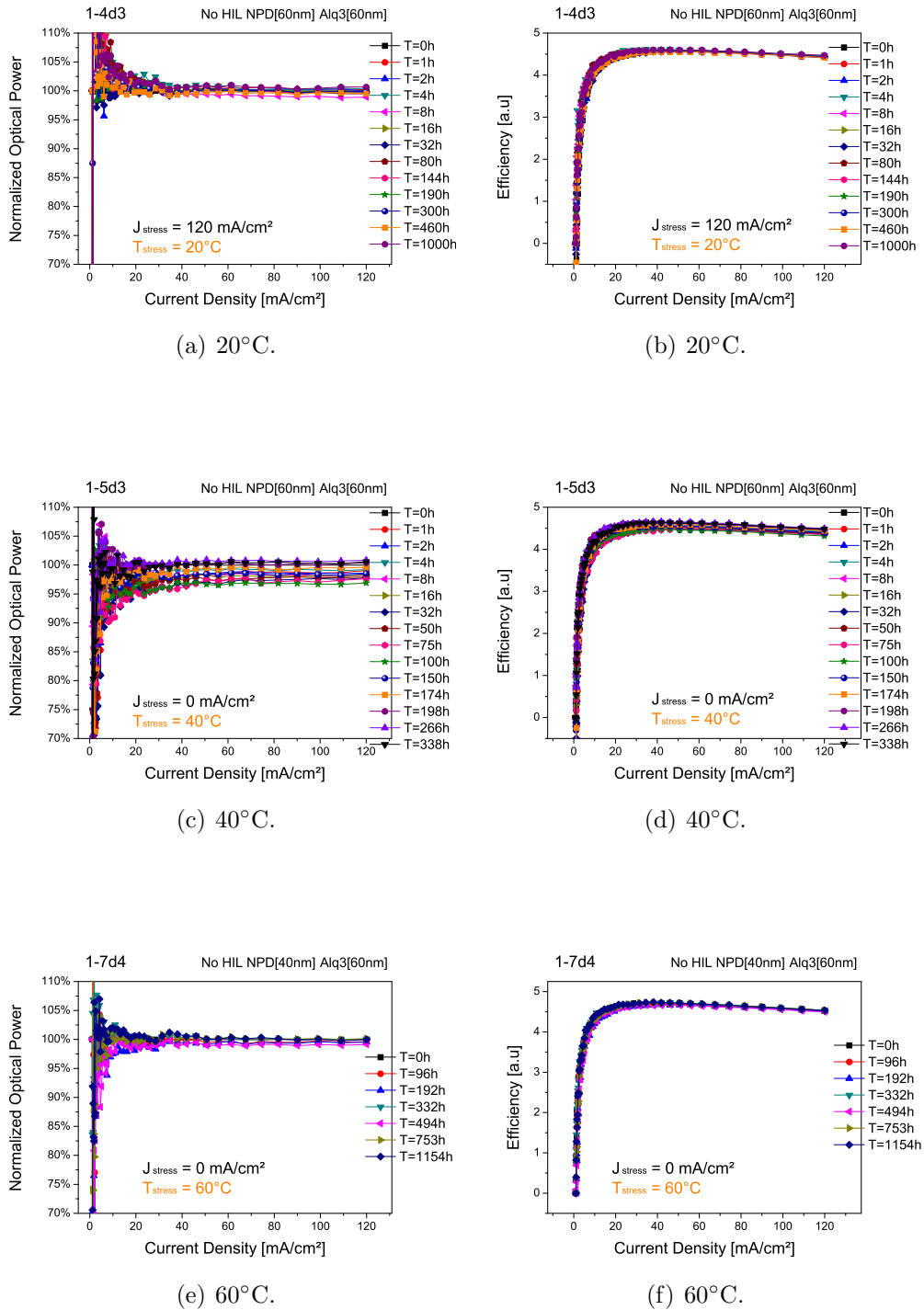


Figure 6.30: Normalized optical power degradation (a-c-e) and efficiency (b-d-f) of woHIL OLEDs not submitted to CCS at different temperature values.

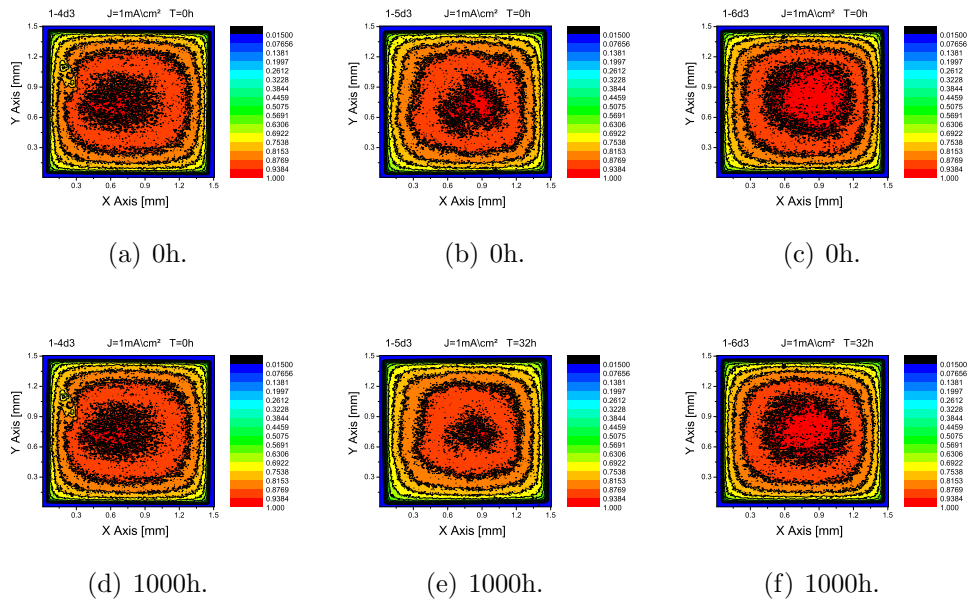


Figure 6.31: Light emission profile for wHIL OLEDs not submitted to CCS at 20 (a-d), 40 (b-e) and 60°C (c-f) read at 1 mA/cm².

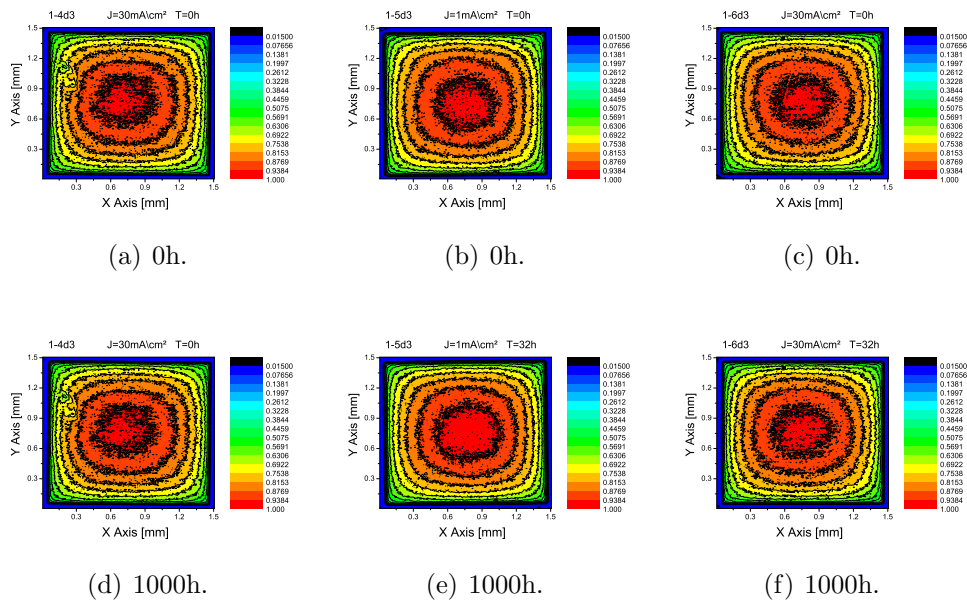


Figure 6.32: Light emission profile for wHIL OLEDs not submitted to CCS at 20 (a-d), 40 (b-e) and 60°C (c-f) read at 30 mA/cm².

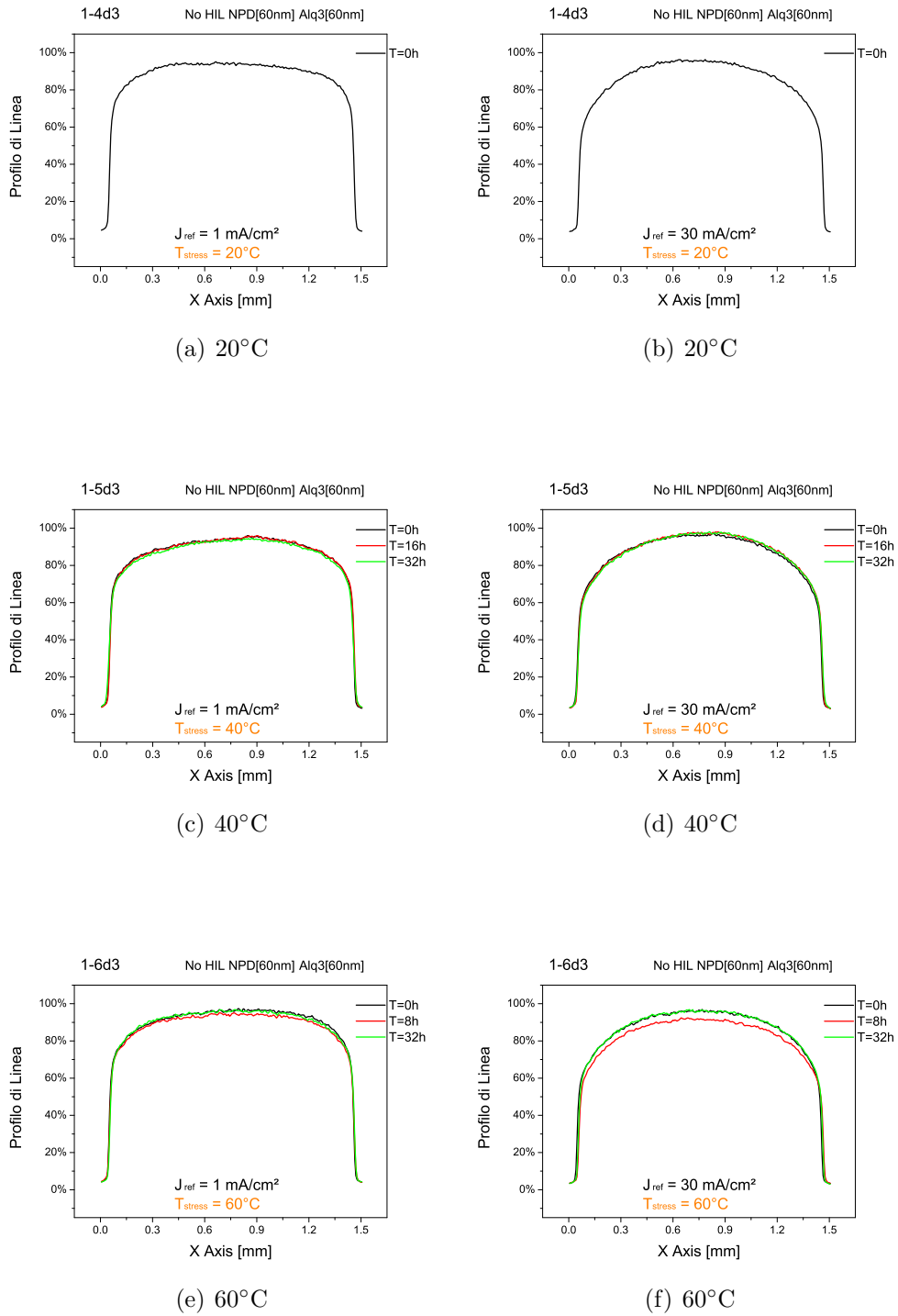


Figura 6.33: Longitudinal light emission profile for woHIL OLEDs not submitted to CCS read at 1 (a-c-e) and 30 mA/cm² (b-d-f).

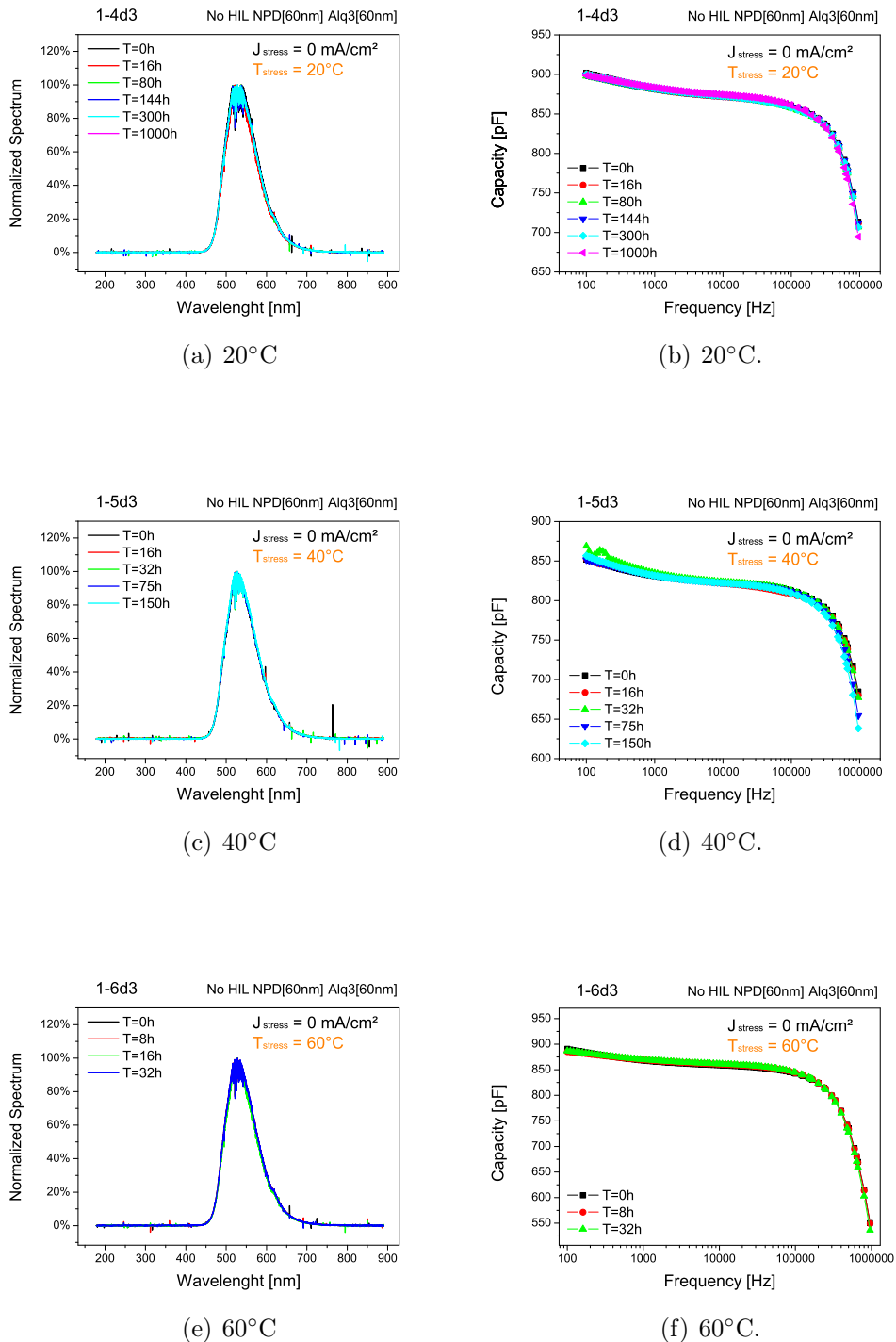


Figure 6.34: Optical power spectral distribution (a-c-e) and C-F characteristics (b-d-f) of woHIL OLEDs not submitted to CCS at different temperature values.

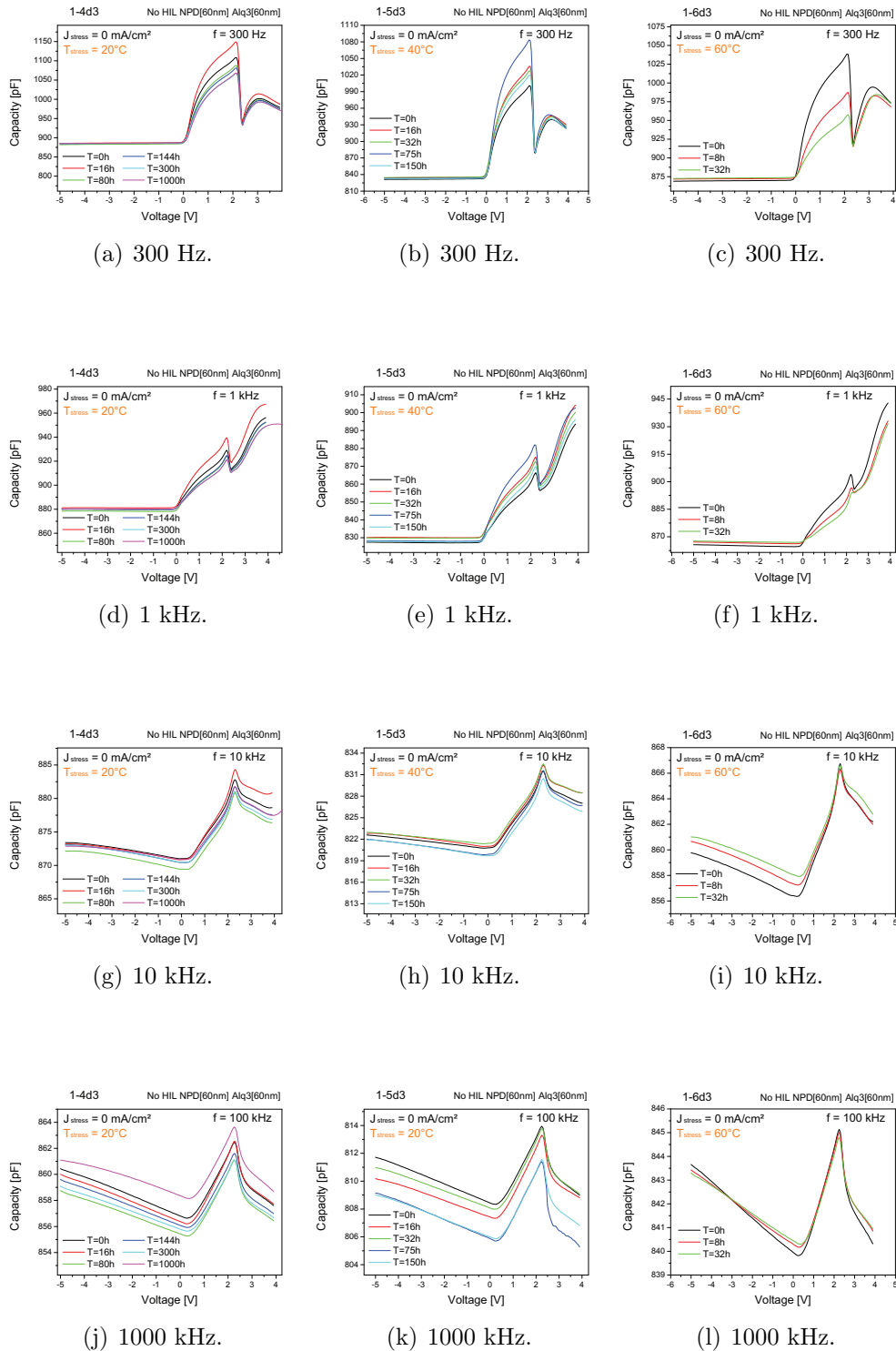


Figure 6.35: C-V characteristics for woHIL OLEDs submitted to CCS at 20 (a-d-g-l), 40 (b-e-h-m) and 60°C (c-f-i-n) at different frequencies.

6.3 Electrical stress for OLED with HIL at different current

In order to have a wider picture of which can be the conditions that lead to an accelerate OLEDs degradation, we also performed a constant temperature stress (CTS) at 20°C on OLEDs submitted to different current density values: $J = 80\text{-}120\text{-}160 \text{ mA/cm}^2$ (in Section 6.1 we have already discussed the middle case). We decided to use wHIL OLEDs for this study, being stronger than woHIL OLEDs and thus more usable and suitable for future uses including commercial. Hence, we carried out all the same characterizations already described before and after stressing a new set of OLEDs with the HIL. As we expected, we found the same general degradation behavior of wHIL OLEDs submitted to CCS at different temperature, where, increasing the temperature (in this case the current density) results in a higher degradation rate.

We carried out the same experiments also on OLED without the HIL. Figures 6.36 (a-c-e) and 6.36 (b-d-f) show the degradation of the J-V curves and the voltage-time characteristics, respectively, during CCS at 20-40-60°C, whereas, Figures 6.37 (a-c-e) and 6.37 (b-d-f) show the corresponding optical power degradation and normalized optical power degradation read at 120 mA/cm². These degradation kinetics and all the others kinetics (LEP, longitudinal LEP, shape, C-F, C-V) follow the same trend described so far where at an increase of the current value corresponds an increase of the degradation of the others electrical and optical parameter.

6.3.1 Reference graphs

OLEDs submitted to CCS at different temperature values

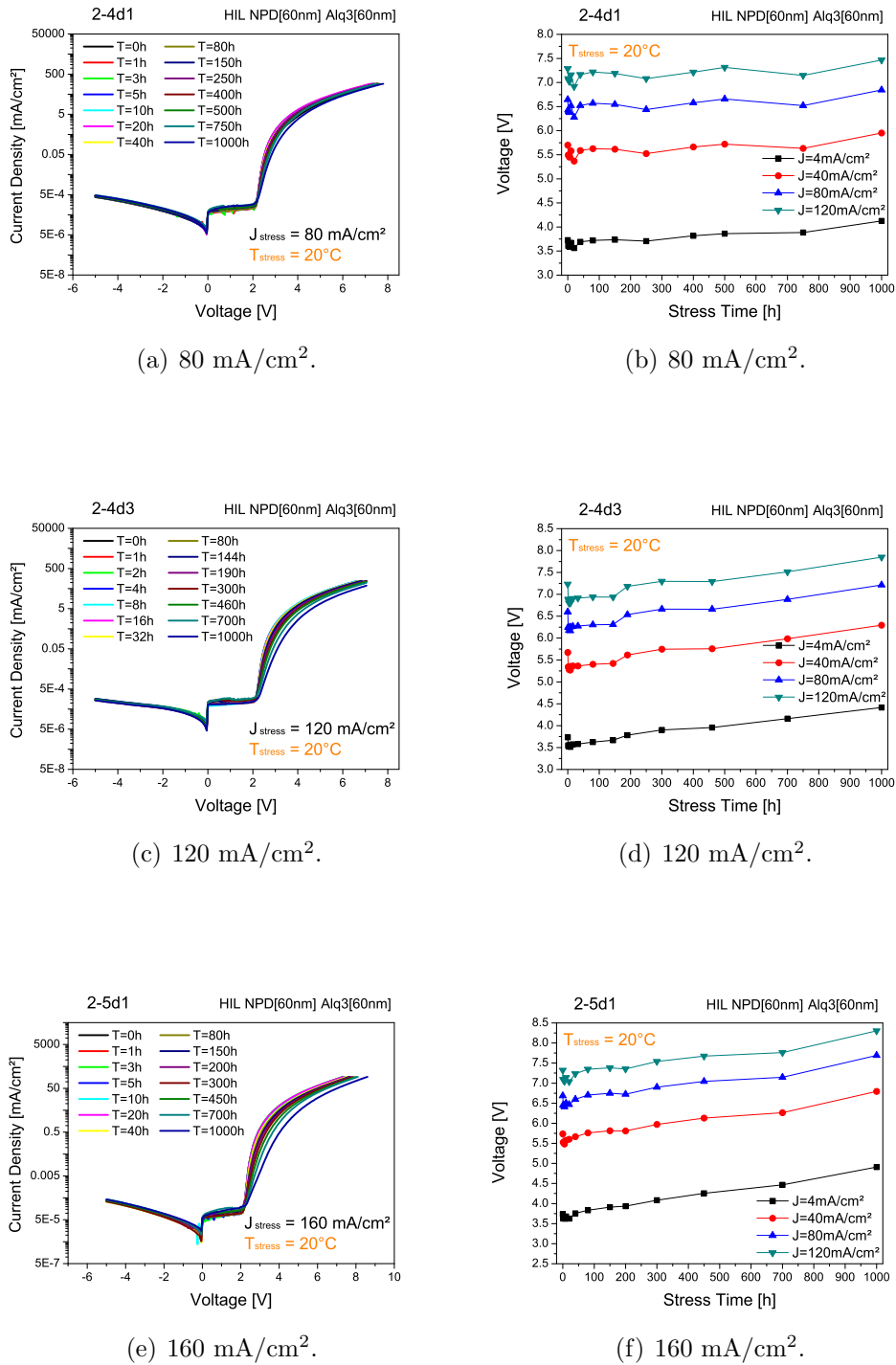
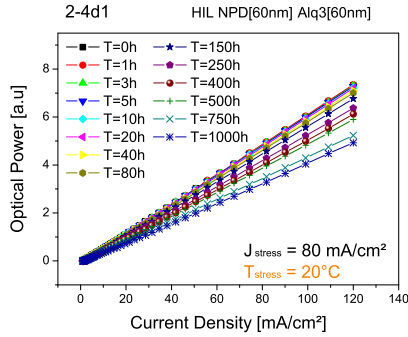
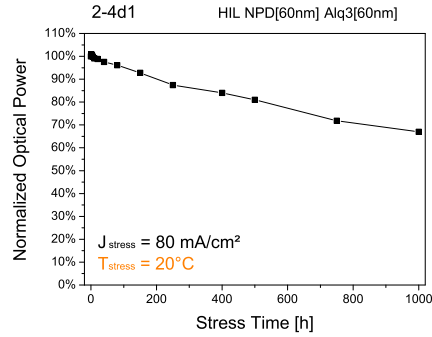


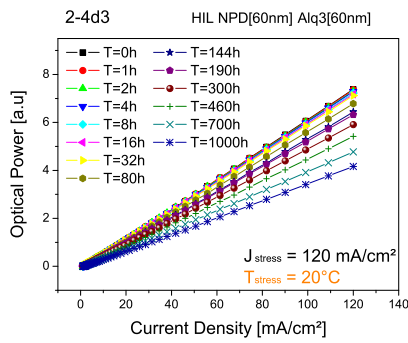
Figure 6.36: I-V characteristics (a-c-e) and voltage-time characteristics (b-d-f) of wHIL OLEDs submitted to CTS at different current values.



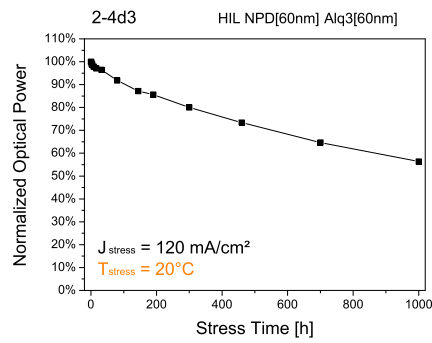
(a) 80 mA/cm².



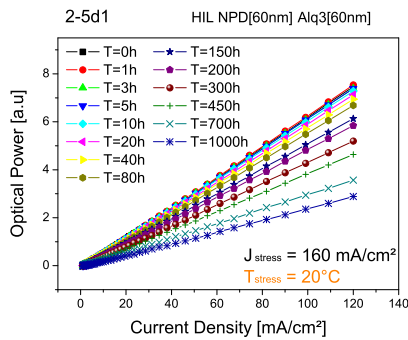
(b) 80 mA/cm².



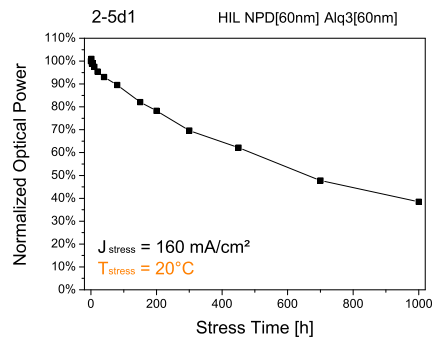
(c) 120 mA/cm².



(d) 120 mA/cm².



(e) 160 mA/cm².



(f) 160 mA/cm².

Figura 6.37: L-I characteristics (a-c-e) and optical power degradation read at 120 mA/cm² (b-d-f) of wHIL OLEDs submitted to CTS at different current values read at 120 mA/cm².

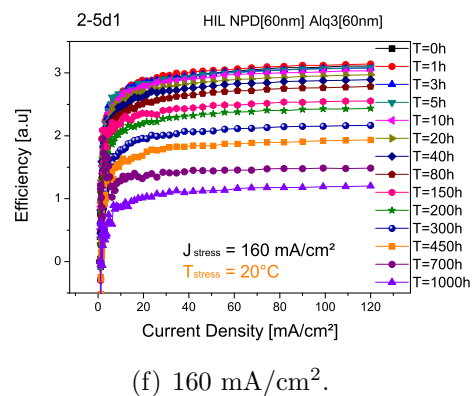
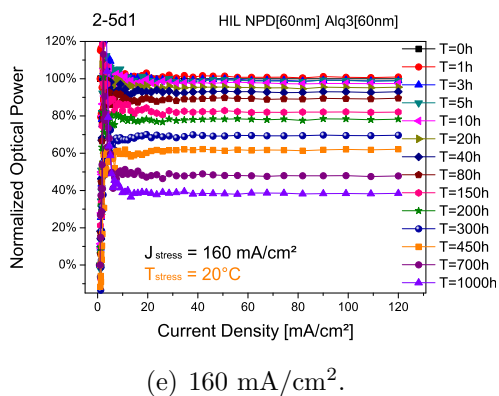
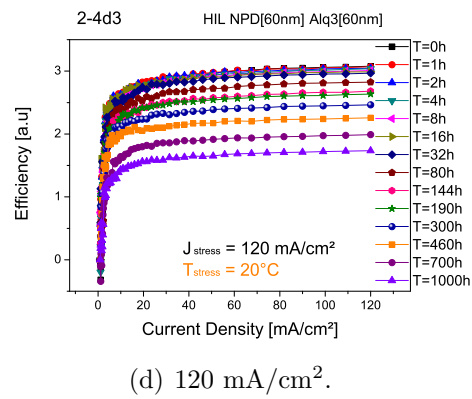
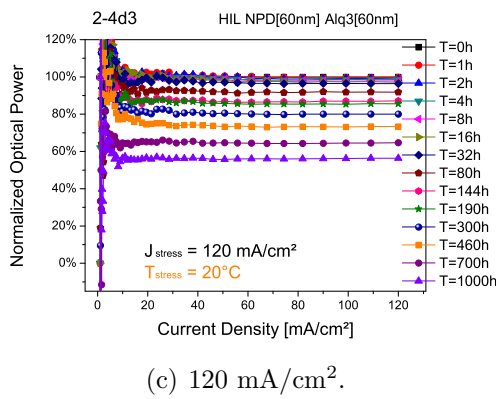
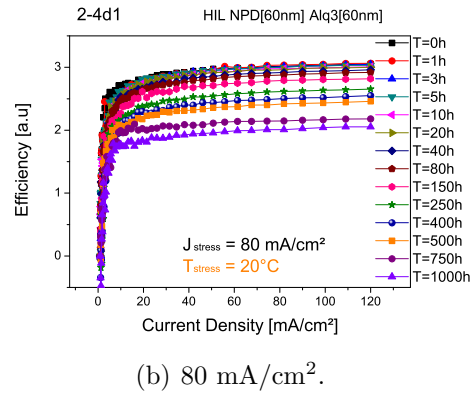
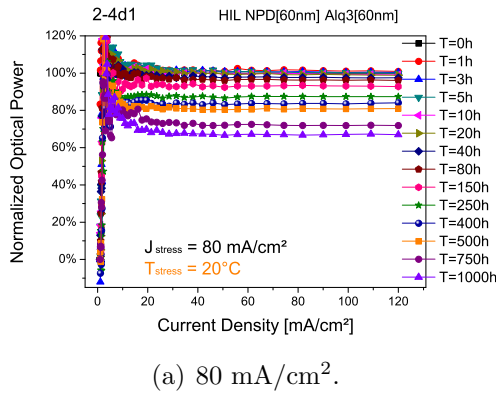


Figure 6.38: Normalized optical power degradation (a-c-e) and efficiency (b-d-f) of wHIL OLEDs submitted to CTS at different current values.

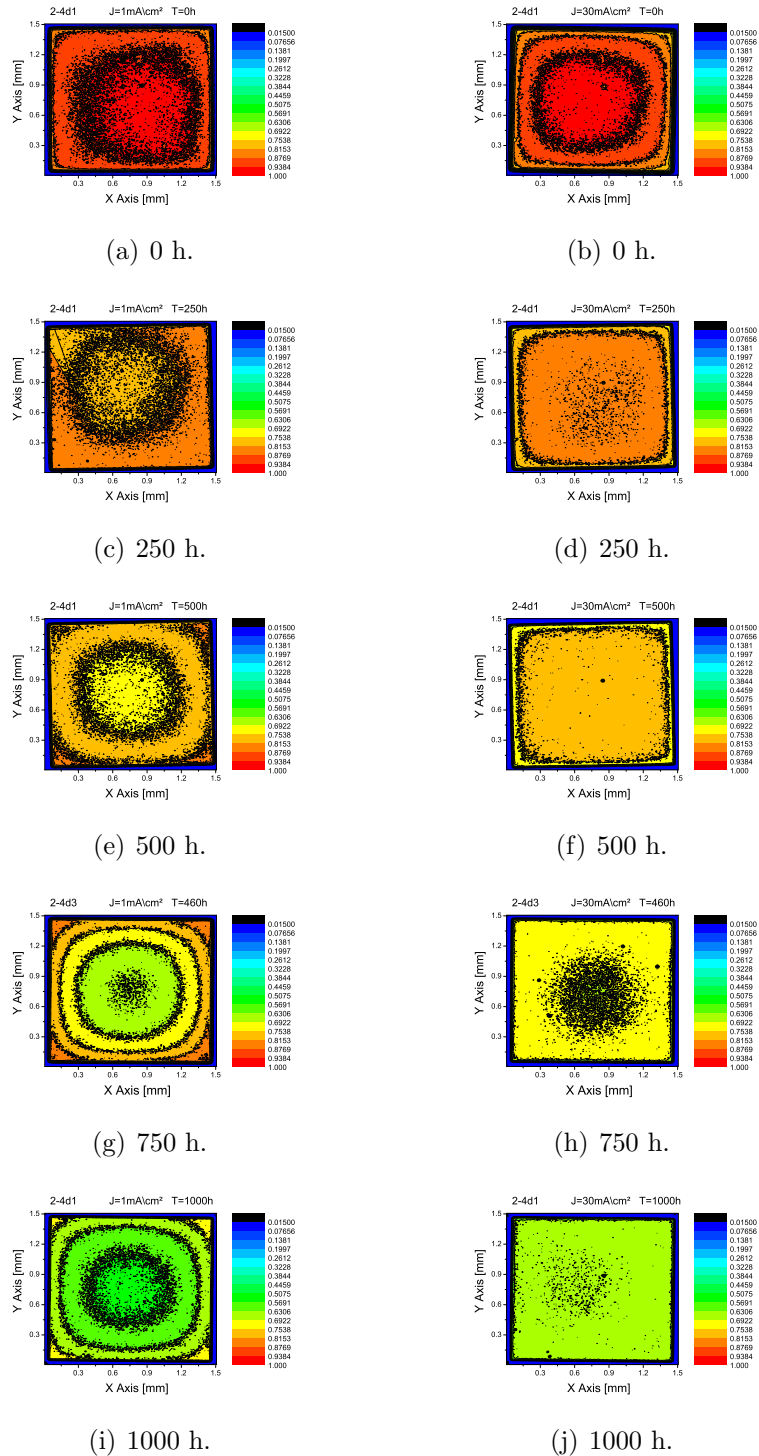


Figure 6.39: Light emission profile of wHIL OLEDs submitted to CTS at 80 mA/cm² read at 1mA/cm² (a-c-e-g-i) and 30mA/cm² (b-d-f-h-l).

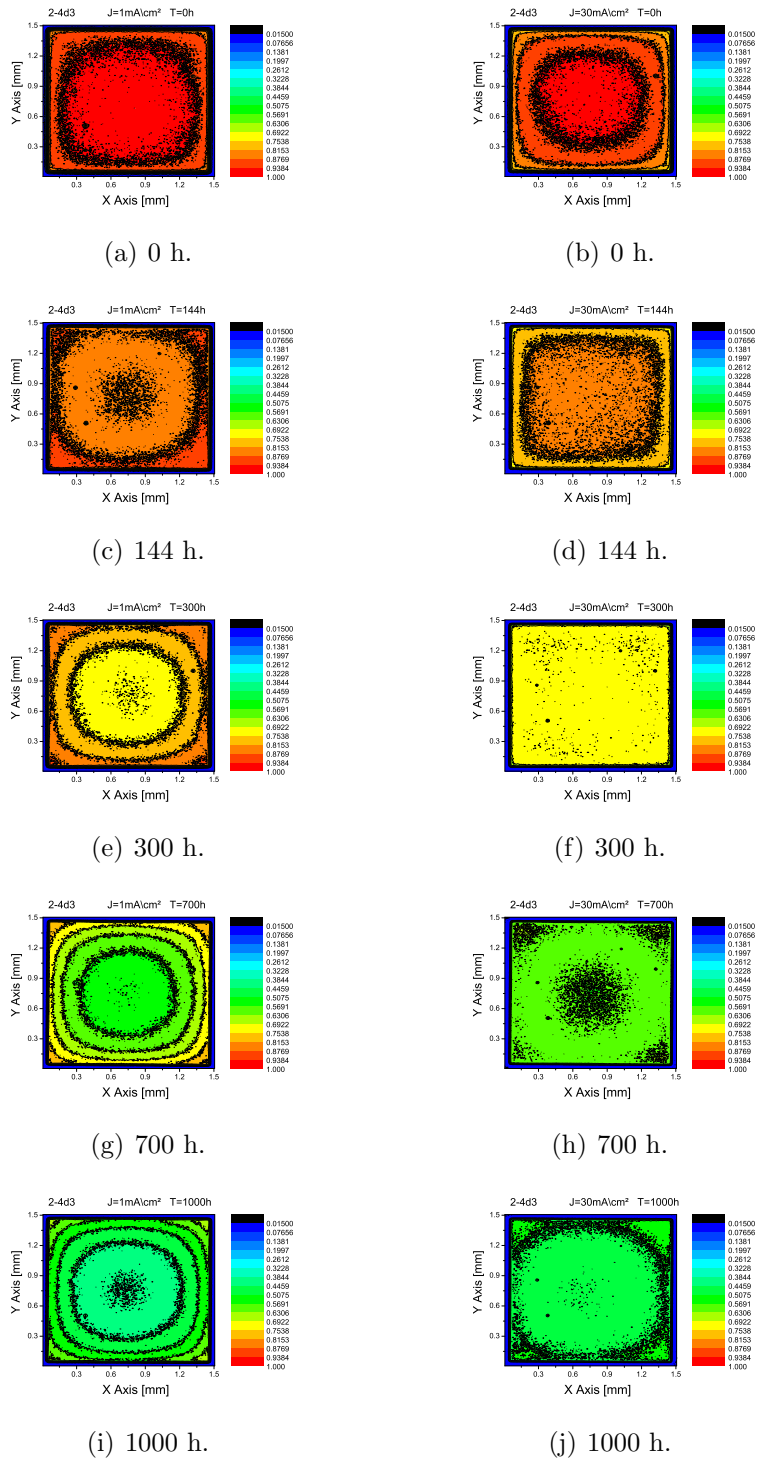


Figure 6.40: Light emission profile of wHIL OLEDs submitted to CTS at 120 mA/cm^2 read at 1mA/cm^2 (a-c-e-g-i) and 30mA/cm^2 (b-d-f-h-l).

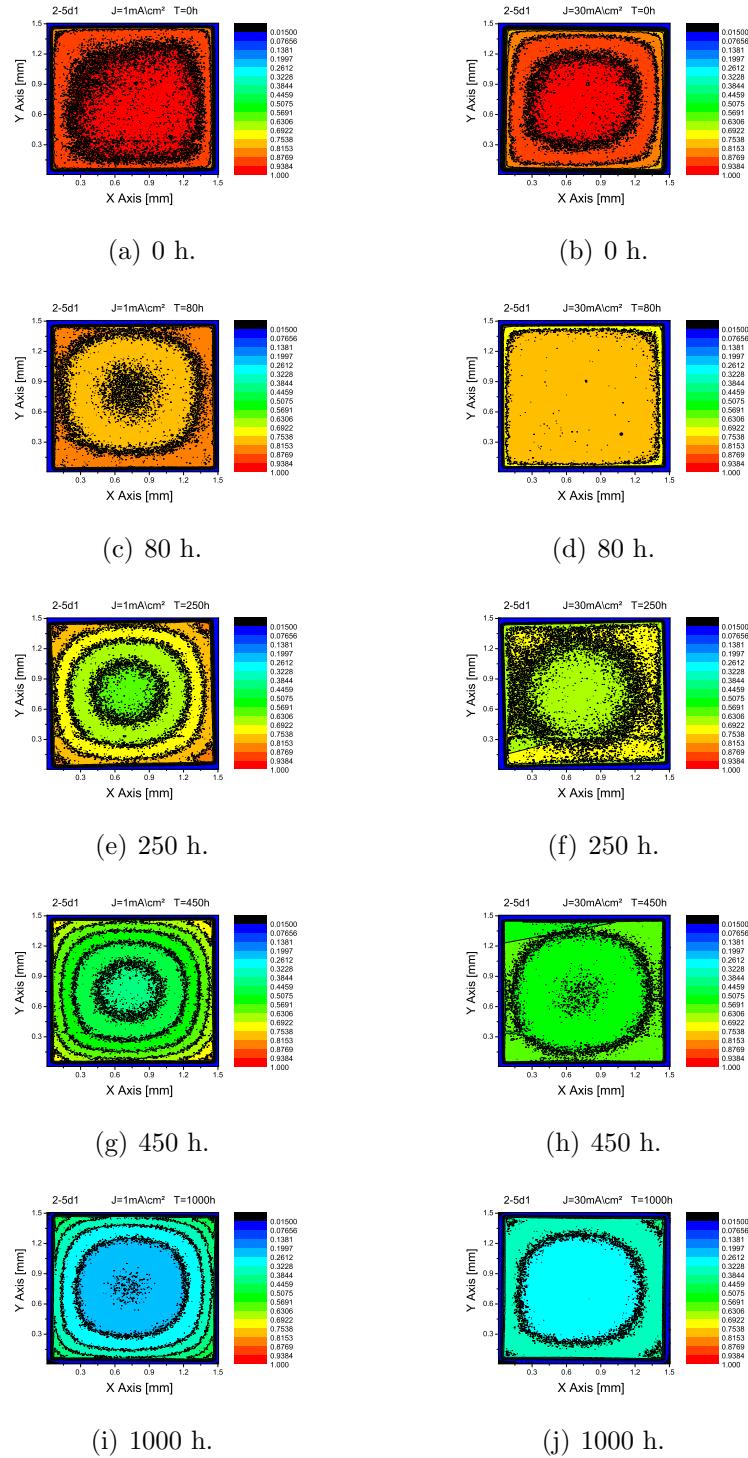


Figure 6.41: Light emission profile of wHIL OLEDs submitted to CTS at 160 mA/cm^2 read at 1mA/cm^2 (a-c-e-g-i) and 30mA/cm^2 (b-d-f-h-l).

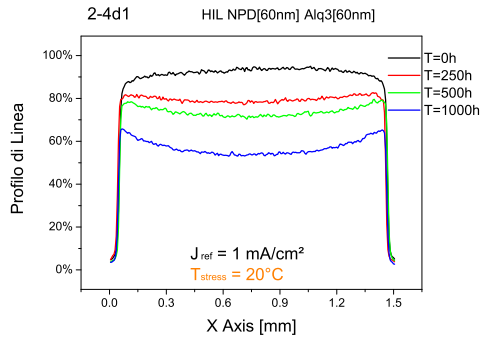
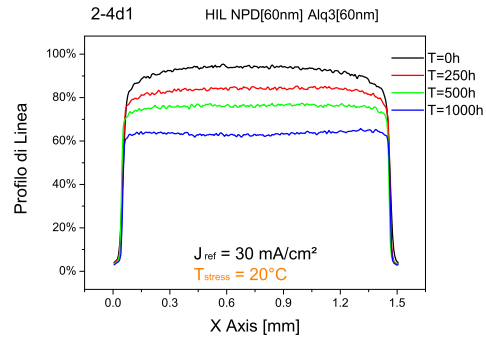
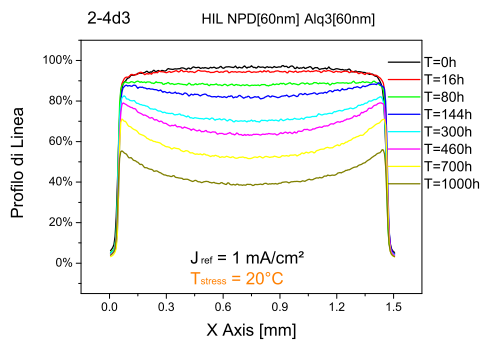
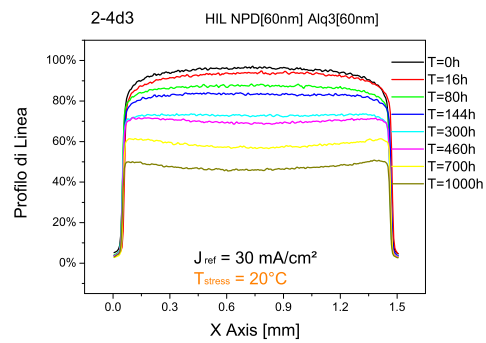
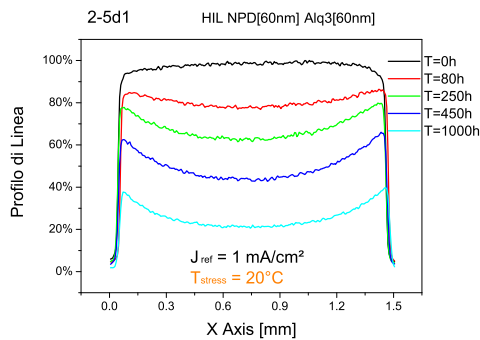
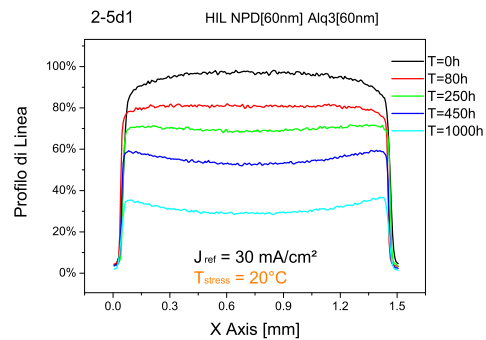
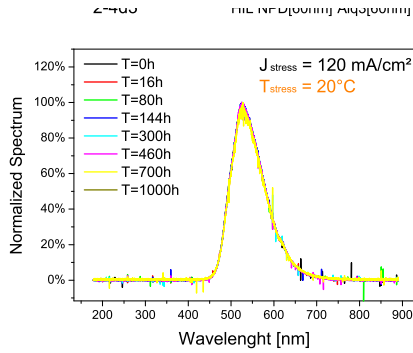
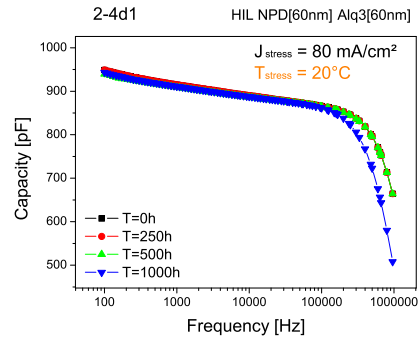
(a) 80 mA/cm^2 .(b) 80 mA/cm^2 .(c) 120 mA/cm^2 .(d) 120 mA/cm^2 .(e) 160 mA/cm^2 .(f) 160 mA/cm^2 .

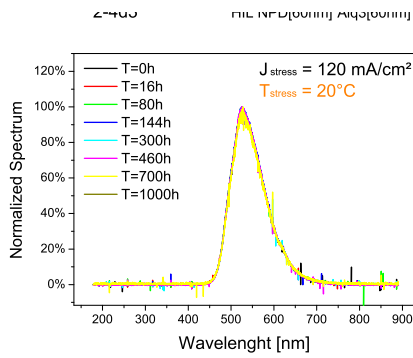
Figura 6.42: Longitudinal light emission profile of wHIL OLEDs submitted to CTS at different current values read at 1 (a-c-e) and 30 mA/cm^2 (b-d-f).



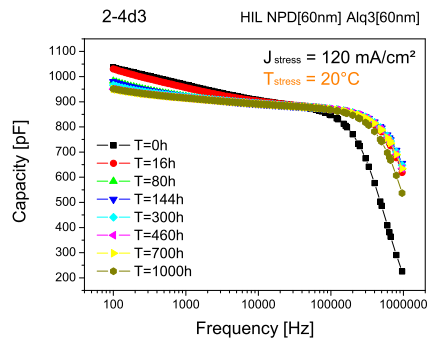
(a) 80 mA/cm².



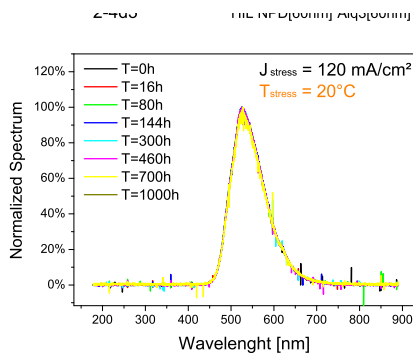
(b) 80 mA/cm².



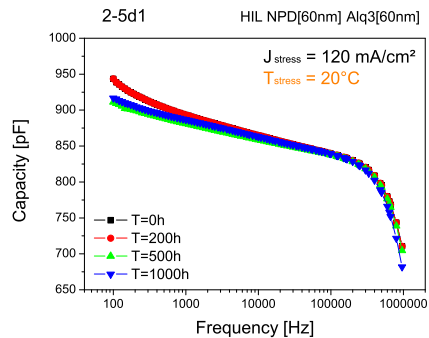
(c) 120 mA/cm².



(d) 120 mA/cm².



(e) 160 mA/cm².



(f) 160 mA/cm².

Figura 6.43: Optical power spectral distribution (a-c-e) and C-F characteristics (b-d-f) of wHIL OLEDs submitted to CTS at different current values.

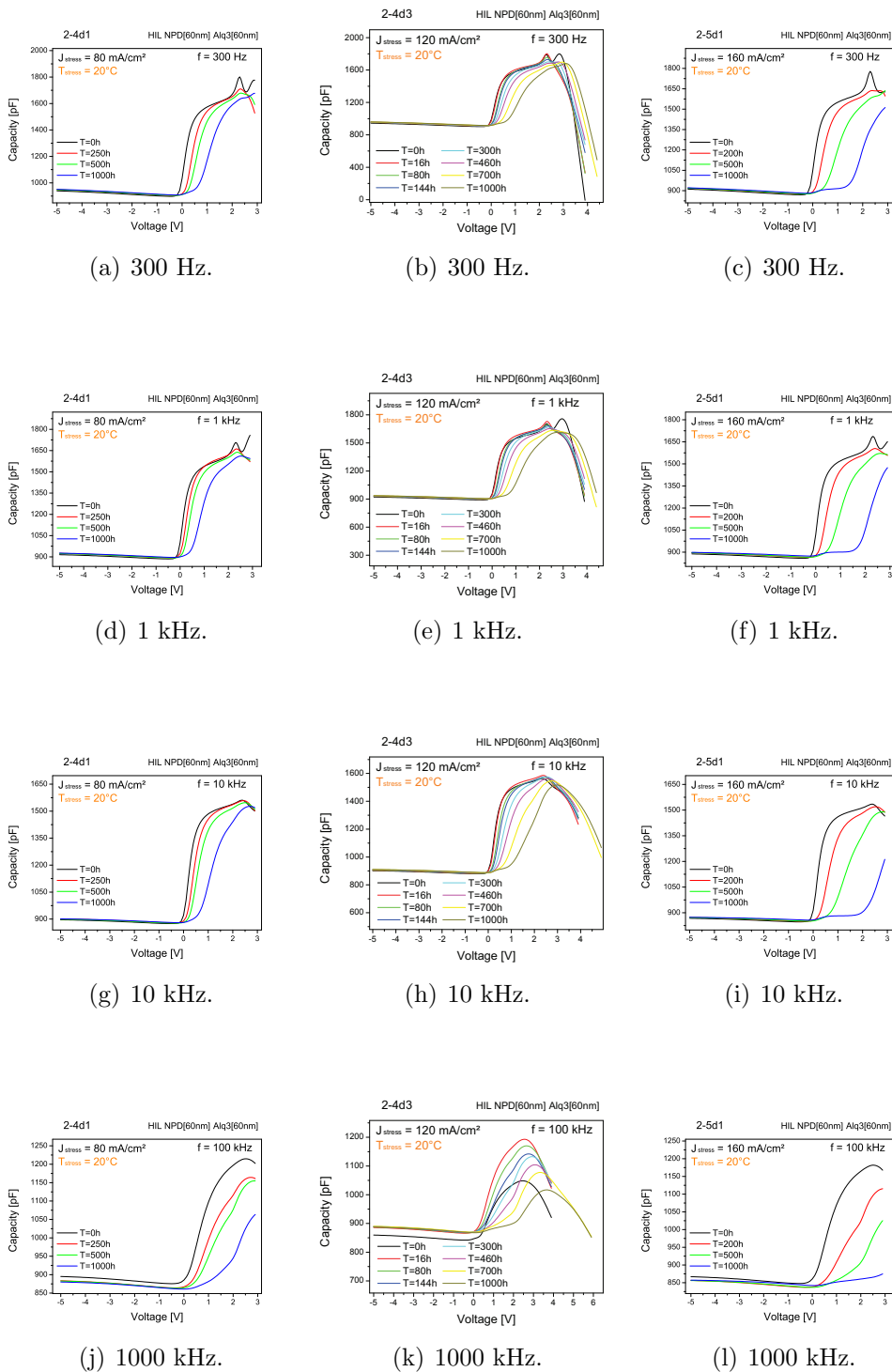


Figure 6.44: C-V characteristics of wHIL OLEDs submitted to CTS at 80 (a-d-g-l), 120 (b-e-h-m) and 160 mA/cm² (c-f-i-n) at different frequencies.

6.4 Comparison and comments

6.4.1 Thermal stress

As shown in Figures 6.45, OLEDs submitted to thermal stress where CCS is not applied, do not show degradation respect to the biased ones. From this, we can conclude that temperature alone is not a degradation factor. Instead, it is an acceleration factor in degradation process when bias is applied which increase going toward higher temperature values.

6.4.2 OLEDs with vs OLEDs without HIL

OLEDs with hole injection layer reveal to be stronger and more reliable than OLEDs without HIL. Even though seems that woHIL OLEDs had an improvement in the voltage-time (Figure 6.46b), we have to consider that, the latter, are submitted to higher operating voltage (about twice than wHIL OLEDs). This lead to a higher electric field which means that the electrons are injected with an higher energy increasing the probability of lattice damages and overheating of the devices, revealing its weak internal structure then confirmed by the rupture of some devices. In Figure 6.46a is reported a comparison between the optical power degradation of wHIL and woHIL OLEDs which confirm as just said.

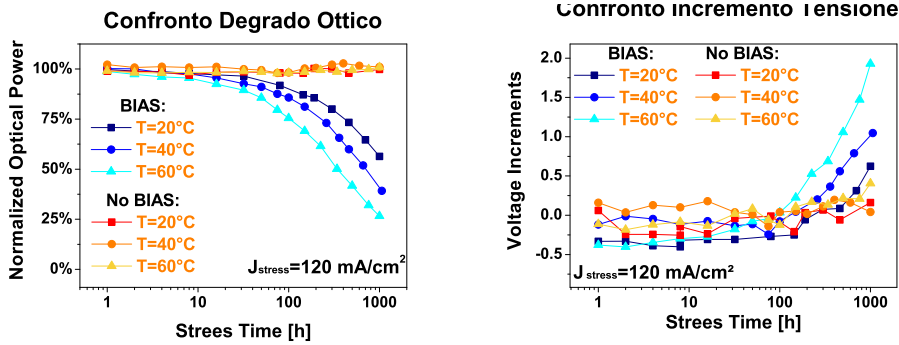
Hence, we have found that the hole injection layer (HIL) is a valid choice for the construction of long-lived devices, with lower consumption and a higher efficiency.

6.4.3 OLEDs with HIL submitted to different current

The analysis of wHIL OLEDs submitted to different current values revealed some interesting results. As we expected the degradation kinetics follow the same trend of OLEDs submitted to CCS ones, showing a increase in degradation with increasing the current values (Figure 6.47a). Increasing the current also the electric field increased. This means, that the carrier will be injected with an higher energy that may lead further degradation process, due to lattice damages or to the overheating of the device. As just said in the previous sections, a temperature increase lead to a increased carrier mobility, specially in the device center area where heat dissipation is more difficult. Thus, the central area degradation is further accelerated.

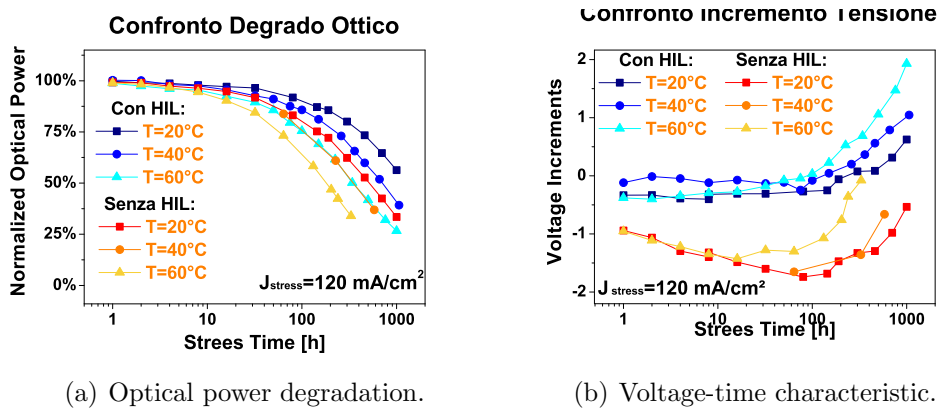
From Figure 6.47b seems that increasing of the current value do not lead to a further degradation process, indeed the curves are for the most part overlapped. But, if we consider the higher current value (160 mA/cm^2), we can notice that, at a certain point of injected charge, the green curve start to separate from the others two. This reveal that the degradation is not only due to the amount of injected charge, but there is also a further

degradation due to the higher energy of the carrier which accelerate the device degradation process.



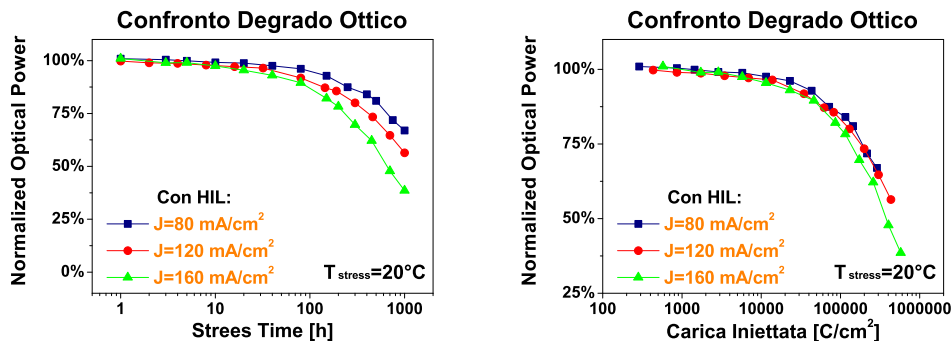
(a) Optical power of thermal stressed devices vs devices submitted to CCS. (b) Voltage-time characteristic thermal stressed devices vs devices submitted to CCS.

Figure 6.45: wHIL OLEDs submitted to CCS vs wHIL OLEDs submitted to thermal stress.



(a) Optical power degradation. (b) Voltage-time characteristic.

Figure 6.46: wHIL OLEDs vs woHIL OLEDs submitted to CCS.



(a) Optical power degradation of wHIL OLEDs. (b) Optical power degradation as function of the injected charge of wHIL OLEDs.

Figure 6.47: wHIL OLEDs submitted to different current values at constant temperature.

Conclusions

In this thesis we have investigated the reliability of two sets of small-molecule OLEDs with simplified structure. The first set consisting of NPD as HTL, Alq₃ as ETL, whereas the second one present the same HTL and ETL composition with a further hole injection layer (HIL) between NPD and ITO electrode used to enhance the hole injection. In order to evaluate the role of temperature in the degradation process, we have carried out specific thermal-electrical stress, at different temperature values and constant current, from which we have experienced which the presence of the HIL improve the reliability and longevity of the devices under test. The degradation kinetics of both sets showed a similar trend, with a more marked deterioration in those devices which did not use the HIL.

Thus, for all devices, we showed a remarkable decrease during constant current stress with neither catastrophic breakdown nor the formation of dark spots. From a preliminary analysis of the emission microscopy images taken before and after stress, we observe a much stronger degradation of the luminescence in the center of the device, with respect to the corners/borders. These results are compatible with a significant current and emission crowding that may determine also a stronger self-heating near the center of the device area. The changes of the electrical characteristics are correlated with the optical degradation. The nature of the stress-induced defects has been studied by a combined analysis of the I–V and C–V curve evolution during stress. The device degradation mechanisms can be tentatively explained by assuming that the constant current stress produces both a fixed interface (positive) trapped charge and a number of neutral interface states, likely correlated with the oxidation of the Alq₃. A rough estimation of the fixed trapped charge shows a good linear relation between the stress time and the amount of trapped charge.

On the basis of achieved data, we can assert that the degradation is due to the device polarization. Indeed, temperature alone is not a degradation factor but it become and accelerating factor when combined with polarization. In this latter case, we observed that degradation increase as the temperature increase.

Hence, in order to evaluate the polarization role, we also carried out further electrical stress at different current values. Data shown that, in addition of the degradation mechanism described above, the carrier injected

energy become considerable in the degradation process. Indeed, to an higher current density, corresponds and higher electrical field and thus and higher carrier energy. The carriers, once they are injected, can produce lattice damages or a further device overheating, in addition to that already described. All this leads to an accelerate degradation.

Acknowledgement

Al termine di questo elaborato desidero ringraziare il mio relatore, prof. Gaudenzio Meneghesso, che mi ha dato l'opportunità di compiere la mia attività di ricerca e tesi in uno dei campi sicuramente più all'avanguardia di questi ultimi anni.

Non di meno voglio ringraziare l'ing. Alessandro Pinato che mi ha seguito e saputo consigliare al meglio in modo professionale dandomi un contributo senza dubbio positivo per la buona riuscita del mio lavoro.

Voglio inoltre ringraziare tutto il laboratorio di microelettronica e i suoi numerosissimi componenti, dai dottorandi a tutti i tesisti e borsisti, che hanno sopportato la mia presenza per questi lunghi ma piacevoli 13 mesi, sempre pronti ad essere d'aiuto ed a scambiare un sorriso amichevole.

È poi doveroso per me ringraziare tutti coloro che mi sono stati accanto durante il percorso di studi, tutti gli amici vicini e lontani che spero saranno felici quanto lo sono io, di brindare tutti insieme per questo mio traguardo finale.

Infine, due ringraziamenti speciali vanno ai miei genitori che mi hanno sempre dimostrato la loro massima disponibilità e fiducia, e ad Elisa che non ha mai smesso di starmi vicino, aiutandomi e sostenendomi in questo importante periodo della mia vita.

Bibliografia

- [1] Alessandro Pinato, Andrea Cester, Member, Matteo Meneghini, Nicola Wrachien, Augusto Tazzoli, Sean Xia, Vadim Adamovich, Michael S. Weaver, Julie J. Brown, Enrico Zanoni and Gaudenzio Meneghesso: *Impact of Trapped Charge and Interface Defects on the Degradation of the Optical and Electrical Characteristics in NPD/Alq₃ OLEDs*.

- [2] Stefan Kappaun, Christian Slugovc and Emil J. W. List: *Phosphorescent Organic Light-Emitting Devices: Working Principle and Iridium Based Emitter Materials*.

- [3] Zakya Kafafi: *Organic Electroluminescence*

- [4] Joseph Shinar: *Organic light-emitting devices: a survey*

- [5] Wolfgang Brütting: *Physics of Organic Semiconductors*

- [6] S. C. Xia, R. C. Kwong, V. I. Adamovich, M. S. Weaver, and J. J. Brown, *OLED device operational lifetime: Insights and challenges*, in Proc. 45th Annu. IEEE Int. Rel. Phys. Symp., 2007, pp. 253–257.

- [7] V. I. Adamovich, M. S. Weaver, R. C. Kwong, and J. J. Brown, *High temperature operation and stability of phosphorescent OLEDs*, Current Appl. Phys., vol. 5, no. 1, pp. 15–18, Jan. 2005.

- [8] S. Chang, G. He, F. Chen, T. Guo, and Y. Yang, *Degradation mechanism of phosphorescent-dye-doped polymer light-emitting diodes*, Appl. Phys. Lett., vol. 79, no. 13, pp. 2088–2090, Sep. 2001.

- [9] P. Cusumano, F. Buttitta, A. Di Cristofalo, and C. Calì, *Effect of driving method on the degradation of organic light emitting diodes*,

- Synth. Met., vol. 139, no. 3, pp. 657–661, Oct. 2003.
- [10] P. N. M. dos Anjos, H. Aziz, N. Hu, and Z. D. Popovic, *Temperature dependence of electroluminescence degradation in organic light emitting devices without and with a copper phthalocyanine buffer layer*, Organ. Electron., vol. 3, no. 1, pp. 9–13, Mar. 2003.
- [11] H. Aziz, Z. D. Popovic, N. Hu, A. Hor, and G. Xu, *Degradation mechanism of small molecule based organic light-emitting devices*, Science, vol. 283, no. 5409, pp. 1900–1902, Mar. 1999.
- [12] D. Y. Kondakov, W. C. Lenhart, and W. F. Nichols, *Operational degradation of organic light-emitting diodes: Mechanism and identification of chemical products*, J. Appl. Phys., vol. 101, no. 2, p. 024 512, Jan. 2007.
- [13] S. Scholza, C. Corten, K. Walzer, D. Kuckling, and K. Leo, *Photochemical reactions in organic semiconductor thin films*, Organ. Electron., vol. 8, no. 6, pp. 709–717, Dec. 2007.
- [14] G. R. Chaji, C. Ng, A. Nathan, A. Werner, J. Birnstock, O. Schneider, and J. Blochwitz-Nimoth, *Electrical compensation of OLED luminance degradation*, IEEE Electron Device Lett., vol. 28, no. 12, pp. 1108–1110, Dec. 2007.
- [15] C. W. Tang and S. A. VanSlyke, *Organic electroluminescent diodes*, Appl. Phys. Lett., vol. 51, no. 12, pp. 913–915, Sep. 1987.
- [16] P. E. Burrows, V. Bulovic, S. R. Forrest, L. S. Sapochak, D. M. McCarty, and M. E. Thompson, *Reliability and degradation of organic light emitting devices*, Appl. Phys. Lett., vol. 65, no. 23, pp. 2922–2924, Dec. 1994.
- [17] Y. Liew, H. Aziz, N. Hu, H. Chan, G. Xu, and Z. Popovic, *Investigation of the sites of dark spots in organic light-emitting devices*, Appl. Phys. Lett., vol. 77, no. 17, pp. 2650–2652, Oct. 2000.

- [18] Y. Kim, D. Choi, H. Lim, and C. S. Ha, *Accelerated pre-oxidation method for healing progressive electrical short in organic light-emitting devices*, Appl. Phys. Lett., vol. 82, no. 14, pp. 2200–2202, Apr. 2003.
- [19] Y. Sato and H. Kanai, *Stability of organic electroluminescent diodes*, Mol. Cryst. Liquid Cryst., vol. 253, pp. 143–150, Aug. 1994.
- [20] E. Han, L. Do, N. Yamamoto, and M. Fujihira, *Crystallization of organic thin film for electroluminescent devices*, Thin Solid Films, vol. 273, no. 1/2, pp. 202–208, Feb. 1996.
- [21] D. F. O'Brien, P. Burrows, S. R. Forrest, B. E. Koene, D. E. Loy, and M. E. Thompson, *Hole transporting materials with high glass transition temperatures for use in organic light-emitting devices*, Adv. Mater., vol. 10, no. 14, pp. 1108–1112, Oct. 1998.
- [22] F. Steuber, J. Staudigel, M. Stossel, J. Simmerer, A. Winnacker, H. Spreitzer, F. Weissortel, and J. Salbeck, *White light emission from organic LED's utilizing spiro compounds with high-temperature stability*, Adv. Mater., vol. 12, no. 2, pp. 130–133, Jan. 2000.
- [23] S. Tokito, H. Tanaka, K. Noda, A. Okada, and Y. Taga, *Temperature dependance of electroluminescent characteristics in the devices fabricated with novel triphenylamine derivatives*, IEEE Trans. Electron Devices, vol. 44, no. 8, pp. 1239–1244, Aug. 1997.
- [24] C. Adachi, K. Nagai, and N. Tamoto, *Molecular design of hole transport materials for obtaining high durability in organic electroluminescent diodes*, Appl. Phys. Lett., vol. 66, no. 20, pp. 2679–2681, May 1995.
- [25] H. Aziz, Z. Popovic, N. Hu, P. Dos Anjos, and A. Ioannidis, *Degradation of tris(8-hydroxyquinoline) (ALQ)-based organic light emitting devices (OLED's)*, in Proc. SPIE—Organic Light Emitting Materials Devices IV, San Diego, CA, Jul. 30–Aug., 4, 2000, vol. 4105, pp. 251–255.

- [26] Z. D. Popovic, H. Aziz, N. Hu, A. Ioannidis, and P. N. M. dos Anjos, *Simultaneous electroluminescence and photoluminescence aging studies of tris(8-hydroxyquinoline) aluminum-based organic light-emitting devices*, J. Appl. Phys., vol. 89, no. 8, pp. 4673–4675, Apr. 2001.
- [27] D. Y. Kondakov, J. R. Sandifer, C. V. Tang, and H. J. Young, *Nonradiative recombination centers and electrical aging of organic light-emitting diodes: Direct connection between accumulation of trapped charge and luminance loss*, J. Appl. Phys., vol. 93, no. 2, pp. 1108–1119, Jan. 2003.
- [28] H. Aziz, Z. D. Popovic, N. X. Hu, A. M. Hor, and G. Xu, *Degradation mechanism of small molecule-based organic light-emitting devices*, Science, vol. 283, no. 5409, pp. 1900–1902, Mar. 1990.
- [29] F. Papadimitrakopoulos, X.-M. Zhang, D. L. Thomsen, III, and K. A. Higginson, *A chemical failure mechanism for aluminum (III) 8-hydroxyquinoline light emitting devices*, Chem. Mater., vol. 8, no. 7, pp. 1363–1365, Jul. 1996.
- [30] S. Berleb, W. Brütting, and G. Paasch, *Interfacial charges and electric field distribution in organic hetero-layer light-emitting devices*, Organ. Electron., vol. 1, no. 1, pp. 41–47, Dec. 2000.
- [31] Jurchescu, O. D., Baas J., Palstra, T. T. M., *App. Phys. Lett.*, 2004, 84, 3061.
- [32] N. Karl: *Charge Carrier Mobility in Organic Crystals*, in R. Farchioni, G. Grosso (Eds.), Organic Electronic Materials, Springer 2001.
- [33] W. Brütting, S. Berleb, A. Mückl, *Organic Electronics* 2, 1 (2001).
- [34] M.A. Baldo, S.R. Forrest, *Phys. Rev. B* 64, 085201 (2001).
- [35] R. Kersting, U. Lemmer, R. F. Mahrt, K. Leo, H. Kurz, H. Bässler, O. Göbel, *Phys. Rev. Lett.*, 1993, 70, 3820.

- [36] R. N. Marks, R. H. Michel, W. Gebauer, R. Zamboni, C. Taliani, R. F. Mahrt, and M. Hopmeier, *J. Phys. Chem. B*, 1998, 102, 7563.
- [37] Wohlgenannt, M. Tandon, K. Mazumdar, S. Ramasesha, S. Vardeny, Z.V. *Formation Crosssections of Singlet and Triplet Excitons in p-conjugated Polymers*. Nature 2001, 409, 494-497.
- [38] Yang X., Neher D. *Polymer Electrophosphorescence Devices. In Organic Light-Emitting Devices*; Müllen, K., Scherf, U., Eds.; Wiley-VCH: Weinheim, 2006; p. 333.
- [39] M. Braun, J. Gmeiner, M. Tzolov, M. Cölle, F. Meyer, W. Milius, H. Hillebrecht, O. Wendland, J. von Schütz, and W. Brütting, *J. Chem. Phys.* 114, 9625 (2001).
- [40] M. Cölle, J. Gmeiner, W. Milius, H. Hillebrecht, and W. Brütting, *Adv. Funct. Mater.* 13, 108 (2003).
- [41] L.S. Sapochak, A. Padmaperuma, N. Washton, F. Endrino, G.T. Schmett, J. Marshall, D. Fogarty, and S.R. Forrest, *J. Am. Chem. Soc.* 123, 6300 (2001).
- [42] K. Naito, and A. Miura., *J. Phys. Chem.* 97, 6240 (1993).
- [43] C. Tang, and S. VanSlyke, *Appl. Phys. Lett.* 51, 913 (1987).
- [44] M. Cölle, R.E. Dinnebier, and W. Brütting, *Chem. Comm.* 23, 2908 (2002).
- [45] G. Kushto, Y. Iizumi, J. Kido, and Z. Kafafi, *J. Phys. Chem. A* 104, 3670 (2000).
- [46] A. Curioni, M. Boero, and W. Andreoni, *Chem. Phys. Lett.* 294, 263 (1998).
- [47] S. Berleb, W. Brütting, and G. Paasch, *Interfacial charges and electric field distribution in organic hetero-layer light-emitting devices*, Organ.

- Electron., vol. 1, no. 1, pp. 41–47, Dec. 2000.
- [48] D. Y. Kondakov, J. R. Sandifer, C. V. Tang, and H. J. Young, *Nonradiative recombination centers and electrical aging of organic light-emitting diodes: Direct connection between accumulation of trapped charge and luminance loss*, J. Appl. Phys., vol. 93, no. 2, pp. 1108–1119, Jan. 2003.
- [49] H. Aziz, Z. D. Popovic, N. X. Hu, A. M. Hor, and G. Xu, *Degradation mechanism of small molecule-based organic light-emitting devices*, Science, vol. 283, no. 5409, pp. 1900–1902, Mar. 1990.
- [50] T. Yamada, F. Rohlfig, and T. Tsutsui, *Distribution of average electric field in tris-(8-hydroxyquinoline)aluminum and 4,4'-bis[N-(1-naphthyl)-N-phenylamino]-biphenyl-based double-layer light-emitting diodes*, Jpn. J. Appl. Phys., vol. 39, no. 3A, pp. 1382–1386, Mar. 2000.
- [51] R. Martin, J. Kress, I. Campbell, and D. Smith, *Phys. Rev. B* 61, 15804 (2000)
- [52] M. Amati, and F. Lelej, *Chem. Phys. Lett.* 363, 451 (2002).
- [53] M. Utz, C. Chen, M. Morton, and F. Papadimitrakopoulos, *J. Am. Chem. Soc.* 125, 1371 (2003).
- [54] M. Cölle, S. Forero-Lenger, J. Gmeiner, and W. Brütting, *Phys. Chem. Chem. Phys.* 5, 2958 (2003).
- [55] W. Massa, (2000). *Crystal structure determination*. Springer, Berlin.
- [56] G. Gustafsson, Y. Cao, G. M. Treacy, F. Klavetter, N. Colaneri, and A. J. Heeger, *Nature* 357, 447 (1992).
- [57] (a) W. Reiss, in *Organic Electroluminescent Materials and Devices*, edited by S. Miyata and H. S. Nalwa, Chap. 2 (Gordon and Breach, NY, 1997); (b) www.erichsen.de.

- [58] E. Haskal, P. C. Duineveld, C. Liedenbaum, P. v. d. Weijer, J. N. Huiberts, and R. J. Visser, in *Organic Electronic and Photonic Materials and Devices*, Proc. Mat. Res. Soc. Symp. 660 (2001), in press.
- [59] M. Utz, M. Nandagopal, M. Mathai, and F. Papadimitrakopoulos, *Appl. Phys. Lett.* 83, 4023 (2003).
- [60] M. Rajeswaran, T.N. Blanton and K.P. Klubek, *Z.Kristallogr. NCS* 218, 439 (2003).
- [61] M. Cölle, (2004). *The Electroluminescent Material Alq₃*, Logos-Verlag, Berlin.
- [62] M. Amati and F. Leij, *Chem. Phys. Lett.*, 358, 144 (2002)
- [63] M. Cölle, C. Gärditz and M. Braun, *J. Appl. Phys.*, 96, 6133 (2004).
- [64] M. A. Baldo and S. R. Forrest, *Phys. Rev. B* 62, 10958 (2000).
- [65] G. G. Malliaras, Y. Shen, and J. C. Scott, in *Organic Light-Emitting Materials and Devices IV*, edited by Z. H. Kafafi, Proc. SPIE 4105, xxx (2000).
- [66] (a) H. Tokailin, H. Higashi, and C. Hosokawa, U. S. Patent No. 5,130,630 (1992); (b) H. Tokailin, M. Matsuura, H. Higashi, C. Hosokawa and T. Kusumoto, in *Electroluminescence: New Materials for Devices and Displays*, edited by E. M. Conwell, M. Stolka, and M. R. Miller, SPIE 1910, 38 (1993); (c) C. Hosokawa, H. Tokailin, H. Higashi, and T. Kusumoto, *J. Appl. Phys.* 78, 5831 (1995); (d) C. Hosokawa, H. Higashi, H. Nakamura, and T. Kusumoto, *Appl. Phys. Lett.* 67, 3853 (1995);
- [67] G. Parthasarathy, P. E. Burrows, V. Khalfin, V. G. Kozlov, and S. R. Forrest, *Appl. Phys. Lett.* 72, 2138 1(998).
- [68] J.-S. Kim, P. K. H. Ho, N. C. Greenham, and R. H. Friend, *J. Appl. Phys.* 88, 1073 (2000).

- [69] M. Wohlgenannt, Kunj Tandon, S. Mazumdar, S. Ramasesha, and Z. V. Vardeny, *Nature* 409, 494 (2001).
- [70] Z. Shuai, D. Beljonne, R. J. Silbey, and J. L. Bredas, *Phys. Rev. Lett.* 84, 131 (2000).
- [71] H. Spreitzer, H. Schenk, J. Salbeck, F. Weissoertel, H. Riel, and W. Reiss, in *Organic Light Emitting Materials and Devices III*, edited by Z. H. Kafafi, Proc. SPIE 3797, 316 (SPIE, Bellingham, WA, 1999).
- [72] Y. Shirota, *J. Mater. Chem.* 10, 1 (2000).
- [73] S. V. Novikov, D. H. Dunlap, V. M. Kenkre, P. E. Parris and A. V. Vannikov, *Phys. Rev. Lett.* 81, 4472 (1998).
- [74] S. W. DeLeeuw, J. W. Perram and E. R. Smith, *Proc. R. Soc. London A* 373, 27 (1989).
- [75] P. S. Davids, Sh. M. Kogan, I. D. Parker, and D. L. Smith, *Appl. Phys. Lett.* 69, 2270 (1996).
- [76] Yu.N.Gartstein and E.M.Conwell, *Chem.Phys. Lett.* 255, 93 (1996).
- [77] E.M. Conwell and M.W. Wu, *Appl. Phys. Lett.* 70, 1867 (1997).
- [78] V. N. Savvate'ev and Z. Ovadyahu, *Slow Relaxation in a Fermi Glass, in Hopping and Related Phenomena: Proceedings of the 6th International Conference on Hopping and Related Phenomena*, edited by O. Millo and Z. Ovadyahu, p. 44 (1995).
- [79] (a) A. J. Pal, R. Osterbacka, K. M. Kallman, and H. Stubb. *Appl. Phys. Lett.* 71, 228 (1997); (b) S. Karg, V. Dyakonov, M. Meier, W. Reiss, G.Paasch, *Synth. Met.* 67, 165 (1994).
- [80] (a) S. Naka, H. Okada, H. Onnagawa, Y. Yamaguchi, and T. Tsutsui, *Synth. Met.* 111-112, 331 (2000); (b) B. J. Chen, W. Y. Lai, Z. Q. Gao, C. S. Lee, S. T. Lee, and W. A. Gambling, *Appl. Phys. Lett.* 75,

4010 (1999); (c) A. J. Campbell, D. D. C. Bradley, H. Antoniadis, M. Inbasekaran, W. W. Wu, and E. P. Woo, *Appl. Phys. Lett.* 76, 1734 (2000); (d) E.W. Forsythe, M. A. Abkowitz, Y. Gao and C.W. Tang, *J. Vac. Sci. Tech. A* 18, 1869 (2000); (e) H. Meyer, D. Haarer, H. Naarmann, and H. H. Horhold, *Phys. Rev. B* 52, 2587 (1995); (f) E. Lebedev, Th. Dittrich, V. Petrova-Koch, S. Karg, and W. Brutting, *Appl. Phys. Lett.* 71, 2686 (1997); (g) P. M. Borsenberger, L. Pautimeier, and H. Bässler, *J. Chem. Phys.* 95, 1258 (1991).

[81] H. Ishii, K. Sugiyama, E. Ito, and K. Seki, *Adv. Mater.* 11, 605 (1999).

[82] J. Kalinowski, in *Organic Electroluminescent Materials and Devices*, edited by S. Miyata and H. S. Nalwa (Gordon and Breach, Amsterdam, 1997), Chap. 1.

[83] Y. Sato, S. Ichinosawa, and H. Kanai, *IEEE Journal of Selected Topics in Quantum Electronics* 4, 40 (1998). Miyata and H. S. Nalwa (Gordon and Breach, Amsterdam, 1997), Chap. 1.

[84] B. H. Cumpston and K. F. Jensen, *Appl. Phys. Lett.* 69, 3941 (1996).

[85] Stefano Toffanin: *Multifunctional organic semiconductors as active materials in electronic and optoelectronic devices.*